TECHNISCHE
MECHANIK

ICMM6

6th International Conference
on Material Modelling | 2019

TECHNISCHE MECHANIK

Wissenschaftliche Zeitschrift für Grundlagen und Anwendungen der Technischen Mechanik
Scientific Journal for Fundamentals and Applications of Engineering Mechanics

The journal **Technische Mechanik** publishes refereed original articles on Engineering Mechanics in its broadest sense. It is intended to provide a forum for a rapid transfer of research results to industry and science. In that sense contributions are encouraged which demonstrate the practical application of new results and scientific findings.

In der **Technischen Mechanik** werden begutachtete Beiträge aus allen Gebieten der Mechanik publiziert. Ein Hauptanliegen besteht in der raschen Verfügbarmachung von Forschungsergebnissen für Industrie und Wissenschaft. In diesem Sinne werden vor allem auch solche Beiträge bevorzugt, die neben neuen Ergebnissen und Erkenntnissen auch deren praktische Anwendung beinhalten.

Inhalt / Contents

Preface

This volume contains selected papers presented at the 6th International Conference on Material Modeling (ICMM6), which took place June 26-28 2019 at the campus of Lund University, Sweden. By all meaningful measures, ICMM6 was a great success, attracting 161 participants from almost 30 countries (ranging from senior colleagues to graduate students) and featuring a technical program that well reflected the cutting-edge of materials modeling research.

ICMM6 included thematic sessions on the following topics

- linear elasticity and viscoelasticity
- nonlinear elasticity
- plasticity and viscoplasticity
- experimental identification and material characterization
- Cosserat, micromorphic and gradient materials
- atomistic/continuum transition on the nanoscale
- optimization and inverse problems in multiscale modeling
- granular materials and particle systems
- biomechanics and biomaterials
- electronic materials
- heterogeneous materials
- coupled field problems
- creep, damage and fatigue
- numerical aspects of material modeling.

The aim of the ICMM conferences is to bring together researchers from different fields of material modeling and material characterization, and to cover essentially all aspects of material modeling thus providing the opportunity for interactions between scientists working in different subareas of material mechanics who otherwise would not come into contact with each other.

All participants were invited to submit full-length papers to a special issue of *Technische Mechanik*. The contributed papers that appear in this volume, represent a cross-section of the conference and have all been submitted to a highly valuated peer-review process.

Matti Ristinmaa, Albrecht Bertram

Lund University, Sweden   photo © Kennet Ruona

The participants of ICMM6, Lund, Sweden, 2019   photo © Stefanos Athanasopoulus

A Hybrid Approach to Describe the Elastic-Plastic Deformation Behavior of 2D Cellular Solids Including Damage Effects

Martin Abendroth[1]⋆, Geralf Hütter[1], Christoph Settgast[1], Alexander Malik[1], Björn Kiefer[1], and Meinhard Kuna[1]

[1] TU Bergakademie Freiberg, Institute of Mechanics and Fluiddynamics, Lampadiusstraße 4, 09599 Freiberg, Germany

Abstract: The constitutive description of the inelastic deformation behavior of porous media is a challenging task. The complex hardening behavior (simultaneous isotropic, kinematic and distortional hardening) and anisotropic yielding depend strongly on the micro-structure of the porous medium and the inelastic behavior of its bulk material.

In previous work, the authors presented a homogenized material model for an elastic-plastic material at the microscopic scale based on an adapted yield function to describe the elastic-plastic deformation behavior, including damage, of open-cell structures. In this approach, the shape of the yield function is not specified completely a priori. The proper shape is rather found by regression with results of cell model simulations using neural networks.

The aim of this contribution is to demonstrate that this hybrid approach shows good agreement with direct simulations. The necessary size of the neural network, the number of training data and the computational efficiency are also discussed. It can be concluded that this model can be used to analyze the deformation behavior of porous structures while considering the coupling of plastic deformations and damage of the bulk material.

Keywords: porous media, elastic-plastic deformation, damage, constitutive modeling, neural network

1 Introduction

Porous media have a wide range of application. This contribution was made within the framework of the DFG-Collaborative Research Center (CRC 920), where ceramic foams are investigated as filters for metal melt filtration applications (Emmel and Aneziris, 2012). Due to the very high application temperatures (1650°C for steel melt filtration) even the ceramic filters made of alumina (Al_2O_3) undergo inelastic deformations during loading (Solarek et al., 2016), which is why a constitutive material model is needed to simulate the mechanical behavior of such structures and to predict strength and deformation prior to an experiment. But independent of the application, the macroscopic deformation behavior of porous media is complex and challenging, especially if homogenization approaches are considered. The micro-structure has a large influence on the shape of yield functions (Wang and McDowell, 2005), even if the bulk material is considered to be a *simple* material (Demiray et al., 2007; Storm et al., 2015), because isotropic, kinematic and distortional hardening can be observed.

To investigate the behavior of porous structures, representative volume elements (RVEs) of idealized periodic structures are often used to reduce the overall complexity. In many cases simple structures are chosen as RVEs, such as Kelvin cells, as done by (Demiray et al., 2007; Storm et al., 2015).

But in general each structure can have its own special yield surface and corresponding evolution, so that a homogenized constitutive material model is needed which is adaptable to changes of the RVE micro-structure and bulk material behavior. There are different approaches to tackle such problems. Models for direct simulations of complex structures have a very large number of degrees of freedom (DOF) and therefore require a large numerical effort. Also FE^2 approaches, where the solution of an RVE is applied for each local point of the porous component, are very expensive. On the other hand, phenomenological constitutive relations for specific micro-structures are hard to find.

In this contribution, an alternative approach is presented, in which neural networks (NN) are used to partially represent the constitutive relations, because of their adaptability to the given problem. (Liang and Chandrashekhara, 2008) and (Javadi and Rezania, 2009) used NNs as a constitutive model for the elastic behavior of elastomeric foams and for soils. (Abendroth and Kuna, 2006) used NNs as replacement for a material test procedure to identify material parameters for constitutive models. A behavior for a combined material (soils) was modeled using NNs by (Wojciechowski, 2011). (Hashash et al., 2004) implemented NNs including their derivatives for elastic-plastic material behavior to compute the consistent algorithmic material tangent. A cyclic plastic analysis considering kinematic and isotropic hardening using a NN based material law was presented by (Furukawa and Hoffman, 2004).

There exist a number of freely available codes for neural network applications, ranging from packages with rather basic functionality such as FFNET from (Wojciechowski, 2011), up to very complex solutions as Googles TensorFlow. For the problems discussed here FFNET is perfectly suited, since it allows to compute derivatives for single hidden layer networks and to export a trained network as FORTRAN code, which can be compiled together with a UMAT for the finite element code ABAQUS.

This contribution is based on previous approaches. In (Settgast et al., 2019a) NNs represent the inelastic stress strain relation directly. In (Settgast et al., 2018) a hybrid approach was presented, where NNs are used as an adaptable part of specific yield

(a) <111>-view   (b) <$\bar{1}$10>-view   (c) Used 2D-RVE (relative density of $\varrho = 36.5\,\%$)
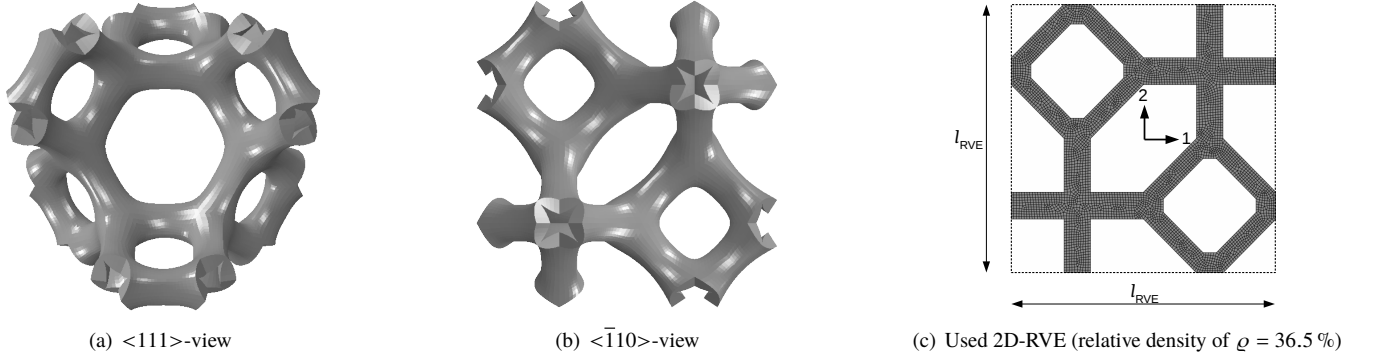
Fig. 1: From Kelvin-cell in 3D to used 2D-RVE as an idealized periodic structure.

surfaces, which was further improved by considering damage at the micro-scale in (Settgast et al., 2019b). In the present paper also practical issues are discussed, which include the necessary amount of training data, the structures and sizes of the neural networks with regard to the predictive accuracy of the model.

2 Homogenization

2.1 Microstructure and macroscopic values

A typical 3D structure used as RVE for an open cell foam is the Kelvin cell, see Fig. 1. To keep the effort for this work within limits, a simplified 2D structure, as depicted in Fig. 1(c), is used, which is derived from the Kelvin cell. It should be mentioned that the 2D projection of the Kelvin foam does not reflect the properties of the 3D Kelvin foam model, but serves as a proper model structure for the presented approach. The structure is periodic, whereas periodic boundary conditions

$$u = \overline{\epsilon} \cdot x + \tilde{u} \tag{1}$$

are applied to control the effective deformation $\overline{\epsilon}$ in finite element simulations. Here, $\tilde{u}$ denotes periodic fluctuations, which are equal at homologous points (x^- and x^+) at the boundary of the RVE, i.e.

$$\tilde{u}(x^-) = \tilde{u}(x^+) \tag{2}$$

The periodic displacement fluctuations lead to the definition of equations for boundary nodes

$$u(x^+) - u(x^-) = \overline{\epsilon} \cdot \left(x^+ - x^- \right) . \tag{3}$$

Detailed information about the implementation of periodic boundary conditions and the corresponding homogenization theory can be found in (Storm et al., 2013).

Following Hill's homogenization theory, the macroscopic values for stress $\overline{\sigma}$, strain $\overline{\epsilon}$, and dissipation due to damage $\overline{D}$ are the volume weighted averages of the corresponding values at micro scale.

$$\overline{\sigma} = \frac{1}{V_{\text{RVE}}} \int_{V_{\text{RVE}}} \sigma \, dV, \tag{4}$$

$$\overline{\epsilon} = \frac{1}{V_{\text{RVE}}} \int_{V_{\text{RVE}}} \epsilon \, dV, \quad \text{and} \tag{5}$$

$$\overline{D} = \frac{1}{V_{\text{RVE}}} \int_{V_{\text{RVE}}} D \, dV \tag{6}$$

2.2 Material model for the micro scale

The constitutive equations for the bulk material at the micro scale describe an elastic-plastic material with a Lemaitre-Kachanov-type damage formulation. The linear elastic behavior is defined by Hooke's law

$$\sigma = \mathbb{C}^0 : \epsilon^{\text{el}} = \mathbb{C}^0 : \left(\epsilon - \epsilon^{\text{pl}} \right), \tag{7}$$

where $\mathbb{C}^0$ denotes the isotropic stiffness tensor in the undamaged state defined with the elastic modulus E and Poisson's ratio $\nu = 0.14$. The ideally plastic behavior is described by a von Mises yield condition

$$\Phi(\sigma) = \sigma_{\text{eq}} - \sigma_{\text{Y}} \tag{8}$$

with von Mises equivalent stress σ_{eq} and yield stress $\sigma_Y = 0.061\,E = \text{const}$. Furthermore, an associated flow rule

$$\dot{\boldsymbol{\epsilon}}^{\text{pl}} = \kappa \frac{\partial \Phi}{\partial \boldsymbol{\sigma}} \tag{9}$$

is assumed to hold, with the plastic multiplier κ. The loading-unloading conditions are equivalent to the Karush-Kuhn-Tucker conditions, which are

$$\Phi \le 0, \quad \kappa \ge 0, \quad \Phi\,\kappa = 0. \tag{10}$$

The damage is considered to be isotropic, with a type damage variable D, which affects the stiffness tensor as

$$\boldsymbol{\sigma} = (1 - D)\,\mathbb{C}^0 : \left(\boldsymbol{\epsilon} - \boldsymbol{\epsilon}^{\text{pl}}\right) \tag{11}$$

as well as the local yield stress

$$\Phi(\boldsymbol{\sigma}) = \sigma_{\text{eq}} - (1 - D)\,\sigma_Y. \tag{12}$$

The damage evolution is driven by the equivalent plastic strain rate

$$\dot{D} = \begin{cases} \frac{\sigma_Y l_{\text{element}}}{2\,G} \dot{\epsilon}^{\text{pl}}_{\text{eq}} & \text{if } \epsilon^{\text{pl}}_{\text{eq}} \ge \epsilon^{\text{pl}_0}_{\text{eq}} \\ 0 & \text{else} \end{cases} \tag{13}$$

and controlled by the constants for the finite element size $l_{\text{element}} = 0.01\,l_{\text{RVE}}$, the RVE size $l_{\text{RVE}} = 1\,\text{mm}$, a material constant $G = 150\,\sigma_Y^2 l_{\text{element}}/E$, and the threshold of the equivalent plastic strain $\epsilon^{\text{pl}_0}_{\text{eq}} = 0$, above which damage occurs.

3 Constitutive modeling using neural networks

3.1 Neural network

All functionalities based on neural networks are realized using the `python` library `ffnet` of (Wojciechowski, 2011), which provides tools to create, train and use feed-forward neural networks (FFNN). All networks used in this work have a similar structure. There is an input layer with n neurons, a single hidden layer having m neurons, and an output layer with k neurons as depicted in Fig. 2. The neurons of the hidden and output layers have a sigmoid activation function

$$h(v_j) = \frac{1}{1 + \exp(-v_j)}, \tag{14}$$

with v_j as nodal input value, representing the sum of the weighted activations $w_l h_l$ of the preceding layer, plus a bias b_j for each neuron j:

$$v_j = \sum_l w_l h_l + b_j. \tag{15}$$

The free parameters of such a network are the $n \cdot m + m \cdot k$ weights and $m + k$ biases, which are adjusted to the given problem by a training procedure. The training procedure minimizes the cost function for a training data set $\mathscr{D}_{\mathcal{T}}$:

$$err^{\text{train}} = \frac{1}{2} \sum_{p \in \mathscr{D}_{\mathcal{T}}} \sum_k \left[val_k^{(p)} - \text{NN}_k\left(inp^{(p)}\right) \right]^2, \tag{16}$$

using a truncated Newton method with normalized inputs $inp^{(p)}$ and outputs $out^{(p)} = \text{NN}(inp^{(p)})$ data. The training data set $\mathscr{D}_{\mathcal{T}}$ is a subset of all data $\mathscr{D}_{\mathcal{D}}$, which also contains a validation data set $\mathscr{D}_{\mathcal{V}}$ representing another subset of size α of all data. Validation data however, are not part of the training data set.

$$\mathscr{D}_{\mathcal{T}} \cup \mathscr{D}_{\mathcal{V}} = \mathscr{D}_{\mathcal{D}} \tag{17}$$
$$\mathscr{D}_{\mathcal{T}} \cap \mathscr{D}_{\mathcal{V}} = \varnothing \tag{18}$$
$$|\mathscr{D}_{\mathcal{V}}| = \alpha\,|\mathscr{D}_{\mathcal{D}}| \quad \text{with} \quad 0 < \alpha < 1 \tag{19}$$

Prior to training, all values for weights and biases are set to random values in the range $[-b, b]$, where $b = 2.38/\sqrt{n}$ depends on the number n of incoming weights to a neuron.

3.2 Hybrid approach

This section explains the constitutive relations for the hybrid approach. The elastic response on the macro scale follows Hooke's law

$$\overline{\boldsymbol{\sigma}} = \overline{\mathbb{C}} : \left(\overline{\boldsymbol{\epsilon}} - \overline{\boldsymbol{\epsilon}}^{\text{pl}}\right). \tag{20}$$
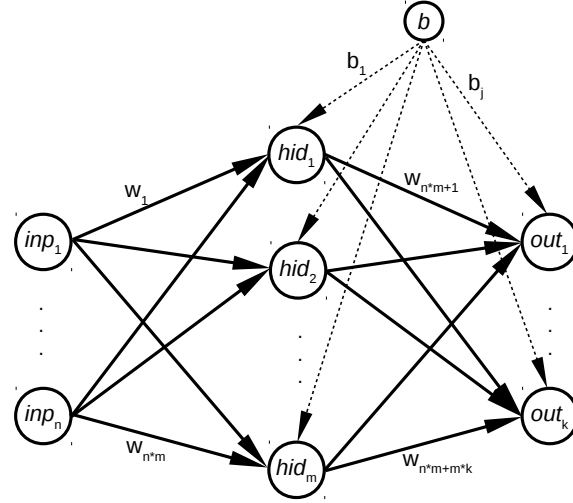
Fig. 2: Structure of the used neural networks (input layer with n neurons, one hidden layer with m neurons and output layer with k neurons, $n \cdot m + m \cdot k$ different weights w are applied at solid arrows and $m + k$ different biases b at dashed arrows).

The components of the effective stiffness tensor $\overline{\mathbb{C}}$ are obtained by three linearly independent load cases for 2D problems or six load cases for 3D problems as described in detail in (Storm et al., 2013). The HELMHOLTZ free energy is assumed in the form

$$\overline{\Psi} = \frac{1}{2}\left(\overline{\boldsymbol{\epsilon}} - \overline{\boldsymbol{\epsilon}}^{\mathrm{pl}}\right) : \overline{\mathbb{C}} : \left(\overline{\boldsymbol{\epsilon}} - \overline{\boldsymbol{\epsilon}}^{\mathrm{pl}}\right). \tag{21}$$

The yield function is adaptable, which means a specific shape is not a priori set. More specifically, it is assumed:

$$\overline{\Phi}^{\mathrm{NN}} = \hat{\overline{\sigma}} - \mathrm{NN}^{\hat{\overline{\sigma}}}(\overline{\epsilon}_{\mathrm{eq}}^{\mathrm{pl}}, \overline{I}_1^{\epsilon}, \left|\overline{\epsilon}_{12}^{\mathrm{pl}}\right|). \tag{22}$$

Here $\hat{\overline{\sigma}} := \|\overline{\boldsymbol{\sigma}}\| = \sqrt{\overline{\boldsymbol{\sigma}} : \overline{\boldsymbol{\sigma}}}$ and $\mathrm{NN}^{\hat{\overline{\sigma}}}(\overline{\epsilon}_{\mathrm{eq}}^{\mathrm{pl}}, \overline{I}_1^{\epsilon}, \left|\overline{\epsilon}_{12}^{\mathrm{pl}}\right|)$ denotes a neural network function having effective equivalent plastic strain $\overline{\epsilon}_{\mathrm{eq}}^{\mathrm{pl}}$, the volumetric plastic strain $\overline{I}_1^{\epsilon}$ and the absolute shear strain $\left|\overline{\epsilon}_{12}^{\mathrm{pl}}\right|$ as arguments to consider isotropic, distortional and volumetric hardening. For a three dimensional case, or other porous structures, the arguments (inputs) for neural networks may be chosen differently. Suitable inputs can be the invariants of effective stress or strain tensors, angles in strain space as well as additional internal variables which characterize the deformation state of the RVE. For highly porous materials, a non-associated flow rule is appropriate

$$\dot{\overline{\boldsymbol{\epsilon}}}^{\mathrm{pl}} = \overline{\kappa}\overline{\boldsymbol{N}}^{\mathrm{pl}} = \dot{\overline{\epsilon}}_{\mathrm{eq}}^{\mathrm{pl}} \underbrace{\frac{\overline{\boldsymbol{N}}^{\mathrm{pl}}}{\|\overline{\boldsymbol{N}}^{\mathrm{pl}}\|}}_{\tilde{\overline{\boldsymbol{N}}}^{\mathrm{pl}}}, \tag{23}$$

with the normalized flow direction

$$\overline{\boldsymbol{N}}^{\mathrm{pl}} = \frac{1}{2}\left(\sin\overline{\alpha}_{\overline{n}} + \cos\overline{\alpha}_{\overline{n}}\right)\boldsymbol{I} + \frac{1}{2}\left(\cos\overline{\alpha}_{\overline{n}} - \sin\overline{\alpha}_{\overline{n}}\right)\frac{\overline{\boldsymbol{s}}}{\sqrt{J_2^{\overline{\boldsymbol{\sigma}}}}}, \tag{24}$$

which is composed of a spherical and deviatoric part. Here, $\boldsymbol{I}$ denotes the unit tensor, $\overline{\boldsymbol{s}}$ the deviatoric stress and $J_2^{\overline{\boldsymbol{\sigma}}}$ the second stress invariant. The ratio of spherical and deviatoric parts is expressed by a second neural network, also with the same general set of arguments $\overline{\epsilon}_{\mathrm{eq}}^{\mathrm{pl}}, \overline{I}_1^{\epsilon}$ and $\left|\overline{\epsilon}_{12}^{\mathrm{pl}}\right|$.

$$\overline{\alpha}_{\overline{n}} = \mathrm{NN}^{\overline{\boldsymbol{N}}}(\overline{\epsilon}_{\mathrm{eq}}^{\mathrm{pl}}, \overline{I}_1^{\epsilon}, \left|\overline{\epsilon}_{12}^{\mathrm{pl}}\right|) \tag{25}$$

In equation (24) it is assumed that the principle axes of stress and plastic flow coincide (Settgast et al., 2019b). The principle structure of all networks is similar to that indicated in Fig. 2. They differ only in the number of neurons in the hidden and output layers.

3.3 Extension for damage

The damage evolution at the macro-scale is assumed to be anisotropic, although it is modeled isotropically at the micro-scale. $\overline{\mathbb{C}}$ is considered as an internal state variable and its changes are described using a third neural network

$$\dot{\overline{\mathbb{C}}} = \dot{\overline{\epsilon}}_{\mathrm{eq}}^{\mathrm{pl}} \, \mathbf{NN}^{\dot{\overline{\mathbb{C}}}}(\overline{\epsilon}_{\mathrm{eq}}^{\mathrm{pl}}, \overline{I}_1^{\epsilon}, \left|\overline{\epsilon}_{12}^{\mathrm{pl}}\right|), \tag{26}$$
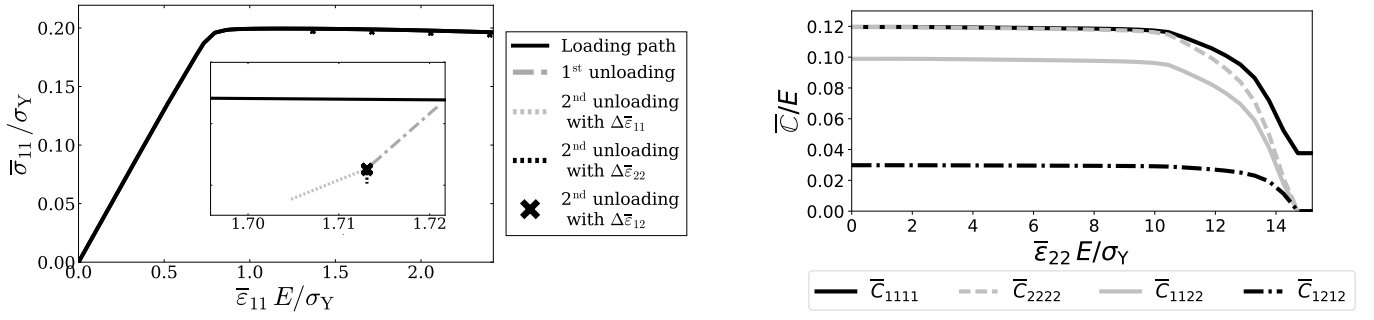
Fig. 3: One specific loading path with unloading steps for the extraction of the coefficients of the effective stiffness tensor $\overline{\mathbb{C}}$ (left) and the evolution of the coefficients of $\overline{\mathbb{C}}$ for uniaxial stretching in 2-direction (right).

with same arguments as the other two. Consequently, the dissipation equation of the model takes the form:

$$\dot{\overline{D}} = \overline{\sigma} : \dot{\overline{\epsilon}}^{\mathrm{pl}} - \frac{\partial \overline{\Psi}}{\partial \dot{\overline{\mathbb{C}}}} :: \dot{\overline{\mathbb{C}}} = \overline{\sigma} : \dot{\overline{\epsilon}}^{\mathrm{pl}} - \frac{1}{2} \left(\overline{\epsilon} - \overline{\epsilon}^{\mathrm{pl}} \right) : \mathbf{NN}^{\dot{\overline{\mathbb{C}}}} (\overline{\epsilon}^{\mathrm{pl}}_{\mathrm{eq}}, \overline{I}^{\epsilon}_1, \left| \overline{\epsilon}^{\mathrm{pl}}_{12} \right|) : \left(\overline{\epsilon} - \overline{\epsilon}^{\mathrm{pl}} \right) \dot{\overline{\epsilon}}^{\mathrm{pl}}_{\mathrm{eq}}. \tag{27}$$

It should be noted that $\dot{\overline{D}} \geq 0$ is not a priori guaranteed from the macroscopic model. However, the training data are, in this case, obtained from a thermodynamically consistent model. Nevertheless, the values of $\dot{\overline{D}}$ are checked during the evaluation of the homogenized material model.

3.4 Generation of training data for the neural networks

To generate all data $\mathscr{D}_{\mathcal{D}}$, a number of RVE simulations are performed. To this end, proportional load paths

$$\overline{\epsilon} = \lambda \, \overline{\epsilon}^* \tag{28}$$

are defined, with $\lambda \in \mathscr{R}^+_0$ and $\lambda = 1$ for initial yielding at the micro-scale. For proportional load paths, only isotropic and distortional hardening can be evaluated. To catch kinematic hardening, non-proportional load paths with checks for yielding at the micro-scale would be necessary. For the 2D structure depicted in Fig. 1(c), the load path in strain space is defined using two angles ϕ and ψ, i.e.

$$\overline{\epsilon} = \mathbf{R}^T \mathbf{A} \mathbf{R} \quad \text{with} \quad \mathbf{A} = \begin{bmatrix} \cos \phi & 0 \\ 0 & \sin \phi \end{bmatrix} \quad \text{and} \quad \mathbf{R} = \begin{bmatrix} \cos \psi & -\sin \psi \\ \sin \psi & \cos \psi \end{bmatrix}, \tag{29}$$

rastered with $\Delta \phi = \Delta \psi$. The step sizes $\Delta \phi$, $\Delta \psi$ and $\Delta \lambda$ define the number of data points available for training and validation. For each load increment, effective stress $\overline{\sigma}$ and strain $\overline{\epsilon}$ are determined and it is checked whether local yielding occurs. If yielding happens at the micro-scale, then $\overline{\Phi} = 0$ and the corresponding stress $\overline{\sigma}$ and the input data ϕ, ψ and $\overline{\epsilon}^{\mathrm{pl}}_{\mathrm{eq}}$ are appended to a data set which is used to train the network $\mathbf{NN}^{\|\overline{\sigma}\|}$. The choice of ϕ and ψ as input data is motivated by the fact that it contains equivalent information about the strain direction as $\overline{I}^{\epsilon}_1$ and $\left| \overline{\epsilon}^{\mathrm{pl}}_{12} \right|$. The plastic strain is determined using

$$\overline{\epsilon}^{\mathrm{pl}} = \overline{\epsilon} - \overline{\mathbb{C}}^{-1} : \overline{\sigma}, \tag{30}$$

which is further used to compute the flow direction

$$\overline{\breve{N}}^{\mathrm{pl}} := \frac{\dot{\overline{\epsilon}}^{\mathrm{pl}}}{\dot{\overline{\epsilon}}^{\mathrm{pl}}_{\mathrm{eq}}}. \tag{31}$$

In Eqn. (30), the actual stiffness tensor is required. Therefore, a partial unloading of the RVE is simulated, making sure that its stress state falls within the elastic limit. From this state $\overline{\epsilon}^{(0)}$, three additional load cases with load increments $\Delta \overline{\epsilon}^{(1)} = [\epsilon_0, 0, 0]$, $\Delta \overline{\epsilon}^{(2)} = [0, \epsilon_0, 0]$, and $\Delta \overline{\epsilon}^{(3)} = [0, 0, \epsilon_0]$ are simulated. From the resulting stress increments $\Delta \overline{\sigma}^{(i)}$ all coefficients of the stiffness tensor can be determined using

$$\overline{\mathbb{C}}_{i1} = \frac{\Delta \overline{\sigma}^{(1)}}{\epsilon_0}, \quad \overline{\mathbb{C}}_{i2} = \frac{\Delta \overline{\sigma}^{(2)}}{\epsilon_0}, \quad \overline{\mathbb{C}}_{i3} = \frac{\Delta \overline{\sigma}^{(3)}}{\epsilon_0}, \quad i \in [1, 2, 3]. \tag{32}$$

Also, ϵ_0 is chosen here such that the resulting stress state is inside the elastic limit. The procedure to extract values of $\overline{\mathbb{C}}$ and the resulting coefficients for a single loading path are shown in Fig. 3, which also indicates the evolving anisotropy of the RVE if damage is considered at the micro-scale. A schematic representation of the whole procedure to generate data for neural network training is shown in Fig. 4.

In this case, the entire data set used for training and validation $\mathscr{D}_{\mathcal{D}}$ is generated using $\Delta \phi = \Delta \psi = 10°$ and $\Delta \lambda = 0.1$ for the ranges $\phi \in [0°, 180°$, $\psi \in [0°, 90°]$ and $\lambda \in [1, 10]$, resulting in 32400 samples.

M. Abendroth, G. Hütter, C. Settgast, A. Malik, B. Kiefer, and M. Kuna

Tech. Mech., Vol. 40, Is. 1, (2020), 5–14
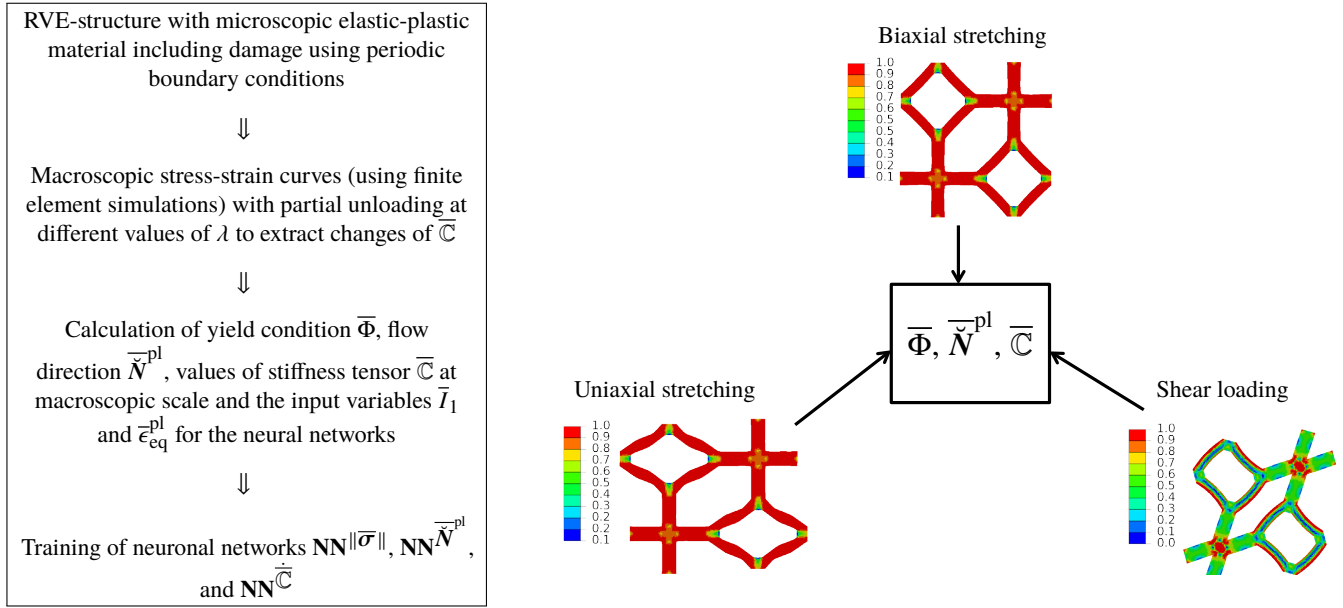
Fig. 4: Steps involved in the generation of the neural networks for the description of the elastic-plastic deformation behavior and damage at the microscopic scale of porous structures, illustrated for the discussed idealized 2D cellular structures.
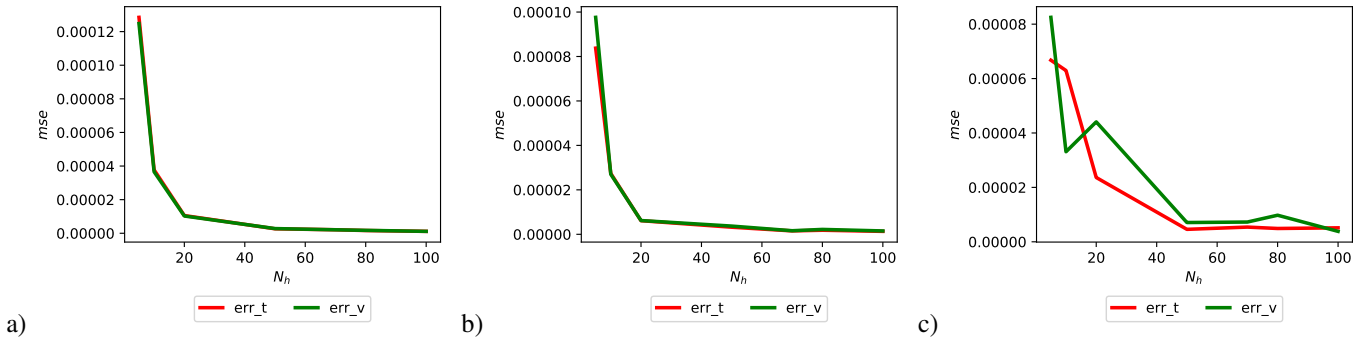
Fig. 5: Errors after training depending on the number of neurons in the hidden layer: a) for $\mathbf{NN}^{\|\overline{\boldsymbol{\sigma}}\|}$, b) for $\mathbf{NN}^{\overline{\breve{N}}^{\mathrm{pl}}}$, c) for $\mathbf{NN}^{\dot{\overline{\mathbb{C}}}}$.
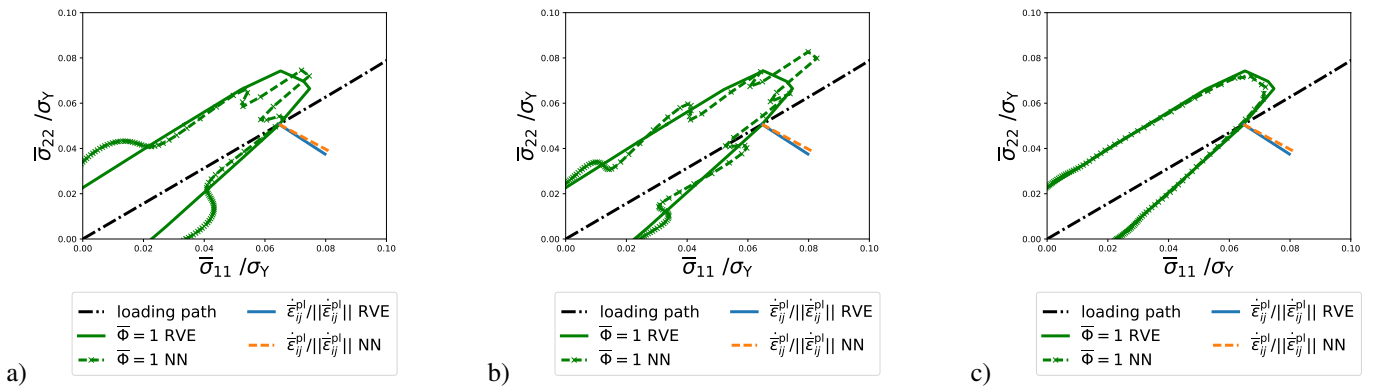
Fig. 6: Approximation quality for the initial yield surface and a loading direction depending on the number neurons in the hidden layer: a) 20, b) 50 and c) 80 neurons.
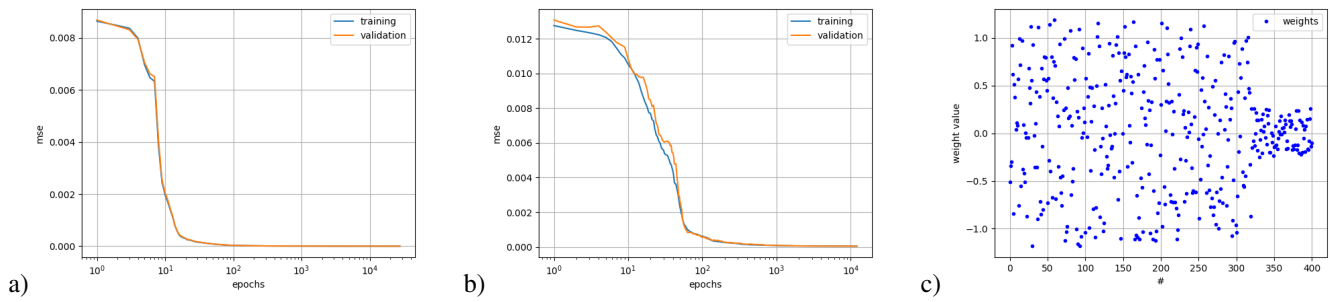
Fig. 7: Error evolution for training and validation data: a) for $\mathbf{NN}^{\|\overline{\boldsymbol{\sigma}}\|}$, b) for $\mathbf{NN}^{\dot{\overline{\tilde{\boldsymbol{N}}}}^{\text{pl}}}$., whereas c) shows the distribution of weight values for $\mathbf{NN}^{\|\overline{\boldsymbol{\sigma}}\|}$.

3.5 Accuracy and numerical effort

The accuracy of a trained NN crucially depends on the number of neurons N_{h} within the network. It should be large enough to represent the complexity of the problem, but small enough to avoid , which is indicated by an increasing error for validation data for an increasing number of neurons. For the present study, the number of neurons within the hidden layer was varied between 5 and 100. Fig. 5 shows the mean square error as a function of the number of hidden neurons for the three different networks after training. It is evident that for the specific problem a number of 80 hidden neurons is a good choice for $\mathbf{NN}^{\|\overline{\boldsymbol{\sigma}}\|}$ and $\mathbf{NN}^{\dot{\overline{\tilde{\boldsymbol{N}}}}^{\text{pl}}}$, whereas 50 hidden neurons are sufficient for $\mathbf{NN}^{\dot{\overline{\mathbb{C}}}}$. The mean square error after training for all networks is around $5 \cdot 10^{-6}$, which corresponds to an absolute error of $\approx 0.2\%$.

Fig. 6 shows the neural network prediction of the initial yield surface. Here it becomes clear that a sufficient number of neurons is necessary to approximate the yield surfaces with a certain accuracy. For a small number of neurons in the neural network, fluctuations in the network function are observed, even though the mean square error after completion of training is very small. This behavior is most likely connected to the sampling strategy, which must be discussed. If the training samples are arranged in a regular grid as it is done here, the network function can show periodic fluctuations. This could potentially be reduced if a latin hypercube sampling (LHS) strategy would be used. The LHS strategy subdivides the sample space into equally-sized hypercubes. Within each hypercube, a certain number of samples is generated randomly. The randomness reduces periodic fluctuations.

Another sign for potential inaccuracies, which was not observed here (see Fig. 7), is a small number of weights having unusual large values, which can lead to spikes in the network function in regions where no training data are present. In such cases, modifications of the training algorithm can be useful, where the cost function penalizes weight outliers within the training algorithm.

One of the most interesting questions is how many training data are necessary to achieve a certain approximation accuracy of the NN. In Fig. 8 the approximation accuracy is compared for networks which were trained with the full data set sampled with $\Delta\phi = \Delta\psi = 10°$ and for networks trained with a data sampled with $\Delta\phi = 30°$ and $\Delta\psi = 10°$. Although the smaller data set contained just one third of all data, the approximation accuracy remains almost constant. But a further reduction of training data decreases the approximation quality drastically.

The main numerical effort associated with this approach is the generation of training samples, which requires a large number of finite element simulations of the RVE. For the given example, all simulations required approximately 10^5 CPU (2.8 GHz) seconds. The much smaller effort lies in the training of the neural networks which naturally depends on the number of training samples, the network size and the number of training epochs and certainly on the training algorithm. For the given problem the truncated Newton algorithm is suitable. The training for a small benchmark problem with 8000 data samples, a 3-50-1 network, 1000 training epochs on a single 2.8 GHz processor took approximately 20 seconds. As a rule of thumb for such rather small problems, the time for network training scales linearly with the number of training data, number of weights, number of samples and number of training epochs.

4 Application for a single RVE

To evaluate the performance of the constitutive modeling approach using neural networks, we compare the results of the model with those of the fully-meshed RVE, as shown in Fig. 1c. All the networks used for this purpose had 80 neurons within the hidden layer.

4.1 Partial unloading

In a first example, no damage is considered, which means that the effective stiffness tensor remains constant $\overline{\mathbb{C}} = \overline{\mathbb{C}}^0$ and no neural network is needed for the evolution of $\overline{\mathbb{C}}$ described in Eqn. (26). Three different loading paths with partial unloading are applied, both to the model and the RVE. In Fig. 8 the responses are compared for a) uniaxial extension in 1-direction, b) isochoric deformation without shear, and c) biaxial strain without shear. For all three cases, one observes a very good agreement between the effective responses of the RVE and the predictions of the model. The time to evaluate a single load path using the fully-meshed RVE is about 250 seconds, compared to 5 seconds for the homogenized model, which corresponds to a speed up factor of 50.

(a) $\Delta\phi = \Delta\psi = 10°, \overline{\epsilon}_{22} = 0, \overline{\epsilon}_{12} = 0$

(b) $\Delta\phi = \Delta\psi = 10°, \overline{\epsilon}_{22} = -\overline{\epsilon}_{11}, \overline{\epsilon}_{12} = 0$

(c) $\Delta\phi = \Delta\psi = 10°, \overline{\epsilon}_{22} = \frac{1}{3}\overline{\epsilon}_{11}, \overline{\epsilon}_{12} = 0$

(d) $\Delta\phi = 30°, \Delta\psi = 10°, \overline{\epsilon}_{22} = 0, \overline{\epsilon}_{12} = 0$

(e) $\Delta\phi = 30°, \Delta\psi = 10°, \overline{\epsilon}_{22} = -\overline{\epsilon}_{11}, \overline{\epsilon}_{12} = 0$

(f) $\Delta\phi = 30°, \Delta\psi = 10°, \overline{\epsilon}_{22} = \frac{1}{3}\overline{\epsilon}_{11}, \overline{\epsilon}_{12} = 0$
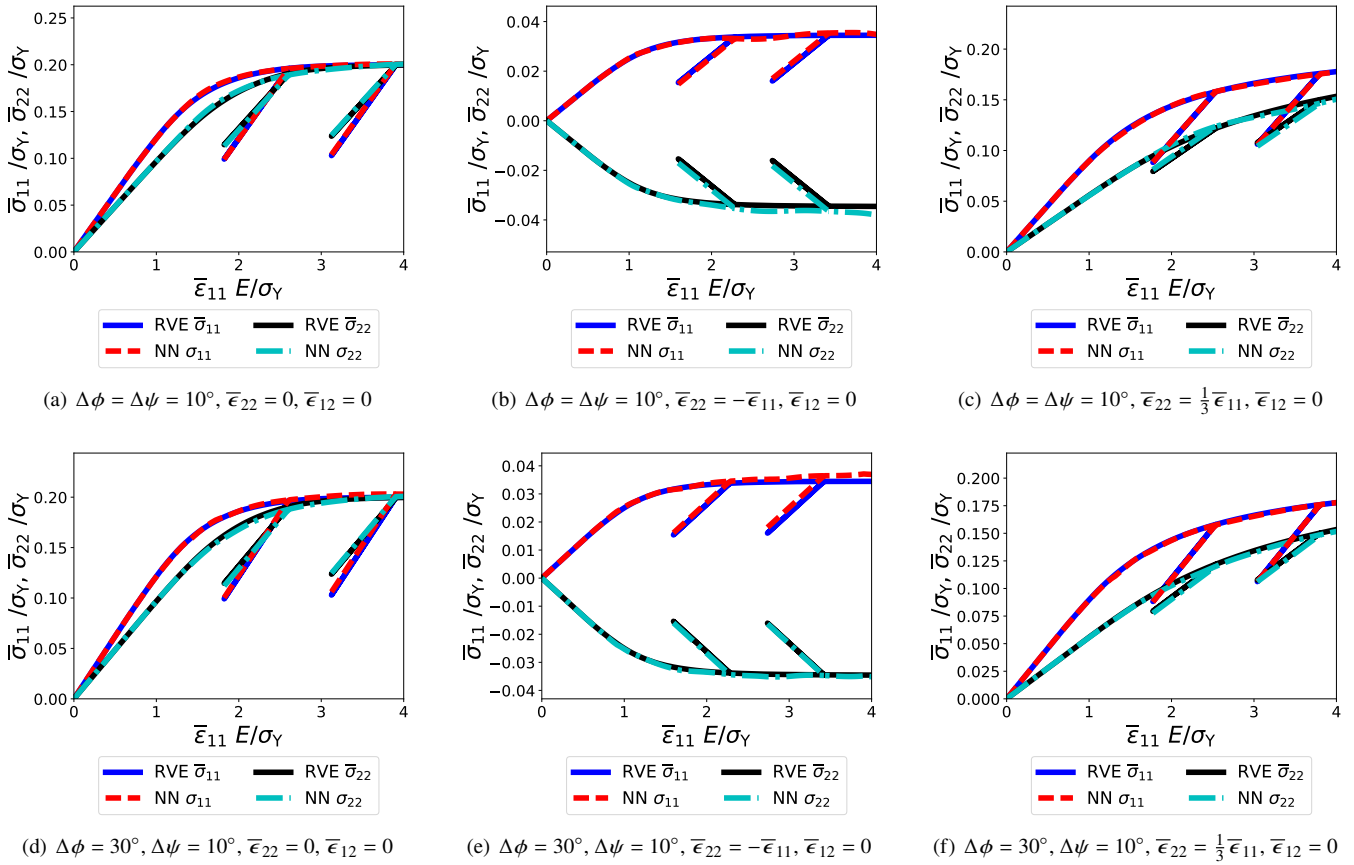
Fig. 8: Stress-strain curves of three different proportional loading cases with partial unloading of RVE-simulations (RVE) and hybrid material model (NN) using elastic-plastic material without damage at microscopic scale from (Settgast et al., 2019b). First row shows results obtained with a NN, which was trained using data sampled with $\Delta\phi = \Delta\psi = 10°$, whereas in the second row the NN was trained with data sampled with $\Delta\phi = 30°$ and $\Delta\psi = 10°$.

(a) uniaxial loading $\overline{\epsilon}_{22}$ (b) biaxial loading $\overline{\epsilon}_{11} = \overline{\epsilon}_{22}$
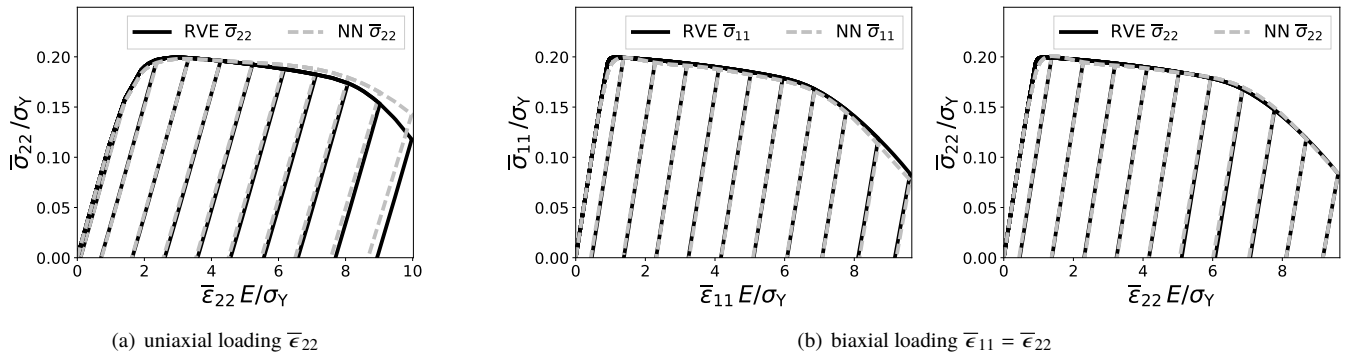
Fig. 9: Macroscopic stress-strain curves for different load cases, where damage is considered (Settgast et al., 2019b).

4.2 Damage at microscopic scale

In the second example damage is considered, which means that the effective stiffness tensor $\overline{\mathbb{C}}$ changes according to Eq. (26), leading to a decreasing load bearing capacity of the RVE with increasing plastic deformation. In Fig. 9, the response of the RVE is compared with the predictions of the NN model for two different load cases: a) an uniaxial loading, as well as b) a biaxial loading. In both cases, several loading-unloading stages are simulated. It is evident that the slope of the unloading curves decreases with increasing damage, due to the decrease in effective stiffness. The overall agreement between the predictions of the NN model and the direct RVE response is very satisfactory. The small differences, especially in the uniaxial case, are due to small approximation errors regarding $|\overline{\sigma}|$. The even smaller deviations in the biaxial load case are due to approximation errors regarding the flow direction $\overline{N}^{\mathrm{pl}}$. It should be mentioned that periodic boundary conditions may overconstrain the localized deformation modes after onset of softening. Other types of less constraining BCs could be used for the generation of training data within the present approach without any problem. Though, this lies beyond the scope of the present manuscript.

5 Conclusions

In this contribution, it was demonstrated that neural networks can be used in constitutive models for porous media, to approximate yield surfaces, the plastic flow direction, and the evolution of damage. For this purpose, training data are needed, which are, for instance, obtained from finite element simulations of RVEs. In the current approach the training data are obtained from proportional load cases, where effective strains are defined. The model predictions were compared with results from direct simulations of the fully-meshed porous structure and show a very satisfactory accuracy. The influence of the neural network size, the data sampling strategy and the training algorithm were also discussed. It was concluded that especially the sampling strategy could be improved to avoid fluctuations of the neural network function. For the tested example, the evaluation of the hybrid model works approximately fifty times faster than the evaluation of the fully-meshed RVE. For three dimensional models, it is expected that the possible speed up increases even further.

It would be also possible to use experimental data instead of numerically generated ones, if a sufficiently elaborate data set were available. For a general application, it is necessary to extend this approach to three dimensions, which is mathematically straightforward, because the set of equations does not change. However, the computational effort to generate a sufficiently large set of data increases, because the RVE has to be three-dimensional and the number of loading direction paths has to be adapted accordingly.

On the other hand no constitutive model currently exists, which is capable of simulating arbitrary porous structures. The presented approach can be applied for structures where the principle shape of their yield and flow potentials is unknown or very difficult to formulate in closed-form.

Finally, useful extensions should consider more internal variables (e.g. volumetric strain, data of internal distortional deformations, a.o.) for the input of the neural networks to increase their predictive accuracy.

Acknowledgment

References

Martin Abendroth and Meinhard Kuna. Identification of ductile damage and fracture parameters from the small punch test using neural networks. *Engineering Fracture Mechanics*, 73(6):710–725, 2006. doi: 10.1016/j.engfracmech.2005.10.007.

Serkan Demiray, Wilfried Becker, and Jörg Hohe. Numerical determination of initial and subsequent yield surfaces of open-celled model foams. *International Journal of Solids and Structures*, 44(7):2093–2108, 2007. doi: 10.1016/j.ijsolstr.2006.06.044.

Marcus Emmel and Christos G Aneziris. Development of novel carbon bonded filter compositions for steel melt filtration. *Ceramics International*, 38(6):5165–5173, 2012. doi: 10.1016/j.ceramint.2012.03.022.

Tomonari Furukawa and Mark Hoffman. Accurate cyclic plastic analysis using a neural network material model. *Engineering Analysis with Boundary Elements*, 28(3):195–204, 2004. doi: 10.1016/S0955-7997(03)00050-X.

Youssef M.A. Hashash, Sungmoon Jung, and Jamshid Ghaboussi. Numerical implementation of a neural network based material model in finite element analysis. *International Journal for Numerical Methods in Engineering*, 59(7):989–1005, 2004. doi: 10.1002/nme.905.

Akbar A. Javadi and Mohammad Rezania. Intelligent finite element method: An evolutionary approach to constitutive modeling. *Advanced Engineering Informatics*, 23(4):442–451, 2009. doi: 10.1016/j.aei.2009.06.008.

Guanghui Liang and K. Chandrashekhara. Neural network based constitutive model for elastomeric foams. *Engineering Structures*, 30(7):2002–2011, 2008. doi: 10.1016/j.engstruct.2007.12.021.

Christoph Settgast, Geralf Hütter, Martin Abendroth, and Meinhard Kuna. A hybrid approach for consideration of the elastic-plastic behaviour of open-cell ceramic foams. In *Proceedings of the ECCM6/ECFD7, 11-15 June 2018, Glasgow, United Kingdom*, pages 2314–2325, 2018.

Christoph Settgast, Martin Abendroth, and Meinhard Kuna. Constitutive modeling of plastic deformation behavior of open-cell foam structures using neural networks. *Mechanics of Materials*, 131:1–10, 2019a. ISSN 0167-6636. doi: 10.1016/j.mechmat.2019.01.015.

Christoph Settgast, Geralf Hütter, Meinhard Kuna, and Martin Abendroth. A hybrid approach to simulate the homogenized irreversible elastic-plastic deformations and damage of foams by neural networks, 2019b.

Johannes Solarek, Christina Bachmann, Yvonne Klemm, Christos G. Aneziris, and Horst Biermann. High-temperature compression deformation behavior of fine-grained carbon-bonded alumina. *Journal of the American Ceramic Society*, 99(4):1390–1397, 4 2016. doi: 10.1111/jace.14070.

Johannes Storm, Martin Abendroth, Dongshuang Zhang, and Meinhard Kuna. Geometry dependent effective elastic properties of open-cell foams based on kelvin cell models. *Advanced Engineering Materials*, 15(12):1292–1298, 2013. doi: 10.1002/adem.201300141.

Johannes Storm, Martin Abendroth, and Meinhard Kuna. Numerical and analytical solutions for anisotropic yield surfaces of the open-cell Kelvin foam. *International Journal of Mechanical Sciences*, 105:70–82, 2015. doi: 10.1016/j.ijmecsci.2015.10.014.

Aijun Wang and David L. McDowell. Yield surfaces of various periodic metal honeycombs at intermediate relative density. *International Journal of Plasticity*, 21(2):285–320, 2005. doi: 10.1016/j.ijplas.2003.12.002.

Marek Wojciechowski. Application of artificial neural network in soil parameter identification for deep excavation numerical model. *Computer Assisted Mechanics and Engineering Sciences*, 18(4):303–311, 2011.

Characterization of Multi-axial Hyperelastic Behavior of Mooney-Rivlin Materials: Results of Finite Element Simulations

Hocine Bechir*, Kamel Yaya, and Amar Djema,

Laboratoire de Mécanique, Matériaux et Énergétique (L2ME), Faculté de Technologie, Université de Bejaia, 06000 Bejaia, Algeria

Abstract: The calibration of the parameters of hyperelastic consitutive equations of elastomeric materials requires multi-axial mechanical test data. For this reason, planar biaxial tests have been used extensively in the literature. The drawback of the biaxial tensile test is that difficult to manage and gives raise to heterogeneous stress and strain fields. Noting that, a homogeneous stress-strain field allows for more precise determination of the mechanical properties of a sample. To this end, we present an alternative to biaxial testing, i.e. a novel test protocol that is consisting to deform a sample by coupling both the deformations of pure shear and of simple shear (or rectilinear shear). The sample is oriented in the plane of a special device, which is attached to a universal tensile testing machine. As a result, the stress-strain relations depend on the direction of stretching, i.e. $\Theta \in]0, \pi/2[$ (angle of orientation of the sample in the device) and displacement U (or γ). We compute analytically the Cauchy stresses on the basis of assumption of homogeneous strain field in core region of the sample. We show that, these stresses are almost equal to that arising from the FE simulations. The homogeineity of fields in the core region allows us to relate the Cauchy stresses to the applied forces (under condition that the boundary value problems are well controlled allowing to obtain uniform stresses). So, the experimental data arising from this test could be suitable for identification or/and validation of hyperelastic models.

Keywords: Hyperelasticity, Multi-axial behavior, Test-design, Finite element simulations

1 Introduction

The modeling of hyperelastic behavior of isotropic elastomers is well established in framework of continuum mechanics Ogden (1997); Holzapfel (2000). In many engineering applications, one needs to implement these models in commercial finite element codes. Consequently, the identification is a crucial step, which consists in estimating the constitutive parameters at best from a measured displacement field and applied forces. Due to the complex behavior of elastomeric materials, the model parameter calibration requires complex experimental protocols, from experimental setup and sample (e.g., complex multiaxial loadings, optimized geometry). In the field of solid mechanics, numerous relevant identification and validation strategies have been development in the context of full-field measurements techniques Hild and Roux (2006); Grédiac et al. (2006); Hartmann and Rodriguez (2018) and references cited therein. Standard tests related with this purpose require sample geometries that can lead to homogeneous deformations (uni-axial tensile, pure shear and equi-bi-axial tensile) Sasso et al. (2008); Galliot and Lushinger (2011). In practice, the constitutive parameters that are identified with those three types test performed separately are generally different Guo and Sluys (2006). To bypass the problem, the material parameters could be identified from experimental data of the biaxial tensile test in order to ensure predictive ability of a hyperelastic model Seibert et al. (2014). We emphasize that, the heterogeneous deformation states of equibiaxial tensile test and an inverse method (so-called, the virtual fields method) have been used Promma et al. (2009) in order to compute the Mooney-Rivlin model constants Mooney (1940). We notice that, the computation of deformation and stress states in core region of a cruciform specimen is a subject of debate Hartmann et al. (2018) (and the literature cited therein). The strains distribution seems to be uniform; nevertheless, the corresponding stress distribution does not. We conclude that, biaxial tensile test seems to give rise to heterogeneous stress and strain fields even near core region of a cruciform sample.

In this work, a concept testing was proposed in order to characterize the multi-axial behavior of elastomeric materials. The testing consists of the coupled stretching and shearing instead of performing them separately. The Cauchy stresses have been investigated on the basis of homogeneous strains in central region of the sample made of a Mooney-Rivlin material. The stress-strain relationship depends both on the stretching-direction and amplitude of displacement prescribed on the specimen edge. On the basis of homogeneous strain fields in core region, we could compute analytically both the Cauchy stress and strain fields. We show that, the Cauchy stresses are almost equal to that arising from the FE simulations. As result, the Cauchy stress field could be related to the applied forces (under condition that the boundary value problems are well controlled allowing to obtain uniform stresses). So, the experimental data arising from this test could be suitable for the identification or/and validation of hyperelastic models.

The plan of the paper is as follows: In Section 2, we recall the basic equations of isotropic hyperelasticity. In Section 3, we have investigated analytically the proposed theoretical approach. In Section 4, we have validated the analytical results by using the Finite Element simulations in order to compute the Cauchy stresses distribution in core region of the sample. In section 5, we

draw some concluding and remarks.

2 Basic equations of isotropic hyperelastcity

In continuum mechanics, the mechanical properties of elastomeric materials are described in terms of strain-energy density function Ψ Ogden (1997); Holzapfel (2000). For isotropic elastic material, Ψ depends on the strain principal invariants

$$I_1 = tr(\mathbf{B}),\ I_2 = \frac{1}{2}\left[(tr(\mathbf{B}))^2 - tr(\mathbf{B}^2)\right],\ I_3 = det(\mathbf{B}), \tag{1}$$

where $\mathbf{B} = \mathbf{FF}^t$ is the left Cauchy-Green tensor and $\mathbf{F}$ is the gradient of the deformation.
The deformation gradient is defined by $\mathbf{F} = \partial\mathbf{x}/\partial\mathbf{X}$, $\mathbf{X}$ and $\mathbf{x}$ are the vector location of a material particle in the undeformed and deformed configurations, respectively.
Rubber-like materials are often assumed to be incompressible provided that the hydrostatic stress does not become too large and so the admissible deformations must be isochoric, (i.e., $det\mathbf{F} = 1$), so that, $I_3 = 1$. The Cauchy stress of an incompressible isotropic elastic material can be determined as follows:

$$\boldsymbol{\sigma} = -p\mathbf{I} + 2\Psi_{,1}\mathbf{B} - 2\Psi_{,2}\mathbf{B}^{-1}, \tag{2}$$

where p is the Lagrange multiplier, $\mathbf{I}$ is the identity tensor and $\Psi_{,i} = (\partial\Psi/\partial I_i)_{i=1,2}$ are the partial derivatives of the strain-energy density function.
We consider the phenomenological Mooney-Rivlin model Mooney (1940) which is suitable to predict the behavior of elastomeric materials in the range of moderate strains. The strain-energy density function is as follows:

$$\Psi = \frac{\mu_0}{2}\left[\alpha\left(I_1 - 3\right) + (1 - \alpha)\left(I_2 - 3\right)\right], \tag{3}$$

where μ_0 is the shear modulus for infinitesimal deformations and $\alpha \in\ ]0, 1]$ is a dimensionless constant.

3 The testing design

Denote the unit vectors associated with a fixed Cartesian coordinates system in the reference configuration by $(\mathbf{E}_1, \mathbf{E}_2, \mathbf{E}_3)$ and in the current configuration by $(\mathbf{e}_1, \mathbf{e}_2, \mathbf{e}_3)$. Consider a rectangular plate made of elastomeric material bonded to two rigid plates, with edges aligned with $\mathbf{E}_1$, $\mathbf{E}_2$ and $\mathbf{E}_3$. $L = mH$ denotes the length of the plate, H its height and $m \geq 2$ is the shape factor; e is the thickness of the plate with $H >> e$. Let us to define the new test as shown in Figs. 1 consisting to apply a loading in a direction $\Theta \in\ ]0, \pi/2[$ on the upper face of the plate in $Y = H$; the bottom face of the plate is blocked in $Y = 0$ (no displacement is possible). For $\Theta = \pi/2$, the deformation reduces to that of the pure shear test; if $\Theta = 0$ then the deformation is that of the simple shear (or rectilinear shear). Consequently, the deformation can be decomposed as a superposition of simultaneous deformations in the direction Y (stretching) and in the direction X (shearing). The resulting deformation depends on the angle Θ of stretching. In core region, we may assume that the deformations are quasi-homogeneous (affine), since the length of plate is more important than height ($L \geq 2H$). In other words, the "boundary-effects" can be neglected at far from the edges of the specimen. Accordingly, we may decompose the coupled deformations into two successive deformations: (i) the first one is the quasi-homogeneous (affine) deformation corresponding to the pure shear with the principal stretch ratio, λ, and (ii) one which uses the homogeneous configuration as the reference state, that is, the rectilinear shear. This multiplicative decomposition of the deformation gradient, so-called Successive Decomposition Procedure (SDP) has been applied Mihai and Goriely (2015) in the context of cellular structures. With these assumptions, let us postulate that a homogeneous isotropic and incompressible material is subjected to the following transformation:

$$x = X + \kappa\lambda Y,\ y = \lambda Y,\ z = \frac{Z}{\lambda}, \tag{4}$$

where λ and κ are the stretch ratio along the X_2-axis and local amount of shear, respectively.
Eq.(4) can be viewed as a special case of the transformation that was investigated in Wineman and Ghandi (1984). The deformation gradient tensor $\mathbf{F}$ is inferred from Eq. (4) as follows:

$$\mathbf{F} = \begin{pmatrix} 1 & \kappa\lambda & 0 \\ 0 & \lambda & 0 \\ 0 & 0 & \lambda^{-1} \end{pmatrix} = \begin{pmatrix} 1 & \kappa & 0 \\ 0 & 1 & 0 \\ 0 & 0 & 1 \end{pmatrix}\begin{pmatrix} 1 & 0 & 0 \\ 0 & \lambda & 0 \\ 0 & 0 & \lambda^{-1} \end{pmatrix} = \mathbf{F}^{(1)}\mathbf{F}^{(2)}, \tag{5}$$

where $\mathbf{F}^{(1)}$ and $\mathbf{F}^{(2)}$ are the gradients tensors of deformation corresponding to simple shear and pure shear, respectively. The decomposition of Eq. (5) is similar to the method adopted in finite elastoplasticity (Lee (1969)), in which the local deformation gradient is decomposed into elastic and plastic parts. Also, this multiplicative decomposition was applied with success in viscoelasticity (Reese and Govindjee (1998)), thermoelasticity and biomechanics (Lubarda (2004)). Consequently, this general

H. Bechir, K. Yaya, A. Djema

Tech. Mech., Vol. 40, Is. 1, (2020), 15–21
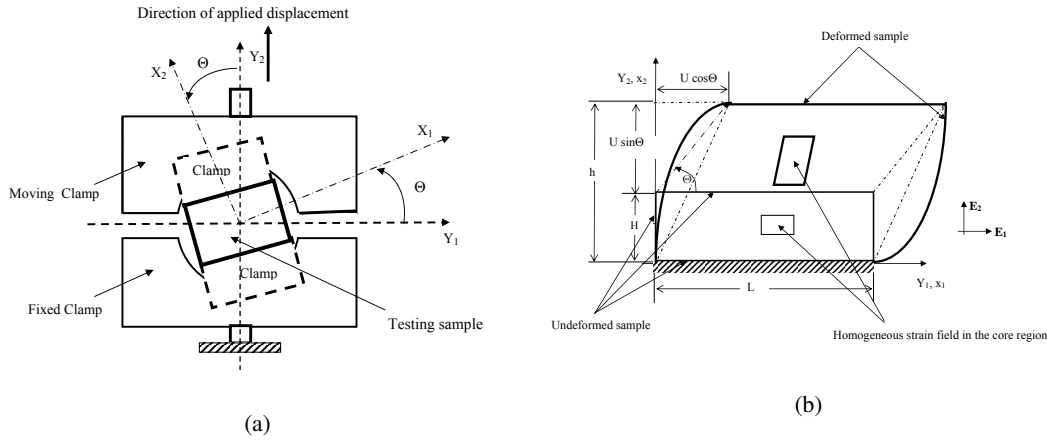
Fig. 1: Schematic representation of the proposed test: (a) the sample is gripped with two clamps, the moving clamp is displacement vertically to induce simultaneously a shearing and stretching of the sample, where $\Theta \in]0, \pi/2[$ is the angle between the principal axes of the sample and the column of the tensile machine. (b) The sample is a thin rectangular sheet of length $L = 0.04m$ width $H = 0.02m$ and of thickness $e = 0.004m$. We represent schematically the deformation that is assumed homogeneous in core region of the sample.

decomposition is carried out to assign various physical causes to kinematical quantities. Noting that the study of state of simple shear, i.e. $\lambda = 1$, had been subject of growing interest (Ogden (1997); Bertram (2008)). Recently, some authors have concluded that "simple shear is not so simple" (Destrade et al. (2012); Horgan and J.G. (2014); and Thiel et al. (2019)). In fact, finite simple shear cannot be maintained by shear stress alone. Normal stresses are needed to maintain the normal strains at zero; this will result in an inhomogeneous field.

Accordingly, we may assume that the stretch ratio is given by

$$\lambda \approx \frac{h}{H} = \frac{H + U \sin \Theta}{H} = 1 + \gamma \sin \Theta, \tag{6}$$

$$\kappa\lambda = \gamma \cos \Theta. \tag{7}$$

The right Cauchy-Green strain tensor and its inverse are as follows:

$$\mathbf{B} = \begin{pmatrix} 1 + \kappa^2\lambda^2 & \kappa\lambda^2 & 0 \\ \kappa\lambda^2 & \lambda^2 & 0 \\ 0 & 0 & \lambda^{-2} \end{pmatrix}, \quad \mathbf{B}^{-1} = \begin{pmatrix} 1 & -\kappa & 0 \\ -\kappa & (1 + \kappa^2\lambda^2)\lambda^{-2} & 0 \\ 0 & 0 & \lambda^2 \end{pmatrix}. \tag{8}$$

Substituting Eq. (3) into Eq. (2) and substituting Eq. (8) into the resulting of Eq. (2), the Cauchy stresses of Mooney-Rivlin model can be expressed as

$$\sigma_{11} = \mu_0 \left[\alpha(1 + \kappa^2\lambda^2 - \lambda^{-2}) + (1 - \alpha)(\lambda^2 - 1)\right], \tag{9}$$

$$\sigma_{12} = \mu_0\kappa((1 - \alpha)\kappa + \alpha\lambda^2), \tag{10}$$

$$\sigma_{22} = \mu_0 \left[\alpha(\lambda^2 - \lambda^{-2}) + (1 - \alpha)(\lambda^2 - (1 + \kappa^2\lambda^2)\lambda^{-2})\right]. \tag{11}$$

We would to relate the measured force at the edges of the specimen to Cauchy stresses of the core region. The boundary conditions of the testing can be expressed in terms of the components of first Piola-Kirchhoff stress tensor i.e. $\mathbf{P}$, as follows:

$$\mathbf{P} = \begin{pmatrix} 0 & P_{12} & 0 \\ 0 & P_{22} & 0 \\ 0 & 0 & 0 \end{pmatrix}, \tag{12}$$

where $P_{22} = \dfrac{\text{Force}(\gamma; \Theta)}{eL} \sin \Theta$ and $P_{12} = \dfrac{\text{Force}(\gamma; \Theta)}{eL} \cos \Theta$.

Lets us compute the Cauchy stress tensor, i.e., $\boldsymbol{\sigma} = P\mathbf{F}^t$ by using Eqs. (5) and (12)

$$\boldsymbol{\sigma} = \begin{pmatrix} \sigma_{11} & \sigma_{12} \\ \sigma_{12} & \sigma_{22} \end{pmatrix} = \begin{pmatrix} 0 & P_{12} \\ 0 & P_{22} \end{pmatrix} \begin{pmatrix} 1 & 0 \\ \kappa\lambda & \lambda \end{pmatrix} = \begin{pmatrix} \kappa\lambda P_{12} & \lambda P_{12} \\ \kappa\lambda P_{22} & \lambda P_{22} \end{pmatrix}. \tag{13}$$

(a)   (b)   (c)
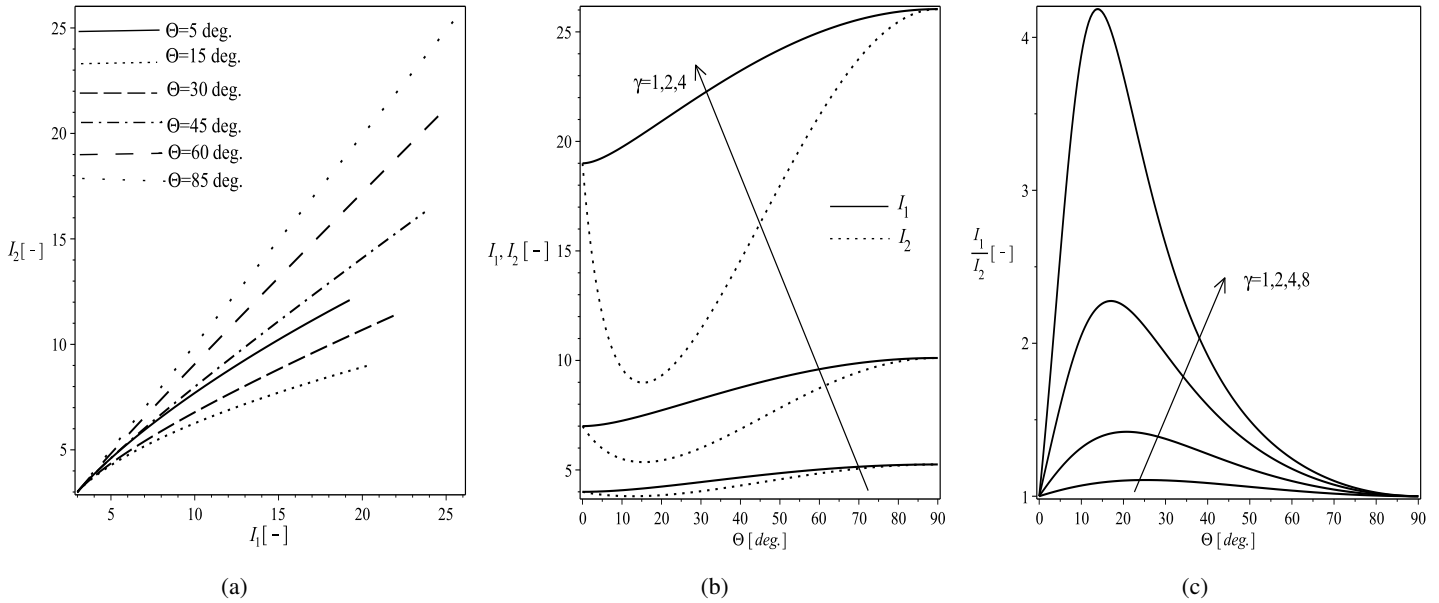
Fig. 2: Plots of the invariants I_2 versus I_1 (a) graphical representation of the plan of invariants, i.e. $I_2(I_1)$, (b) graphical representation of the invariants I_1 and I_2 versus Θ, (c) graphical representation of the ratio I_1/I_2 versus Θ.

So, the Cauchy stresses are as follows:

$$\sigma_{11} = \kappa\lambda\,P_{12},\ \sigma_{12} = \lambda\,P_{12} = \kappa\lambda\,P_{22},\ \text{and } \sigma_{22} = \lambda\,P_{22}. \tag{14}$$

Notice that, the parameter γ needs to be chosen sufficiently great in order to satisfy

$$\frac{P_{12}}{P_{22}} = \tan^{-1}\Theta = \lim_{\gamma\to+\infty}\frac{\gamma\cos\Theta}{1+\gamma\sin\Theta}. \tag{15}$$

We can check the validity of the present approach by comparison the predictions of Eqs. (9), (10) and (11) with the results of FE-simulations(See next Section).

We compute the principal invariants of the left Cauchy-Green strain tensor by using Eqs. (6), (7) and (8), and obtain the following expressions:

$$
\begin{aligned}
I_1(\mathbf{B}) &= 1 + \lambda^2 - \lambda^{-2} + \kappa^2\lambda^2 \\
&= \frac{3 + \gamma^2 + 6\gamma(1+\gamma\sin\Theta)\sin\Theta + 2\gamma^3(\cos^2\Theta + 2\sin\Theta)\sin^2\Theta + \gamma^4\sin^2\Theta}{(1+\gamma\sin\Theta)^2},
\end{aligned}
\tag{16}
$$

$$
\begin{aligned}
I_2(\mathbf{B}) &= 1 + \lambda^2 - \lambda^{-2} + \kappa^2 \\
&= \frac{3 + \gamma^2 + 6\gamma(1+\gamma\sin\Theta)\sin\Theta + 4\gamma^3\sin^3\Theta + \gamma^4\sin^4\Theta}{(1+\gamma\sin\Theta)^2}.
\end{aligned}
\tag{17}
$$

When $\Theta = 0$ or $\Theta = \pi/2$, the first and the second invariants are equal. If $\Theta = \pi/2$ then the test reduces to the pure shearing(stretching), and for $\Theta = 0$, it is corresponding to the simple shear testing. We plot in Fig.2(a) the graphical representation of the plan of invariants, i.e. $I_2(I_1)$ for values of $\gamma = 0..4$. The multi-axial state of deformation could be reached by varying the angle Θ, so the corresponding domain represents the admissible deformation state of incompressible elastomeric materials. The graphs of I_1 and I_2 versus θ are shown in Fig. 2(b) for different values of γ. The second invariant, i.e. I_2 strongly changes. According to Horgan and Smayda (2012) it should be included in the strain energies for isotropic materials; while I_1 is an increasing function. The ratios I_1/I_2 are displayed in Fig. 2(c), the curves are nonlinear and their maximums seem to be slightly depending on Θ and γ, and $I_1 > I_2$. We notice that, this "new" testing does not cover the deformation states of the biaxial test, i.e. $I_2 > I_1$. We emphasize that, Baaser et al. (2013) have analyzed the tension modes, i.e. $I_1 > I_2$ in terms of the variables (λ, m) ; the mode of deformation in his representation is dictated by the numerical value of the parameter m.

4   Finite Elements Analysis and Simulations

We study numerically by FE the proposed test in order to highlight the discrepancies between the results of FE-simulations and predictions of Eqs. (9), (10) and (11). A finite element calculation is performed by assuming both plane stress state and a nearly-incompressibility approach. Thus, a mixed formulation pressure-displacement was used in order to avoid element locking.

For that purpose, the strain-energy density function is decomposed into an isochoric and volumetric parts. To this end, we declare the model of Eq. (3) as slightly- compressible by replacing the principal invariants I_1 and I_2 by equivalent invariant ones Simo and Hughes (1998). Consequently, the strain-energy density function has been decomposed as the sum of the two energies related to distortional and dilatational deformations, so that Eq. (3) becomes

$$\Psi = \tilde{\Psi}(\bar{I}_1, \bar{I}_2) + \hat{\Psi}(J), \tag{18}$$

where $\bar{I}_1 = I_1/I_3^{1/3}$ and $\bar{I}_2 = I_2/I_3^{2/3}$.

We point out that, $\tilde{\Psi}(\bar{I}_1, \bar{I}_2) = \frac{\mu_0}{2}\alpha(\bar{I}_1 - 3) + (1 - \alpha)(\bar{I}_2 - 3)$ and $\hat{\Psi}(J) = \frac{\kappa_0}{2}(J - 1)^2$ where κ_0 is the bulk modulus. We have implemented the strain-energy density function of Eq. (3) in a FE code.

The material parameters $c_{10} = \alpha\mu_0/2$ and $c_{01} = (1 - \alpha)\mu_0/2$ are of a Silicone rubber Seibert et al. (2014) (see, Table I); i.e. the constants of Mooney-Rivlin model Mooney (1940).

A secure bond between the sample and the clamps can be challenging to achieve experimentally. Indeed, the material response is sensitive to gripping techniques used to apply the loads. For instance, the sandpaper could be incorporated if slippage presented a problem. These techniques can also minimize the amount of clamping pre-strain that causes the bulging toward the sample center and outside of the clamps. Therefore, effects from the free and clamped edges could influence the predicted strain and stress fields in the sample. Accordingly, the "perfect" boundary conditions have been assumed for the FE simulations, and these applied through the nodes that were in contact with clamps. So, two-dimensional FE-model has been used by considering plane-stress condition; which is consisting of quadrilateral elements with two degrees of freedom at each node. Each node has two in-plane translational degrees of freedom corresponding to the vertical (axial) direction and horizontal (transversal) direction. The meshing and the boundary conditions are shown in Figs. 3, along the bottom surface of the plate (in $Y = 0$), the displacements of nodes were fixed at zero in all directions. Along the top surface of the plate (in $Y = H$), we have applied the displacements to all nodes, where $u_X = U \cos\Theta$ and $u_Y = U \sin\Theta$ are respectively, the axial and transversal component. The normalized displacement $\gamma = U/H$ was incrementally increased for each value Θ ($0 < \Theta < \pi/2$). The finite element meshes of the deformed specimen are shown in Fig. 4. The FE-simulations seem not be able to predict the shape deformed at the corners of the sample probably due to the bending. Indeed, near the bonding surfaces, the bending deformation could dominate those resulting from the stretching and shearing, especially at small strains ($\gamma << 1$ and $\Theta \to 0$ $deg.$). The bending seems to decrease significantly at large strains (for instance $\gamma \geq 4$ and $\Theta \to 0$ $deg.$), so that, the stretching and shearing strains may co-exist, and are depending on Θ. Anyway, there was a small core area in which the strains were homogeneous; with any "digital image correlation" measurement systems, it is straightforward to determine the in-plane components of the deformation gradient. We may assume that the corresponding stress distribution vary in same way for homogeneous, elastic materials. Therefore, we may establish a relationship between the local stresses in central region and applied forces on the clamp edges of the sample. We represent respectively, in Figs. 5, the graphs of normal and shear Cauchy stress distributions in core region arising from the FE- simulations and analytically computed. A good agreement was obtained for moderate strains, i.e. $\gamma \leq 2$.
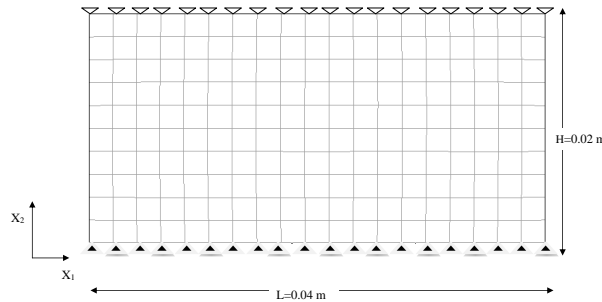
Fig. 3: Mesh and boundary conditions for FE analysis of the shearing/stretching test specimen. The boundary conditions of the test are symbolized by $\triangledown$ a displacement is imposed on the nodes along the top surface of the specimen, and $\blacktriangle$ the displacements at the nodes of the bottom surface are fixed at zero in all directions.

Tab. 1: Model parameters values

parameter	value
c_{10} [MPa]	0.111
c_{01} [MPa]	0.039
μ_0 [MPa]	0.9
κ_0[MPa]	2000

(a) $\Theta = 5$; $\gamma = 2$ (b) $\Theta = 17$; $\gamma = 2$ (c) $\Theta = 30$; $\gamma = 2$

(d) $\Theta = 5$; $\gamma = 4$ (e) $\Theta = 17$; $\gamma = 4$ (f) $\Theta = 30$; $\gamma = 4$
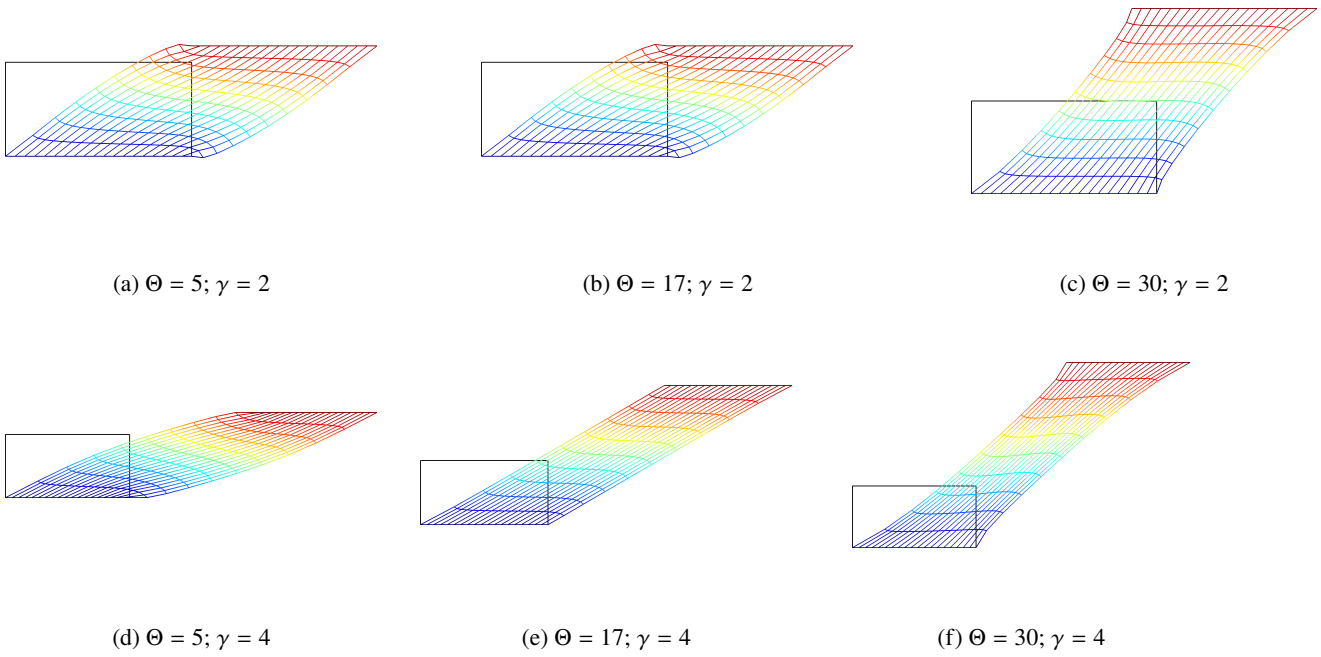
Fig. 4: Mesh and shape of the deformed sample for $\Theta = 5$, 17 and 30 deg.; $\gamma = 2$ and 4.

(a)

(b)
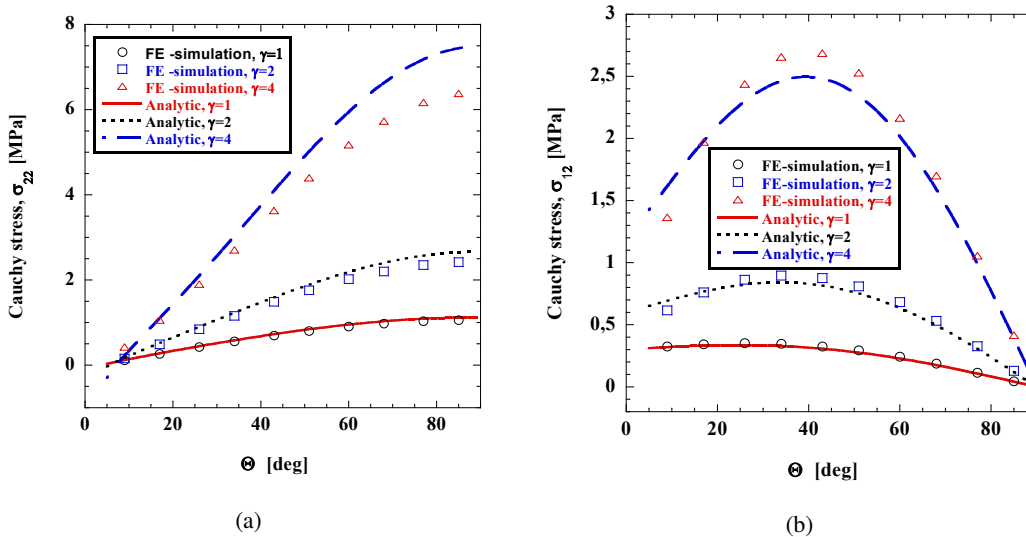
Fig. 5: Graphs of the Cauchy stresses vs. for $\gamma = 2$ and 4 in the core region of the sample, inferred from Eqs. (9), (10) and (11) and of that arising from the FE simulations.

5 Conclusion

In this work, we have presented the design of a novel testing in order to characterize the multi-axial behavior of elastomeric materials. The stress-strain responses depend on both the stretching-direction and amplitude of displacement prescribed on the edge of the sample. We show that, the strain and stress fields are quasi-homogeneous in core region of the sample. So, the experimental data arising from this test could be suitable for identification or/and validation of hyperelastic models. As consequence, this test could be representing an alternative to tensile and rectilinear shear testing performed separatley.

Acknowledgment

H. Bechir, K. Yaya, A. Djema

Tech. Mech., Vol. 40, Is. 1, (2020), 15–21

References

H. Baaser, Ch. Hopmann, and A. Schobel. Reformulation of strain invariants at incompressibility. *Arch. Appl. Mech.*, 83(2): 273–280, 2013.

A Bertram. *Elasticity and Plasticity of Large Deformations: An Introduction*. 2nd Edition, Springer, 2008.

M. Destrade, J.G. Murphy, and G. Saccomandi. Simple shear is not so simple. *Int. J. of Nonlinear Mech.*, 47:210–214, 2012.

C. Galliot and R.H. Lushinger. Uniaxial and biaxial mechanical properties of ETFE foils. *Polym. Testing*, 30(4):356–365, 2011.

M. Grédiac, Pierron F., S. Avril, and E. Toussaint. The virtual fields method for extracting constitutive parameters from full-field measurements. *a review, Strain*, 42(4):233–253, 2006.

Z. Guo and L.J. Sluys. Application of a new constitutive model for the description of rbber-like materials under monotonic loading. *Int. J. Solids and Struct.*, 43(9):2799–2819, 2006.

S. Hartmann and S. Rodriguez. in Advanced Strutural Materials. *Springer International Publishing, Cham*, 80, 2018.

S. Hartmann, R.R. Gilbert, and C. Sguazzo. Basic studies in biaxial tensile tests. *GAMM-Mutteilungen*, 41(1), 2018. doi: 10.1002/gamm.201800004.

F. Hild and S. Roux. Digital image correlation: from displacement measurement to identification of elastic properties. *a review, Strain*, 42(2):69–80, 2006.

G. Holzapfel. *Nonlinear Solid Mechanics*. ISBN-471-82304, Wiley, 2000.

C.O. Horgan and Murphy J.G. Simple shearing of incompressible and slightly compressible isotropic nonlinearly elastic materials. *J. Elast.*, 98:205–221, 2014.

C.O. Horgan and M. Smayda. The importance of the second strain invariant in the constitutive modeling of elastomers and soft biomaterials. *Mech. Mater.*, 51:43–52, 2012.

H. Lee. Elastic-plastic deformation at finite strains. *Jurnal of Applied Mechanics*, 36:1–14, 1969.

V.A. Lubarda. Constitutive theories based on the multiplicative decomposition of deformation gradient: Thermoelasticity, elastoplasticity and biomechanics. *Appl. Mech. Rev.*, 57(2):95–108, 2004.

L.A Mihai and A. Goriely. Finite deformation in cellular with hyperelastic cell walls. *Int. J. Solid and Struct.*, 53:107–128, 2015.

M. Mooney. A theory of Large Elastic Deformation. *J. Appl. Phys.*, 11(9):582–592, 1940.

R.W. Ogden. *Nonlinear Elastic Deformations*. Dover Publications Inc. Mineola, New York, 1997.

N Promma, B. Raka, M. Grédiac, E. Toussaint, J-B. Le Cam, X. Blanchard, and F. Hild. Application of the virtual fields method to mechanical characterization of elastomeric materials. *Int. J. Solids and Struct.*, 46:698–715, 2009.

S. Reese and S. Govindjee. A theory of finite viscoelasticity and numerical aspects. *Int. J. Solid and Struct.*, 35:3455–3482, 1998.

M. Sasso, G. Palmieri, G. Chiappini, and D. Amodio. Characterization of hyperelastic rubber-like materials by biaxial and uniaxial stretching tests based on optical methods. *Polym. Testing*, 27:995–1004, 2008.

H. Seibert, H. Schreffer, and S Diebels. Biaxial testing of elastomers-Experimental setup, measurement and experimental optimisation of specimen's shape. *Techishche Mechanik*, 34:72–89, 2014.

J.C. Simo and T.J.R. Hughes. *Computational Inelasticity*. Springer, New York, 1998. doi: 10.1007/978-1-4612-0555-5.

J. Thiel, C.and Voss, R. Martin, and P. Neff. Shear, pure and simple. *Int. J. of Nonlinear Mech.*, 112:57–72, 2019.

A. Wineman and M. Ghandi. On local and global universal relations in elasticity. *J. Elast.*, 14:97–1029, 1984.

Experimental and Numerical Investigation of the Material Behavior of semi-crystalline Polyamide 6

Sebastian Felder[1]⋆, Ngoc Anh Vu [2], Stefanie Reese[1], and Jaan-Willem Simon[1]

[1] RWTH Aachen University, Institute of Applied Mechanics (IFAM), Mies-van-der-Rohe-Str. 1, 52074 Aachen, Germany
[2] University of Twente, Department of Mechanics of Solids, Surfaces and Systems, P.O. box 217, 7500 AE Enschede, The Netherlands

Abstract: In the current work, the tensile properties of semi-crystalline Polyamide 6 are experimentally investigated for varying degrees of crystallinity, temperatures, and loading rates. Based on the experimental results, a phenomenological constitutive framework at finite strains is derived in a thermodynamically consistent manner. To this end, a hyperelastic-plastic intermolecular resistance and viscous molecular network resistance are considered. Non-linear kinematic and isotropic hardening as well as non-linear relaxation behavior are incorporated, to account for the experimentally observed behavior. It is evident that the mechanical behavior of semi-crystalline polymers exhibits complex dependencies on the degree of crystallinity and the temperature. To capture these experimental findings, both quantities serve as input parameters. A staggered parameter identification scheme is proposed to obtain a unique set of material parameters. Finally, the great capabilities of the proposed framework, to accurately predict the three-dimensional, visco-hyperelastic-plastic material response are demonstrated.

Keywords: semi-crystalline polymers, degree of crystallinity, hyperelastic-visco-plasticity, finite strains

1 Introduction

In contrast to thermoset polymers, which form irreversible chemical bonds throughout the curing process, thermoplastic polymers (TP) can undergo repeated heating above the melting point and cooling cycles. Consequently, TPs are well-suited for numerous technically relevant forming processes (e.g. extrusion or injection molding), where the polymer is reshaped into the desired geometry after heating. Semi-crystalline polymers (SCPs) represent a specific class of TPs, where the amorphous melt partly crystallize during the cooling phase. The resulting degree of crystallinity is in general depending on the processing conditions (e.g. the cooling rate, presence of moisture, and applied stress) cf. Fornes and Paul (2003). Naturally, the macroscopic material response is dictated by the underlying microstructure and is thus depending on the degree of crystallinity (see e.g. Jenkins (1992), Mohagheghian et al. (2015), and Ayoub et al. (2011)). SCPs can undergo large deformations and exhibit a complex visco-plastic material behavior (see e.g. Rae et al. (2007) and El-Qoubaa and Othman (2016)). In addition, significant thermo-mechanical coupling effects can be observed (i.e. the mechanical response is strongly influenced by the temperature and material self-heating occurs at higher loading rates, see e.g. Maurel-Pantel et al. (2015) and Parodi et al. (2018).

Due to this complex material behavior, a strong demand for computational models arises, which accurately predict the material and structural response of SCPs. Over the last decades, several constitutive frameworks, based on phenomenological modeling approaches on the continuum level (Srivastava et al. (2010), Ayoub et al. (2010), and Praud et al. (2017)) or exploiting multiscale modeling strategies (e.g. Li and Shojaei (2012) and Uchida and Tada (2013)), were proposed. Thermo-mechanically coupled models were developed among others by Maurel-Pantel et al. (2015) and Garcia-Gonzalez et al. (2017) for PA66 and PEEK, respectively. Despite the significant influence of the material internal microstructure (such as crystal volume fraction) on the effective material properties, only a limited number of authors accounted for this in their models. In the phenomenological model of Dusunceli and Colak (2008) and the formulation of Ayoub et al. (2011) and Abdul-Hameed et al. (2014), where the microstructure is represented by two-phases, the degree of crystallinity serves as a constant input parameter. However, in all these studies the effect of the degree of crystallinity was examined only for one specific temperature.

Over the last decades, numerous experimental investigations were published regarding the material behavior of SCPs. However, for Polyamide 6, which is the SCP of interest in the current work, the experimental data is scattered over the literature and, to the authors' knowledge, no comprehensive (true) stress stretch data, incorporating all of the following features, is available:

- Experimental investigation of the mechanical response for monotonic, cyclic, and relaxation test at finite strains;
- Consideration of a wide range of temperatures, spanning the glass transition temperature $\theta_g \approx 80\,°C$;
- Accounting for different loading rates;
- Investigation of the influence of the crystallographic structure on the mechanical properties.

In the current work, an experimental approach is presented, in order to obtain a data base with the aforementioned characteristics. Based on these results, a phenomenological hyperelastic-visco-plastic constitutive framework is developed in a thermodynamically consistent manner. To capture the biphasic nature of the polymer and to account for different isothermal conditions, both the degree of crystallinity and temperature serve as input parameters. Finally, the model parameters are identified in a staggered procedure.

First computations reveal the promising potential of this new model to accurately and efficiently predict the rate-dependent mechanical response for different degrees of crystallinity and at various temperatures.

2   Experimental investigation

Tensile experiments were conducted for Polyamide 6 (*Ultramid B40*, kindly provided by BASF SE). Dried specimens (type 5A in accordance with ISO 527-2:2012), produced by injection moulding, were tested in monotonic, cyclic, and relaxation tests at 22.4 °C, 50 °C, 120 °C, and 160 °C. To alter the initial degree of crystallinity χ_I = 23 %, annealing was applied for 5 hours at 180 °C, which resulted in a second set of specimens with χ_{II} = 28 %. In all experiments, the displacement of the cross head speed of the utilized *Zwick Z005* universal testing machine was prescribed and two different loading speeds (v_{min} = 1 mm/min and v_{max} = 10 mm/min) were investigated. The stretch field at the surface of the specimen was obtained by employing a 2D *ARAMIS 4M* digital image correlation (DIC) system. From the deformed cross section, the true stress in longitudinal x-direction σ_x was calculated. Noteworthy, only sections with almost constant stretch rates of $\dot{\lambda}_{x,min} \approx 0.0005 \text{ s}^{-1}$ and $\dot{\lambda}_{x,max} \approx 0.0058 \text{ s}^{-1}$ corresponding to v_{min} and v_{max}, were investigated.
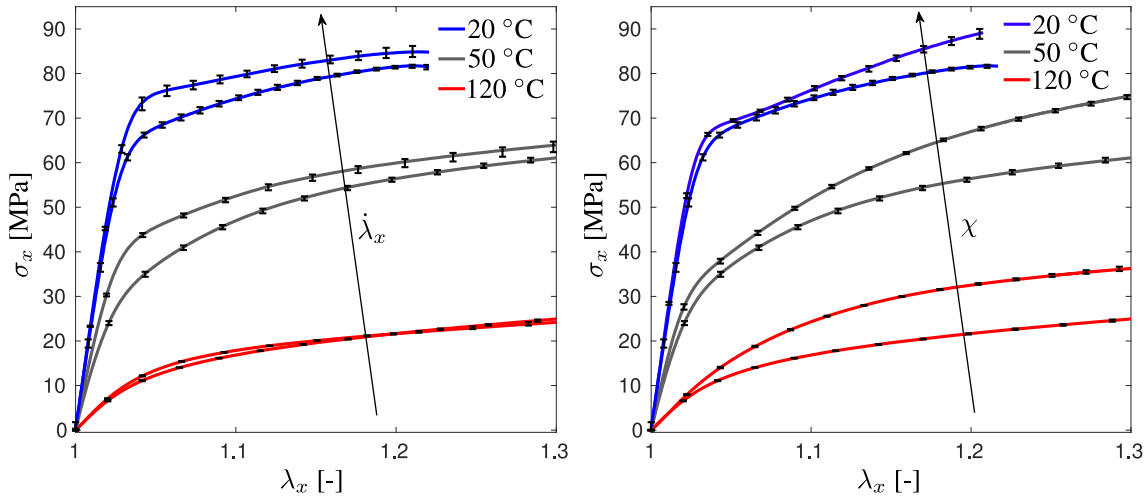
Fig. 1: Monotonic, uniaxial tensile tests at various temperatures: Effect of loading rate ($\dot{\lambda}_x = 0.0005 \text{ s}^{-1}$ vs. $\dot{\lambda}_x = 0.0058 \text{ s}^{-1}$) for $\chi = 23 \%$ (left). Effect of degree of crystallinity ($\chi = 23 \%$ vs. $\chi = 28 \%$) for $\dot{\lambda}_x = 0.0005 \text{ s}^{-1}$ (right).

In Figure 1 the longitudinal stress σ_x over stretch λ_x response for monotonic loading conditions is depicted. The significant influence of the temperature and degree of crystallinity on the rate dependent mechanical response was evident. Although the temperature on the surface of the specimens was not measured, self-heating of the material due to dissipative effects seemed to be present at higher loading rates and moderate stretch levels of $\lambda_1 \approx 1.07$ (already reported by e.g. Maurel-Pantel et al. (2015) and Parodi et al. (2018) for PA66 and PA6, respectively). At higher loading speeds, strain induced hardening competes with self-heating induced thermal-softening. This leads to a decrease of the slope of the stress-stretch curves and eventually to an intersection of the curves for v_{min} and v_{max} at higher temperatures (e.g. 120 °C).
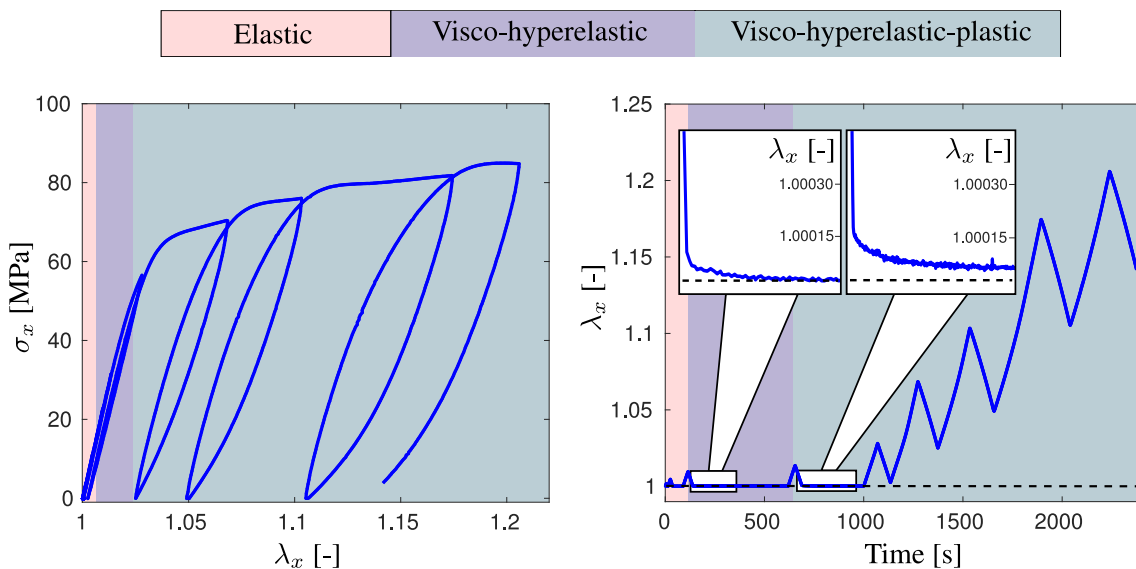
Fig. 2: Cyclic-loading-unloading-recovery experiment at room temperature

Cyclic-loading-unloading-recovery experiments were performed to reveal the complex deformation processes of the considered polymer. The stress over stretch and stretch over time relations are shown in Figure 2, for one exemplary cyclic experiment at room

temperature. Three distinct deformation regimes were observed: (i) In the elastic regime, the undeformed configuration (λ_x=1.0) was directly recovered after displacement controlled unloading to zero force. (ii) In the visco-hyperelastic regime, a remaining stretch level after unloading to zero force was present. However during the recovery step, where a zero force was prescribed, the remaining stretches were dissolved. (iii) In the visco-hyperelastic-plastic regime, the remaining stretch after unloading to zero force, converged towards an equilibrium plastic stretch level, at the end of the recovery step.

To assess the influence of the temperature and deformation level on the time-dependent material behavior, stepwise relaxation experiments were conducted. To this end, a loading speed of $v_{max} = 10$ mm/min was prescribed stepwise until a certain stretch level ($\lambda_x \approx 1.01$ and $\lambda_x \approx 1.15$) was reached. Subsequently, the displacement was held constant to allow for stress relaxation (see Figure 3). The data revealed a complex, non-linear dependency of the relaxation time on the stress and stretch level as well as on the temperature. This became more evident, by applying a post-processing scheme of the experimental data (see Section 4), which is founded on the proposed strategy of Amin et al. (2006).
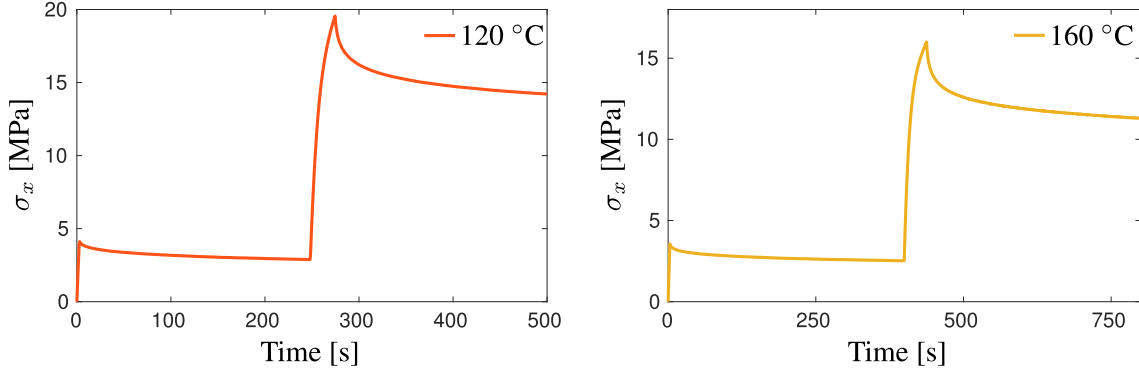
Fig. 3: Stepwise relaxation experiments at stretch levels of $\lambda_x \approx 1.01$ and $\lambda_x \approx 1.15$ at 120 °C and 160 °C

3   Material model formulation

In order to model the mechanical response of semi-crystalline PA6, the resistance of deformation is governed by a parallel arrangement of an intermolecular resistance and a molecular network resistance, in line with the contributions of e.g. Srivastava et al. (2010) and Ayoub et al. (2011). The intermolecular resistance is captured by means of an elasto-plastic model. To obtain the experimentally observed time dependent material behavior, the network resistance is represented by a viscous model to account for molecular orientation and relaxation. In the following, quantities associated with these resistances are distinguished by the subscripts m (inter**m**olecular) and n (molecular **n**etwork), respectively.

3.1   Multiplicative split of the deformation gradient

For the elasto-plastic model the classical multiplicative split of the total deformation gradient $\boldsymbol{F} = \boldsymbol{F}_{em}\boldsymbol{F}_p$, into an elastic $\boldsymbol{F}_{em}$ and plastic part $\boldsymbol{F}_p$ is proposed. Since, polymers exhibit a significant Bauschinger-like effect upon unloading (cf. e.g. Hasan and Boyce (1995) and Anand et al. (2009)), non-linear kinematic hardening of Frederick-Armstrong type is incorporated in the constitutive framework. To this end, a physically motivated (cf. Lion (2000)), additional multiplicative decomposition of the plastic part of the deformation gradient $\boldsymbol{F}_p = \boldsymbol{F}_{pe}\boldsymbol{F}_{pi}$, is employed. Furthermore, to model the viscous response of the SCP, a decomposition of the total deformation gradient $\boldsymbol{F} = \boldsymbol{F}_{en}\boldsymbol{F}_i$, into an elastic $\boldsymbol{F}_{en}$ and an inelastic part $\boldsymbol{F}_i$ is assumed (cf. Lubliner (1985) and Reese and Govindjee (1998)).

3.2   Constitutive relations and thermodynamic consistency

An additive split of the specific Helmholtz free energy into the contributions of the intermolecular and network resistance, denoted by ψ_m and ψ_n, respectively, is proposed

$$\psi = \psi_m(\boldsymbol{C}_{em}, \boldsymbol{C}_{pe}, \kappa, \chi, \theta) + \psi_n(\boldsymbol{C}_{en}, \chi, \theta)$$
$$\psi_m = \psi_{em}(\boldsymbol{C}_{em}, \chi, \theta) + \psi_{kin}(\boldsymbol{C}_{pe}, \chi, \theta) + \psi_{iso}(\kappa, \chi, \theta) \tag{1}$$

which depends on the deformation only through the right Cauchy-Green deformation tensors

$$\boldsymbol{C}_{em} = \boldsymbol{F}_{em}^T\boldsymbol{F}_{em} = \boldsymbol{F}_p^{-T}\boldsymbol{C}\boldsymbol{F}_p^{-1}, \quad \boldsymbol{C}_{pe} = \boldsymbol{F}_{pe}^T\boldsymbol{F}_{pe} = \boldsymbol{F}_{pi}^{-T}\boldsymbol{C}_p\boldsymbol{F}_{pi}^{-1}, \quad \boldsymbol{C}_{en} = \boldsymbol{F}_{en}^T\boldsymbol{F}_{en} = \boldsymbol{F}_i^{-T}\boldsymbol{C}\boldsymbol{F}_i^{-1} \tag{2}$$

based on the principle of material frame indifference. Here, $\boldsymbol{C} = \boldsymbol{F}^T\boldsymbol{F}$ is the right Cauchy-Green tensor and $\boldsymbol{C}_p = \boldsymbol{F}_p^T\boldsymbol{F}_p$ represents the plastic right Cauchy-Green tensor. In expression (1), the energy related to intermolecular reactions ψ_{em}, the stored energy due to isotropic hardening ψ_{iso}, which is depending on the accumulated plastic strain κ, and a defect-energy associated with plastic deformations ψ_{kin} are introduced. The latter allows to phenomenologically account for the Bauschinger-like phenomena. Furthermore, all energy terms are assumed to depend on the degree of crystallinity χ and the temperature θ. Noteworthy, isothermal conditions ($\dot{\theta} = 0$) and no evolution of the crystalline phase ($\dot{\chi} = 0$) are assumed, such that χ and θ serve as input

parameters. With this new approach, the dependence of the effective material behavior on different crystal volume fractions (resulting from varying processing conditions) and different isothermal conditions is captured.

The constitutive equations are derived in a thermodynamically consistent manner from the Clausius-Duhem inequality

$$\boldsymbol{S} : \frac{1}{2}\dot{\boldsymbol{C}} - \rho_0\dot{\psi} \geq 0 \tag{3}$$

which is here stated for isothermal processes, concomitant with the previous assumptions. The total second Piola-Kirchhoff stress tensor is denoted by $\boldsymbol{S}$ and ρ_0 is the density in the reference configuration. It is assumed that $\psi_{e\mathfrak{m}}$, $\psi_{e\mathfrak{n}}$, and ψ_{kin} are isotropic functions of $\boldsymbol{C}_{e\mathfrak{m}}$, $\boldsymbol{C}_{e\mathfrak{n}}$, and $\boldsymbol{C}_{pe}$, respectively. To obtain the constitutive relations, the total time derivative of the Helmholtz free energy (1) is inserted into the latter inequality and the following quantities are defined. The second Piola-Kirchhoff stress tensors

$$\boldsymbol{S}_{\mathfrak{m}} = 2\rho_0 \boldsymbol{F}_p^{-1} \frac{\partial \psi_{e\mathfrak{m}}}{\partial \boldsymbol{C}_{e\mathfrak{m}}} \boldsymbol{F}_p^{-T}, \quad \boldsymbol{S}_{\mathfrak{n}} = 2\rho_0 \boldsymbol{F}_i^{-1} \frac{\partial \psi_{\mathfrak{n}}}{\partial \boldsymbol{C}_{e\mathfrak{n}}} \boldsymbol{F}_i^{-T} \tag{4}$$

are corresponding to the intermolecular and molecular network resistance, respectively. The quantities

$$\boldsymbol{M}_{\mathfrak{m}} = 2\rho_0 \boldsymbol{C}_{e\mathfrak{m}} \frac{\partial \psi_{e\mathfrak{m}}}{\partial \boldsymbol{C}_{e\mathfrak{m}}}, \quad \boldsymbol{M}_{kin} = 2\rho_0 \boldsymbol{C}_{pe} \frac{\partial \psi_{kin}}{\partial \boldsymbol{C}_{pe}}, \quad \boldsymbol{M}_{\mathfrak{n}} = 2\rho_0 \boldsymbol{C}_{e\mathfrak{n}} \frac{\partial \psi_{\mathfrak{n}}}{\partial \boldsymbol{C}_{e\mathfrak{n}}} \tag{5}$$

represent symmetric stress tensors of Mandel-type and

$$\bar{\boldsymbol{X}} = 2\rho_0 \boldsymbol{F}_{pe} \frac{\partial \psi_{kin}}{\partial \boldsymbol{C}_{pe}} \boldsymbol{F}_{pe}^T, \quad R = -\rho_0 \frac{\partial \psi_{iso}}{\partial \kappa} \tag{6}$$

are the back stress tensor and the stress-like driving force of isotropic hardening, respectively. Following the standard arguments of Coleman and Noll (1961), the total second Piola-Kirchhoff stress tensor

$$\boldsymbol{S} = \boldsymbol{S}_{\mathfrak{m}} + \boldsymbol{S}_{\mathfrak{n}} \tag{7}$$

is obtained. Next, a yield function of von Mises type is assumed

$$\Phi = ||\text{dev}(\boldsymbol{M}_{\mathfrak{m}}) - \text{dev}(\bar{\boldsymbol{X}})|| - \sqrt{\frac{2}{3}}(\sigma_y - R) \tag{8}$$

where $|| * ||$ and $\text{dev}(*)$ denote the Frobenius norm and the deviatoric part of a quantity, respectively, and the initial yield stress $\sigma_y(\chi, \theta)$ is introduced. In the following, $\boldsymbol{D}_{(*)} = \text{sym}(\boldsymbol{L}_{(*)})$ is defined as the symmetric part of the corresponding velocity gradient $\boldsymbol{L}_{(*)} = \dot{\boldsymbol{F}}_{(*)} \boldsymbol{F}_{(*)}^{-1}$, with $(*) = i, p, pi$. The plastic flow rule and evolution equation for kinematic and isotropic hardening

$$\boldsymbol{D}_p = \dot{\gamma} \frac{\partial \Phi}{\partial \boldsymbol{M}_{\mathfrak{m}}} = \dot{\gamma} \frac{\text{dev}(\boldsymbol{M}_{\mathfrak{m}}) - \text{dev}(\bar{\boldsymbol{X}})}{||\text{dev}(\boldsymbol{M}_{\mathfrak{m}}) - \text{dev}(\bar{\boldsymbol{X}})||} \tag{9}$$

$$\boldsymbol{D}_{pi} = \dot{\gamma} \frac{b}{c} \text{dev}(\boldsymbol{M}_{kin}) \tag{10}$$

$$\dot{\kappa} = \dot{\gamma} \frac{\partial \Phi}{\partial R} \tag{11}$$

corresponding to the intermolecular resistance, are derived in an associative manner. In the expression above the plastic multiplier $\dot{\gamma}$ was introduced. The evolution equation for kinematic hardening (10) is of Frederick-Armstrong type, where $b(\theta, \chi)$ and $c(\theta, \chi)$ are material parameters. Finally, the Kuhn-Tucker-conditions $\Phi \leq 0$, $\dot{\gamma} \geq 0$, and $\Phi\dot{\gamma} = 0$ supplement the elasto-plastic constitutive framework. The evolution of the inelastic deformation within the molecular network

$$\boldsymbol{D}_i = \frac{1}{2\tau\mu_{\mathfrak{n}}} \text{dev}(\boldsymbol{M}_{\mathfrak{n}}) + \frac{1}{9\tau K_{\mathfrak{n}}} \text{tr}(\boldsymbol{M}_{\mathfrak{n}})\boldsymbol{I} \tag{12}$$

is chosen in line with the suggested form of Reese and Govindjee (1998). Here, the bulk modulus $K_{\mathfrak{n}}(\chi, \theta)$ and shear modulus $\mu_{\mathfrak{n}}(\chi, \theta)$, corresponding to the molecular network resistance are introduced. To model the relaxation behavior observed in experiments, the relaxation time τ is assumed to be a non-linear function of the overstress $\boldsymbol{S}_{\mathfrak{n}}$, the deformation and the temperature and is provided in Section 4.

This set of evolution equations (9)-(12) sufficiently satisfies the Clausius-Duhem inequality. For a detailed proof, the reader is referred to the works of Reese and Govindjee (1998) and Vladimirov et al. (2008).

All constitutive relations are derived with respect to several intermediate configurations. However, in order to implement the proposed framework as a material subroutine, tensorial pull back operations of the stress quantities $\boldsymbol{M}_{\mathfrak{m}}$, $\boldsymbol{M}_{kin}$, $\bar{\boldsymbol{X}}$, and $\boldsymbol{M}_{\mathfrak{n}}$ are performed, to represent all relations with respect to the reference configuration (see Table 1). As a result, the back stress tensor with respect to the reference configuration $\tilde{\boldsymbol{X}}$ and the asymmetric stress like quantities $\boldsymbol{Y}$ and $\boldsymbol{Y}_{kin}$ are introduced (cf. Vladimirov et al. (2008)).

Up to now, no specific choices for the different free energy terms were made. Consequently, the proposed formulation offers great flexibility, since the relations for the thermodynamic driving forces have been derived in a completely general manner. For

Tab. 1: Constitutive equations with respect to the reference configuration

Intermolecular resistance	Molecular network resistance
Stresses $S_{\mathrm{m}} = 2\rho_0 F_p^{-1} \dfrac{\partial \psi_{e\mathrm{m}}}{\partial C_{e\mathrm{m}}} F_p^{-T}$, $\tilde{X} = 2\rho_0 F_{pi}^{-1} \dfrac{\partial \psi_{kin}}{\partial C_{pe}} F_{pi}^{-T}$, $Y = C S_{\mathrm{m}} - C_p \tilde{X}, \quad Y_{kin} = C_p \tilde{X}$, $R = -\rho_0 \dfrac{\partial \psi_{iso}}{\partial \kappa}$	**Stress** $S_{\mathrm{n}} = 2\rho_0 F_i^{-1} \dfrac{\partial \psi_{\mathrm{n}}}{\partial C_{e\mathrm{n}}} F_i^{-T}$
Evolution equations $\dot{C}_p = 2\dot{\gamma} \dfrac{\mathrm{dev}(Y)C_p}{\sqrt{\mathrm{dev}(Y) : \mathrm{dev}(Y)^T}}$, $\dot{C}_{pi} = 2\dot{\gamma}\dfrac{b}{c}\mathrm{dev}(Y_{kin})C_{pi}, \quad \dot{\kappa} = \sqrt{\dfrac{2}{3}}\dot{\gamma}$	**Evolution equation** $\dot{C}_i = \left(\dfrac{1}{\tau\mu_{\mathrm{n}}}\mathrm{dev}(CS_{\mathrm{n}}) + \dfrac{2}{9\tau K_{\mathrm{n}}}\mathrm{tr}(CS_{\mathrm{n}})I \right) C_i$
Yield function $\Phi = \sqrt{\mathrm{dev}(Y) : \mathrm{dev}(Y)^T} - \sqrt{\dfrac{2}{3}}(\sigma_y - R)$	
Kuhn-Tucker-conditions $\Phi \leq 0, \ \dot{\gamma} \geq 0, \text{ and } \Phi\dot{\gamma} = 0$	

Second Piola-Kirchhoff stress
$S = S_{\mathrm{m}} + S_{\mathrm{n}}$

the intermolecular resistance, a Neo-Hookean material with combined linear and non-linear isotropic hardening of Voce type is assumed. The corresponding volumetric energy terms Ψ read

$$\Psi_{e\mathrm{m}} = \frac{\mu_{\mathrm{m}}}{2}\left(\mathrm{tr}(C_{e\mathrm{m}}) - 3\right) - \mu_{\mathrm{m}}\ln(J_{e\mathrm{m}}) + \frac{\Lambda_{\mathrm{m}}}{4}\left(\det(C_{e\mathrm{m}}) - 1 - 2\ln(J_{e\mathrm{m}})\right) \tag{13}$$

$$\Psi_{kin} = \frac{c}{2}(\mathrm{tr}(C_{pe}) - 3) - c\ln(J_{pe}) \tag{14}$$

$$\Psi_{iso} = (\sigma_\infty - \sigma_y)\left(\kappa + \frac{\exp(-\beta\kappa)}{\beta}\right) + \frac{1}{2}H\kappa^2 \tag{15}$$

Here, the Lamé constants and isotropic hardening parameters are defined by $\mu_{\mathrm{m}}(\theta,\chi)$, $\Lambda_{\mathrm{m}}(\theta,\chi)$, $\sigma_\infty(\theta,\chi)$, $\beta(\theta,\chi)$, and $H(\theta,\chi)$, respectively. Furthermore, the identities $J_{e\mathrm{m}} = \det F_{e\mathrm{m}}$ and $J_{pe} = \det F_{pe}$ are introduced. For simplicity, the elastic energy contribution of the molecular network resistances is chosen to be of Neo-Hookean type as well, namely

$$\Psi_{\mathrm{n}} = \frac{\mu_{\mathrm{n}}}{2}\left(\mathrm{tr}(C_{e\mathrm{n}}) - 3\right) - \mu_{\mathrm{n}}\ln(J_{e\mathrm{n}}) + \frac{\Lambda_{\mathrm{n}}}{4}\left(\det(C_{e\mathrm{n}}) - 1 - 2\ln(J_{e\mathrm{n}})\right) \tag{16}$$

where the Lamé constants corresponding to the molecular network resistance are represented by $\mu_{\mathrm{n}}(\chi,\theta)$ and $\Lambda_{\mathrm{n}}(\chi,\theta)$, respectively and $J_{e\mathrm{n}} = \det F_{e\mathrm{n}}$ holds. It is assumed that the material parameters are functions of the temperature and total degree of crystallinity, to capture the experimentally observed dependency of the macroscopic material response on these quantities. The specific relations are provided in Section 4.

The algorithmic treatment of the constitutive equations corresponding to the elasto-plastic model is based on the proposed strategy by Dettmer and Reese (2004) and Vladimirov et al. (2008). The numerical time integration and solution procedure for the evolution equation of the viscous model is adopted from Reese and Govindjee (1998). These are not further discussed in the current work.

4 Material parameter characterization

The material parameters were obtained from the experimental results discussed in Section 2. A staggered parameter identification procedure was developed to obtain a unique set of parameters for each temperature separately.

1. The elastic constants were governed from the material response under monotonic tension in the elastic deformation regime (cf. Section 2). The Poisson's ratio of intermolecular and molecular network resistance were assumed to be equal (i.e. $\nu_{\mathrm{m}} = \nu_{\mathrm{n}}$) and were calculated from the negative ratio of the transverse and longitudinal stretch data. The Young's moduli E_{m} and E_{n} were governed from the initial stiffness of PA6 for different degrees of crystallinity. For simplicity, it was assumed that only the stiffness of the intermolecular resistance depends linearly on χ.

2. In the second identification step, the function for the relaxation time τ was determined, based on the relaxation data for different stretch levels. To this end, a post-processing scheme for the recorded stress relaxation data, which was originally proposed by Amin et al. (2006), was utilized to assess the influence of the temperature and overstress and stretch level on the evolution of the relaxation time. A non-linear relation was evident at higher stretch levels, in contrast to a almost linear relation at small stretches (exemplary depicted in Figure 4 for relaxation data at 120 °C). To capture the evolution of the relaxation time, the following function was assumed

$$\tau = \tau_0 \frac{||\boldsymbol{C}||_s^\varphi}{\exp(||\boldsymbol{\sigma}_\mathfrak{n}||_s)^\delta} \tag{17}$$

In the expression above $|| * ||_s$ is defined as the second norm of a tensor (i.e. $|| * ||_s = \sqrt{\omega_{\max}}$, with $\omega_{\max}$ being the maximum eigenvalue of $(*)^T(*)$) and $\boldsymbol{\sigma}_\mathfrak{n}$ represents the Cauchy stress corresponding to the molecular network resistance.

The additional material parameters $\tau_0(\theta)$, $\varphi(\theta)$, and $\delta(\theta)$ were obtained by simultaneously minimizing the summed square of residuals (defined as the difference between the observed experimental data and fitted model response) for different stretch levels. To this end, the Trust-region algorithm, which is provided as an intrinsic functions in the commercial software *MATLAB*, was utilized without introducing additional scale (weight) factors. Noteworthy, with the proposed nonlinear function for the relaxation time (17), a better fit for the nonlinear evolution at higher stretch levels was achieved (cf. Figure 4). The comparatively weak fit at small stretches might be improved by introducing additional material parameters. However, it should be emphasized that the visco-elastic material response was accurately captured with this choice of constitutive equation and corresponding set of parameters (see Section 5).
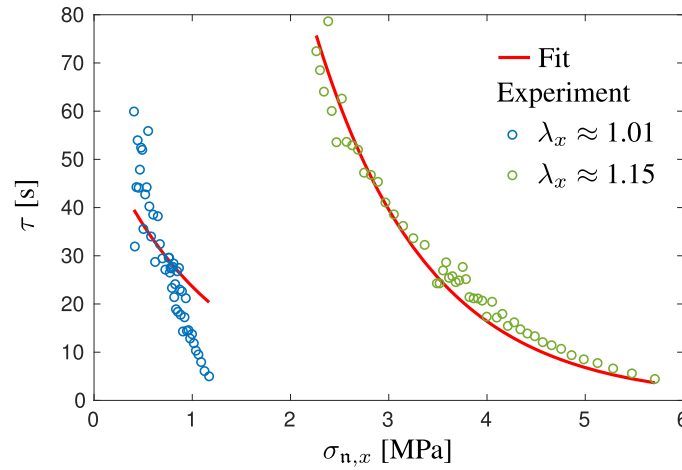
Fig. 4: Relaxation time overstress relation: Experimental data and corresponding fit for different λ_x at 120 °C and χ_I.

3. The initial yield stress $\sigma_y(\chi, \theta)$ was directly obtained from the onset of yield, which was determined from the cyclic experiments for different degrees of crystallinity.

4. Due to the lack of cyclic tension compression data, kinematic hardening was neglected by setting the corresponding parameter c to zero. Finally, the isotropic hardening parameters (i.e $\beta(\theta, \chi)$, $\sigma_\infty(\theta, \chi)$, and $H(\theta, \chi)$) were obtained from the monotonic tensile test data, by simultaneously minimizing the least-square residuals of the 3D stress-stretch response for different loading rates and degrees of crystallinity.

Tab. 2: Set of mechanical parameters for 120 °C

$E_\mathfrak{m} = \chi E_\mathfrak{m}^0(\theta)$	$E_\mathfrak{n} = E_\mathfrak{n}(\theta)$	$\nu_{\mathfrak{m},\mathfrak{n}}(\theta)$	$\sigma_y = \chi \sigma_y^0(\theta)$	$\beta = \chi \beta_0(\theta)$	$H = \chi H_0(\theta)$	$\sigma_\infty = \chi^{\alpha(\theta)} \sigma_\infty^0(\theta)$	$\tau(\boldsymbol{\sigma}_\mathfrak{n}, \boldsymbol{C}, \theta)$ cf. (17)
$E_\mathfrak{m}^0$: 1050 [MPa]	$E_\mathfrak{n}$: 201 [MPa]	0.35 [-]	σ_y^0: 30 [MPa]	β_0: 228 [-]	H_0: 215 [MPa]	σ_∞^0: 1253 [MPa]	τ_0: 48 [s]
						α: 3.061 [-]	φ: 2.38 [-]
							δ: 0.714 [-]

Up to now, the staggered parameter identification procedure was only conducted for 120 °C (corresponding set of parameters see Table 2), where all required experimental data was already available. However, the general procedure is suited for all other considered temperatures and will lead to equivalent results.

The corresponding stress over stretch response of the model was well fitted to the experimental data (see Figure 5). Noteworthy, due to the material self-heating at higher loading rates (cf. Section 2), the isothermal model ($\dot{\theta} = 0$) was only calibrated up to stretch levels of $\lambda_x = 1.07$ for $\dot{\lambda}_{x,max} \approx 0.0058$ s^{-1}. Consequently, the model response leads to an overestimation of the stress after this stretch level for the higher loading rate. To capture the phenomenon of material self-heating and corresponding thermal-softening correctly, a fully thermo-mechanically-coupled model formulation needs to be developed in the future.
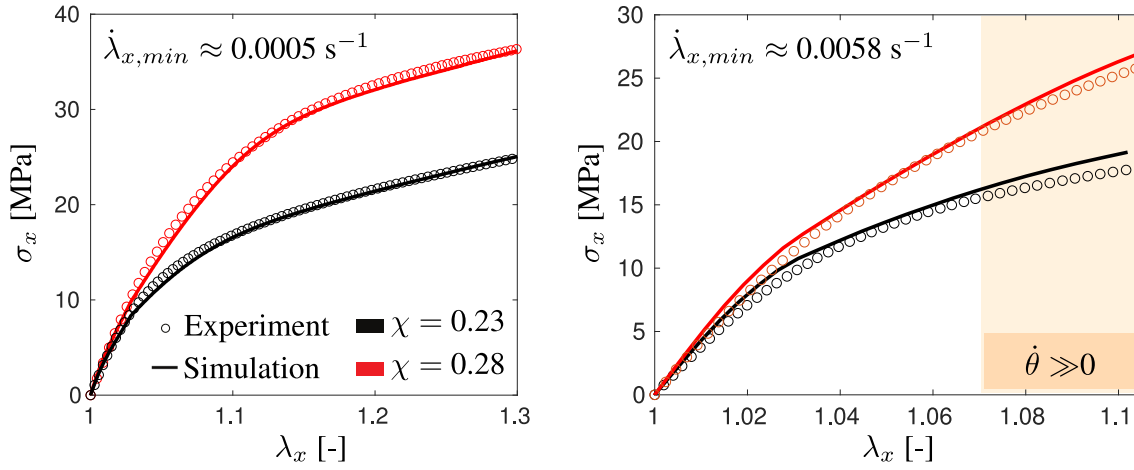
Fig. 5: Monotonic, uniaxial extension - Experimental data and corresponding model fit at 120 °C

5 Model verification

In order to verify, the obtained parameters, the model response was evaluated for the cyclic loading-unloading-recovery procedure and compared with the experimental data. To this end, the proposed theory was implemented as a user material subroutine *UMAT* into the commercial FEM software *ABAQUS*/Standard and a single element test was considered. The stress in longitudinal x-direction obtained from the experimental data as a function of time was prescribed as a traction boundary condition. The resulting stress over stretch response is in excellent agreement with the experimental records (see Figure 6 on the left).

Furthermore, the recorded stretch in transversal y-direction over time was compared with the model response (see Figure 6 on the right). The latter results emphasized the great capabilities of the proposed constitutive framework to accurately predict the three-dimensional, visco-hyperelastic-plastic material response of Polyamide 6 at large deformations ($\lambda_x > 1.4$).
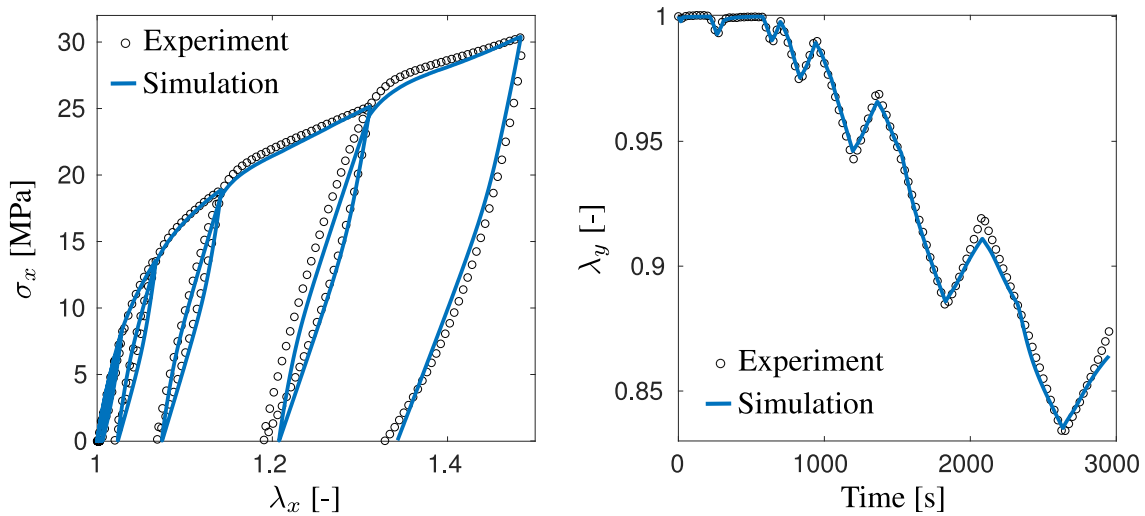
Fig. 6: Experimental data and corresponding model prediction for cyclic loading-unloading-recovery procedure at 120 °C and χ_I: Longitudinal stress σ_x over stretch λ_x response (left). Transversal stretch λ_y over time (right).

6 Conclusion

In the current work, a constitutive framework was proposed for analyzing, predicting, and optimizing the material and structural response of semi-crystalline polymers. This new theory was founded on a preceding comprehensive experimental study, where particular attention was paid on investigating the material response of semi-crystalline Polyamide 6 over a wide range of temperatures and for different degrees of crystallinity. The experimental observations provided important insights into the complex dependencies of the effective material properties on the aforementioned factors and revealed three distinct deformation regimes (i.e. elastic, visco-hyperelastic, and visco-hyperelastic-plastic regime).

Based on these results, a material model, which is valid for finite strains, was developed in a thermodynamically consistent manner. To phenomenologically capture the observed deformation regimes, a parallel arrangement of an elasto-plastic and viscous model was proposed. Furthermore, to account for the significant influence of the temperature and degree of crystallinity on the mechanical response, both quantities served as model inputs. The material parameters were obtained from a staggered identification procedure, which was performed up to now only for 120 °C, due to the lack of a complete experimental database. However, first computational results demonstrated the great capabilities of the proposed framework, to accurately predict the

three-dimensional, visco-hyperelastic-plastic material response of Polyamide 6 at large deformations.

To fully characterize and validate the constitutive framework in the future, much work needs to be done. First of all, the experimental study must be completed for all considered temperatures. Based on these results, the proposed parameter identification procedure can be applied in a straight forward manner and will lead to a set of material parameters for each temperature. Of particular interest is, in addition, the investigation of stress relaxation for different degrees of crystallinity, which is not incorporated in the model yet. To improve the models capabilities in the context of more complex multidimensional stress states, additional shear-, compression- and combined loading procedures need to be conducted. Furthermore, to characterize the kinematic hardening response, combined tension-compression experiments are required. Based on these results, the energy contributions and yield surface can be adjusted in a straight forward manner, due to the general derivation of the proposed model and corresponding high flexibility.

Moreover, infrared thermography measurements should be performed during testing to confirm the material self-heating at higher loading rates. These results and the set of material parameters at different temperatures will provide an important foundation for a thermo-mechanically coupled model formulation.

Acknowledgments

References

H. Abdul-Hameed, T. Messager, F. Zaïri, and M. Naït-Abdelaziz. Large-strain viscoelastic-viscoplastic constitutive modeling of semi-crystalline polymers and model identification by deterministic/evolutionary approach. *Computational Materials Science*, 90:241 – 252, 2014. doi: https://doi.org/10.1016/j.commatsci.2014.03.043.

A. F. M. S. Amin, A. Lion, S. Sekita, and Y. Okui. Nonlinear dependence of viscosity in modeling the rate-dependent response of natural and high damping rubbers in compression and shear: Experimental identification and numerical verification. *International Journal of Plasticity*, 22(9):1610 – 1657, 2006. doi: https://doi.org/10.1016/j.ijplas.2005.09.005.

L. Anand, N. M. Ames, V. Srivastava, and S. A. Chester. A thermo-mechanically coupled theory for large deformations of amorphous polymers. part i: Formulation. *International Journal of Plasticity*, 25(8):1474 – 1494, 2009. ISSN 0749-6419. doi: https://doi.org/10.1016/j.ijplas.2008.11.004.

G. Ayoub, F. Zaïri, M. Naït-Abdelaziz, and J. M. Gloaguen. Modelling large deformation behaviour under loading - unloading of semicrystalline polymers: Application to a high density polyethylene. *International Journal of Plasticity*, 26(3):329 – 347, 2010. doi: https://doi.org/10.1016/j.ijplas.2009.07.005.

G. Ayoub, F. Zaïri, C. Fréderix, J.M. Gloaguen, M. Naït-Abdelaziz, R. Seguela, and J.M. Lefebvre. Effects of crystal content on the mechanical behaviour of polyethylene under finite strains: Experiments and constitutive modelling. *International Journal of Plasticity*, 27(4):492 – 511, 2011. doi: https://doi.org/10.1016/j.ijplas.2010.07.005.

B. D. Coleman and W. Noll. Foundations of linear viscoelasticity. *Reviews of Modern Physics*, 33:239–249, Apr 1961. doi: 10.1103/RevModPhys.33.239.

W. Dettmer and S. Reese. On the theoretical and numerical modelling of Armstrong-Frederick kinematic hardening in the finite strain regime. *Computer Methods in Applied Mechanics and Engineering*, 193(1 – 2):87 – 116, 2004. doi: 10.1016/j.cma.2003.09.005.

N. Dusunceli and O. U. Colak. Modelling effects of degree of crystallinity on mechanical behavior of semicrystalline polymers. *International Journal of Plasticity*, 24(7):1224 – 1242, 2008. doi: https://doi.org/10.1016/j.ijplas.2007.09.003.

Z. El-Qoubaa and R. Othman. Strain rate sensitivity of polyetheretherketone's compressive yield stress at low and high temperatures. *Mechanics of Materials*, 95:15 – 27, 2016. doi: https://doi.org/10.1016/j.mechmat.2015.12.008.

T.D. Fornes and D.R. Paul. Crystallization behavior of nylon 6 nanocomposites. *Polymer*, 44(14):3945 – 3961, 2003. doi: https://doi.org/10.1016/S0032-3861(03)00344-6.

D. Garcia-Gonzalez, R. Zaera, and A. Arias. A hyperelastic-thermoviscoplastic constitutive model for semi-crystalline polymers: Application to peek under dynamic loading conditions. *International Journal of Plasticity*, 88:27 – 52, 2017. doi: https://doi.org/10.1016/j.ijplas.2016.09.011.

O. A. Hasan and M. C. Boyce. A constitutive model for the nonlinear viscoelastic viscoplastic behavior of glassy polymers. *Polymer Engineering & Science*, 35(4):331 – 344, 1995. doi: 10.1002/pen.760350407.

A. D. Jenkins. *Polymers: chemistry & physics of modern materials*, volume 28. J. M. G. Cowie Blackie & Son Ltd, Glasgow & London Chapman & Hall, New York, 1991, 1992. doi: 10.1002/pi.4990280115.

G. Li and A. Shojaei. A viscoplastic theory of shape memory polymer fibres with application to self-healing materials. *Proceedings of the Royal Society A: Mathematical, Physical and Engineering Sciences*, 468(2144):2319 – 2346, 2012. doi: 10.1098/rspa.2011.0628.

A. Lion. Constitutive modelling in finite thermoviscoplasticity: a physical approach based on nonlinear rheological models. *International Journal of Plasticity*, 16(5):469 – 494, 2000. doi: 10.1016/S0749-6419(99)00038-8.

J. Lubliner. A model of rubber viscoelasticity. *Mechanics Research Communications*, 12(2):93 – 99, 1985. doi: https://doi.org/10.1016/0093-6413(85)90075-8.

A. Maurel-Pantel, E. Baquet, J. Bikard, J. L. Bouvard, and N. Billon. A thermo-mechanical large deformation constitutive model for polymers based on material network description: Application to a semi-crystalline polyamide 66. *International Journal of Plasticity*, 67:102 – 126, 2015. doi: https://doi.org/10.1016/j.ijplas.2014.10.004.

I. Mohagheghian, G. J. McShane, and W. J. Stronge. Impact perforation of monolithic polyethylene plates: Projectile nose shape dependence. *International Journal of Impact Engineering*, 80:162 – 176, 2015. doi: https://doi.org/10.1016/j.ijimpeng.2015.02.002.

E. Parodi, P. W. M. Gerrit, and L. E. Govaert. Prediction of plasticity-controlled failure in polyamide 6: Influence of temperature and relative humidity. *Journal of Applied Polymer Science*, 135(11):45942, 2018. doi: 10.1002/app.45942.

F. Praud, G. Chatzigeorgiou, J. Bikard, and F. Meraghni. Phenomenological multi-mechanisms constitutive modelling for thermoplastic polymers, implicit implementation and experimental validation. *Mechanics of Materials*, 114:9 – 29, 2017. doi: https://doi.org/10.1016/j.mechmat.2017.07.001.

P. J. Rae, E. N. Brown, and E. B. Orler. The mechanical properties of poly(ether-ether-ketone) (peek) with emphasis on the large compressive strain response. *Polymer*, 48(2):598 – 615, 2007. doi: https://doi.org/10.1016/j.polymer.2006.11.032.

S. Reese and S. Govindjee. A theory of finite viscoelasticity and numerical aspects. *International Journal of Solids and Structures*, 35(26):3455 – 3482, 1998. doi: https://doi.org/10.1016/S0020-7683(97)00217-5.

V. Srivastava, S. A. Chester, N. M. Ames, and L. Anand. A thermo-mechanically-coupled large-deformation theory for amorphous polymers in a temperature range which spans their glass transition. *International Journal of Plasticity*, 26(8):1138 – 1182, 2010. doi: https://doi.org/10.1016/j.ijplas.2010.01.004. Special Issue In Honor of Lallit Anand.

M. Uchida and N. Tada. Micro-, meso- to macroscopic modeling of deformation behavior of semi-crystalline polymer. *International Journal of Plasticity*, 49:164 – 184, 2013. doi: https://doi.org/10.1016/j.ijplas.2013.03.007.

I. N. Vladimirov, M. P. Pietryga, and S. Reese. On the modelling of non-linear kinematic hardening at finite strains with application to springback – comparison of time integration algorithms. *International Journal for Numerical Methods in Engineering*, 75 (1):1 – 28, 2008. doi: 10.1002/nme.2234.

On material-convective elasto-plasticity

Klaus Heiduschke [*]

Alumnus of Institut für Mechanik, ETH Zürich, Switzerland

Abstract: A material-convective continuum formulation is presented which differs significantly from the finite elasto-plasticity descriptions of general-purpose finite element simulation tools like *Dyna3D*, *Abaqus*, *Marc*, etc. The material-convective continuum formulation offers physical significance in particular with respect to the geometrical interpretation of the (plastic) deformation tensors—in contrast to the so-called Updated Lagrangian Formulation of general-purpose finite element simulation tools which is unphysical due to its inaccurate (directional non-convective) integration of the (plastic) deformation increments: this inaccurately integrated (plastic) deformation does not obey the geometrical interpretation of proper (plastic) deformation tensors and may even lead to a violation of the first fundamental law of thermodynamics, the conservation of energy. The material-convective time integrals are the reverse of the material-convective time derivatives, and the only material-convective time derivative of a symmetric second-order Eulerian tensor is its Green-Naghdi rate which is rotationally and translationally convected with the material.

Keywords: material-convective continuum formulation, Green-Naghdi rate, material-convective time integration, non-material Zaremba-Jaumann rate, geometrical interpretation of deformation tensors

1 Introduction

The modeling of finite elasto-plasticity must be based on proper definitions of the deformation tensors—for the total deformation tensors $\mathsf{b} = \mathsf{R}.\mathsf{C}.\mathsf{R}^\mathsf{T}$ as well as for the partial (elastic ${}^e\mathsf{b} = \mathsf{R}.{}^e\mathsf{C}.\mathsf{R}^\mathsf{T}$, plastic ${}^p\mathsf{b} = \mathsf{R}.{}^p\mathsf{C}.\mathsf{R}^\mathsf{T}, \cdots$) ones. The six internal degrees of freedom of properly defined symmetric (total or partial) deformation tensors may be interpreted as three principal values (eigenvalues) and three orthogonal principal axes (eigenvectors), whose eigenvalues are functions of the present and reference edge lengths of the corresponding present $d\hat{v}$ and reference $d\hat{V}$ principal infinitesimal volume elements only [and do not depend on the geometrical path through the whole time history of all deformation configurations]. For rate-type theories of plasticity, the Eulerian plastic deformation tensor ${}^p\mathsf{b}$ must be integrated from the Eulerian plastic flow rule ${}^p\mathring{\mathsf{b}} = \cdots$ translational- and rotational-convective with the material. For a Lagrangean material description, the *material velocity* vector

$$\mathbf{v} = \dot{\mathbf{x}}(\mathbf{X}, t) = \frac{\partial \mathbf{x}(\mathbf{X}, t)}{\partial t} \tag{1}$$

is given by the time derivative of the motion $\mathbf{x}(\mathbf{X}, t)$ of a material point/particle, but what is its material-convective rotation velocity or spin? The questions of the *material-convective rotation*

$$\mathsf{R} = \mathsf{R}^{-\mathsf{T}} = \sqrt{\mathsf{F}^{-\mathsf{T}}.\mathsf{F}^{-1}}.\mathsf{F} = \sqrt{\mathsf{F}.\mathsf{F}^\mathsf{T}}.\mathsf{F}^{-\mathsf{T}} = \mathsf{F}.\sqrt{\mathsf{F}^{-1}.\mathsf{F}^{-\mathsf{T}}} = \mathsf{F}^{-\mathsf{T}}.\sqrt{\mathsf{F}^\mathsf{T}.\mathsf{F}} \tag{2}$$

and the *material-convective spin*

$$\Omega = \dot{\mathsf{R}}.\mathsf{R}^\mathsf{T} = -\mathsf{R}.\dot{\mathsf{R}}^\mathsf{T} = -\Omega^\mathsf{T} \tag{3}$$

tensors are discussed with respect to the polar decomposition $\mathsf{F} = \mathsf{v}.\mathsf{R} = \mathsf{R}.\mathsf{U}$ of the deformation gradient F into the proper orthogonal (orthonormal $\mathsf{R}^{-1} = \mathsf{R}^\mathsf{T}$ and right-handed $|\mathsf{R}| = 1$) material-convective rotation tensor R (2) and the positive definite, symmetric Eulerian *left* or Lagrangean *right stretch tensors*

$$\mathsf{v} = \mathsf{v}^\mathsf{T} = \sqrt{\mathsf{F}.\mathsf{F}^\mathsf{T}} = \mathsf{R}.\mathsf{U}.\mathsf{R}^\mathsf{T} \qquad \text{or} \qquad \mathsf{U} = \mathsf{U}^\mathsf{T} = \sqrt{\mathsf{F}^\mathsf{T}.\mathsf{F}} = \mathsf{R}^\mathsf{T}.\mathsf{v}.\mathsf{R}, \tag{4}$$

where '.' denotes the *dot product operator* (or *single contraction*) and where F^{-1}, F^T or $\mathsf{F}^{-\mathsf{T}}$ are, respectively, the *inverse*, the *transpose* or the *inverse transpose* of a second-order tensor F. The spectral representation of the deformation gradient

$$\mathsf{F} = \partial \mathbf{x}/\partial \mathbf{X} = \partial \hat{x}_i/\partial \hat{X}_j \, \hat{\mathbf{E}}_i \otimes \hat{\mathbf{E}}_j = \hat{U}_k \underbrace{\hat{\mathbf{e}}_k \otimes \hat{\mathbf{E}}_k}_{\mathsf{R}} = \underbrace{\hat{U}_k \hat{\mathbf{e}}_k \otimes \hat{\mathbf{e}}_k}_{\mathsf{v}}.\mathsf{R} = \mathsf{R}.\underbrace{\hat{\mathbf{E}}_k \otimes \hat{\mathbf{E}}_k \hat{U}_k}_{\mathsf{U}} = \frac{d\hat{\mathbf{x}}_k \otimes d\hat{\mathbf{X}}_k}{\|d\hat{\mathbf{X}}_k\|^2} \tag{5}$$

unveils the polar decomposition $\mathsf{F} = \mathsf{v}.\mathsf{R} = \mathsf{R}.\mathsf{U}$ as well as the definition of the principal quantities (marked with a *hat*): the Eulerian $d\hat{\mathbf{x}}_k$ and Lagrangean $d\hat{\mathbf{X}}_k$ *eigenvectors* with respect to the present κ and reference κ_0 configurations, the *stretch eigenvalues*

$\hat{U}_k = \|d\hat{\mathbf{x}}_{(k)}\|/\|d\hat{\mathbf{X}}_{(k)}\|$, the Eulerian *unit eigenvectors* $\hat{\mathbf{e}}_k = d\hat{\mathbf{x}}_{(k)}/\|d\hat{\mathbf{x}}_{(k)}\| = \mathsf{R}.\hat{\mathbf{E}}_k$ with respect to the present configuration κ and the Lagrangean *unit eigenvectors* $\hat{\mathbf{E}}_k = d\hat{\mathbf{X}}_{(k)}/\|d\hat{\mathbf{X}}_{(k)}\| = \mathsf{R}^\mathsf{T}.\hat{\mathbf{e}}_k$ with respect to the reference configuration κ_0. The '$\otimes$' operators denote dyadic products, the length of a vector $\mathbf{x}$ is given by the (2-)norm $\|\mathbf{x}\| = \sqrt{x_k x_k} = \sqrt{(x_1)^2 + (x_2)^2 + (x_3)^2}$ and, throughout this work, the *summation convention is applied to repeated indices* (if they are not enclosed in brackets).

This work has the following structure: after summarizing the kinematical relations of the finite total deformation in Sections 2 and 3 some finite (partial) deformation measures (like $^@\mathsf{C} = \{\mathsf{C}, {}^e\mathsf{C}, {}^p\mathsf{C}, \cdots\}$ the total, elastic, plastic, $\cdots$ Cauchy-Green deformation tensors) including their geometrical interpretation are introduced in Sections 4 and 5. These finite deformation measures are defined by their spectral representation, and they may be pushed-forward $^@\mathsf{b} = \mathsf{R}.^@\mathsf{C}.\mathsf{R}^\mathsf{T}$ or pulled-back $^@\mathsf{C} = \mathsf{R}^\mathsf{T}.^@\mathsf{b}.\mathsf{R}$ to their Eulerian $^@\mathsf{b}$ or Lagrangean $^@\mathsf{C}$ flavors by the polar rotation (2) of the deformation gradient (5). The corresponding partial deformation-rate tensors $^@\mathsf{d} = \{^e\mathsf{d}, {}^p\mathsf{d}\} = \frac{1}{2}\mathsf{R}.^@\mathsf{U}^{-1}.^@\dot{\mathsf{C}}.^@\mathsf{U}^{-1}.\mathsf{R}^\mathsf{T}$ do not coincide $^@\mathsf{d} \neq \overline{^@\mathsf{d}} = \{\overline{^e\mathsf{d}}, \overline{^p\mathsf{d}}\}$ with the additive contributions $\overline{^e\mathsf{d}} + \overline{^p\mathsf{d}} = \mathsf{d}$ of the total deformation rate (from the stress power equation) in Section 6. Finally, non-material «co-rotational» rates in conjunction with the hypo-elasticity of Truesdell and the Updated Lagrangian Formulation (often applied for finite plasticity analysis within general-purpose finite element simulation tools) are critically discussed in Section 7.

2   The material-convective Lagrangean description $\mathbf{x}(\mathbf{X}, t)$

From a Lagrangean point of view, the deformation gradient (5) maps the vicinity vector $d\mathbf{X}$ of a position vector $\mathbf{X}$ in the reference configuration κ_0 to the vicinity vector

$$dx = \mathsf{F}.d\mathbf{X} = d\mathbf{X}.\mathsf{F}^\mathsf{T} \tag{6}$$

of a position vector $\mathbf{x}$ in the present configuration κ, and the vicinity vectors $d\mathbf{x}$ and $d\mathbf{X}$ describe the kinematical behavior of infinitesimal material line elements in the present κ and reference κ_0 configurations. The infinitesimal mass element dm [the *unit mass* $dm = \rho_0\, dV = \rho\, dv$ with the mass densities ρ_0, ρ and the infinitesimal volumes dV, dv in the reference κ_0, present κ configurations] depicted in Figure 1 is therefore transformed material-convectively from a cube ($\rho_0\, dV$) in the reference configuration κ_0 to a skewed parallelepiped ($\rho\, dv$) in the present configuration κ.

The three arbitrary orthogonal Lagrangean material line elements $d\mathbf{X}_k$ of Figure 1 with the corresponding three arbitrary orthogonal Lagrangean unit vectors $\mathbf{E}_k = d\mathbf{X}_{(k)}/\|d\mathbf{X}_{(k)}\|$ are transformed (6) to the Eulerian material line elements $d\mathbf{x}_k$ which are in general not orthogonal, and the three orthogonal Lagrangean material unit vectors $\mathbf{E}_k$ stay neither orthogonal nor unit vectors when mapped (6) with the material to $\mathsf{F}.\mathbf{E}_k$. Therefore, an arbitrary material-convective Eulerian basis is *defined* by the orthonormal Eulerian base vectors

$$\mathbf{e}_k := \mathsf{R}.\mathbf{E}_k = \mathbf{E}_k.\mathsf{R}^\mathsf{T} \tag{7}$$

co-rotated with the material-convective rotation R tensor (2) relative to the arbitrary orthonormal Lagrangean base vectors $\mathbf{E}_k$ so that the component bases refered to in this work can solely be defined as orthogonal unit vector bases

$$\mathbf{E}_i.\mathbf{E}_j = \mathbf{e}_i.\mathbf{e}_j = \hat{\mathbf{E}}_i.\hat{\mathbf{E}}_j = \hat{\mathbf{e}}_i.\hat{\mathbf{e}}_j = \delta_{ij} = \begin{cases} 1 & \{i = j\} \\ 0 & \{i \neq j\} \end{cases} \tag{8}$$

where δ_{ij} denotes Kronecker's delta; the components S_{ij}, $\hat{S}_k$ of corresponding Lagrangean $\mathsf{S} = S_{ij}\mathbf{E}_i \otimes \mathbf{E}_j = \hat{S}_k\hat{\mathbf{E}}_k \otimes \hat{\mathbf{E}}_k$ and Eulerian $\mathsf{s} = \mathsf{R}.\mathsf{S}.\mathsf{R}^\mathsf{T} = S_{ij}\mathbf{e}_i \otimes \mathbf{e}_j = \hat{S}_k\hat{\mathbf{e}}_k \otimes \hat{\mathbf{e}}_k$ symmetric tensors are then identical—relative to their material-convective bases $\mathbf{e}_i \otimes \mathbf{e}_j = \{\mathsf{R}.\mathbf{E}_i\} \otimes \{\mathbf{E}_j.\mathsf{R}^\mathsf{T}\}$ and $\hat{\mathbf{e}}_{(k)} \otimes \hat{\mathbf{e}}_{(k)} = \{\mathsf{R}.\hat{\mathbf{e}}_{(k)}\} \otimes \{\hat{\mathbf{e}}_{(k)}.\mathsf{R}^\mathsf{T}\}$. The arbitrary orthogonal material-convective base unit vectors $\mathbf{E}_k$, $\mathbf{e}_k$ (7); the unit vectors

$$\mathbf{E} = \frac{d\mathbf{X}}{\|d\mathbf{X}\|}, \qquad \mathbf{e} := \mathsf{R}.\mathbf{E} = \mathbf{E}.\mathsf{R}^\mathsf{T}, \qquad \mathbf{i} = \frac{d\mathbf{x}}{\|d\mathbf{x}\|}, \qquad \mathbf{I} := \mathsf{R}^\mathsf{T}.\mathbf{i} = \mathbf{i}.\mathsf{R} \tag{9}$$

pointing along the edges $d\mathbf{X}$, $d\mathbf{x}$ of the infinitesimal mass elements $dm = \rho_0\, dV$ in the reference configuration κ_0 and $dm = \rho\, dv$ in the present configuration κ;
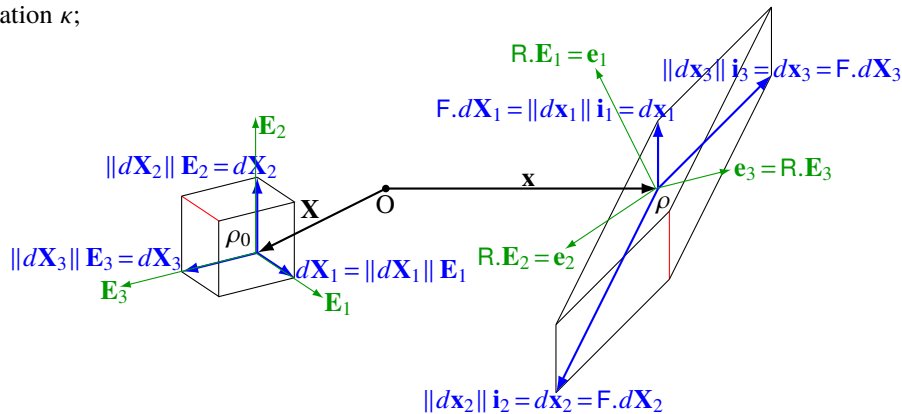
Figure 1. Lagrangean mapping of an infinitesimal mass element $dm = \rho_0\, dV = \rho\, dv$ from a cube ($\rho_0\, dV$) in the reference configuration κ_0 to a skewed parallelepiped ($\rho\, dv$) in the present configuration κ within an arbitrary material-convective base vector system $\mathbf{e}_k := \mathsf{R}.\mathbf{E}_k$ (without a *hat*)
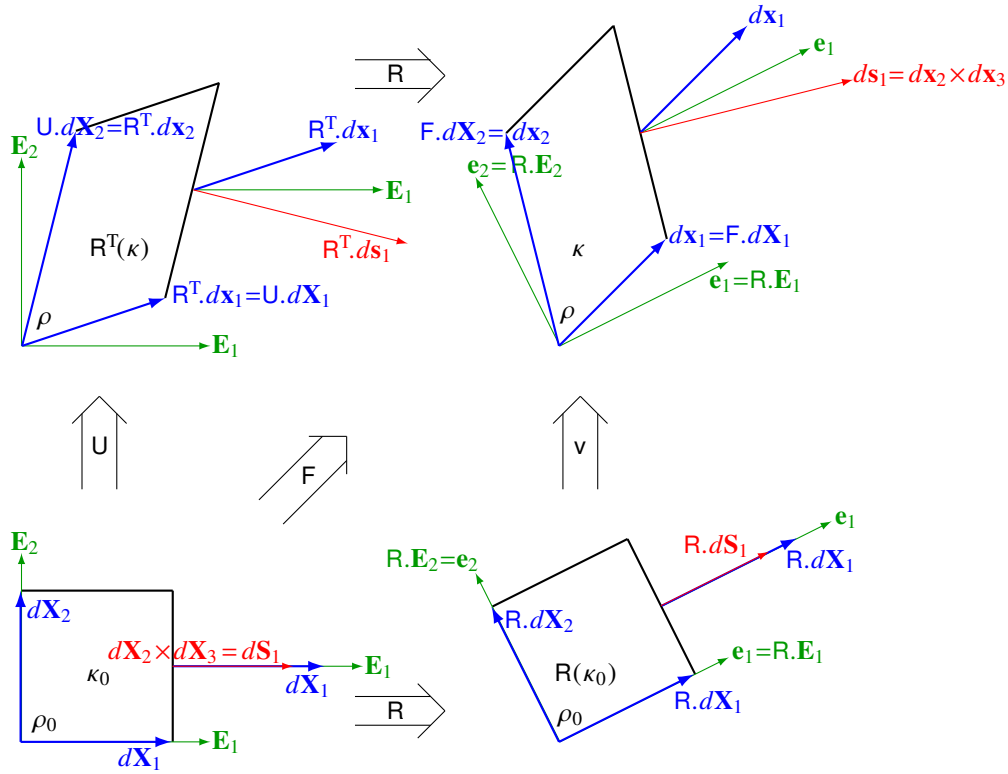
Figure 2. Lagrangean view on the polar decomposition of the deformation gradient $F = v.R = R.U$ within an arbitrary material-convective base vector system $e_k := R.E_k$ (without a *hat*) exemplified for a plane finite deformation of an infinitesimal mass element $dm = \rho_0\,dV = \rho\,dv$ mapped (6) from a cube ($\rho_0\,dV$) in the reference configuration κ_0 to a skewed parallelepiped ($\rho\,dv$) in the present configuration κ

and the unit vectors

$$\mathbf{N} = \frac{d\mathbf{S}}{\|d\mathbf{S}\|}, \qquad \mathbf{n} := \mathsf{R}.\mathbf{N} = \mathbf{N}.\mathsf{R}^T, \qquad \mathbf{m} = \frac{d\mathbf{s}}{\|d\mathbf{s}\|}, \qquad \mathbf{M} := \mathsf{R}^T.\mathbf{m} = \mathbf{m}.\mathsf{R} \qquad (10)$$

of the surface normals $d\mathbf{S}$, $d\mathbf{s} = \dfrac{\rho_0}{\rho}\mathsf{F}^{-T}.d\mathbf{S}$ [Nanson's formula] differ for the mapping (6) in their Eulerian flavor from each other, $\mathbf{e} \neq \mathbf{i} \neq \mathbf{m}$, as shown in Figure 1 and exemplified for a plane finite deformation in Figure 2 [which also illustrates the polar decomposition of the deformation gradient $F = v.R = R.U$].

Within a principal vector basis (unit eigenvector system marked with a *hat*)

$$\hat{\mathbf{e}}_k = \mathsf{R}.\hat{\mathbf{E}}_k = \hat{\mathbf{E}}_k.\mathsf{R}^T, \qquad (11)$$

the eigenvectors are represented by the edges of infinitesimal mass elements dm, see Figure 3 for the Lagrangean view. These edges are mapped (6) material-convectively from a cube $dm = \rho_0\,d\hat{V}$ in the reference configuration κ_0 to a rectangular parallelepiped $dm = \rho\,d\hat{v}$ in the present configuration κ. The corresponding unit eigenvectors/principal base vectors $\hat{\mathbf{E}}_k$, $\hat{\mathbf{e}}_k = \mathsf{R}.\hat{\mathbf{E}}_k$; the edge vectors $d\hat{\mathbf{X}}_k$, $d\hat{\mathbf{x}}_k = \hat{U}_{(k)}\mathsf{R}.d\hat{\mathbf{X}}_{(k)}$; and the surface normal vectors $d\hat{\mathbf{S}}_k$, $d\hat{\mathbf{s}}_k = \dfrac{\hat{U}_1\hat{U}_2\hat{U}_3}{\hat{U}_{(k)}}\mathsf{R}.d\hat{\mathbf{S}}_{(k)}$ [from Eq.(5) and Nanson's formula] of the infinitesimal mass elements $dm = \rho_0\,d\hat{V}$ in the reference configuration κ_0 and $dm = \rho\,d\hat{v}$ in the present configuration κ are therefore collinear
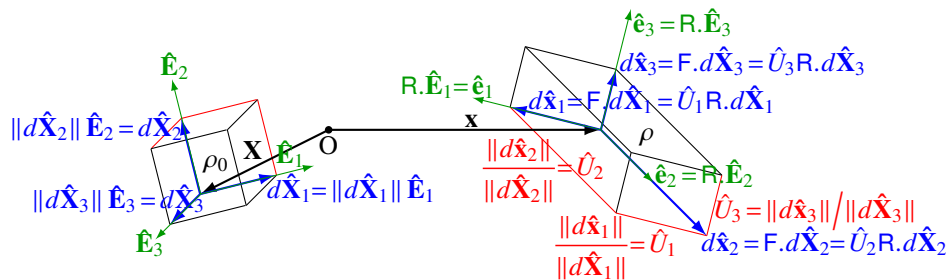
Figure 3. Lagrangean mapping of the eigenvectors relative to the principal base vector systems $\hat{\mathbf{e}}_k = \mathsf{R}.\hat{\mathbf{E}}_k$ (marked with a *hat* and represented by the edges of infinitesimal mass elements $dm = \rho_0\,d\hat{V} = \rho\,d\hat{v}$) from a Lagrangean cube ($\rho_0\,d\hat{V}$) in the reference configuration κ_0 to an Eulerian rectangular parallelepiped ($\rho\,d\hat{v}$) in the present configuration κ

K. Heiduschke

Tech. Mech., Vol. 40, Is. 1, (2020), 31–45

such that

$$\hat{\mathbf{I}}_k = \hat{\mathbf{E}}_k = \frac{d\hat{\mathbf{X}}_{(k)}}{\|d\hat{\mathbf{X}}_{(k)}\|} = \hat{\mathbf{M}}_k = \hat{\mathbf{N}}_k = \frac{d\hat{\mathbf{S}}_{(k)}}{\|d\hat{\mathbf{S}}_{(k)}\|}, \qquad \hat{\mathbf{e}}_k = \hat{\mathbf{i}}_k = \frac{d\hat{\mathbf{x}}_{(k)}}{\|d\hat{\mathbf{x}}_{(k)}\|} = \hat{\mathbf{n}}_k = \hat{\mathbf{m}}_k = \frac{d\hat{\mathbf{s}}_{(k)}}{\|d\hat{\mathbf{s}}_{(k)}\|} \qquad (12)$$

holds.

2.1 Superposed rigid body motions

Under a superposed rigid body motion (hereafter denoted by SRBM and marked with a *subscript plus*)

$$_+\mathbf{x}(\mathbf{X}, _+t) = \mathbf{a}(t) + \mathsf{Q}(t).\mathbf{x}(\mathbf{X}, t), \qquad _+t = t - a \qquad (13)$$

characterized by the translation vector $\mathbf{a}(t)$ and second-order rotation tensor $\mathsf{Q}(t)$ [both functions of time t only]

- *Lagrangean tensors (written in uppercase) are invariant*, like the reference position vector $_+\mathbf{X} = \mathbf{X}$ [which specifies a material point/particle by its position in the reference configuration κ_0 at $t = 0$] or the symmetric second-order right stretch tensor $_+\mathsf{U} = \mathsf{U}$

- *Eulerian tensors (written in lowercase) are altered* in particular through the rotation $\mathsf{Q} = \mathsf{Q}^{-\mathsf{T}}$ of the SRBM, like the present position vector (13) or the symmetric second-order left stretch tensor $_+\mathsf{v} = \mathsf{Q}.\mathsf{v}.\mathsf{Q}^\mathsf{T}$

2.2 Time derivatives of Lagrangean tensor fields

By its physical definition, the Lagrangean description is convected with the material. Therefore, the time derivative

$$\dot{\mathsf{S}} = \dot{S}_{ij}\mathbf{E}_i \otimes \mathbf{E}_j = \overset{\circ}{\mathsf{S}} \qquad (14)$$

of a symmetric second-order Lagrangean tensor $\mathsf{S} = S_{ij}\mathbf{E}_i \otimes \mathbf{E}_j = \mathsf{S}^\mathsf{T} = S_{ij}\mathbf{E}_j \otimes \mathbf{E}_i$ is identical to its material-convective rate $\overset{\circ}{\mathsf{S}}$ since the time derivatives $\dot{\mathbf{E}}_k = \mathbf{0}$ of arbitrary Lagrangean base unit vectors $\mathbf{E}_k$ vanish. In a Lagrangean description $\dot{\mathsf{S}}$ and $\overset{\circ}{\mathsf{S}}$ need *not* to be distinguished. The time derivative (14) of a symmetric second-order Lagrangean tensor $\mathsf{S} = \hat{S}_k \hat{\mathbf{E}}_k \otimes \hat{\mathbf{E}}_k$ reads in spectral representation

$$\dot{\mathsf{S}} = \dot{\hat{S}}_k \hat{\mathbf{E}}_k \otimes \hat{\mathbf{E}}_k + \hat{S}_k \dot{\hat{\mathbf{E}}}_k \otimes \hat{\mathbf{E}}_k + \hat{S}_k \hat{\mathbf{E}}_k \otimes \dot{\hat{\mathbf{E}}}_k = \dot{\hat{S}}_k \hat{\mathbf{E}}_k \otimes \hat{\mathbf{E}}_k + \Lambda.\mathsf{S} - \mathsf{S}.\Lambda, \qquad (15)$$

where the time derivatives

$$\dot{\hat{\mathbf{E}}}_k = \Lambda.\hat{\mathbf{E}}_k = -\hat{\mathbf{E}}_k.\Lambda = \underline{\lambda} \times \hat{\mathbf{E}}_k = -\hat{\mathbf{E}}_k \times \underline{\lambda} = -\in_{ijk} \hat{\lambda}_i \, \hat{\mathbf{E}}_j \qquad (16)$$

of the Lagrangean principal base vectors $\hat{\mathbf{E}}_k$ (unit eigenvectors) can either be expressed as dot products with the antisymmetric second-order Lagrangean principal spin tensor

$$\Lambda = -\Lambda^\mathsf{T} = -\in_{ijk} \lambda_k \, \mathbf{E}_i \otimes \mathbf{E}_j \qquad (17)$$

or as cross products with the dual Lagrangean principal spin vector $\underline{\lambda}$. The components of dual tensors $\underline{\lambda} = \lambda_k \mathbf{E}_k$ and $\Lambda = \Lambda_{ij}\mathbf{E}_i \otimes \mathbf{E}_j = -\Lambda^\mathsf{T} = -\Lambda_{ji}\mathbf{E}_i \otimes \mathbf{E}_j$ obey

$$\lambda_k = -\tfrac{1}{2} \in_{ijk} \Lambda_{ij}, \qquad \Lambda_{ij} = -\Lambda_{ji} = -\in_{ijk} \lambda_k \qquad (18)$$

where

$$\in_{ijk} = \frac{(i-j)(j-k)(k-i)}{2} = \begin{cases} 1 & \{ijk = 123, 231, 312\} \\ -1 & \{ijk = 321, 132, 213\} \\ 0 & \{otherwise\} \end{cases} \qquad (19)$$

denotes the Levi-Civita (1925) epsilon [also known as alternating unit symbol].

3 The spatial Eulerian description $\mathbf{X}(\mathbf{x}, t)$ with material convection

From an Eulerian point of view, the inverse deformation gradient

$$\mathsf{F}^{-1} = \partial\mathbf{X}/\partial\mathbf{x} = \partial\hat{X}_i/\partial\hat{x}_j \, \hat{\mathbf{e}}_i \otimes \hat{\mathbf{e}}_j = \frac{1}{\hat{U}_k} \underbrace{\hat{\mathbf{E}}_k \otimes \hat{\mathbf{e}}_k}_{\mathsf{R}^\mathsf{T}} = \mathsf{R}^\mathsf{T}.\underbrace{\hat{\mathbf{e}}_k \otimes \hat{\mathbf{e}}_k \, 1/\hat{U}_k}_{\mathsf{v}^{-1}} = \underbrace{1/\hat{U}_k \hat{\mathbf{E}}_k \otimes \hat{\mathbf{E}}_k}_{\mathsf{U}^{-1}}.\mathsf{R}^\mathsf{T} = \frac{d\hat{\mathbf{X}}_k \otimes d\hat{\mathbf{x}}_k}{\|d\hat{\mathbf{x}}_k\|^2} \qquad (20)$$

maps the vicinity vector $d\mathbf{x}$ of a position vector $\mathbf{x}$ in the present configuration κ back to the vicinity vector

$$d\mathbf{X} = \mathsf{F}^{-1}.d\mathbf{x} = d\mathbf{x}.\mathsf{F}^{-\mathsf{T}} \qquad (21)$$

of a position vector $\mathbf{X}$ in the reference configuration κ_0, and the vicinity vectors $d\mathbf{X}$ and $d\mathbf{x}$ describe [like in Eq.(6)] the kinematical behavior of infinitesimal material line elements in the reference κ_0 and present κ configurations. The infinitesimal mass element $dm = \rho \, dv = \rho_0 \, dV$ [the *unit mass*] depicted in Figure 4 is therefore transformed material-convectively from a cube ($\rho \, dv$) in the present configuration κ back to a skewed parallelepiped ($\rho_0 \, dV$) in the reference configuration κ_0.
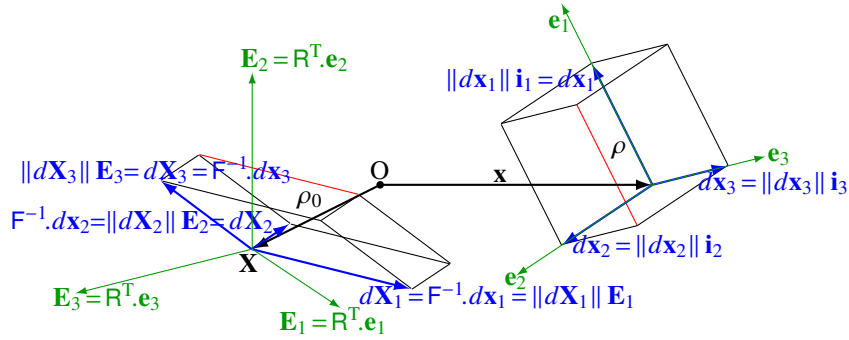
Figure 4. Eulerian mapping of an infinitesimal mass element $dm = \rho\, dv = \rho_0\, dV$ from a cube ($\rho\, dv$) in the present configuration κ back to a skewed parallelepiped ($\rho_0\, dV$) in the reference configuration κ_0 within an arbitrary material-convective base vector system $\mathbf{E}_k := \mathsf{R}^T . \mathbf{e}_k$ (without a *hat*)

The arbitrary orthogonal material-convective base unit vectors $\mathbf{E}_k := \mathsf{R}^T . \mathbf{e}_k$; the unit vectors $\mathbf{i}$ (9c), $\mathbf{E}$ (9a) pointing along the edges $d\mathbf{x}$, $d\mathbf{X}$ of the infinitesimal mass elements $dm = \rho\, dv$ in the present configuration κ and $dm = \rho_0\, dV$ in the reference configuration κ_0; and the unit vectors $\mathbf{m}$ (10c), $\mathbf{N}$ (10a) of the surface normals $d\mathbf{s}$, $d\mathbf{S} = \dfrac{\rho}{\rho_0}\mathsf{F}^T . d\mathbf{s}$ [Nanson's inverse formula] differ for the reverse mapping (21) in their Lagrangean flavor from each other, $\mathbf{E} \neq \mathbf{I} \neq \mathbf{N}$, as shown in Figure 4 and exemplified for a plane finite deformation in Figure 5 [which also illustrates the polar decomposition of the inverse deformation gradient $\mathsf{F}^{-1} = \mathsf{R}^T . \mathsf{v}^{-1} = \mathsf{U}^{-1} . \mathsf{R}^T$].

Within a principal vector basis (unit eigenvector system marked with a *hat*) the eigenvectors are represented by the edges of infinitesimal mass elements dm, see Figure 6 for the Eulerian view. These edges are mapped back (21) material-convectively from a cube $dm = \rho\, d\hat{v}$ in the present configuration κ to a rectangular parallelepiped $dm = \rho_0\, d\hat{V}$ in the reference configuration κ_0. The corresponding unit eigenvectors $\hat{\mathbf{e}}_k$, $\hat{\mathbf{E}}_k = \mathsf{R}^T . \hat{\mathbf{e}}_k$; the edge vectors $d\hat{\mathbf{x}}_k$, $d\hat{\mathbf{X}}_k = 1/\hat{U}_{(k)}\mathsf{R}^T . d\hat{\mathbf{x}}_{(k)}$; and the surface normal vectors $d\hat{\mathbf{s}}_k$, $d\hat{\mathbf{S}}_k = \dfrac{\hat{U}_{(k)}}{\hat{U}_1 \hat{U}_2 \hat{U}_3}\mathsf{R}^T . d\hat{\mathbf{s}}_{(k)}$ [from Eq.(20) and Nanson's inverse formula] of the infinitesimal mass elements $dm = \rho\, d\hat{v}$ in the present configuration κ and $dm = \rho_0\, d\hat{V}$ in the reference configuration κ_0 are therefore collinear, such that (12) holds.
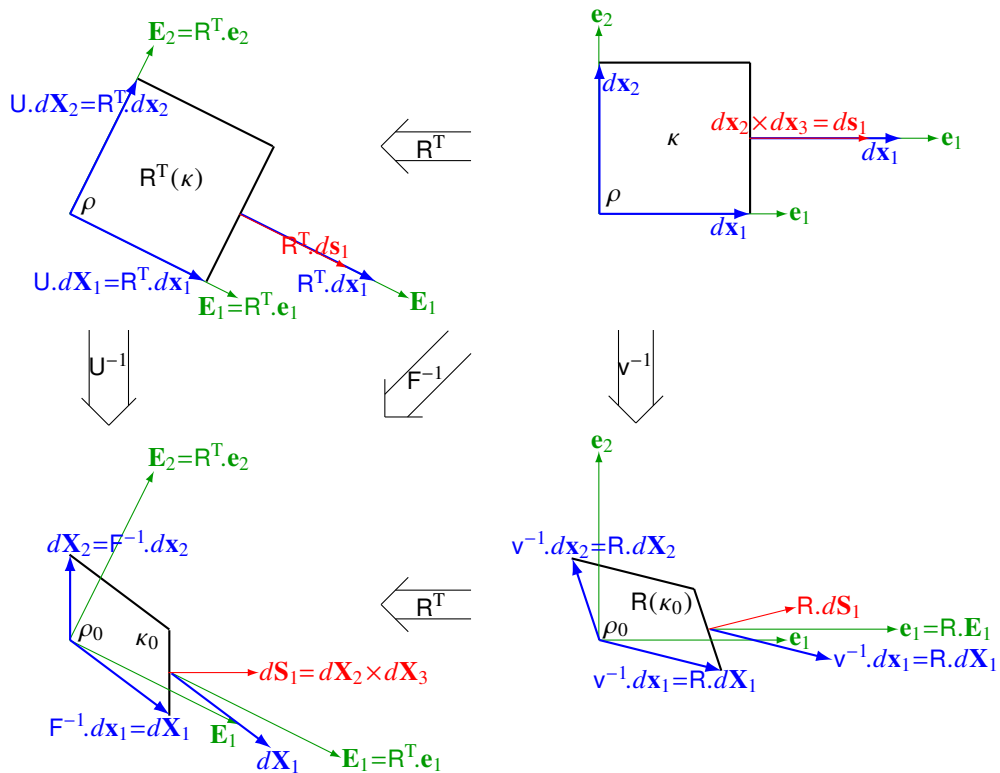
Figure 5. Eulerian view on the polar decomposition of the inverse deformation gradient $\mathsf{F}^{-1} = \mathsf{R}^T . \mathsf{v}^{-1} = \mathsf{U}^{-1} . \mathsf{R}^T$ within an arbitrary material-convective base vector system $\mathbf{E}_k := \mathsf{R}^T . \mathbf{e}_k$ (without a *hat*) exemplified for a plane finite deformation of an infinitesimal mass element $dm = \rho\, dv = \rho_0\, dV$ mapped (21) from a cube ($\rho\, dv$) in the present configuration κ back to a skewed parallelepiped ($\rho_0\, dV$) in the reference configuration κ_0
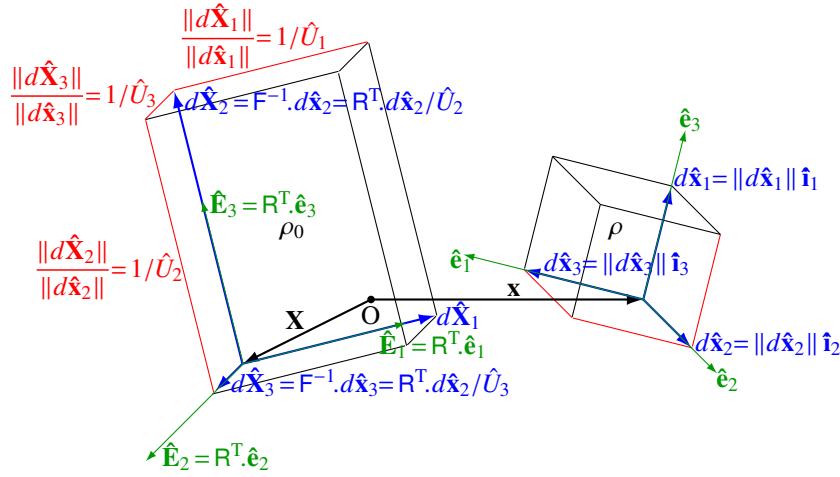
Figure 6. Eulerian mapping of the eigenvectors relative to the principal base vector systems $\hat{\mathbf{E}}_k = \mathsf{R}^{\mathsf{T}}.\hat{\mathbf{e}}_k$ (marked with a *hat* and represented by the edges of infinitesimal mass elements $dm = \rho \, d\hat{v} = \rho_0 \, d\hat{V}$) from an Eulerian cube ($\rho \, d\hat{v}$) in the present configuration κ back to a Lagrangean rectangular parallelepiped ($\rho_0 \, d\hat{V}$) in the reference configuration κ_0

3.1   Time derivatives of Eulerian scalar $\varphi(\mathbf{x}, t)$, vector $\mathbf{a}(\mathbf{x}, t)$ and symmetric second-order tensor $\mathsf{s}(\mathbf{x}, t)$ fields

The non-material time derivative

$$\frac{d\varphi(\mathbf{x}, t)}{dt} = \left.\frac{\partial \varphi}{\partial t}\right|_{\mathbf{x}} + \frac{\partial \varphi}{\partial \mathbf{x}}.\tilde{\mathbf{c}} \tag{22}$$

of a scalar $\varphi(\mathbf{x}, t)$ field follows from the product rule with a non-material translation velocity vector $\tilde{\mathbf{c}} = \partial \mathbf{x}/\partial t$. If $\tilde{\mathbf{c}}$ is replaced by the material translation velocity $\mathbf{v}$ vector (1) then the time derivative (22) turns into the translational-convective time derivative

$$\dot{\varphi}(\mathbf{x}, t) = \left.\frac{\partial \varphi}{\partial t}\right|_{\mathbf{x}} + \frac{\partial \varphi}{\partial \mathbf{x}}.\mathbf{v} = \mathring{\varphi}(\mathbf{x}, t) \tag{23}$$

which is, for a scalar $\varphi(\mathbf{x}, t)$ with no directional orientation, identical to the material-convective rate $\mathring{\varphi}(\mathbf{x}, t)$ field.
Similarly, the non-material time derivative of an Eulerian vector $\mathbf{a}(\mathbf{x}, t) = \tilde{a}_k \tilde{\mathbf{e}}_k$ field follows as

$$\frac{d\mathbf{a}(\mathbf{x}, t)}{dt} = \left.\frac{\partial \mathbf{a}}{\partial t}\right|_{\mathbf{x}} + \frac{\partial \mathbf{a}}{\partial \mathbf{x}}.\tilde{\mathbf{c}} = \underbrace{\left(\left.\frac{\partial \tilde{a}_k}{\partial t}\right|_{\mathbf{x}} + \frac{\partial \tilde{a}_k}{\partial \mathbf{x}}.\tilde{\mathbf{c}}\right)}_{d\tilde{a}_k(\mathbf{x}, t)/dt}\tilde{\mathbf{e}}_k + \tilde{a}_k\underbrace{\overbrace{\left(\left.\frac{\partial \tilde{\mathbf{e}}_k}{\partial t}\right|_{\mathbf{x}} + \frac{\partial \tilde{\mathbf{e}}_k}{\partial \mathbf{x}}.\tilde{\mathbf{c}}\right)}^{\dot{\tilde{\mathbf{e}}}_k = \tilde{\Theta}.\tilde{\mathbf{e}}_k = -\tilde{\mathbf{e}}_k.\tilde{\Theta}}}_{\tilde{\Theta}.\mathbf{a} = -\mathbf{a}.\tilde{\Theta}} \tag{24}$$

where the non-material time derivatives of the non-convective base unit vectors $\tilde{\mathbf{e}}_k$ are given by

$$\dot{\tilde{\mathbf{e}}}_k = \left.\frac{\partial \tilde{\mathbf{e}}_k}{\partial t}\right|_{\mathbf{x}} + \frac{\partial \tilde{\mathbf{e}}_k}{\partial \mathbf{x}}.\tilde{\mathbf{c}} = \tilde{\Theta}.\tilde{\mathbf{e}}_k = -\tilde{\mathbf{e}}_k.\tilde{\Theta} \tag{25}$$

with a non-material antisymmetric second-order spin tensor $\tilde{\Theta} = -\tilde{\Theta}^{\mathsf{T}}$. If the non-material translation velocity $\tilde{\mathbf{c}}$ vector and the non-material spin $\tilde{\Theta}$ tensor are, respectively, replaced by the material translation velocity $\mathbf{v}$ vector (1) and the antisymmetric second-order Eulerian tensor (3) of material-convective spin Ω [see Dienes (1979, 1986)] then the time derivative $d\tilde{a}_k/dt \, \tilde{\mathbf{e}}_k$ relative to the $\tilde{\Theta}$-co-rotated basis $\tilde{\mathbf{e}}_k$ in Eq.(24) turns into the *material-convective vector rate* $\mathring{\mathbf{a}}(\mathbf{x}, t)$, the first underbraced term of the translational-convective time derivative

$$\dot{\mathbf{a}}(\mathbf{x}, t) = \left.\frac{\partial \mathbf{a}}{\partial t}\right|_{\mathbf{x}} + \frac{\partial \mathbf{a}}{\partial \mathbf{x}}.\mathbf{v} = \underbrace{\overbrace{\left(\left.\frac{\partial a_k}{\partial t}\right|_{\mathbf{x}} + \frac{\partial a_k}{\partial \mathbf{x}}.\mathbf{v}\right)}^{\mathring{a}_k(\mathbf{x}, t)}\mathbf{e}_k}_{\mathring{\mathbf{a}}(\mathbf{x}, t)} + a_k\underbrace{\overbrace{\left(\left.\frac{\partial \mathbf{e}_k}{\partial t}\right|_{\mathbf{x}} + \frac{\partial \mathbf{e}_k}{\partial \mathbf{x}}.\mathbf{v}\right)}^{\dot{\mathbf{e}}_k = \Omega.\mathbf{e}_k = -\mathbf{e}_k.\Omega}}_{\Omega.\mathbf{a} = -\mathbf{a}.\Omega} \tag{26}$$

of a materially co-rotated (2) Eulerian vector $\mathbf{a}(\mathbf{x}, t) = a_k \mathbf{e}_k = \mathsf{R}.\mathbf{A}$ with respect to its corresponding Lagrangean vector $\mathbf{A} = a_k \mathbf{E}_k$. The overbraced

$$\dot{\mathbf{e}}_k = \left.\frac{\partial \mathbf{e}_k}{\partial t}\right|_{\mathbf{x}} + \frac{\partial \mathbf{e}_k}{\partial \mathbf{x}}.\mathbf{v} = \Omega.\mathbf{e}_k = -\mathbf{e}_k.\Omega \tag{27}$$

at the r.h.s. of Eq.(26) denote the time derivatives of the material-convective base unit vectors (7) defined with the antisymmetric second-order Eulerian tensor (3) of material-convective spin Ω, which follow from $\dot{\mathbf{e}}_k = \dot{\mathsf{R}}.\mathbf{E}_k = \dot{\mathsf{R}}.\mathsf{R}^{\mathsf{T}}.\mathbf{e}_k$ and the inverse of Eq.(7).
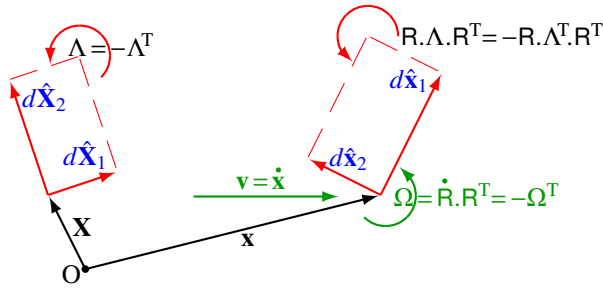
Figure 7. Kinematics of Lagrangean $d\hat{\mathbf{X}}_k$ and Eulerian $d\hat{\mathbf{x}}_k$ eigenvectors

In the same vein, the non-material time derivative

$$\frac{d\mathsf{s}(\mathbf{x},t)}{dt} = \frac{\partial \mathsf{s}}{\partial t}\bigg|_{\mathbf{x}} + \frac{\partial \mathsf{s}}{\partial \mathbf{x}}.\tilde{\mathbf{c}} = \underbrace{\left(\frac{\partial \tilde{s}_{ij}}{\partial t}\bigg|_{\mathbf{x}} + \frac{\partial \tilde{s}_{ij}}{\partial \mathbf{x}}.\tilde{\mathbf{c}}\right)}_{d\tilde{s}_{ij}(\mathbf{x},t)/dt}\tilde{\mathbf{e}}_i\otimes\tilde{\mathbf{e}}_j + \underbrace{\tilde{s}_{ij}\tilde{\Theta}.\tilde{\mathbf{e}}_i\otimes\tilde{\mathbf{e}}_j}_{\tilde{\Theta}.\mathsf{s}} - \underbrace{\tilde{s}_{ij}\tilde{\mathbf{e}}_i\otimes\tilde{\mathbf{e}}_j.\tilde{\Theta}}_{\mathsf{s}.\tilde{\Theta}} \tag{28}$$

of a symmetric second-order Eulerian tensor $\mathsf{s}(\mathbf{x},t) = \tilde{s}_{ij}\tilde{\mathbf{e}}_i\otimes\tilde{\mathbf{e}}_j$ field is defined with a non-material translation velocity $\tilde{\mathbf{c}}$ and a non-material time derivative (25) of the non-convective base unit vectors $\tilde{\mathbf{e}}_k$. If the non-material translation velocity $\tilde{\mathbf{c}}$ vector and the non-material spin $\tilde{\Theta}$ tensor are, respectively, replaced by the material translation velocity $\mathbf{v}$ vector (1) and the tensor (3) of material-convective spin Ω then the time derivative $d\tilde{s}_{ij}/dt\,\tilde{\mathbf{e}}_i\otimes\tilde{\mathbf{e}}_j$ relative to the $\tilde{\Theta}$-co-rotated basis $\tilde{\mathbf{e}}_i\otimes\tilde{\mathbf{e}}_j$ in Eq.(28) turns into the *material-convective tensor rate* $\mathring{\mathsf{s}}(\mathbf{x},t)$, the first underbraced term of the translational-convective time derivative

$$\dot{\mathsf{s}}(\mathbf{x},t) = \frac{\partial \mathsf{s}}{\partial t}\bigg|_{\mathbf{x}} + \frac{\partial \mathsf{s}}{\partial \mathbf{x}}.\mathbf{v} = \underbrace{\overbrace{\left(\frac{\partial s_{ij}}{\partial t}\bigg|_{\mathbf{x}} + \frac{\partial s_{ij}}{\partial \mathbf{x}}.\mathbf{v}\right)}^{\mathring{s}_{ij}(\mathbf{x},t)}\mathbf{e}_i\otimes\mathbf{e}_j}_{\mathring{\mathsf{s}}(\mathbf{x},t)} + \underbrace{s_{ij}\Omega.\mathbf{e}_i\otimes\mathbf{e}_j}_{\Omega.\mathsf{s}} - \underbrace{s_{ij}\mathbf{e}_i\otimes\mathbf{e}_j.\Omega}_{\mathsf{s}.\Omega} \tag{29}$$

of a symmetric second-order Eulerian tensor $\mathsf{s}(\mathbf{x},t) = s_{ij}\mathbf{e}_i\otimes\mathbf{e}_j = \mathsf{R}.\mathsf{S}.\mathsf{R}^\mathsf{T}$ with respect to its corresponding Lagrangean tensor $\mathsf{S} = s_{ij}\mathbf{E}_i\otimes\mathbf{E}_j$. The time derivative (29) of a symmetric second-order Eulerian tensor $\mathsf{s} = \hat{S}_k\hat{\mathbf{e}}_k\otimes\hat{\mathbf{e}}_k = \mathsf{R}.\mathsf{S}.\mathsf{R}^\mathsf{T}$ reads in spectral representation

$$\dot{\mathsf{s}} = \dot{\hat{S}}_k\hat{\mathbf{e}}_k\otimes\hat{\mathbf{e}}_k + \hat{S}_k\dot{\hat{\mathbf{e}}}_k\otimes\hat{\mathbf{e}}_k + \hat{S}_k\hat{\mathbf{e}}_k\otimes\dot{\hat{\mathbf{e}}}_k = \dot{\hat{S}}_k\hat{\mathbf{e}}_k\otimes\hat{\mathbf{e}}_k + \Gamma.\mathsf{s} - \mathsf{s}.\Gamma \tag{30}$$

where the time derivatives

$$\dot{\hat{\mathbf{e}}}_k = \left(\mathsf{R}.\hat{\mathbf{E}}_k\right)^{\displaystyle\cdot} = \dot{\mathsf{R}}.\hat{\mathbf{E}}_k + \mathsf{R}.\dot{\hat{\mathbf{E}}}_k = (\underbrace{\dot{\mathsf{R}}.\mathsf{R}^\mathsf{T}}_{\Omega} + \mathsf{R}.\Lambda.\mathsf{R}^\mathsf{T}).\hat{\mathbf{e}}_k = \Gamma.\hat{\mathbf{e}}_k = -\hat{\mathbf{e}}_k.\Gamma \tag{31}$$

of the Eulerian principal base vectors $\hat{\mathbf{e}}_k$ (unit eigenvectors) follow with the antisymmetric second-order Eulerian principal spin tensor

$$\Gamma = -\Gamma^\mathsf{T} = \Omega + \mathsf{R}.\Lambda.\mathsf{R}^\mathsf{T} = -\epsilon_{ijk}\underbrace{(\omega_k + \lambda_k)}_{\gamma_k}\mathbf{e}_i\otimes\mathbf{e}_j \tag{32}$$

compiled from $\Omega = -\epsilon_{ijk}\omega_k\,\mathbf{e}_i\otimes\mathbf{e}_j$ and $\mathsf{R}.\Lambda.\mathsf{R}^\mathsf{T} = -\epsilon_{ijk}\lambda_k\,\mathbf{e}_i\otimes\mathbf{e}_j$ [cf. Eqs.(7), (17) and Figure 7].

3.2   The material-convective Green-Naghdi rate of a symmetric second-order Eulerian tensor $\mathsf{s}(\mathbf{x},t)$ field

Since the material-convective rate $\mathring{\mathsf{S}}$ of a symmetric second-order Lagrangean tensor S is identical (14) to its time derivative $\dot{\mathsf{S}}$, the material-convective rate

$$\mathring{\mathsf{s}} = \mathsf{R}.\underbrace{(\mathsf{R}^\mathsf{T}.\mathsf{s}.\mathsf{R})^{\displaystyle\cdot}}_{\dot{\mathsf{S}}}.\mathsf{R}^\mathsf{T} = \dot{\mathsf{s}} - \Omega.\mathsf{s} + \mathsf{s}.\Omega \tag{33}$$

of its corresponding material-convectively forward-rotated symmetric second-order Eulerian tensor $\mathsf{s} = \mathsf{R}.\mathsf{S}.\mathsf{R}^\mathsf{T}$ is given by the forward-rotation $\mathsf{R}.\dot{\mathsf{S}}.\mathsf{R}^\mathsf{T}$ of the time derivative $\dot{\mathsf{S}} = (\mathsf{R}^\mathsf{T}.\mathsf{s}.\mathsf{R})^{\displaystyle\cdot} = \mathring{\mathsf{S}}$ of the back-rotated Lagrangean tensor $\mathsf{S} = \mathsf{R}^\mathsf{T}.\mathsf{s}.\mathsf{R}$—consistent with Eq.(29) where the $\mathbf{e}_i\otimes\mathbf{e}_j$ components $\mathring{s}_{ij}$ of the material-convective tensor rate $\mathring{\mathsf{s}} = \mathring{s}_{ij}\mathbf{e}_i\otimes\mathbf{e}_j$ are defined relative to the material-convective (7) basis $\mathbf{e}_i\otimes\mathbf{e}_j = \{\mathsf{R}.\mathbf{E}_i\}\otimes\{\mathbf{E}_j.\mathsf{R}^\mathsf{T}\}$. The only material-convective time derivative (denoted with a *superscript ring*) of a symmetric second-order Eulerian tensor is given by the *Green-Naghdi rate* (33) [see Eqs.(8.20)–(8.23) of Green&Naghdi (1965) p.273] which convects the material rotationally with the antisymmetric tensor Ω of the material-convective spin (3) and

translationally with the material velocity $\mathbf{v}$ vector (1). With (30) and (32), the material-convective rate (33) of the symmetric second-order Eulerian tensor $\mathbf{s} = \hat{S}_k\,\hat{\mathbf{e}}_k\otimes\hat{\mathbf{e}}_k = \mathsf{R}.\mathsf{S}.\mathsf{R}^{\mathsf{T}}$ reads in spectral representation

$$\mathring{\mathbf{s}} = \dot{\hat{S}}_k\,\hat{\mathbf{e}}_k\otimes\hat{\mathbf{e}}_k + (\mathsf{R}.\Lambda.\mathsf{R}^{\mathsf{T}}).\mathbf{s} - \mathbf{s}.(\mathsf{R}.\Lambda.\mathsf{R}^{\mathsf{T}}) = \mathsf{R}.(\underbrace{\dot{\hat{S}}_k\,\hat{\mathbf{E}}_k\otimes\hat{\mathbf{E}}_k + \Lambda.\mathsf{S} - \mathsf{S}.\Lambda}_{\mathring{\mathsf{S}}}).\mathsf{R}^{\mathsf{T}}, \tag{34}$$

cf. Eq.(15).

4   Finite deformation kinematics

From the polar decomposition of the deformation gradient $\mathsf{F} = \mathsf{R}.\mathsf{U}$ into the material-convective rotation R tensor (2) and the right stretch $\mathsf{U} = \hat{U}_k\,\hat{\mathbf{E}}_k\otimes\hat{\mathbf{E}}_k$ tensor (4b) and with the material-convective spin Ω tensor (3) and the spin tensors Λ, Γ of the Lagrangean (17), Eulerian (32) principal axes, the velocity gradient

$$\dot{\mathsf{F}}.\mathsf{F}^{-1} = (\dot{\mathsf{R}}.\mathsf{U}+\mathsf{R}.\dot{\mathsf{U}}).(\mathsf{U}^{-1}.\mathsf{R}^{\mathsf{T}}) = (\dot{\hat{U}}_k\,\hat{\mathbf{e}}_k\otimes\hat{\mathbf{E}}_k + \hat{U}_k\,\dot{\hat{\mathbf{e}}}_k\otimes\hat{\mathbf{E}}_k + \hat{U}_k\,\hat{\mathbf{e}}_k\otimes\dot{\hat{\mathbf{E}}}_k).(\hat{\mathbf{E}}_\ell\otimes\hat{\mathbf{e}}_\ell\,{}^1\!/\hat{U}_\ell)$$

$$= \underbrace{\dot{\mathsf{R}}.\mathsf{R}^{\mathsf{T}}}_{\Omega}+\mathsf{R}.(\dot{\mathsf{U}}.\mathsf{U}^{-1}).\mathsf{R}^{\mathsf{T}} = \frac{\dot{\hat{U}}_k}{\hat{U}_k}\,\hat{\mathbf{e}}_k\otimes\hat{\mathbf{e}}_k + \underbrace{\Omega+\mathsf{R}.\Lambda.\mathsf{R}^{\mathsf{T}}}_{\Gamma}-\mathsf{F}.\Lambda.\mathsf{F}^{-1} = \frac{\dot{\hat{U}}_k}{\hat{U}_k}\,\hat{\mathbf{e}}_k\otimes\hat{\mathbf{e}}_k + \Omega + \mathsf{R}.(\Lambda-\mathsf{U}.\Lambda.\mathsf{U}^{-1}).\mathsf{R}^{\mathsf{T}} \tag{35}$$

may additively be split into (its symmetric part) the Eulerian deformation-rate tensor

$$\mathsf{d} = \tfrac{1}{2}(\dot{\mathsf{F}}.\mathsf{F}^{-1}+\mathsf{F}^{-\mathsf{T}}.\dot{\mathsf{F}}^{\mathsf{T}}) = \tfrac{1}{2}\mathsf{R}.(\dot{\mathsf{U}}.\mathsf{U}^{-1}+\mathsf{U}^{-1}.\dot{\mathsf{U}}).\mathsf{R}^{\mathsf{T}} = \frac{\dot{\hat{U}}_k}{\hat{U}_k}\,\hat{\mathbf{e}}_k\otimes\hat{\mathbf{e}}_k - \tfrac{1}{2}\mathsf{R}.(\mathsf{U}.\Lambda.\mathsf{U}^{-1}-\mathsf{U}^{-1}.\Lambda.\mathsf{U}).\mathsf{R}^{\mathsf{T}}$$

$$= \tfrac{1}{2}(\mathring{\mathsf{v}}.\mathsf{v}^{-1}+\mathsf{v}^{-1}.\mathring{\mathsf{v}}) = \tfrac{1}{2}\mathsf{v}^{-1}.\mathring{\mathsf{b}}.\mathsf{v}^{-1} = \tfrac{1}{2}\mathsf{F}^{-\mathsf{T}}.\dot{\mathsf{C}}.\mathsf{F}^{-1} \tag{36}$$

and into (its antisymmetric part) the Eulerian vorticity tensor

$$\mathsf{w} = \tfrac{1}{2}(\dot{\mathsf{F}}.\mathsf{F}^{-1}-\mathsf{F}^{-\mathsf{T}}.\dot{\mathsf{F}}^{\mathsf{T}}) = \Omega+\tfrac{1}{2}\mathsf{R}.(\dot{\mathsf{U}}.\mathsf{U}^{-1}-\mathsf{U}^{-1}.\dot{\mathsf{U}}).\mathsf{R}^{\mathsf{T}} = \Omega-\tfrac{1}{2}\mathsf{R}.(\mathsf{U}.\Lambda.\mathsf{U}^{-1}+\mathsf{U}^{-1}.\Lambda.\mathsf{U}-2\Lambda).\mathsf{R}^{\mathsf{T}}. \tag{37}$$

The $\mathring{\mathsf{b}}$ and $\dot{\mathsf{C}}$ at the r.h.s. of Eq.(36) are material-convective rates [cf. (33) and (14)] of the positive definite, symmetric left and right Cauchy (1827b)-Green (1839) deformation tensors

$$\mathsf{b} = \mathsf{b}^{\mathsf{T}} = \mathsf{F}.\mathsf{F}^{\mathsf{T}} = \mathsf{v}^2 = \mathsf{R}.\mathsf{C}.\mathsf{R}^{\mathsf{T}} \qquad\text{and}\qquad \mathsf{C} = \mathsf{C}^{\mathsf{T}} = \mathsf{F}^{\mathsf{T}}.\mathsf{F} = \mathsf{U}^2 = \mathsf{R}^{\mathsf{T}}.\mathsf{b}.\mathsf{R}, \tag{38}$$

respectively. The Lagrangean deformation-rate tensor

$$\mathsf{D} = \mathsf{R}^{\mathsf{T}}.\mathsf{d}.\mathsf{R} = \tfrac{1}{2}(\dot{\mathsf{U}}.\mathsf{U}^{-1}+\mathsf{U}^{-1}.\dot{\mathsf{U}}) = \frac{\dot{\hat{U}}_k}{\hat{U}_k}\,\hat{\mathbf{E}}_k\otimes\hat{\mathbf{E}}_k - \tfrac{1}{2}(\mathsf{U}.\Lambda.\mathsf{U}^{-1}-\mathsf{U}^{-1}.\Lambda.\mathsf{U}) = \tfrac{1}{2}\mathsf{U}^{-1}.\dot{\mathsf{C}}.\mathsf{U}^{-1} \tag{39}$$

follows from the material-convective backward rotation of Eq.(36). The principal components $\hat{w}_k$, $\hat{\omega}_k$, $\hat{\lambda}_k$ of the antisymmetric tensors $\mathsf{w} = -\epsilon_{ijk}\,\hat{w}_k\,\hat{\mathbf{e}}_i\otimes\hat{\mathbf{e}}_j$, $\Omega = -\epsilon_{ijk}\,\hat{\omega}_k\,\hat{\mathbf{e}}_i\otimes\hat{\mathbf{e}}_j$, $\Lambda = -\epsilon_{ijk}\,\hat{\lambda}_k\,\hat{\mathbf{E}}_i\otimes\hat{\mathbf{E}}_j$ [cf. (17)] are, from the r.h.s. of Eq.(37), related by

$$\hat{w}_1 = \hat{\omega}_1 - \tfrac{1}{2}\Big(\tfrac{\hat{U}_2}{\hat{U}_3}+\tfrac{\hat{U}_3}{\hat{U}_2}-2\Big)\hat{\lambda}_1, \qquad \hat{w}_2 = \hat{\omega}_2 - \tfrac{1}{2}\Big(\tfrac{\hat{U}_3}{\hat{U}_1}+\tfrac{\hat{U}_1}{\hat{U}_3}-2\Big)\hat{\lambda}_2, \qquad \hat{w}_3 = \hat{\omega}_3 - \tfrac{1}{2}\Big(\tfrac{\hat{U}_1}{\hat{U}_2}+\tfrac{\hat{U}_2}{\hat{U}_1}-2\Big)\hat{\lambda}_3. \tag{40}$$

4.1   Symmetric total or partial Cauchy-Green deformation tensors and their rates

The left ${}^{@}\mathsf{b} = \{\mathsf{b}, {}^{e}\mathsf{b}, {}^{p}\mathsf{b}, \cdots\}$ and right ${}^{@}\mathsf{C} = \{\mathsf{C}, {}^{e}\mathsf{C}, {}^{p}\mathsf{C}, \cdots\}$ total or partial (elastic, plastic, $\cdots$) Cauchy-Green deformation tensors are [analogously to the definitions (38)] defined through the *same* material-convective rotation R tensor (2) as

$$ {}^{@}\mathsf{b} = ({}^{@}\hat{U}_k)^2\;{}^{@}\hat{\mathbf{e}}_k\otimes{}^{@}\hat{\mathbf{e}}_k = \mathsf{R}.{}^{@}\mathsf{C}.\mathsf{R}^{\mathsf{T}}, \qquad {}^{@}\mathsf{C} = ({}^{@}\hat{U}_k)^2\;{}^{@}\hat{\mathbf{E}}_k\otimes{}^{@}\hat{\mathbf{E}}_k, \qquad {}^{@}\hat{\mathbf{e}}_k = \mathsf{R}.{}^{@}\hat{\mathbf{E}}_k = {}^{@}\hat{\mathbf{E}}_k.\mathsf{R}^{\mathsf{T}}, \tag{41}$$

with the total or partial (elastic, plastic, $\cdots$) eigenvalues ${}^{@}\hat{U}_k = \{\hat{U}_k, {}^{e}\hat{U}_k, {}^{p}\hat{U}_k, \cdots\}$, i.e. the principal stretch ratios, and the unit eigenvectors ${}^{@}\hat{\mathbf{E}}_k = \{\hat{\mathbf{E}}_k, {}^{e}\hat{\mathbf{E}}_k, {}^{p}\hat{\mathbf{E}}_k, \cdots\}$, i.e. the principal directions. Under SRBM the tensors of Eq.(41) obey: ${}^{@}_{+}\mathsf{b} = \mathsf{Q}.{}^{@}\mathsf{b}.\mathsf{Q}^{\mathsf{T}}$, ${}^{@}_{+}\hat{\mathbf{e}}_k = \mathsf{Q}.{}^{@}\hat{\mathbf{e}}_k = {}^{@}\hat{\mathbf{e}}_k.\mathsf{Q}^{\mathsf{T}}$ and ${}^{@}_{+}\mathsf{C} = {}^{@}\mathsf{C}$, ${}^{@}_{+}\hat{\mathbf{E}}_k = {}^{@}\hat{\mathbf{E}}_k$. With the left ${}^{@}\mathsf{v} = \{\mathsf{v}, {}^{e}\mathsf{v}, {}^{p}\mathsf{v}, \cdots\}$ and right ${}^{@}\mathsf{U} = \{\mathsf{U}, {}^{e}\mathsf{U}, {}^{p}\mathsf{U}, \cdots\}$ total or partial (elastic, plastic, $\cdots$) stretch tensors given by

$$ {}^{@}\mathsf{v} = {}^{@}\hat{U}_k\;{}^{@}\hat{\mathbf{e}}_k\otimes{}^{@}\hat{\mathbf{e}}_k = \mathsf{R}.{}^{@}\mathsf{U}.\mathsf{R}^{\mathsf{T}} \qquad\text{and}\qquad {}^{@}\mathsf{U} = {}^{@}\hat{U}_k\;{}^{@}\hat{\mathbf{E}}_k\otimes{}^{@}\hat{\mathbf{E}}_k = \mathsf{R}^{\mathsf{T}}.{}^{@}\mathsf{v}.\mathsf{R}, \tag{42}$$

the total or partial (elastic, plastic, $\cdots$) Eulerian deformation-rate tensors may be defined by

$$ {}^{@}\mathsf{d} = \tfrac{1}{2}({}^{@}\mathring{\mathsf{v}}.{}^{@}\mathsf{v}^{-1}+{}^{@}\mathsf{v}^{-1}.{}^{@}\mathring{\mathsf{v}}) = \tfrac{1}{2}\,{}^{@}\mathsf{v}^{-1}.{}^{@}\mathring{\mathsf{b}}.{}^{@}\mathsf{v}^{-1} = \tfrac{1}{2}\mathsf{R}.({}^{@}\dot{\mathsf{U}}.{}^{@}\mathsf{U}^{-1}+{}^{@}\mathsf{U}^{-1}.{}^{@}\dot{\mathsf{U}}).\mathsf{R}^{\mathsf{T}} = \tfrac{1}{2}\mathsf{R}.{}^{@}\mathsf{U}^{-1}.{}^{@}\dot{\mathsf{C}}.{}^{@}\mathsf{U}^{-1}.\mathsf{R}^{\mathsf{T}} \tag{43}$$

[cf. Eq.(36)], the corresponding material-convectively back-rotated Lagrangean deformation-rate tensors by

$$ {}^{@}\mathsf{D} = \mathsf{R}^{\mathsf{T}}.{}^{@}\mathsf{d}.\mathsf{R} = \tfrac{1}{2}({}^{@}\dot{\mathsf{U}}.{}^{@}\mathsf{U}^{-1}+{}^{@}\mathsf{U}^{-1}.{}^{@}\dot{\mathsf{U}}) = \tfrac{1}{2}\,{}^{@}\mathsf{U}^{-1}.{}^{@}\dot{\mathsf{C}}.{}^{@}\mathsf{U}^{-1} \tag{44}$$

[cf. Eq.(39)], and the total or partial (elastic, plastic, $\cdots$) Eulerian vorticity tensors by

$$ {}^{@}\mathsf{w} = \Omega+\tfrac{1}{2}({}^{@}\mathring{\mathsf{v}}.{}^{@}\mathsf{v}^{-1}-{}^{@}\mathsf{v}^{-1}.{}^{@}\mathring{\mathsf{v}}) = \Omega+\tfrac{1}{2}\mathsf{R}.({}^{@}\dot{\mathsf{U}}.{}^{@}\mathsf{U}^{-1}-{}^{@}\mathsf{U}^{-1}.{}^{@}\dot{\mathsf{U}}).\mathsf{R}^{\mathsf{T}} \tag{45}$$

[cf. Eq.(37)]. Under SRBM the Eulerian tensor of material-convective spin (3) obeys $_{+}\Omega = \dot{\mathsf{Q}}.\mathsf{Q}^{\mathsf{T}}+\mathsf{Q}.\Omega.\mathsf{Q}^{\mathsf{T}}$, the Eulerian vorticity tensors (45) obey ${}^{@}_{+}\mathsf{w} = \dot{\mathsf{Q}}.\mathsf{Q}^{\mathsf{T}}+\mathsf{Q}.{}^{@}\mathsf{w}.\mathsf{Q}^{\mathsf{T}}$, the left or right stretch tensors obey ${}^{@}_{+}\mathsf{v} = \mathsf{Q}.{}^{@}\mathsf{v}.\mathsf{Q}^{\mathsf{T}}$ or ${}^{@}_{+}\mathsf{U} = {}^{@}\mathsf{U}$, and the rate of deformation tensors (43) or (44) obey ${}^{@}_{+}\mathsf{d} = \mathsf{Q}.{}^{@}\mathsf{d}.\mathsf{Q}^{\mathsf{T}}$ or ${}^{@}_{+}\mathsf{D} = {}^{@}\mathsf{D}$, respectively.

4.2 Symmetric total or partial generalized strain tensors, their rates and their work-conjugate stresses

By applying total or partial Eulerian $^@\mathfrak{b} = {}^@B_{ijk\ell}\,\mathbf{e}_i\otimes\mathbf{e}_j\otimes\mathbf{e}_k\otimes\mathbf{e}_\ell = {}^@\mathfrak{a}^{-1}$, $^@\mathfrak{a} = {}^@A_{ijk\ell}\,\mathbf{e}_i\otimes\mathbf{e}_j\otimes\mathbf{e}_k\otimes\mathbf{e}_\ell = {}^@\mathfrak{b}^{-1}$ or Lagrangean $^@\mathcal{B} = {}^@B_{ijk\ell}\,\mathbf{E}_i\otimes\mathbf{E}_j\otimes\mathbf{E}_k\otimes\mathbf{E}_\ell = {}^@\mathcal{A}^{-1}$, $^@\mathcal{A} = {}^@A_{ijk\ell}\,\mathbf{E}_i\otimes\mathbf{E}_j\otimes\mathbf{E}_k\otimes\mathbf{E}_\ell = {}^@\mathcal{B}^{-1}$ fourth-order transformation tensors, which are inverse to each other $^@B_{ijmn}\,{}^@A_{mnk\ell} = \frac{1}{2}(\delta_{ik}\,\delta_{j\ell} + \delta_{i\ell}\,\delta_{jk})$, which obey the symmetries $^@B_{ijk\ell} = {}^@B_{ij\ell k} = {}^@B_{jik\ell} = {}^@B_{k\ell ij}$ and $^@A_{ijk\ell} = {}^@A_{ij\ell k} = {}^@A_{jik\ell} = {}^@A_{k\ell ij}$ and which are defined through the distinct eigenvalues $^@\hat{U}_\lambda = \{\hat{U}_\lambda, {}^e\hat{U}_\lambda, {}^p\hat{U}_\lambda, \cdots\}$ and the corresponding symmetric second-order Eulerian $^@v_\lambda = {}^@\mathfrak{b}_\lambda = \{\mathfrak{b}_\lambda, {}^e\mathfrak{b}_\lambda, {}^p\mathfrak{b}_\lambda, \cdots\}$ or Lagrangean $^@U_\lambda = {}^@C_\lambda = \{C_\lambda, {}^eC_\lambda, {}^pC_\lambda, \cdots\}$ eigenprojection tensors, kinematical relations similar to Eqs.(43)–(44) of Eulerian

$$^@\mathsf{d} = {}^@\mathfrak{a}..{}^@\mathring{\mathsf{e}}, \qquad\qquad {}^@\mathring{\mathsf{e}} = {}^@\mathfrak{b}..{}^@\mathsf{d} \tag{46}$$

or Lagrangean

$$^@\mathsf{D} = {}^@\mathcal{A}..{}^@\dot{\mathsf{E}}, \qquad\qquad {}^@\dot{\mathsf{E}} = {}^@\mathcal{B}..{}^@\mathsf{D} \tag{47}$$

type may be specified for the symmetric total or partial Eulerian $^@\mathring{\mathsf{e}} = \mathsf{R}.{}^@\dot{\mathsf{E}}.\mathsf{R}^T$ or Lagrangean $^@\dot{\mathsf{E}} = \mathsf{R}^T.{}^@\mathring{\mathsf{e}}.\mathsf{R}$ material-convective (Green-Naghdi) rates of generalized strain tensors [for a comprehensive discussion of the definition, calculation and algorithmic treatment of the generalized strain-rate kinematics see Heiduschke (2019)], where '..' denotes the *double dot product operator* $\mathsf{a}..\mathsf{b} = \mathrm{tr}(\mathsf{a}.\mathsf{b}^T) = a_{ij}\,b_{ij} = \mathrm{tr}(\mathsf{a}^T.\mathsf{b}) = \mathsf{b}..\mathsf{a}$, that is the *double contraction* defined here by the traces of dot products of the second-order tensors a and b.

The relations of the symmetric Eulerian tensor t of Cauchy (1823, 1827a) stress or of the symmetric Lagrangean tensor $\mathsf{T} = \frac{\rho_0}{\rho}\mathsf{R}^T.\mathsf{t}.\mathsf{R}$ of back-rotated Kirchhoff (1852) stress to the symmetric total or partial Eulerian $^@\mathsf{s} = \frac{\rho}{\rho_0}\mathsf{R}.{}^@\mathsf{S}.\mathsf{R}^T$ or Lagrangean $^@\mathsf{S} = \frac{\rho_0}{\rho}\mathsf{R}^T.{}^@\mathsf{s}.\mathsf{R}$ work-conjugate tensors of generalized stress are given through the same fourth-order transformation tensors $^@\mathfrak{a}$, $^@\mathfrak{b}$, $^@\mathcal{A}$, $^@\mathcal{B}$ in Eulerian form by

$$^@\mathsf{s} = {}^@\mathfrak{a}..\mathsf{t}, \qquad\qquad \mathsf{t} = {}^@\mathfrak{b}..{}^@\mathsf{s} \tag{48}$$

or in Lagrangean form by

$$^@\mathsf{S} = {}^@\mathcal{A}..\mathsf{T}, \qquad\qquad \mathsf{T} = {}^@\mathcal{B}..{}^@\mathsf{S} \tag{49}$$

respectively.

4.3 The non-material Zaremba-Jaumann rate

The Zaremba-Jaumann rate tensor

$$^{ZJ}\mathring{\mathsf{s}} = \dot{\mathsf{s}} - \mathsf{w}.\mathsf{s} + \mathsf{s}.\mathsf{w} \tag{50}$$

[see Zaremba (1903) eq.(32) on p.607, eq.(37) on p.610; and Jaumann (1911) eq.(11c) on p.395] has about the same structure as the material-convective Green-Naghdi rate $\mathring{\mathsf{s}} = \dot{\mathsf{s}} - \Omega.\mathsf{s} + \mathsf{s}.\Omega$ tensor (33) just with the Eulerian vorticity w tensor (37) instead of the material-convective spin Ω tensor (3). Therefore the Zaremba-Jaumann rate $^{ZJ}\mathring{\mathsf{s}}$ is, in general, not rotationally convected with the material and thus a *non-material rate*. The difference between the material-convective Green-Naghdi rate $\mathring{\mathsf{s}}$ and the non-material Zaremba-Jaumann rate $^{ZJ}\mathring{\mathsf{s}}$ is [from (37)] given by

$$\mathring{\mathsf{s}} - {}^{ZJ}\mathring{\mathsf{s}} = -(\Omega-\mathsf{w}).\mathsf{s} + \mathsf{s}.(\Omega-\mathsf{w}) = \tfrac{1}{2}\mathsf{R}.(\underbrace{\dot{\mathsf{U}}.\mathsf{U}^{-1}-\mathsf{U}^{-1}.\dot{\mathsf{U}}}_{2\Lambda-\mathsf{U}.\Lambda.\mathsf{U}^{-1}-\mathsf{U}^{-1}.\Lambda.\mathsf{U}}).\mathsf{R}^T.\mathsf{s} - \tfrac{1}{2}\mathsf{s}.\mathsf{R}.(\underbrace{\dot{\mathsf{U}}.\mathsf{U}^{-1}-\mathsf{U}^{-1}.\dot{\mathsf{U}}}_{2\Lambda-\mathsf{U}.\Lambda.\mathsf{U}^{-1}-\mathsf{U}^{-1}.\Lambda.\mathsf{U}}).\mathsf{R}^T \tag{51}$$

[cf. Green&McInnis (1967) eq.(2.17) on p.222].

4.4 Material-convective rates and corresponding time integrals with respect to the plastic flow rules

For the rate-type theories of plasticity, the (translational-convective) time derivative

$$^p\dot{\mathsf{C}} = {}^p\dot{C}_{ij}\mathbf{E}_i\otimes\mathbf{E}_j = {}^p\mathring{\mathsf{C}} = \underbrace{{}^p\dot{\hat{C}}_k\,{}^p\hat{\mathbf{E}}_k\otimes{}^p\hat{\mathbf{E}}_k}_{{}^p\Lambda\ co\text{-}rotated\ with\ the\ plastic\ Lagrangean\ principal\ axes} + \overbrace{{}^p\hat{C}_k\,{}^p\dot{\hat{\mathbf{E}}}_k\otimes{}^p\hat{\mathbf{E}}_k}^{{}^p\Lambda.{}^p\mathsf{C}} + \overbrace{{}^p\hat{C}_k\,{}^p\hat{\mathbf{E}}_k\otimes{}^p\dot{\hat{\mathbf{E}}}_k}^{-{}^p\mathsf{C}.{}^p\Lambda} \tag{52}$$

of the symmetric Lagrangean right Cauchy-Green plastic deformation tensor $^p\mathsf{C}$ (41b) [which is identical to the material-convective plastic rate $^p\mathring{\mathsf{C}}$] constitutes the *plastic flow rule* $^p\mathring{\mathsf{C}} = \cdots$ which specifies the material flow behavior of plasticity; the plastic flow rule must be properly time integrated in order to obtain a proper plastic deformation tensor/measure

$$^p\mathsf{C}(t) = \int_{\tau=0}^{t} {}^p\dot{C}_{ij}(\tau)\,d\tau\,\mathbf{E}_i\otimes\mathbf{E}_j + {}^p\mathsf{C}(0) = {}^pC_{ij}(t)\,\mathbf{E}_i\otimes\mathbf{E}_j$$
$$= \int_{\tau=0}^{t} \underbrace{{}^p\dot{\hat{C}}_k(\tau)\,{}^p\hat{\mathbf{E}}_k(\tau)\otimes{}^p\hat{\mathbf{E}}_k(\tau)}_{{}^p\Lambda\ co\text{-}rotated\ with\ the\ plastic\ Lagrangean\ principal\ axes}\,d\tau + {}^p\mathsf{C}(0) = {}^p\hat{C}_k(t)\,{}^p\hat{\mathbf{E}}_k(t)\otimes{}^p\hat{\mathbf{E}}_k(t)\,. \tag{53}$$

The material-convective time integral ${}^{P}\mathsf{C} = \int {}^{P}\dot{\mathsf{C}}\,dt + {}^{P}\mathsf{C}_0 = {}^{P}C_{ij}\,\mathbf{E}_i \otimes \mathbf{E}_j = (\int {}^{P}\dot{C}_{ij}\,dt + {}^{P}C_{ij}(0))\mathbf{E}_i \otimes \mathbf{E}_j$ of a symmetric Lagrangean plastic flow tensor ${}^{P}\dot{\mathsf{C}}$ is simply given by its arbitrary $\mathbf{E}_i \otimes \mathbf{E}_j$ components ${}^{P}C_{ij} = \int {}^{P}\dot{C}_{ij}\,dt + {}^{P}C_{ij}(0)$ which follow from the time integrals of each single plastic flow component. The spectral representation at the r.h.s. of Eq.(52) reveals that the plastic Lagrangean unit eigenvectors ${}^{P}\hat{\mathbf{E}}_k$ are spinning with ${}^{P}\Lambda$ [cf. Eqs.(16)–(19)]; thus the terms ${}^{P}\dot{\hat{C}}_k\,{}^{P}\hat{\mathbf{E}}_k \otimes {}^{P}\hat{\mathbf{E}}_k$ [in matrix component notation placed on the diagonal] represent the ${}^{P}\Lambda$ co-rotated tensor rate [underbraced in Eq.(52)] which corresponds to the ${}^{P}\Lambda$ co-rotated time integral [underbraced in Eq.(53)]. *Only if* the plastic deformation is *integrated material-convectively* from the corresponding plastic flow rule ${}^{P}\dot{\mathsf{C}} = \mathsf{R}^{\mathrm{T}}.{}^{P}\overset{\circ}{\mathsf{b}}.\mathsf{R} = \cdots$ then the resulting *plastic deformation* ${}^{P}\mathsf{C} = \mathsf{R}^{\mathrm{T}}.{}^{P}\mathsf{b}.\mathsf{R}$ is a *proper tensor* with *geometrical interpretation*—as further discussed in (the next) section 5.

The translational-convective time derivative

$$
{}^{P}\dot{\mathsf{b}} = \overbrace{{}^{P}\dot{C}_{ij}\mathbf{e}_i \otimes \mathbf{e}_j}^{} + \underbrace{{}^{P}C_{ij}\dot{\mathbf{e}}_i \otimes \mathbf{e}_j}_{\Omega.{}^{P}\mathsf{b}} + \underbrace{{}^{P}C_{ij}\mathbf{e}_i \otimes \dot{\mathbf{e}}_j}_{-{}^{P}\mathsf{b}.\Omega} = \overbrace{{}^{P}\dot{\hat{C}}_k\,{}^{P}\hat{\mathbf{e}}_k \otimes {}^{P}\hat{\mathbf{e}}_k}^{} + \overbrace{{}^{P}\hat{C}_k\,{}^{P}\dot{\hat{\mathbf{e}}}_k \otimes {}^{P}\hat{\mathbf{e}}_k}^{{}^{P}\Gamma.{}^{P}\mathsf{b}} + \overbrace{{}^{P}\hat{C}_k\,{}^{P}\hat{\mathbf{e}}_k \otimes {}^{P}\dot{\hat{\mathbf{e}}}_k}^{-{}^{P}\mathsf{b}.{}^{P}\Gamma}
$$

$$\underbrace{}_{{}^{P}\Gamma \text{ co-rotated with the plastic Eulerian principal axes}} \tag{54}$$

with ${}^{P}\overset{\circ}{\mathsf{b}}$ [*materially* Ω *co-rotated Green-Naghdi rate*] overbraced at l.h.s.

of the symmetric Eulerian left Cauchy-Green plastic deformation tensor ${}^{P}\mathsf{b}$ (41a) shows at the l.h.s. of Eq.(54) that the material-convectively co-rotated Eulerian unit vectors $\mathbf{e}_k$ (7) spin (27) with Ω (3); thus the ${}^{P}\dot{C}_{ij}\mathbf{e}_i \otimes \mathbf{e}_j$ terms [cf. Eq.(29)] represent the materially Ω co-rotated Green-Naghdi rate [overbraced at the l.h.s. of Eq.(54)] which corresponds to the materially Ω co-rotated time integral

$$
{}^{P}\mathsf{b}(t) = \int_{\tau=0}^{t} \overbrace{{}^{P}\dot{C}_{ij}(\tau)\,\mathbf{e}_i(\tau) \otimes \mathbf{e}_j(\tau)}^{\Omega \text{ co-rotated with the material}}\,d\tau + {}^{P}\mathsf{b}(0) = {}^{P}C_{ij}(t)\,\mathbf{e}_i \otimes \mathbf{e}_j
$$

$$
= \int_{\tau=0}^{t} \underbrace{{}^{P}\dot{\hat{C}}_k(\tau)\,{}^{P}\hat{\mathbf{e}}_k(\tau) \otimes {}^{P}\hat{\mathbf{e}}_k(\tau)}_{{}^{P}\Gamma \text{ co-rotated with the plastic Eulerian principal axes}}\,d\tau + {}^{P}\mathsf{C}(0) = {}^{P}\hat{C}_k(t)\,{}^{P}\hat{\mathbf{e}}_k(t) \otimes {}^{P}\hat{\mathbf{e}}_k(t)
$$

$$\tag{55}$$

[overbraced at the l.h.s. of Eq.(55)]. The spectral representation at the r.h.s. of Eq.(54) reveals that the plastic Eulerian unit eigenvectors ${}^{P}\hat{\mathbf{e}}_k$ are spinning with ${}^{P}\Gamma$ [cf. Eqs.(31)–(32)]; thus the terms ${}^{P}\dot{\hat{C}}_k\,{}^{P}\hat{\mathbf{e}}_k \otimes {}^{P}\hat{\mathbf{e}}_k$ [in matrix component notation placed on the diagonal] represent the ${}^{P}\Gamma$ co-rotated tensor rate [underbraced at the r.h.s. of Eq.(54)] which corresponds to the ${}^{P}\Gamma$ co-rotated time integral [underbraced at the r.h.s. of Eq.(55)].

5 The geometrical interpretation of total and partial Cauchy-Green deformation tensors

The total or partial (elastic, plastic, $\cdots$) reference ${}^{@}\underline{L} = \{\underline{L} = d\mathbf{X},\, {}^{e}\underline{L},\, {}^{P}\underline{L}, \cdots\}$ and present ${}^{@}\underline{\ell} = \{\underline{\ell} = d\mathbf{x},\, {}^{e}\underline{\ell},\, {}^{P}\underline{\ell}, \cdots\}$ vicinity vectors of a particle's reference $\mathbf{X}$ and present $\mathbf{x}$ position are related to each other [analogously to Eq.(6)] by

$$
{}^{@}\underline{\ell} = (\mathsf{R}.{}^{@}\mathsf{U}).{}^{@}\underline{L} = ({}^{@}\mathsf{v}.\mathsf{R}).{}^{@}\underline{L} = {}^{@}\underline{L}.(\mathsf{R}^{\mathrm{T}}.{}^{@}\mathsf{v}) = {}^{@}\underline{L}.({}^{@}\mathsf{U}.\mathsf{R}^{\mathrm{T}}) \tag{56}
$$

and [analogously to Eq.(21)] inversely by

$$
{}^{@}\underline{L} = ({}^{@}\mathsf{U}^{-1}.\mathsf{R}^{\mathrm{T}}).{}^{@}\underline{\ell} = (\mathsf{R}^{\mathrm{T}}.{}^{@}\mathsf{v}^{-1}).{}^{@}\underline{\ell} = {}^{@}\underline{\ell}.({}^{@}\mathsf{v}^{-1}.\mathsf{R}) = {}^{@}\underline{\ell}.(\mathsf{R}.{}^{@}\mathsf{U}^{-1}). \tag{57}
$$

For a Lagrangean description with (56) the total and partial (elastic, plastic, $\cdots$) left (41a) and right (41b) Cauchy-Green deformation tensors may be projected onto the Lagrangean $\mathbf{E} = \dfrac{{}^{@}\underline{L}}{\|{}^{@}\underline{L}\|} = \dfrac{\mathsf{R}^{\mathrm{T}}.\{{}^{@}\mathsf{v}^{-1}.{}^{@}\underline{\ell}\}}{\|{}^{@}\mathsf{v}^{-1}.{}^{@}\underline{\ell}\|} = \mathsf{R}^{\mathrm{T}}.\mathbf{e} = \mathbf{e}.\mathsf{R}$ and Eulerian $\mathbf{e} = \mathsf{R}.\mathbf{E} = \mathbf{E}.\mathsf{R}^{\mathrm{T}}$ unit vector directions [cf. Eqs.(9a) and (9b)] of the total or partial reference vicinities ${}^{@}\underline{L} = \{\underline{L},\, {}^{e}\underline{L},\, {}^{P}\underline{L}\}$ in order to result in the (scalar) quadratic stretch ratios (without a *hat*)

$$
\left({}^{@}U\right)^2 = \left(\frac{\|{}^{@}\underline{\ell}\|}{\|{}^{@}\underline{L}\|}\right)^2 = \frac{{}^{@}\underline{\ell}.{}^{@}\underline{\ell}}{{}^{@}\underline{L}.{}^{@}\underline{L}} = \underbrace{\frac{1}{\|{}^{@}\underline{L}\|}{}^{@}\underline{L}}_{\mathbf{E}}.{}^{@}\mathsf{C}.\underbrace{{}^{@}\underline{L}\frac{1}{\|{}^{@}\underline{L}\|}}_{\mathbf{E}} = \mathbf{E}.{}^{@}\mathsf{C}.\mathbf{E} = \mathbf{e}.{}^{@}\mathsf{b}.\mathbf{e}. \tag{58}
$$

The Lagrangean deformation tensor projection (58) [multiplied by $\|{}^{@}\underline{L}\|^2$] of a right Cauchy-Green (partial) deformation tensor ${}^{@}\mathsf{C}$ exhibits according to [Ogden (1984) p.95 with Ogden's $\mathsf{A} := \mathsf{F}$] the following geometrical interpretation: since ${}^{@}\mathsf{C}$ is symmetric and positive definite, the quadratic form

$$
{}^{@}\underline{L}.{}^{@}\mathsf{C}.{}^{@}\underline{L} = \|{}^{@}\underline{\ell}\|^2 = constant \tag{59}
$$

represents a *reciprocal Lagrangean deformation ellipsoid* with principal axes $\{{}^{@}\hat{\mathbf{E}}_1,\, {}^{@}\hat{\mathbf{E}}_2,\, {}^{@}\hat{\mathbf{E}}_3\}$ and semi-axes proportional to $\{{}^{1}/{}^{@}\hat{U}_1,\, {}^{1}/{}^{@}\hat{U}_2,\, {}^{1}/{}^{@}\hat{U}_3\}$ formed from the reference vicinity vectors ${}^{@}\underline{L}$ centered at the particle's reference position vector $\mathbf{X}$ which material is mapped onto an *Eulerian sphere*

$$
{}^{@}\underline{\ell}.{}^{@}\underline{\ell} = \|{}^{@}\underline{\ell}\|^2 = constant \tag{60}
$$

of radius $\|^@\underline{\ell}\|$ centered at the particle's present position vector $\mathbf{x}$. If the quadratic form (59) is forward-rotated with R and expressed by the left Cauchy-Green (partial) deformation tensors $^@\mathsf{b} = \mathsf{R}.^@\mathsf{C}.\mathsf{R}^T$ as

$$\{^@\underline{L}.\mathsf{R}^T\}.^@\mathsf{b}.\{\mathsf{R}.^@\underline{L}\} = (^@\mathsf{b}.\{\mathsf{R}.^@\underline{L}\}).\{\mathsf{R}.^@\underline{L}\} = \|^@\underline{\ell}\|^2 = constant \tag{61}$$

then the $^@\mathsf{b}$ may geometrically be interpreted as a *reciprocal Eulerian deformation ellipsoid* with principal axes $\{^@\hat{\mathbf{e}}_1, {}^@\hat{\mathbf{e}}_2, {}^@\hat{\mathbf{e}}_3\}$ and semi-axes proportional to $\{1/^@\hat{U}_1, 1/^@\hat{U}_2, 1/^@\hat{U}_3\}$ centered at the particle's present position vector $\mathbf{x}$.

For an Eulerian description with (57) the total or partial (elastic, plastic, $\cdots$) left and right inverse Cauchy-Green deformation tensors may be projected onto the Eulerian $\mathbf{i} = \dfrac{^@\underline{\ell}}{\|^@\underline{\ell}\|} = \dfrac{\mathsf{R}.\{^@\mathsf{U}.^@\underline{L}\}}{\|^@\mathsf{U}.^@\underline{L}\|} = \mathsf{R}.\mathbf{I} = \mathbf{I}.\mathsf{R}^T$ and Lagrangean $\mathbf{I} = \mathsf{R}^T.\mathbf{i} = \mathbf{i}.\mathsf{R}$ unit vector directions [cf. Eqs.(9c) and (9d)] of the total or partial present vicinities $^@\underline{\ell} = \{\underline{\ell}, {}^e\underline{\ell}, {}^p\underline{\ell}\}$ in order to result in the (scalar) inverse quadratic stretch ratios (without a *hat*)

$$\left(\frac{1}{^@U}\right)^2 = \left(\frac{\|^@\underline{L}\|}{\|^@\underline{\ell}\|}\right)^2 = \frac{^@\underline{L}.^@\underline{L}}{^@\underline{\ell}.^@\underline{\ell}} = \underbrace{\frac{1}{\|^@\underline{\ell}\|}^@\underline{\ell}}_{\mathbf{i}}.^@\mathsf{b}^{-1}.\underbrace{^@\underline{\ell}\frac{1}{\|^@\underline{\ell}\|}}_{\mathbf{i}} = \mathbf{i}.^@\mathsf{b}^{-1}.\mathbf{i} = \mathbf{I}.^@\mathsf{C}^{-1}.\mathbf{I}. \tag{62}$$

The Eulerian deformation tensor projection (62) [multiplied by $\|^@\underline{\ell}\|^2$] of an inverse left Cauchy-Green (partial) deformation tensor $^@\mathsf{b}^{-1}$ exhibits according to [Ogden (1984) pp.94–95 with Ogden's $\mathsf{B} := \mathsf{F}^{-T}$] the following geometrical interpretation: since $^@\mathsf{b}^{-1}$ is symmetric and positive definite, the quadratic form

$$^@\underline{\ell}.^@\mathsf{b}^{-1}.^@\underline{\ell} = \|^@\underline{L}\|^2 = constant \tag{63}$$

represents an *Eulerian deformation ellipsoid* with principal axes $\{^@\hat{\mathbf{e}}_1, {}^@\hat{\mathbf{e}}_2, {}^@\hat{\mathbf{e}}_3\}$ and semi-axes proportional to $\{^@\hat{U}_1, {}^@\hat{U}_2, {}^@\hat{U}_3\}$ formed from the present vicinity vectors $^@\underline{\ell}$ centered at the particle's present position vector $\mathbf{x}$ which material is mapped back onto the *Lagrangean sphere*

$$^@\underline{L}.^@\underline{L} = \|^@\underline{L}\|^2 = constant \tag{64}$$

of radius $\|^@\underline{L}\|$ centered at the particle's reference position vector $\mathbf{X}$ [cf. Finger (1892) pp.1105–1122]. If the quadratic form (63) is back-rotated with R^T and expressed by the inverse right Cauchy-Green (partial) deformation tensors $^@\mathsf{C}^{-1} = \mathsf{R}^T.^@\mathsf{b}^{-1}.\mathsf{R}$ as

$$\{^@\underline{\ell}.\mathsf{R}\}.^@\mathsf{C}^{-1}.\{\mathsf{R}^T.^@\underline{\ell}\} = (^@\mathsf{C}^{-1}.\{\mathsf{R}^T.^@\underline{\ell}\}).\{\mathsf{R}^T.^@\underline{\ell}\} = \|^@\underline{L}\|^2 = constant \tag{65}$$

then the $^@\mathsf{C}^{-1}$ may geometrically be interpreted as a *Lagrangean deformation ellipsoid* with principal axes $\{^@\hat{\mathbf{E}}_1, {}^@\hat{\mathbf{E}}_2, {}^@\hat{\mathbf{E}}_3\}$ and semi-axes proportional to $\{^@\hat{U}_1, {}^@\hat{U}_2, {}^@\hat{U}_3\}$ centered at the particle's reference position vector $\mathbf{X}$.

The total and partial (elastic, plastic, $\cdots$) stretch ratios (without a *hat*)

$$^@U = \frac{\|^@\underline{\ell}\|}{\|^@\underline{L}\|} = \sqrt{\mathbf{E}.^@\mathsf{C}.\mathbf{E}} = \sqrt{\mathbf{e}.^@\mathsf{b}.\mathbf{e}} = \frac{1}{\sqrt{\mathbf{i}.^@\mathsf{b}^{-1}.\mathbf{i}}} = \frac{1}{\sqrt{\mathbf{I}.^@\mathsf{C}^{-1}.\mathbf{I}}} \tag{66}$$

of the $\mathbf{E}$, $\mathbf{e}$ or $\mathbf{i}$, $\mathbf{I}$ unit directions (9) follow from the Lagrangean (58) or Eulerian (62) deformation tensor projections, respectively.

6 The additivity of the (partial) stress power and Truesdell's hypo-elasticity

The additive split of the Eulerian (total) deformation-rate tensor

$$\mathsf{d} = \overline{^e\mathsf{d}} + \overline{^p\mathsf{d}} + \cdots \tag{67}$$

into the partial (elastic, plastic, $\cdots$) deformation rates $\{\overline{^e\mathsf{d}}, \overline{^p\mathsf{d}}, \cdots\}$—collectively referred to as

$$\overline{^@\mathsf{d}} = \{\mathsf{d}, \overline{^e\mathsf{d}}, \overline{^p\mathsf{d}}, \cdots\} = \tfrac{1}{2}\mathsf{F}^{-T}.\dot{\overline{^@\mathsf{C}}}.\mathsf{F}^{-1} \tag{68}$$

—is a physical consequence of the *additivity of the (partial) stress power per unit mass*

$$p = \frac{1}{\rho}\,\mathsf{t}..\mathsf{d} = \overbrace{\frac{1}{\rho}\,\mathsf{t}..\overline{^e\mathsf{d}}}^{^ep} + \overbrace{\frac{1}{\rho}\,\mathsf{t}..\overline{^p\mathsf{d}}}^{^pp} + \cdots = \frac{1}{2\rho_0}\,\mathfrak{S}..\dot{\mathsf{C}} = \frac{1}{2\rho_0}\underbrace{(\mathsf{U}^{-1}.\mathsf{T}.\mathsf{U}^{-1})}_{\mathfrak{S}}..\dot{\overline{^e\mathsf{C}}} + \frac{1}{2\rho_0}\underbrace{(\mathsf{U}^{-1}.\mathsf{T}.\mathsf{U}^{-1})}_{\mathfrak{S}}..\dot{\overline{^p\mathsf{C}}} + \cdots \tag{69}$$

with the reversible elastic ^ep and the irreversible (plastic, $\cdots$) contributions $\{^pp, \cdots\}$—collectively referred to as

$$^@p = \{p, {}^ep, {}^pp, \cdots\} = \frac{1}{\rho}\,\mathsf{t}..\overline{^@\mathsf{d}} = \frac{1}{2\rho_0}(\mathsf{U}^{-1}.\mathsf{T}.\mathsf{U}^{-1})..\dot{\overline{^@\mathsf{C}}} = \frac{1}{2\rho_0}\mathfrak{S}..\dot{\overline{^@\mathsf{C}}} \tag{70}$$

—where

'..' denotes the *double dot product operator* (or the *double contraction*),

     t denotes the symmetric Eulerian tensor of Cauchy (1823, 1827a) stress,

     $T = \frac{\rho_0}{\rho} R^T . t . R$ denotes the symmetric Lagrangean tensor of back-rotated Kirchhoff (1852) stress,

     $\mathfrak{S} = U^{-1} . T . U^{-1} = \frac{\rho_0}{\rho} F^{-1} . t . F^{-T}$ denotes the symmetric Lagrangean tensor of second Piola (1825)-Kirchhoff (1852) stress

and the partial (elastic, plastic, $\cdots$) contributions of $^@d$ (43) and $^@d \neq \overline{^@d}$ (68) as well as $^@\dot{C} = \{\dot{C}, ^e\dot{C}, ^p\dot{C}, \cdots\} = ^@\dot{U}.^@U + ^@U.^@\dot{U} = 2 ^@U.R^T.^@\dot{d}.R.^@U$ and $^@\dot{C} \neq \overline{^@\dot{C}} = \{\dot{C}, \overline{^e\dot{C}}, \overline{^p\dot{C}}, \cdots\} = 2 F^T . \overline{^@d} . F$ differ in general from each other.

The notion of *hypo-elasticity* [Truesdell (1955)] for the modeling of hypo-elastic material is taken as a synonym for incremental stress-strain realations (of stress-rate and strain-rate type) [like eq.(99.4) of Truesdell&Noll (1965) p.403], which reads in our notation

$$^{ZJ}\overset{\circ}{t} = \dot{t} - w.t + t.w = \mathfrak{h}(t, d) \tag{71}$$

and which is defined with the non-material Zaremba-Jaumann rate $^{ZJ}\overset{\circ}{t}$ tensor of Cauchy stress [cf. (50)]. The modeling of hypo-elastic material may then be generalized to hypo-{elastic, plastic, $\cdots$} material by applying the additive split (67) to the tensors $\overline{^@d}$ of the (partial) deformation rate (68). But how should the corresponding non-material Zaremba-Jaumann rate be defined—with the Eulerian tensor (37) of total vorticity w as

$$^{ZJ}\overset{\circ}{t} = \dot{t} - w.t + t.w = \mathfrak{h}(t, \overline{^ed}) \tag{72}$$

or with the Eulerian tensor of elastic vorticity ^ew [cf. Eq.(45)] as

$$^{eZJ}\overset{\circ}{t} = \dot{t} - ^ew.t + t.^ew = \mathfrak{h}(t, \overline{^ed}) \; ? \tag{73}$$

Since both Zaremba-Jaumann rates $^{ZJ}\overset{\circ}{t}$ and $^{eZJ}\overset{\circ}{t}$ are non-material rate tensors, they are both inappropriate for the modeling of anisotropic (elastic) material behavior—as pointed out by Green&McInnis (1967). A proper material description should be based on material-convective rates and Truesdell's generalized hypo-elastic material equations should better be written with the Green-Naghdi rate $\overset{\circ}{t}$ [cf. (33)] and the material-convective spin Ω tensor (3) as

$$\overset{\circ}{t} = \dot{t} - \Omega.t + t.\Omega = \mathfrak{h}(t, \overline{^ed}) \; . \tag{74}$$

For a material-convective rate (33) of a symmetric second-order Eulerian tensor [cf. (54)] the corresponding material-convective time integral of that tensor is well defined [cf. (55)]. This is *not* the case with Zaremba-Jaumann rates and other non-material rate tensors which corresponding time integrals «lose» the orientation of the material and, therefore, are inappropriate for the formulation of material anisotropy.

7   Critical discussion of non-material «co-rotational» rates and the Updated Lagrangian Formulation

The non-material Zaremba-Jaumann rate $^{ZJ}\overset{\circ}{t}$ tensor of Cauchy stress [cf. (50)] only differs from the material-convective Green-Naghdi rate $\overset{\circ}{t}$ tensor [cf. (33)] if the Eulerian vorticity w tensor (37) differs from the material-convective Ω tensor (3) and this is, from the spectral representation at the r.h.s. of Eq.(37), only the case for moving Lagrangean principal axes, i.e. if their spin $\Lambda \neq 0$ does not vanish. The following three finite-deformation examples with moving Lagrangean principal axes exhibit flaws of the non-material Zaremba-Jaumann rate—as generally pointed out by Green&McInnis (1967) with respect to Truesdell's hypo-elasticity [see Truesdell (1955); Truesdell&Noll (1965)].

7.1   Simple shear

For the example of monotonically increasing simple finite shear [see e.g. Fig.1 of Lee et al. (1983) p.554] unphysical oscillatory shear stress is predicted for the time integrals of the Zaremba-Jaumann stress rate only [see Figs.2–3 of Lee et al. (1983) p.555; Figs.1–4 of Dafalias (1983) pp.563–564; Fig.1 of Johnson&Bammann (1984) p.736; Fig.2 of Flanagan&Taylor (1987) p.311; Figs.1–5 of Bruhns et al. (2001) pp.678–679; and many others]. These examples emphasize that not every «co-rotational» rate is appropriate for a proper material formulation.

7.2   Closed elastic deformation cycles

For the examples of closed elastic deformation cycles the corresponding tensors of the somehow time integrated Zaremba-Jaumann stress rate at the beginning and the end of a cycle deviate from each other, allegorizing a *perpetuum mobile* and, therefore, violating the conservation of energy [see e.g. Figs.1 and 2 of Kojic&Bathe (1987) pp.176 and 178; Figs.1–4, 7, 10, 12 of Meyers et al. (2003) pp.95–101; Figs.1–7 of Bruhns (2009) pp.196–203]. These examples show for closed elastic deformation cycles that Truesdell's hypo-elasticity with the Zaremba-Jaumann stress rate $^{ZJ}\overset{\circ}{t}$ [cf. (50)] or with other non-material «co-rotational» rate tensors can violate the first fundamental law of thermodynamics.

7.3 Updated Lagrangian Formulation

The comparison of the deformation, depicted in Figure 8, with its time derivation and subsequent integration [based on various time integration procedures] may, especially for the so-called *Updated Lagrangian Formulation*, lead to a violation of the first fundamental law of thermodynamics [see Figs.1–5 of Heiduschke (1995a) pp.2167, 2171 and Heiduschke (1996) pp.749, 752–753].

$$\varphi = 0° \qquad 15° \qquad 30° \qquad 45° \qquad 60° \qquad 75° \qquad 90°$$
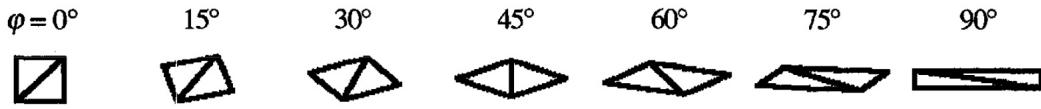
Figure 8. Two-dimensional homogeneos pure distortional (isochoric, equivoluminal) finite deformation with a material-convective rotation angle φ and constantly moving Lagrangean principal axes

When the Updated Lagrangian Formulation is applied within general-purpose finite element simulation tools (like *Dyna3D* and its derivates, *Abaqus*, *Marc*, $\cdots$) then the resulting tensor-rate integrals are also *not* integrated *convective with the material*, and these simulations do not obey the conservation of energy so that the stress and plastic strain tensor components provided just reflect unphysical house numbers.

8 Conclusion

A sound formulation of continuum mechanics requires a geometrical interpretation of the involved deformation tensors describing the total and partial (elastic, plastic, $\cdots$) deformation with respect to the tensorial orientations and magnitudes; deformation tensors which possess such a geometrical interpretation are *proper deformation tensors*. In particular the plastic Cauchy-Green deformation measures $^P\mathsf{b} = \mathsf{R}.^P\mathsf{C}.\mathsf{R}^\mathrm{T}$ and $^P\mathsf{C}$ are proper deformation tensors only if they are integrated translational- and rotational-convective with the material from the corresponding plastic flow rules $^P\mathring{\mathsf{b}} = \mathsf{R}.^P\dot{\mathsf{C}}.\mathsf{R}^\mathrm{T} = \cdots$ and $^P\dot{\mathsf{C}} = \cdots$ of a Green-Naghdi type. There are many non-material formulations (including Treusdell's hypo-elasticity and the Updated Lagrangian Formulation of the general-purpose finite element simulation tools {*Dyna3D* and its derivates, *Abaqus*, *Marc*, and the like} which do not follow the material translational- and rotational-convectively; these non-material formulations may even violate the energy conservation balance. A proper continuum formulation must therefore be described translational- and rotational-convective with the material, as suggested in the work at hand, where the total and partial deformation tensors are rotated with the *same* material-convective rotation R tensor (2) back and forth to their Lagrangean and Eulerian flavors. For a material-convective formulation the time derivatives of the total and partial Eulerian deformation tensors should be defined with the Green-Naghdi rate (33) which is co-rotated with the material by the material-convective rotation R tensor (2) and its associated spin Ω tensor (3). For incremental Eulerian material laws [like the hypo-elasticity of Truesdell (1955) or Truesdell&Noll (1965)], where the rates of deformation tensors are specified within the constitutive equations, the time integrals of these rates only result in proper deformation tensors when they are integrated translational- and rotational-convective with the material. Otherwise, the resulting inaccurately integrated deformation tensor components are just unphysical house numbers, which may even lead to a violation of the first fundamental law of thermodynamics, the conservation of energy, as pointed out in the critical discussion of Section 7.
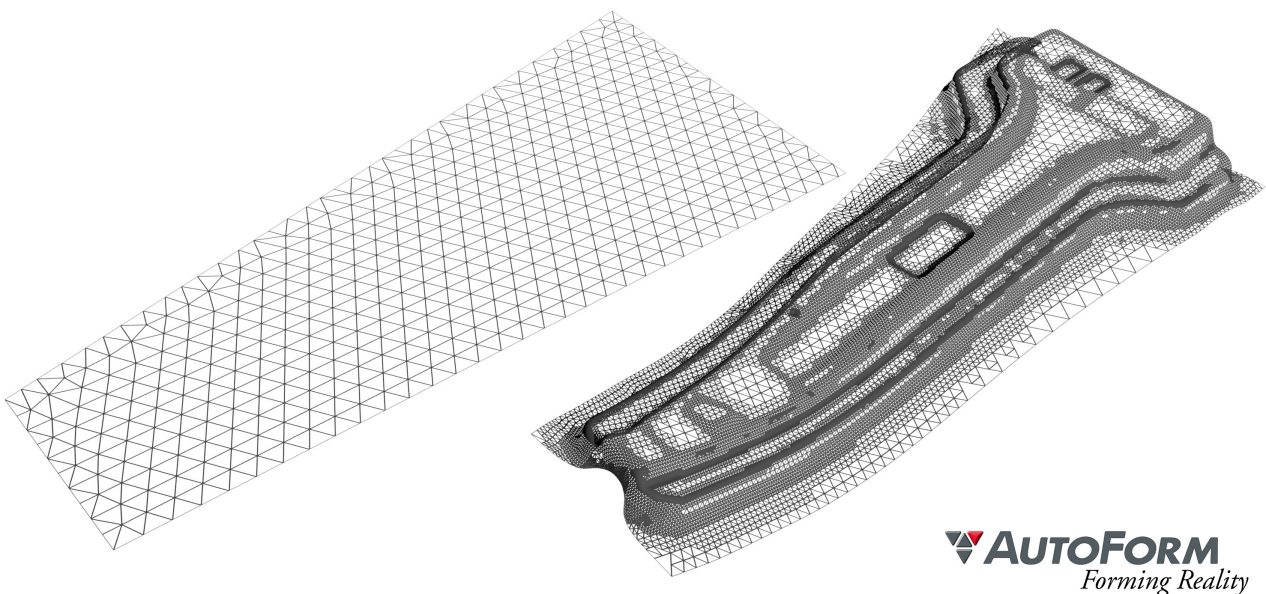
Figure 9. Initial and final configurations/finite element triangular meshes (recursively refined within the critical forming domains) for the deep drawing process of a B-pillar reinforcement modeled through a material-convective logarithmic strain space formulation

K. Heiduschke

Tech. Mech., Vol. 40, Is. 1, (2020), 31–45

Anisotropic material behavior requires a material-convective continuum formulation as presented in this work. The logarithmic strain space formulation—which is implemented into the special-purpose finite element simulation tools *Urmel* [see Heiduschke (1998)], *Pafix* (subsequently renamed to *Hynamic*) [see Anderheggen et al. (1993); Heiduschke (1995b)], and *AutoForm* [see Anderheggen (1991); Heiduschke et al. (1991); Kubli (1996); Heiduschke (1997)]—is such a material-convective description which has proven as most accurate, stable and efficient.

A sheet metal forming process of a B-pillar reinforcement is simulated through a material-convective logarithmic strain space formulation from the initial configuration κ_0 with a triangular mesh for the plane metal sheet to the final configuration κ where the finite element mesh is automatically refined recursively within the critical forming domains, see Figure 9.

Acknowledgment and Funding Information

References

E. Anderheggen. On the design of a new program for simulating thin sheet metal forming processes. In *FE-simulation of 3-D sheet metal forming processes in automotive industry*, pages 231–245. VDI-Bericht 894, Düsseldorf, 1991.

E. Anderheggen, D. Ekchian, K. Heiduschke and P. Bartelt. A contact algorithm for explicit dynamic FEM analysis. In C.A. Brebbia, M.H. Aliabadi (eds.) *Contact Mechanics, Proc. 1st Int. Conf.*, pages 271–283. Southhampton UK, 13-15 July 1993.

O.T. Bruhns, H. Xiao and A. Meyers. A self-consistent Eulerian rate type model for finite deformation elastoplasticity with isotropic damage. *Int. J. Solids Struct.* 38:657–683, 2001.

O.T. Bruhns. Eulerian elastoplasticity: basic issues and recent results. *Theor. Appl. Mech.* 36:167–205, Belgrade, 2009.

A.L. Cauchy. Sur l'équilibre et le mouvement intérieur des corps solides ou fluides, élastiques ou non élastiques. In *Bulletin de la Société philomatique*, pages 300–304. Paris, 1823. http://gallica.bnf.fr/ark:/12148/bpt6k901948/f308

A.L. Cauchy. De la pression ou tension dans un corps solide. In *Exercices de mathématiques*, volume 2, pages 42–56. Paris, 1827a. http://www.google.ch/books?id=NBMOAAAAQAAJ

A.L. Cauchy. Sur la condensation et la dilatation des corps solides. In *Exercices de mathématiques* volume 2, pages 60–69. Paris, 1827b. http://www.google.ch/books?id=NBMOAAAAQAAJ

Y.F. Dafalias. Corotational rates for kinematic hardening at large plastic deformations. *J. Appl. Mech.* 50:561–565, 1983.

J.K. Dienes. On the analysis of rotation and stress rate in deforming bodies. *Acta Mechanica* 32:217–232, 1979.

J.K. Dienes. A discussion of material rotation and stress rate. *Acta Mechanica* 65:1–11, 1986.

J. Finger. Über die gegenseitigen Beziehungen gewisser in der Mechanik mit Vortheil anwendbaren Flächen zweiter Ordnung nebst Anwendungen auf Probleme der Astatik. In *Sitzungsberichte der Kaiserlichen Akademie der Wissenschaften, mathematisch-naturwissenschaftliche Classe, Abtheilung II a*, Band 101, Seiten 1105–1142, 1892. https://www.zobodat.at/pdf/SBAWW_101_2a_1105-1142.pdf

D.P. Flanagan and L.M. Taylor. An accurate numerical algorithm for stress integration with finite rotations. *Comput. Methods Appl. Mech. Eng.* 62:305–320, 1987.

G. Green. On the propagation of light in crystallized media. In *Transactions of the Cambridge Philosophical Society 7, Part II*, pages 121–140, 1839. http://ia600300.us.archive.org/20/items/transactionsofca07camb/transactionsofca07camb.pdf

A.E. Green and P.M. Naghdi. A general theory of an elastic-plastic continuum. *Arch. Rational Mech. Anal.* 18:251–281, 1965.

A.E. Green and B.C. McInnis. Generalized hypo-elasticity. *Proc. Royal Soc. Edinburgh* A57:220–230, 1967.

K. Heiduschke, E. Anderheggen and J. Reissner. Constitutive equations for sheet metal forming. In *FE-simulation of 3-D sheet metal forming processes in automotive industry*, pages 17–37. VDI-Bericht 894, Düsseldorf, 1991.

K. Heiduschke. Why, for finite deformations, the updated Lagrangian formulation is obsolete. In *Complas* 4, pages 2165–2176. Barcelona, Spain, 3-6 April 1995a.

K. Heiduschke. Axisymmetric three- and four-node finite elements for large strain elasto-plasticity. *Int. J. Numer. Meth. in Engng.* 38:2303–2324, 1995b.

K. Heiduschke. Computational aspects of the logarithmic strain space description. *Int. J. Solids Struct.* 33:747–760, 1996.

K. Heiduschke. An elastic isotropic, plastic orthotropic constitutive model based on deviator transformations. *Int. J. Solids Struct.* 34:2339–2356, 1997.

K. Heiduschke. Solder joint lifetime assessment of electronic devices. *Int. J. Numer. Meth. in Engng.* 41:211–231, 1998.

K. Heiduschke. Generalized strain space formulations and eigenprojection tensors. *Acta Mechanica*, 230:3379–3422, 2019. doi: 10.1007/s00707-019-02447-2

G. Jaumann. Geschlossenes System physikalischer und chemischer Differentialgesetze. In *Sitzungsberichte der Kaiserlichen Akademie der Wissenschaften, mathematisch-naturwissenschaftliche Klasse, Abteilung IIa*, Band 120, IV. Heft, Seiten 385–530, Wien, 1911. http://www.physikdidaktik.uni-karlsruhe.de/publication/historische_Arbeiten/Jaumann_1911.pdf

G.C. Johnson and D.J. Bammann. A discussion of stress rates in finite deformation problems. *Int. J. Solids Struct.* 20:725–737, 1984.

G.R. Kirchhoff. Über die Gleichungen des Gleichgewichtes eines elastischen Körpers bei nicht unendlich kleinen Verschiebungen seiner Theile. In *Sitzungsberichte der Kaiserlichen Akademie der Wissenschaften in Wien, mathematisch-naturwissenschaftliche Classe*, Band 9, Seiten 762–773, 1852. http://biodiversitylibrary.org/page/6482116

M. Kojic and K.-J. Bathe. Studies of finite element procedures—Stress solution of a closed elastic strain path with stretching and shearing using the updated Lagrangian Jaumann formulation. *Computers&Structures* 26:175–179, 1987.

W. Kubli. Prozessoptimierte implizite FEM-Formulierung für die Umformsimulation grossflächiger Blechbauteile, Diss. ETH Nr. 11175. In *Fortschrittberichte VDI Reihe 20*, Nr. 204, Düsseldorf, 1996.

E.H. Lee, R.L. Mallet and T.B. Wertheimer. Stress analysis for anisotropic hardening in finite-deformation plasticity. *J. Appl. Mech.* 50:554–560, 1983.

T. Levi-Civita. Lezioni di calcolo differenziale assoluto. In A. Stock (ed.) *Raccolte e compilate dal Dott. Enrico Persico*, Roma, 1925. http://mathematica.sns.it/opere/411/

A. Meyers, H. Xiao and O.T. Bruhns. Elastic stress ratchetting and corotational stress rates. *Technische Mechanik* 23:92–102, 2003.

R.W. Ogden. *Non-linear elastic deformations*. Ellis Horwood Limited, Chichester, 1984.

G. Piola. Nuova analisi per tutte le questioni della meccanica molecolare. In *Memorie di matematica e di fisica della Società Italiana delle Scienze* 21, pages 155–321, Modena, 1825. http://books.google.ch/books?id=cv6ngCOYD7MC

C.A. Truesdell. Hypo-elasticity. *Arch. Rational Mech. Anal.* 4:83–133, 1955.

C.A. Truesdell and W. Noll. The non-linear field theories of mechanics. In S. Flügge (ed.) *Handbuch der Physik* III/3, Springer, Berlin·Heidelberg·New York 1965; **+** Corrigenda and addenda **=** Second edition 1992; Third edition by S.S. Antman 2004.

S. Zaremba. Sur une forme perfectionnée de la théorie de la relaxation. In *Bull. Intern. Acad. Sci. Cracovie*, pages 594–614, 1903.

A Hashin-Shtrikman type semi-analytical homogenization procedure in multiscale modeling to account for coupled problems

David Jaworek[1]★, Johanna Waimann[1], Christian Gierden[1], Stephan Wulfinghoff[2], and Stefanie Reese[1]

[1] Institute of Applied Mechanics, RWTH Aachen University, Mies-van-der-Rohe-Str. 1, 52074 Aachen, Germany
[2] Institute for Material Science, Kiel University, Kaiserstraße 2, 24143 Kiel, Germany

Abstract: Heterogeneous materials are important for a vast amount of applications e.g. in automotive industry or in aerospace. For instance, when producing components, it can be desired to use materials with a heterogeneous microstructure in order to achieve specific material properties. The resulting properties highly depend on the manufacturing process itself, which can involve mechanical and/or thermal loadings. Therefore, it is necessary to properly depict the microstructural material behavior in order to allow for the calibration of the manufacturing process and for the solution of the inverse problem. Constitutive models can be used to depict the material response in a simplified manner. These simplifications allow for a more flexible use of the model but restrict it to a certain range of applications. Thus, it is beneficial to take the material's microscopic structure into account and couple its behavior to the macroscopical response. As multiscale methods (e.g. FE2 , FE-FFT) are computationally expensive, semi-analytical homogenization procedures are investigated to account for the transition between different length scales. There are various well known homogenization techniques discussed in literature such as e.g. the Voigt and Reuss bounds, the self-consistent method as well as the Mori-Tanaka method. In our presentation, the focus lies on a Hashin-Shtrikman type formulation in similarity with the one proposed by Wulfinghoff et al. (2018). This homogenization technique will then be applied to a heterogeneous elastoplastic material under mechanical and thermal loading. After presenting the homogenized material model, we will proof its applicability by various numerical calculations.

Keywords: Process signatures, heterogeneous material, homogenization, Hashin-Shtrikman, Talbot-Willis, plasticity

1 Introduction

In production engineering the desired material modifications (change of the material properties) highly depend on the chosen process as well as on the chosen process quantities (such as experimental setup, material properties, loading, etc.). For example it is possible to consider processes with different dominant impacts such as mechanical loads (deep rolling, cf. Meyer et al. (2011)), thermal loads (EDM, cf. Klink et al. (2011)), or chemical loads (ECM, cf. Klocke et al. (2013)). However, even for similar processes (e.g. the processes deep rolling and drilling with predominantly mechanical impact) a comparison is often merely impossible due to significantly different boundary conditions. Therefore, material loads have to be derived from the process parameters in order to make different processes comparable. On the one hand, a governing material load could be the strain state inside the material. On the other hand, possible material modifications could be a change of the hardness or a change in the residual stresses. Another problem is linking the material modifications to the process parameters as the direct dependence is usually not known or only known a priori under very special conditions. The term "process signature" describes the interrelation between material loads and material modifications and was established in course of the transregional collaborative research center SFB/TRR 136 (cf. Brinksmeier et al. (2011, 2014)). The idea is depicted in Fig. 1.

For materials with microstructural features (such as steel), these modifications can be measured on either the microscopic or the macroscopic scale. Therefore, it is necessary to employ a strategy to link the two scales. Early works involved procedures such a FE[2] (Smit et al. (1998); Feyel (2003)). Later, more advanced multi scale approaches as e.g. FE-FFT based methods (Moulinec
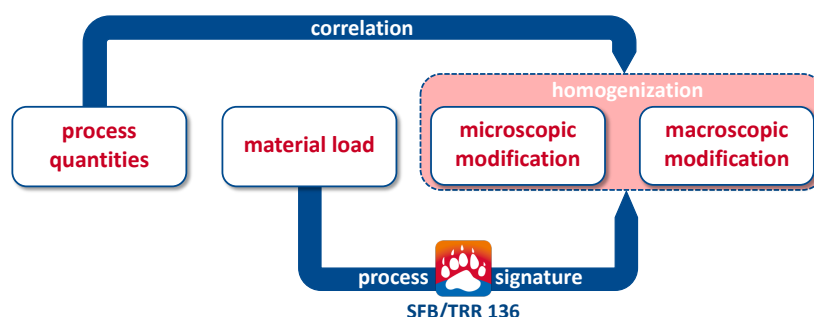
Fig. 1: Schematic sketch of process including process signature.

and Suquet (1995, 1998); Kochmann et al. (2016)) were developed. The range of possible formulations is very wide starting from first order homogenization techniques (Voigt (1889); Reuss (1929)) to more advanced homogenization techniques such as e.g. Mori-Tanaka (Mori and Tanaka (1973)), the self-consistent scheme (Kröner (1958); Hill (1965)), or also Hashin-Shtrikman type formulation (Hashin and Shtrikman (1962a,b)) and Talbot-Willis type method (Willis (1981); Talbot and Willis (1985)). As the process simulations are in general quite complex and hence involve high computational effort, it is necessary to use suitable multi scale approaches. This work deals with the investigation of a Hashin-Shtrikman type homogenization procedure (cf. also Ponte Castaneda and Suquet (1998)) applied for predominantly mechanical processes under isothermal and non-isothermal conditions. In section 2 the Hashin-Shtrikman type homogenization method is presented with application to statistically isotropic elasto-plastic composites. Thereupon, in section 3 different numerical investigations are carried out starting with a Gauss point study for mechanical with and without temperature impact and then continuing with a short Finite element study. Section 4 gives a conclusion and an outlook.

2 Problem Description

The microscopic boundary value problem (BVP) depicted in Fig. 2 is considered. The domain Ω is bounded by dΩ with prescribed displacements $\bar{u}$ on the Dirichlet boundary dΩ_u and $div\,\tau(x)$ acting inside the inhomogeneities. The body is assumed to be statistically istotropic and to consist of randomly distributed ellipsoidal inhomogeneities. Following Eshelby (1957), the inhomogeneities do not interact with each other. This allows for the calculation of the response inside the inhomogeneities separately from the matrix response.
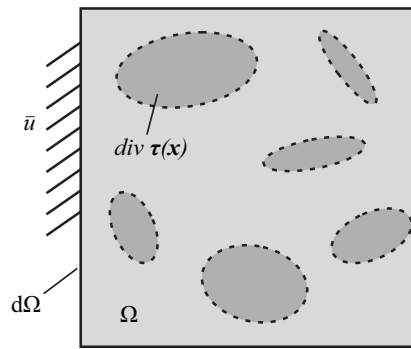
Fig. 2: Heterogeneous BVP.

The strong form of the problem is given by

$$
\left.
\begin{aligned}
\mathbf{0} &= \mathrm{div}\left(\boldsymbol{\tau} + \mathbb{C}^{(0)} : \boldsymbol{\varepsilon}\right) \\
\boldsymbol{\tau}(\boldsymbol{x}, \boldsymbol{\varepsilon}) &= \boldsymbol{\sigma}(\boldsymbol{x}, \boldsymbol{\varepsilon}) - \mathbb{C}^{(0)} : \boldsymbol{\varepsilon}(\boldsymbol{x}) \\
\boldsymbol{\sigma}(\boldsymbol{x}, \boldsymbol{\varepsilon}) &= \mathbb{C}(\boldsymbol{x}) : \boldsymbol{\varepsilon}(\boldsymbol{x}) \\
\boldsymbol{\varepsilon}(\boldsymbol{x}) &= \nabla^{sym} \boldsymbol{u}(\boldsymbol{x})
\end{aligned}
\right\}
\quad \text{in } \Omega, \quad \boldsymbol{u}(\boldsymbol{x}) = \bar{\boldsymbol{u}} = \bar{\boldsymbol{\varepsilon}}\boldsymbol{x} \text{ on } \partial\Omega,
\tag{1}
$$

in which the stress $\boldsymbol{\sigma}(\boldsymbol{x}, \boldsymbol{\varepsilon})$ can involve any elastic or non-elastic constitutive relation. The polarization stress $\boldsymbol{\tau}(\boldsymbol{x}, \boldsymbol{\varepsilon})$ is the difference between the actual stress field $\boldsymbol{\sigma}(\boldsymbol{x}, \boldsymbol{\varepsilon})$ and the stress in a homogeneous reference material of stiffness $\mathbb{C}^{(0)}$. The deformations are assumed to be small and the strain field $\boldsymbol{\varepsilon}(\boldsymbol{x})$ is calculated as the symmetric part of the gradient of the displacement field $\boldsymbol{u}(\boldsymbol{x})$. In accordance with Hashin and Shtrikman (1962a,b), the microscopic field quantities are assumed to be phase-wise constant. They can therefore be expressed by

$$
\boldsymbol{\sigma}(\boldsymbol{x}) = \sum_{r=1}^{N_r} \chi^{(r)}(\boldsymbol{x})\,\boldsymbol{\sigma}^{(r)}, \quad
\boldsymbol{\varepsilon}(\boldsymbol{x}) = \sum_{r=1}^{N_r} \chi^{(r)}(\boldsymbol{x})\,\boldsymbol{\varepsilon}^{(r)}, \quad
\boldsymbol{\tau}(\boldsymbol{x}) = \sum_{r=1}^{N_r} \chi^{(r)}(\boldsymbol{x})\,\boldsymbol{\tau}^{(r)},
\tag{2}
$$

where any quantity $(\bullet)^{(r)}$ represents the phase-wise constant counterpart of $(\bullet)$ in phase r for which $\boldsymbol{x} \in \Omega^{(r)}$. Moreover, $\chi^{(r)}(\boldsymbol{x})$ represents an indicator function which is defined as

$$
\chi^{(r)}(\boldsymbol{x}) =
\begin{cases}
1 & \text{if } \boldsymbol{x} \in \Omega^{(r)} \\
0 & \text{otherwise}
\end{cases}
.
\tag{3}
$$

Combining Eqs. (1) and (2), the microscopical phase-wise constant polarization stress field $\boldsymbol{\tau}^{(r)}$ can be expressed in terms of the phase-wise constant stresses and strains as

$$
\boldsymbol{\tau}^{(r)} = \boldsymbol{\sigma}^{(r)}(\boldsymbol{\varepsilon}^{(r)}) - \mathbb{C}^{(0)} : \boldsymbol{\varepsilon}^{(r)}.
\tag{4}
$$

It is important to mention, that the macroscopic strain field $\bar{\boldsymbol{\varepsilon}}$ is assumed to be constant on the material point level whereas the microscopic strain field $\boldsymbol{\varepsilon}(\boldsymbol{x})$ is allowed to fluctuate. Utilizing the Lippmann-Schwinger equation (cf. Kröner (1977)), the

microscopic strain field $\boldsymbol{\varepsilon}(\boldsymbol{x})$ can be calculated by

$$\boldsymbol{\varepsilon}(\boldsymbol{x}) = \bar{\boldsymbol{\varepsilon}} - \underbrace{\int_{\Omega} \boldsymbol{\Gamma}_{\infty}(\boldsymbol{x}, \boldsymbol{x}') : \boldsymbol{\tau}(\boldsymbol{x}') \, \mathrm{d}\boldsymbol{x}'}_{\tilde{\boldsymbol{\varepsilon}}(\boldsymbol{x})} . \tag{5}$$

Here, the microscopic strain fluctuation $\tilde{\boldsymbol{\varepsilon}}(\boldsymbol{x})$ can be obtained by the linear mapping the 2nd order polarization stress field tensor $\boldsymbol{\tau}(\boldsymbol{x}')$ by the 4th order $\boldsymbol{\Gamma}$-operator. The $\boldsymbol{\Gamma}$-operator itself is the second derivative of the Green's function $\boldsymbol{\Gamma}_{\infty}(\boldsymbol{x}, \boldsymbol{x}')$ and can be calculated by

$$\boldsymbol{\Gamma}_{\infty}(\boldsymbol{x}, \boldsymbol{x}') = \frac{\partial^2 \boldsymbol{G}_{\infty}(\boldsymbol{x}, \boldsymbol{x}')}{\partial \boldsymbol{x} \partial \boldsymbol{x}'} . \tag{6}$$

Integrating Eq. (5) over $\Omega^{(r)}$ (the domain of phase r) results in an expression for the average strain field in phase r which reads

$$\boldsymbol{\varepsilon}^{(r)} = \int_{\Omega^{(r)}} \boldsymbol{\varepsilon}(\boldsymbol{x}) \, \mathrm{d}\boldsymbol{x} = \bar{\boldsymbol{\varepsilon}} - \frac{1}{\lambda^{(r)}} \sum_{s=1}^{N} \left(\mathbb{E}^{(rs)} : \boldsymbol{\tau}^{(s)} \right) . \tag{7}$$

Here, the microstructural tensor $\mathbb{E}^{(rs)}$ describes the interrelation between phases r and s. It is an abbreviation for the volume average over phase r of the convolution integral and reads

$$\mathbb{E}^{(rs)} = \int_{\Omega} \chi^{(r)}(\boldsymbol{x}) \int_{\Omega} \boldsymbol{\Gamma}_{\infty}(\boldsymbol{x}, \boldsymbol{x}') \chi^{(s)}(\boldsymbol{x}') \, \mathrm{d}\boldsymbol{x}' \mathrm{d}\boldsymbol{x} . \tag{8}$$

For the special case of spherical inhomogeneities with an statistically isotropic distribution and a linear elastic reference material, the microstructural tensor simplifies to

$$\mathbb{E}^{(rs)} = \lambda^{(r)} (\delta_{rs} - \lambda^{(s)}) \, \mathbb{P}^{(0)} \quad , \quad \mathbb{P}^{(0)} = \mathbb{P}^{(0)}(\kappa^{(0)}, \mu^{(0)}) = const. \tag{9}$$

From Eq. (9), it is apparent, that the microstructural realization does not influence the results as long as the phase fractions are chosen to be constant. In that case $\mathbb{E}^{(rs)}$ solely depends on the phase fractions $\lambda^{(r)}$ as well as on the elastic constants of the homogeneous reference material $\kappa^{(0)}$ and $\mu^{(0)}$.

Hence, for a two-phase composite with volumetric phase fractions $\lambda^{(M)}$ (matrix) and $\lambda^{(I)}$ (inhomogeneities), all microstructural realizations shown in Fig. 3 result in the same macroscopic response when considering the aforementioned simplification.
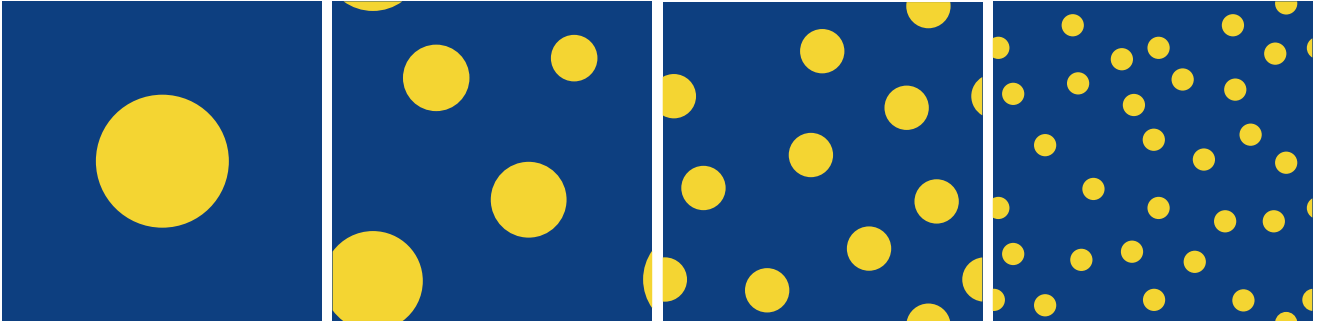
Fig. 3: Different micro structural realizations of same phase fractions.

Subsequently, the microscopic stress and strain tensors $\boldsymbol{\sigma}(\boldsymbol{x})$ and $\boldsymbol{\varepsilon}(\boldsymbol{x})$ can be averaged over the volume of the domain by

$$\bar{\boldsymbol{\sigma}} = \int_{\Omega} \boldsymbol{\sigma}(\boldsymbol{x}) \, \mathrm{d}\boldsymbol{x} = \sum_{r=1}^{N_r} \lambda^{(r)} \boldsymbol{\sigma}^{(r)}, \quad \bar{\boldsymbol{\varepsilon}} = \int_{\Omega} \boldsymbol{\varepsilon}(\boldsymbol{x}) \, \mathrm{d}\boldsymbol{x} = \sum_{r=1}^{N_r} \lambda^{(r)} \boldsymbol{\varepsilon}^{(r)}, \tag{10}$$

where $\bar{\boldsymbol{\sigma}}$ and $\bar{\boldsymbol{\varepsilon}}$ denote the macroscopical stress and strain tensors.

3 Numerical investigations

3.1 Gauss point study - mechanical loading

In order to evaluate the accuracy of the discussed homogenization procedure, a Gauss point study is carried out. For simplicity, the first realization (cf. Fig. 3) is chosen for carrying out full-field simulations which will then compared with the homogenization procedure. The inclusions are assumed to behave purely elastic. The matrix material is modeled by means of an elasto-plastic constitutive law involving $J2$-plasticity with Voce-type hardening (e.g. as presented in Brepols et al. (2018)). The hardening behavior is described using the yield stress σ_y which is given by

$$\sigma_y = \sigma_{y0} + (\sigma_{y\infty} - \sigma_{y0})(1 - \exp(-\beta \varepsilon_P^{eq})) \tag{11}$$

in which ε_P^{eq} is the equivalent plastic strain. The elastic and plastic parameters of the matrix as well as the elastic parameters of the inclusions are given in Tab. 1.

Matrix	Young's modulus $E^{(M)}$	200 GPa
	Poisson's ratio $\nu^{(M)}$	0.34
	Initial yield strength σ_{y0}	350 MPa
	Ultimate strength $\sigma_{y\infty}$	750 MPa
	Hardening parameter β	200
	Volumetric phase fraction $\lambda^{(M)}$	0.85
Inhomogeneities	Young's modulus $E^{(I)}$	400 GPa
	Poisson's ratio $\nu^{(I)}$	0.34
	Volumetric phase fraction $\lambda^{(I)}$	0.15

Tab. 1: Material parameters

A stress-driven computation is carried out with a uniaxial tensile stress of $\sigma_{11} = 750$ MPa. The stress-strain response for the uniaxial strain ε_{11} is shown in Fig. 4, whereas the transversal strain ε_{22} is presented in Fig. 5. As can be observed, the Voigt and Reuss bounds (1st order homogenizations) are compared with the full field solution and the Hashin-Shtrikman lower bound. The error in the strain between the Hashin-Shtrikman homogenization and the full field can be compared for the crucial points $\sigma_{11} = 350$ MPa (yield strength of matrix material) and the final stress of $\sigma_{11} = 750$ MPa. There is no error present for the elastic response whereas the error in the strain ε_{11} for a stress level of $\sigma_{11} = 750$ MPa reads 4.49%. The results are also summarized in Tab. 2.

Method	Run time	Strain ε_{11} at $\sigma_{11} = 350$ MPa	Strain ε_{11} at $\sigma_{11} = 750$ MPa	Error at $\sigma_{11} = 750$ MPa
FFT	89664 s	0.0016	0.0085	4.49%
HS Homogenization	0.012 s	0.0016	0.0089	-

Tab. 2: CPU times and speed-up factors
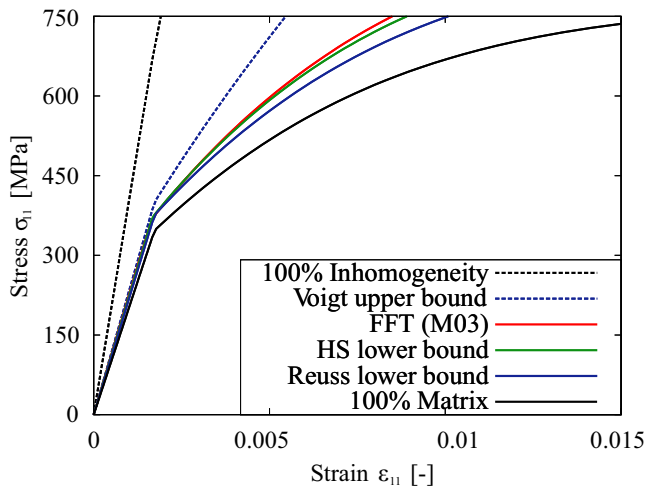
Fig. 4: Uniaxial tension: σ_{11} vs. ε_{11}.
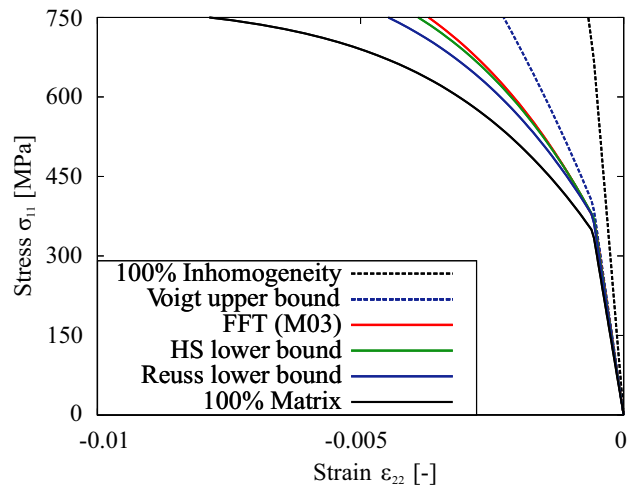
Fig. 5: Uniaxial tension: σ_{11} vs. ε_{22}.

3.2 Gauss point study - mechanical loading with isothermal temperature state

Furthermore, the material response could also be temperature dependent and therefore the elastic and elasto-plastic properties of the microstructure are evolving with temperature change. Considering a steel of type 42CrMo4, the material properties can be taken from literature (e.g. Miokovic (2005)). The Koistinen-Marburger model is used to model phase transformations (Koistinen and Marburger (1959)), where the volumetric phase fraction of the matrix can be calculated by

$$\lambda^{(M)} = \begin{cases} \exp\left[b(\theta_S - \theta)\right] & \text{if } \theta < \theta_S \\ 1 & \text{otherwise} \end{cases}. \tag{12}$$

In Eq. (12), θ is the current temperature, θ_S is the phase transformation start temperature, and b is a constant that controls the shape of the curve. For $\theta_S = 500°C$ and $b = -0.01\frac{1}{°C}$, the curve looks as shown in Fig. 6.

D. Jaworek, J. Waimann, S. Wulfinghoff, and S. Reese

Tech. Mech., Vol. 40, Is. 1, (2020), 46–52
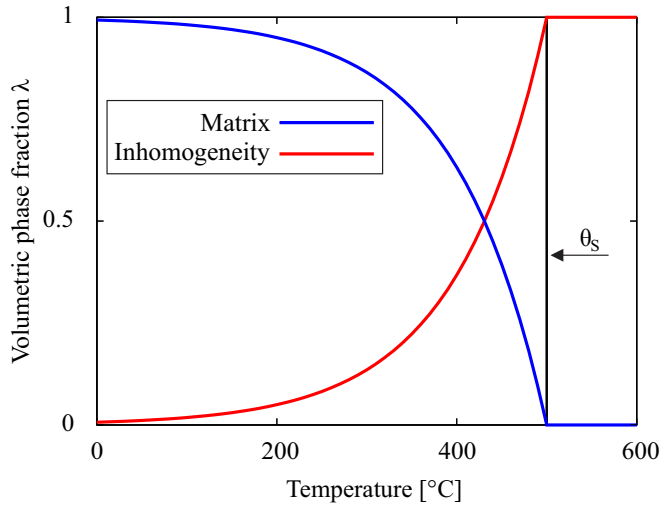
Fig. 6: Temperature induced phase transformation.
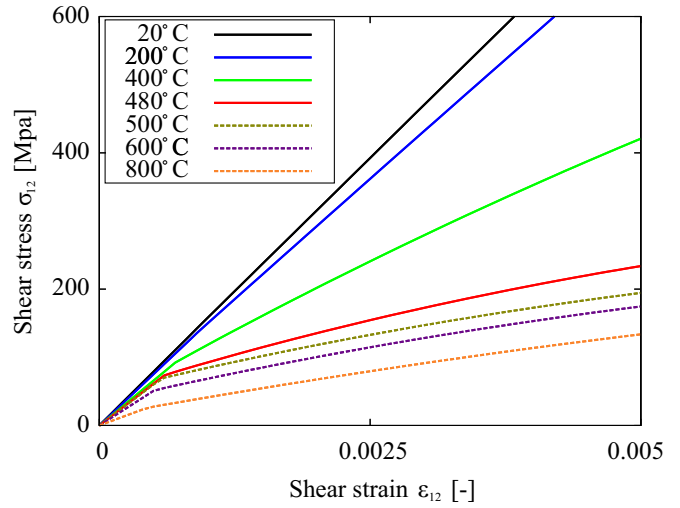
Fig. 7: Temperature dependent results for isothermal loading.

Now, the homogenization method can be evaluated again for different isothermal temperature states. As can be observed in Fig. 7, the overall response is linear elastic for low temperatures as the specimen then only consists of the linear elastic inhomogeneity material. For increasing temperatures, the response becomes softer until we reach a fully elasto-plastic response for temperatures over 500 °C which is the temperature at which the phase transformation is completed and only matrix material is present.

3.3 Finite Element study - mechanical loading for non-isothermal temperature states

Further, a simple tensile experiment can be calculated using the Finite Element Analysis Program (FEAP) (Taylor (2014)) where the procedure has been implemented as a user material routine (UMAT).

The structure is symmetric with respect to its geometry and loading in all directions and therefore only $\frac{1}{8}$ of the specimen size is used.
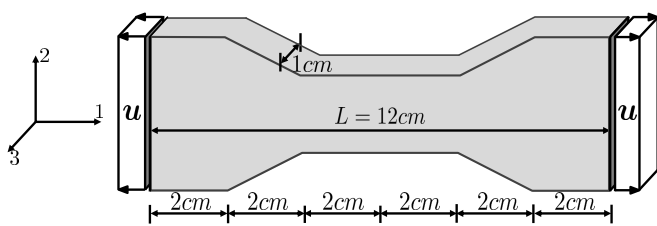
Fig. 8: Schematic view of the 3D tensile specimen.
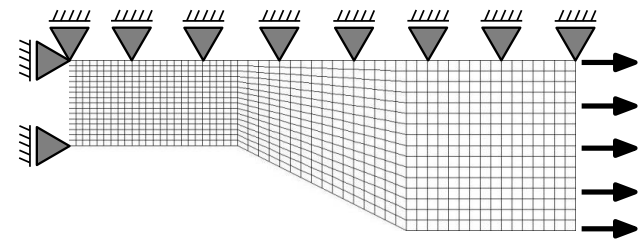
Fig. 9: Reduced mesh involving symmetric BCs.

In order to take a very week one-directional thermal coupling into account, the material parameters are set to be temperature dependent as described in section 3.2.

Applying a gradually increasing displacement u until reaching $u_{max} = 0.02\ L = 0.24$ cm, while decreasing the temperature from 600 °C to 20 °C, the evolution of the von Mises stresses over time can be measured for different integration points. The phase transformation sets in as soon as reaching the phase transformation start temperature $\theta_S = 500$ °C (cf. Figs. 6 and 10).
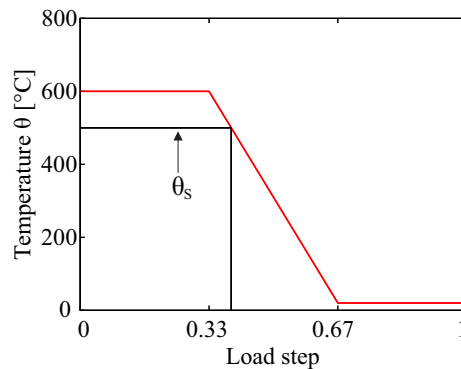
Fig. 10: Temperature load.

Fig. 11 illustrates the evolution of the von Mises stress σ_V over time for three points in the specimen. Furthermore, the von Mises stress distribution over time is shown for the last step.
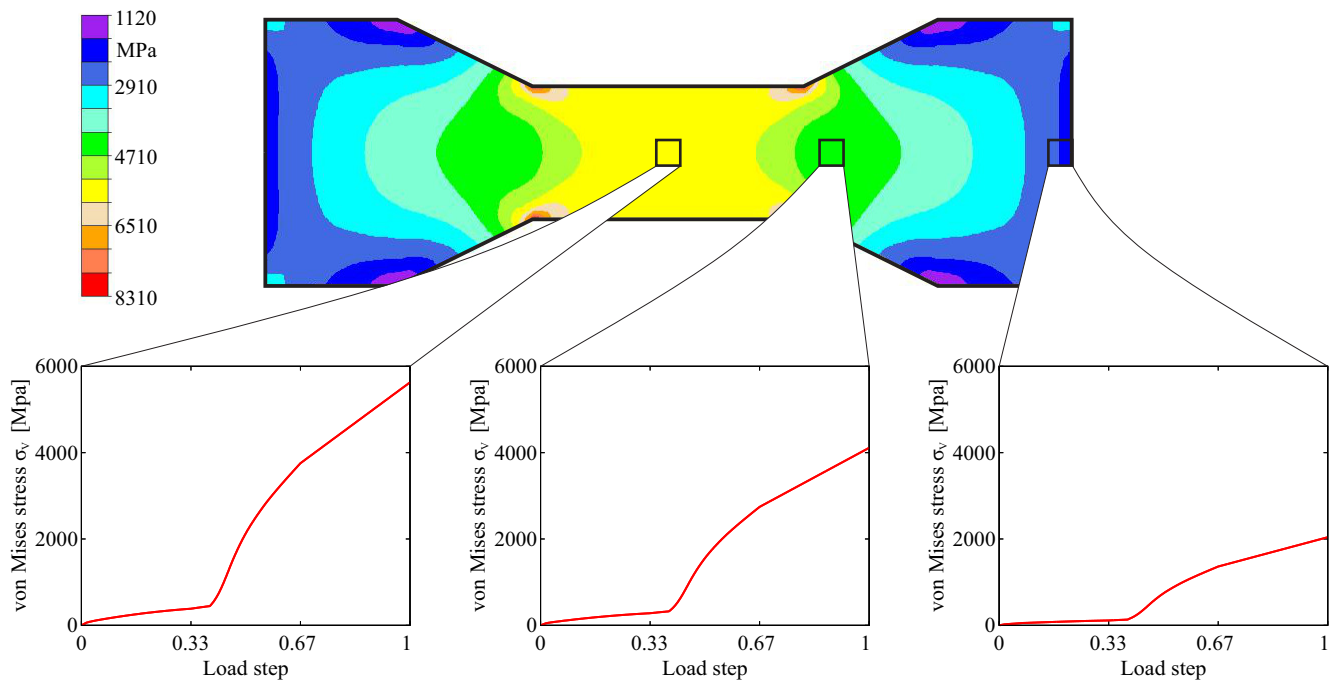
Fig. 11: Finite element simulation results.

In the beginning the specimen only consists of matrix material and thus behaves elasto-plastically for temperatures higher than 500 °C. With decreasing temperature the response becomes stiffer as the material stiffness increases and as the phase transformation sets in. When reaching very low temperatures (here 20 °C), the specimen nearly only consists of linear elastic inhomogeneity and therefore the response is purely elastic.

4 Conclusions and Outlook

The presented homogenization framework following the procedure by Hashin and Shtrikman and incorporating the developments by Talbot and Willis allows for the computation of elasto-plastic composites under small strains. The results obtained are in good agreement with the reference solution provided by FE-FFT simulations. One assumption is the statistically isotropic distribution of the spherical inhomogeneities which simplifies the computation of the microstructural tensor $\mathbb{E}^{(rs)}$. It is shown, that the method can be applied for mechanical calculations under isothermal or non-isothermal conditions.

As the simplification of a statistically isotropic microstructure with spherical inclusions is very limiting, further research should tackle this problem and take more complex micro structural distributions into account. This could be achieved incorporating a more elaborate approach for the calculation of $\mathbb{E}^{(rs)}$. Moreover, in order to simulate thermal processes properly, a consistent thermo-mechanical coupling is to be developed and coupled with the homogenization procedure. Further, a more profound model for capturing the microstructural evolution of the phases should be considered when investigating thermal or thermo-mechanical processes. One possible approach would be incorporating a phase transformation model based on variational methods (cf. e.g. Carstensen et al. (2002); Hackl and Fischer (2008); Junker et al. (2014)).

Acknowledgements

References

T. Brepols, S. Wulfinghoff, and S. Reese. *A Micromorphic Damage-Plasticity Model to Counteract Mesh Dependence in Finite Element Simulations Involving Material Softening*, pages 235–255. Springer International Publishing, Cham, 2018. doi: https://doi.org/10.1007/978-3-319-65463-8_12.

E. Brinksmeier, R. Gläbe, F. Klocke, and D.A. Lucca. Process signatures - an alternative approach to predicting functional workpiece properties. *Procedia Engineering*, 19:44 – 52, 2011. ISSN 1877-7058. doi: https://doi.org/10.1016/j.proeng.2011.11.078. 1st CIRP Conference on Surface Integrity (CSI).

E. Brinksmeier, F. Klocke, D. A. Lucca, J. Sölter, and D. Meyer. Process signatures - a new approach to solve the inverse surface integrity problem in machining processes. *Procedia CIRP*, 13:429–434, 2014. doi: https://doi.org/10.1016/j.procir.2014.04.073.

C. Carstensen, K. Hackl, and A. Mielke. Non-convex potentials and microstructures in finite-strain plasticity. *Proc. R. Soc. Lond. A*, 458:299–317, 2002. doi: https://doi.org/10.1098/rspa.2001.0864.

J. D. Eshelby. The determination of the elastic field of an ellipsoidal inclusion, and related problems. *Proceedings of the Royal Society of London A*, 241(1226):376–396, 1957. doi: https://doi.org/10.1098/rspa.1957.0133.

D. Jaworek, J. Waimann, S. Wulfinghoff, and S. Reese

Tech. Mech., Vol. 40, Is. 1, (2020), 46–52

F. Feyel. A multilevel finite element method (fe2) to describe the response of highly non-linear structures using generalized continua. *Computer Methods in Applied Mechanics and Engineering*, 192(28):3233 – 3244, 2003. ISSN 0045-7825. doi: https://doi.org/10.1016/S0045-7825(03)00348-7. Multiscale Computational Mechanics for Materials and Structures.

K. Hackl and F. D. Fischer. On the relation between the principle of maximum dissipation and inelastic evolution given by dissipation potentials. *Proceedings of the Royal Society A*, 464:117–132, 2008. doi: https://doi.org/10.1098/rspa.2007.0086.

Z. Hashin and S. Shtrikman. On some variational principles in anisotropic and nonhomogeneous elasticity. *Journal of the Mechanics and Physics of Solids*, 10(4):335–342, 1962a. doi: https://doi.org/10.1016/0022-5096(62)90004-2.

Z. Hashin and S. Shtrikman. A variational approach to the theory of the elastic behaviour of polycrystals. *Journal of the Mechanics and Physics of Solids*, 10(4):343–352, 1962b. doi: https://doi.org/10.1016/0022-5096(62)90005-4.

R. Hill. A self-consistent mechanics of composite materials. *Journal of the Mechanics and Physics of Solids*, 13(4):213 – 222, 1965. ISSN 0022-5096. doi: https://doi.org/10.1016/0022-5096(65)90010-4.

P. Junker, J. Makowski, and K. Hackl. The principle of the minimum of the dissipation potential for non-isothermal processes. *Continuum Mechanics and Thermodynamics*, 26(3):259–268, May 2014. doi: https://doi.org/10.1007/s00161-013-0299-4.

A. Klink, Y.B. Guo, and F. Klocke. Surface integrity evolution of powder metallurgical tool steel by main cut and finishing trim cuts in wire-edm. *Procedia Engineering*, 19:178–183, 12 2011. doi: 10.1016/j.proeng.2011.11.098.

F. Klocke, M. Zeis, S. Harst, A. Klink, D. Veselovac, and M. Baumgaertner. Modeling and simulation of the electrochemical machining (ecm) material removal process for the manufacture of aero engine components. *Procedia CIRP*, 8:265 – 270, 2013. ISSN 2212-8271. doi: https://doi.org/10.1016/j.procir.2013.06.100. 14th CIRP Conference on Modeling of Machining Operations (CIRP CMMO).

J. Kochmann, S. Wulfinghoff, S. Reese, J. R. Mianroodi, and B. Svendsen. Two-scale fe-fft- and phase-field-based computational modeling of bulk microstructural evolution and macroscopic material behavior. *Computer Methods in Applied Mechanics and Engineering*, 305:89 – 110, 2016. ISSN 0045-7825. doi: https://doi.org/10.1016/j.cma.2016.03.001.

D.P. Koistinen and R.E. Marburger. A general equation prescribing the extent of the austenite-martensite transformation in pure iron-carbon alloys and plain carbon steels. *Acta Metallurgica*, 7(1):59 – 60, 1959. ISSN 0001-6160. doi: https://doi.org/10.1016/0001-6160(59)90170-1.

E. Kröner. Berechnung der elastischen konstanten des vielkristalls aus den konstanten des einkristalls. *Zeitschrift für Physik*, 151(4):504–518, Aug 1958. doi: https://doi.org/10.1007/BF01337948.

E. Kröner. Bounds for effective elastic moduli of disordered materials. *Journal of the Mechanics and Physics of Solids*, 25(2):137–155, 1977. doi: https://doi.org/10.1016/0022-5096(77)90009-6.

D. Meyer, E. Brinksmeier, and F. Hoffmann. Surface hardening by cryogenic deep rolling. *Procedia Engineering*, 19:258 – 263, 2011. ISSN 1877-7058. doi: https://doi.org/10.1016/j.proeng.2011.11.109. 1st CIRP Conference on Surface Integrity (CSI).

T. Miokovic. *Analyse des Umwandlungsverhaltens bei ein- und mehrfacher Kurzzeithärtung bzw. Laserstrahlhärtung des Stahls 42CrMo4*. PhD thesis, 2005. URL https://publikationen.bibliothek.kit.edu/1000003805.

T. Mori and K. Tanaka. Average stress in matrix and average elastic energy of materials with misfitting inclusions. *Acta Metallurgica*, 21(5):571 – 574, 1973. ISSN 0001-6160. doi: https://doi.org/10.1016/0001-6160(73)90064-3.

H. Moulinec and P. Suquet. A fft-based numerical method for computing the mechanical properties of composites from images of their microstructure. *Microstructure-Property Interactions in Composite Materials*, pages 235–246, 1995. doi: https://doi.org/10.1007/978-94-011-0059-5$_2$0.

H. Moulinec and P. Suquet. A numerical method for computing the overall response of nonlinear composites with complex microstructure. *Computer Methods in Applied Mechanics and Engineering*, 157(1):69 – 94, 1998. ISSN 0045-7825. doi: https://doi.org/10.1016/S0045-7825(97)00218-1.

P. Ponte Castaneda and P. Suquet. Nonlinear composites. *Advances in Applied Mechanics*, 34:171–302, 1998. doi: https://doi.org/10.1016/S0065-2156(08)70321-1.

A. Reuss. Berechnung der fliessgrenze von mischkristallen auf grund der plastizitätsbedingung für einkristalle. *Zeitschrift fuer angewandte Mathematik und Mechanik*, 9:49–59, 1929. doi: https://doi.org/10.1002/zamm.19290090104.

R. J. M. Smit, W. A. M. Brekelmans, and H. E. H. Meijer. Prediction of the mechanical behavior of nonlinear heterogeneous systems by multi-level finite element modeling. *Computer Methods in Applied Mechanics and Engineering*, 155(1):181 – 192, 1998. ISSN 0045-7825. doi: https://doi.org/10.1016/S0045-7825(97)00139-4.

D. R. S. Talbot and J. R. Willis. Variational principles for inhomogeneous nonlinear media. *IMA Journal of Applied Mathematics*, 35(4b):39–54, 1985. doi: https://doi.org/10.1093/imamat/35.1.39.

R. L. Taylor. FEAP - finite element analysis program, 2014. URL http://www.ce.berkeley/feap.

W. Voigt. Ueber die beziehung zwischen den beiden elasticitätsconstanten isotroper körper. *Annalen der Physik*, 38:573–587, 1889. doi: https://doi.org/10.1002/andp.18892741206.

J. R. Willis. Variational and related methods for the overall properties of composites. *Advances in Applied Mechanics*, 21:1–78, 1981. doi: https://doi.org/10.1016/S0065-2156(08)70330-2.

S. Wulfinghoff, F. Cavaliere, and S. Reese. Model order reduction of nonlinear homogenization problems using a hashin-shtrikman type finite element method. *Computer Methods in Applied Mechanics and Engineering*, 330(1):149–179, 2018. doi: https://doi.org/10.1016/j.cma.2017.10.019.

Gradient-extended brittle damage modeling

Thank Thank Nguyen[1]*, Marek Fassin[2], Robert Eggersmann[2], Stefanie Reese[2], and Stephan Wulfinghoff[1]

[1] Kiel University, Institute for Materials Science, Computational Materials Science, Kaiserstr. 2, 24143 Kiel, Germany
[2] RWTH Aachen University, Institute of Applied Mechanics, Mies-van-der-Rohe Str. 1, 52074 Aachen, Germany

Abstract: An elastic-brittle anisotropic model is presented based on the work by Fassin et al. (2019a). After discussing the local model equations and the incorporation of crack-closure, the gradient extension using the micromorphic approach according to Forest (2009) is briefly summarized. In order to run unit cell simulations on the microlevel, relevant material parameters have to be identified. Therefore, the energy dissipation provides a differential equation with a linear and quadratic term for the damage variable. Finally, the isotropic damage model is used to show numerical examples with variation of fracture toughness and volume fraction of pores.

Keywords: anisotropic damage, gradient damage, micromorphic approach

1 Introduction

Due to the renewable energy act proposed by the German government, a significant amount of electric power must be covered by renewable energies. However, a huge amount of the electric power supply will still be provided by fossil power plants. The repeated turn on and off procedures of fossil power plant generators are associated with high demands on the materials' strength in cyclic loading. This can be accounted for by making use of innovative materials which are characterized by improved functional properties and higher performance. In this context, carbon fiber-reinforced (CFR) epoxy resin has widely been used. Before such materials can be applied in the generators, their material behavior and performance must be analyzed. Since the overall mechanical behavior of such heterogeneous media is to a large extent determined by the micro-structure, numerical simulations can be conducted to study the local material behavior and the effective constitutive response. In particular, the initiation and growth of damage at the micro-scale is crucial and needs to be taken care of. Due to the manufacturing processes, micro-cracks and -voids (Fig. 1) are present which grow and coalesce under certain loadings leading to damage processes in the matrix material.

2 Model equation

This section briefly presents the anisotropic gradient-extended damage model, recently published in Fassin et al. (2019a) and its extension to tension compression asymmetry (Fassin et al. (2019b)).

2.1 Local damage model

The free energy density ψ is assumed to consist of three parts

$$\psi = \psi_{\mathrm{e}}(\boldsymbol{\varepsilon}, \boldsymbol{D}) + \underbrace{\psi_{\mathrm{h}}^{\alpha}(\alpha) + \psi_{\mathrm{h}}^{\boldsymbol{D}}(\boldsymbol{D})}_{\psi_{\mathrm{h}}}, \tag{1}$$

representing the elastic, the damage hardening and an additional hardening term with the strain tensor $\boldsymbol{\varepsilon}$, the hardening variable α and the symmetric second order damage tensor $\boldsymbol{D}$. The elastic strain energy for an initially isotropic and material is also split into three parts

$$\psi_{\mathrm{e}}(\boldsymbol{\varepsilon}, \boldsymbol{D}) = \underbrace{\tfrac{1}{2}(1-g)\lambda \mathrm{tr}^2(\boldsymbol{\varepsilon})}_{\lambda\text{-term}} + \underbrace{(1-\vartheta)(1-g)\mu \boldsymbol{I} : \boldsymbol{\varepsilon}^2}_{\mu_{\mathrm{iso}}\text{-term}} + \underbrace{\vartheta\mu(\boldsymbol{I}-\boldsymbol{D}) : \boldsymbol{\varepsilon}^2}_{\mu_{\mathrm{aniso}}\text{-term}} \tag{2}$$

with $g = f(\mathrm{tr}(\boldsymbol{D})) \rightarrow$ e.g. $g = \mathrm{tr}(\boldsymbol{D})/3$, μ and λ are the Lamé parameters. The λ-term and μ_{iso}-term are related to isotropic damage since the terms are damaged by the scalar $(1 - g(\boldsymbol{D}))$. The material parameter ϑ controls the degree of damage anisotropy related to both μ-terms: For the choice $\vartheta = 0$, the third term in Eq. (2) vanishes and fully isotropic damage is obtained. In contrast, fully anisotropic damage is achieved for $\vartheta = 1$ and the second term vanishes. Thus, for $\vartheta = 0$ we obtain

$$\psi_e(\boldsymbol{\varepsilon}, \boldsymbol{D}) = \frac{1}{2}(1-g)\lambda\mathrm{tr}^2(\boldsymbol{\varepsilon}) + \mu(\boldsymbol{I}-\boldsymbol{D}) : \boldsymbol{\varepsilon}^2. \tag{3}$$

The quadratic energy with the hardening parameter K_1 is given in Eq. (4). For anisotropic damage the additional hardening represented by Eq. (5) is a convex function of the eigenvalues D_i of the damage tensor with the property $f \rightarrow \infty$ for $D_i \rightarrow 1$. Eq. (5) ensures that the eigenvalues of the damage tensor do not exceed the value of 1.

$$\psi_h^\alpha(\alpha) = \frac{1}{2}K_1\,\alpha^2 \tag{4}$$

$$\psi_h^{\boldsymbol{D}}(\boldsymbol{D}) = \frac{1}{2}K_h^{\boldsymbol{D}} \sum_{i=1}^{3} f(D_i) \tag{5}$$

$$\tag{6}$$

By evaluating the second law of thermodynamics

$$\mathcal{D} = \boldsymbol{\sigma} : \dot{\boldsymbol{\varepsilon}} - \dot{\psi} = (\boldsymbol{\sigma} - \partial_{\boldsymbol{\varepsilon}}\psi_e) : \dot{\boldsymbol{\varepsilon}} - \partial_{\boldsymbol{D}}\psi : \dot{\boldsymbol{D}} - \partial_\alpha\psi \cdot \dot{\alpha} \geq 0 \tag{7}$$

the thermodynamically conjugate forces like the stress can be derived

$$\boldsymbol{\sigma} = \frac{\partial\psi}{\partial\boldsymbol{\varepsilon}} = \lambda(1-g)\mathrm{tr}\boldsymbol{\varepsilon}\boldsymbol{I} + \mu\big[(\boldsymbol{I}-\boldsymbol{D})\boldsymbol{\varepsilon} + \boldsymbol{\varepsilon}(\boldsymbol{I}-\boldsymbol{D})\big] \tag{8}$$

as well as the damage driving force $\boldsymbol{Y}$

$$\boldsymbol{Y} = -\frac{\partial\psi}{\partial\boldsymbol{D}} = -\frac{\partial\psi_e}{\partial\boldsymbol{D}} - \frac{\partial\psi_h}{\partial\boldsymbol{D}} = \boldsymbol{Y}_e - \boldsymbol{Y}_h \tag{9}$$

$$\boldsymbol{Y}_e = -\frac{\partial\psi_e}{\partial\boldsymbol{D}} = \frac{\lambda}{2}\mathrm{tr}\boldsymbol{\varepsilon}\boldsymbol{I} + \mu\boldsymbol{\varepsilon}^2 \tag{10}$$

$$\boldsymbol{Y}_h = \frac{\partial\psi_h}{\partial\boldsymbol{D}} = K_h^{\boldsymbol{D}} \sum_{i=1}^{3} f'(D_i)\,\boldsymbol{n}_i^D \otimes \boldsymbol{n}_i^D \tag{11}$$

which is split according to the free energy density function into an elastic and hardening part.
Introducing an initial damage threshold Y_0^c and the abbreviation $\beta = \frac{\partial\psi}{\partial\alpha} = \frac{\partial\psi_h}{\partial\alpha} = K_1\,\alpha$ the damage criterion reads:

$$\Phi = \underbrace{\|\boldsymbol{Y}_e - \boldsymbol{Y}_h\|}_{\boldsymbol{Y}} - (Y_0^c + \beta) \leq 0. \tag{12}$$

Then the following associative evolution equations for the internal variables are chosen

$$\dot{\boldsymbol{D}} = \dot{\lambda}\frac{\partial\Phi}{\partial\boldsymbol{Y}} = \dot{\lambda}\frac{\boldsymbol{Y}}{\|\boldsymbol{Y}\|}, \qquad \dot{\alpha} = -\dot{\lambda}\frac{\partial\Phi}{\partial\beta} = \dot{\lambda} \tag{13}$$

with the Kuhn-Tucker conditions

$$\dot{\lambda} \geq 0, \quad \Phi \leq 0, \quad \dot{\lambda}\Phi = 0. \tag{14}$$

2.2 Tension compression asymmetry

Tension compression asymmetry (TCA) is incorporated in this model as follows. The strain $\boldsymbol{\varepsilon}$ is split into a positive and negative part (compare to Ladeveze and Lemaitre (1984))

$$\boldsymbol{\varepsilon} = \boldsymbol{\varepsilon}^+ + \boldsymbol{\varepsilon}^-, \quad \mathrm{tr}(\boldsymbol{\varepsilon}) = \mathrm{tr}^+(\boldsymbol{\varepsilon}) + \mathrm{tr}^-(\boldsymbol{\varepsilon}) \tag{15}$$

$$\boldsymbol{\varepsilon}^+ = \sum_{i \in A} \varepsilon_i \boldsymbol{n}_i \otimes \boldsymbol{n}_i, \quad A = \{i : \varepsilon_i \geq 0\}, \quad \mathrm{tr}^+(\boldsymbol{\varepsilon}) = \langle\mathrm{tr}(\boldsymbol{\varepsilon})\rangle \tag{16}$$

$$\boldsymbol{\varepsilon}^- = \sum_{i \in B} \varepsilon_i \boldsymbol{n}_i \otimes \boldsymbol{n}_i, \quad B = \{i : \varepsilon_i < 0\}, \quad \mathrm{tr}^-(\boldsymbol{\varepsilon}) = -\langle-\mathrm{tr}(\boldsymbol{\varepsilon})\rangle. \tag{17}$$

Accordingly the elastic part of the free energy is also divided into a positive part, which is corresponding to tension, where damage is fully active and a negative part

$$\psi_e(\boldsymbol{\varepsilon}, \boldsymbol{D}) = \underbrace{\frac{\lambda}{2}(1-g)\,[\mathrm{tr}^+(\boldsymbol{\varepsilon})]^2 + \mu(\boldsymbol{I}-\boldsymbol{D}) : \boldsymbol{\varepsilon}_+^2}_{\psi_e^+} + \underbrace{\frac{\lambda}{2}(1-h_{tc}\,g)\,[\mathrm{tr}^-(\boldsymbol{\varepsilon})]^2 + \mu(\boldsymbol{I}-h_{tc}\,\boldsymbol{D}) : \boldsymbol{\varepsilon}_-^2}_{\psi_e^-}. \tag{18}$$

The material parameter h_{tc} controls the degree of tension compression asymmetry (TCA) within the material: For the choice $h_{tc} = 1$ the compression related part is damaged in an analogous manner to the tension related part (no crack-closure is considered). In contrast, the highest possible degree of TCA is achieved for $h_{tc} = 0$. For this case, the compression related part is not damaged at all.

2.3 Gradient extension: micromorphic approach

The gradient extension is realized by adding one additional scalar micromorphic field variable according to Forest (2009). The additional global field variable α_χ is the counterpart to the local variable α and causes additional terms in the internal virtual work

$$g_{\text{int}} = \int_B \boldsymbol{\sigma} : \nabla^s \delta \boldsymbol{u} \, \mathrm{dV} + \int_B \left(\beta_\chi \, \delta \alpha_\chi + \boldsymbol{\xi} \cdot \nabla \delta \alpha_\chi \right) \mathrm{dV} \tag{19}$$

$$g_{\text{ext}} = \int_B \boldsymbol{f} \cdot \delta \boldsymbol{u} \, \mathrm{dV} + \int_{\partial B_t} \bar{\boldsymbol{t}} \cdot \delta \boldsymbol{u} \, \mathrm{dA} \tag{20}$$

with the Cauchy stress tensor $\boldsymbol{\sigma}$, the generalized stresses β_χ and $\boldsymbol{\xi}$, body force $\boldsymbol{f}$ an the prescribed traction vector $\bar{\boldsymbol{t}}$ on the boundary ∂B_t. $\delta \boldsymbol{u}$ and $\delta \alpha_\chi$ are suitable test functions. The micromorphic extension is neglected in the external virtual work, as Eq. (20) shows. Making use of the principle of virtual work

$$g_{\text{int}} \overset{!}{=} g_{\text{ext}} \tag{21}$$

the equations of linear momentum balance are obtained in the standard way

$$\text{div}(\boldsymbol{\sigma}) + \boldsymbol{f} = \boldsymbol{0} \quad \text{in} \quad B \tag{22}$$

$$\boldsymbol{\sigma} \, \boldsymbol{n} = \bar{\boldsymbol{t}} \quad \text{on} \quad \partial B_t \tag{23}$$

$$\boldsymbol{u} = \bar{\boldsymbol{u}} \quad \text{on} \quad \partial B_u. \tag{24}$$

For the additional field variable the micromorphic balance equation and the corresponding Neumann boundary condition on ∂B_Ξ are

$$\text{div}(\boldsymbol{\xi}) - \beta_\chi = 0 \quad \text{in} \quad B \tag{25}$$

$$\bar{\Xi} = \boldsymbol{\xi} \cdot \boldsymbol{n} = 0 \quad \text{on} \quad \partial B_\Xi. \tag{26}$$

In addition, the free energy of the local from Eq. (1) has to be extended by an additional micromorphic energy, which consists of two parts

$$\psi_{\text{micr}} = \frac{1}{2} H_\chi \, (\alpha_\chi - \alpha)^2 \; + \; \frac{1}{2} E l^2 \, \nabla \alpha_\chi \cdot \nabla \alpha_\chi. \tag{27}$$

The first part of Eq. (27) acts as a penalty energy which forces the micromorphic field variable α_χ to be as close as possible to the local variable α with the penalty parameter H_χ. The second part takes into account the energy stored by the gradiend of the micromorphic field variable α_χ.

With the additionally introduced micromorphic energy the expressions for the generalized stresses can then be derived

$$\beta_\chi = \frac{\partial \psi}{\partial \alpha_\chi} = H_\chi(\alpha_\chi - \alpha), \quad \boldsymbol{\xi} = \frac{\partial \psi}{\partial \nabla \alpha_\chi} = E l^2 \nabla \alpha_\chi. \tag{28}$$

3 Application and numerical results

Fassin et al. (2019a) showed that isotropic and anisotropic damage models yield to the same result if no diffusive damage occurs. Since this work focuses on the modeling of crack formation as shown in Fig. 1 and no diffusive damage.
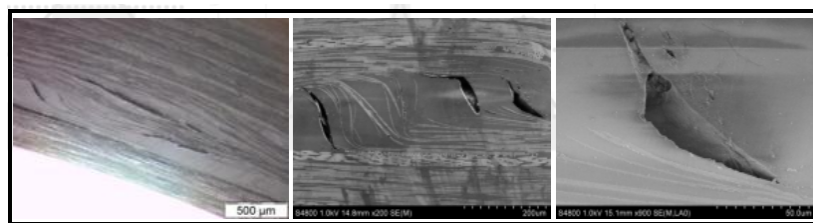
Fig. 1: Crack formations in the matrix material.

It is sufficient to make use of the simplified gradient-extended isotropic damage model for the simulations of the epoxy matrix on the microlevel.

3.1 1-D isotropic damage

In order to identify relevant material parameters from the more classical fracture mechanic theory like the strain energy release rate or stress at fracture, the first variation of the free energy functional with respect to D (Eq. (29)-(31)) provides the essential criteria. The procedure is similar to Francfort and Marigo (1998), Bourdin et al. (2008) and Pham et al. (2011).
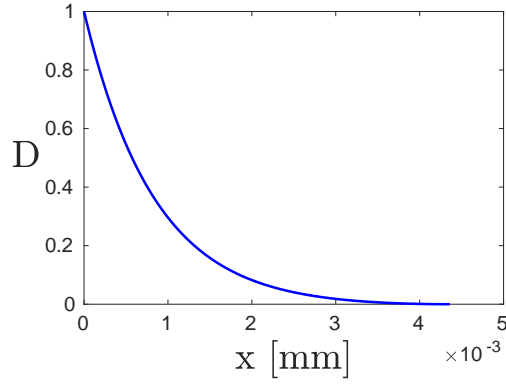
Fig. 2: Solution for D.

With the evaluation of Eq. (29) the strain energy release rate G_c can be formulated dependent on the internal length l, which controls the thickness of the damage localization zone.

$$\delta_D \int_V \psi \mathrm{d}V = 0 \rightarrow \quad \dots \quad \frac{\mathrm{d}E}{\mathrm{d}A} = \sqrt{2E}\, 2l \int_0^1 \sqrt{w(D)}\mathrm{d}D = G_c \tag{29}$$

$$\psi = w(D) + \tfrac{1}{2}El^2 \nabla D \cdot \nabla D \tag{30}$$

$$w(D) = Y_0^c D + \tfrac{1}{2}K_1 D^2 \tag{31}$$

The damage criterion provides a useful criterion for the stress at fracture σ_c which is corresponding to the damage threshold Y_0^c.

$$\Phi = 0 \rightarrow \quad \psi_0(\varepsilon) = Y_0^c \quad \rightarrow \sqrt{2E\,Y_0^c} = \sigma_c \tag{32}$$

$$Y_0^c + K_1 D - El^2 D'' = 0 \quad \text{with} \quad D(x_0) = D'(x_0) = 0. \tag{33}$$

The solution of Eq. (33) is plotted in Fig. 2. $2x_0$ represents the whole crack width or rather the thickness of the damage localization zone. Thus, the strain energy release rate G_c, stress at fracture σ_c and the crack width x_0 can be controlled at the same time.

3.2   Unit cell simulations with variations of the fracture toughness

As numerical example a quadratic unit cell with 60% fiber and 2% pore volume fraction is considered (see Fig. 3). Periodic boundary conditions are defined. It is noted that the unit cell can't be considered as statistically representative. The material parameters are set such that no damage will occurs in the fiber material with E=220000 N/mm^2, v=0.2, Y_0^c=∞ Nmm/mm. For the matrix material the parameters E=3000 N/mm^2, v=0.3, K_1=100.0 Nmm/mm^3, H_χ=10^6 Nmm/mm^3, l=1.5552 · 10^{-4} mm, Y_0^c=1.1258 Nmm/mm^3 are used.

0.02 mm

0.02 mm
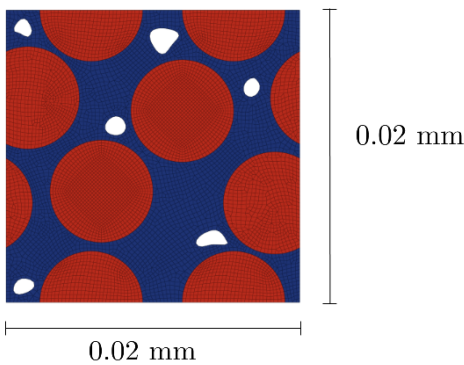
Fig. 3: Unit cell geometry.

0%   4%   8%   12%
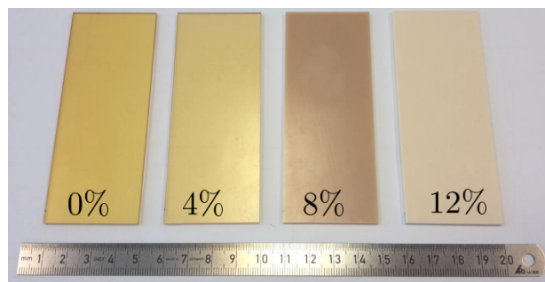
Fig. 4: Specimen with variation of CSR particles.

In this first example the variation of the fracture toughness is shown. In reality, soft and elastic Core-Shell-Rubber particles (CSR) are embedded in the epoxy matrix. With increasing volume fraction of CSR particles (Fig. 4) the fracture toughness increases and the limit stress σ_c decreases. The new material parameters in Tab. 1 for varying CSR volume fraction are identified with the criteria of subsection 3.1.

The limit stress σ_c is decreasing for increasing CSR fraction. With Eq. (32) the initial damage threshold (the last column of Tab. 1) has to decrease, in analogy. The crack width x_0 for the given geometry in Fig. 3 remains constant.

The average stress over the average strain is plotted for the load case $\varepsilon_{yy} > 0$ for each CSR variation in Fig. 5 and shows the increasing maximum stress for increasing matrix fracture toughness.

Tab. 1: List of material parameters for matrix material with varying CSR volume fraction.

CSR	E [N/mm^2]	K_1 [Nmm/mm^3]	l [mm]	Y_0^c [Nmm/mm^3]
0%	3000	100.0	1.5552e-04	1.1258
4%	2752	200.0	1.9877e-04	0.9419
8%	2604	300.0	2.1169e-04	0.8619
12%	2440	350.0	2.2885e-04	0.8133
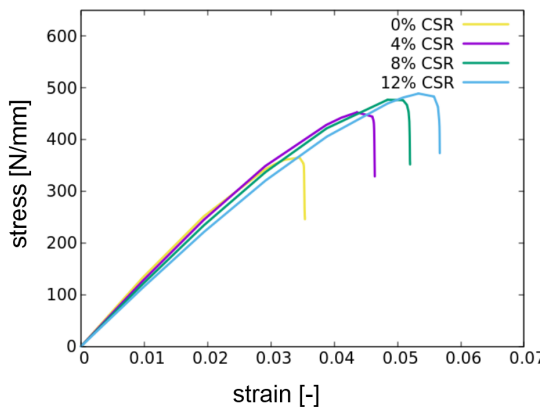
Fig. 5: Average stress over average strain for varying CSR volume fraction.
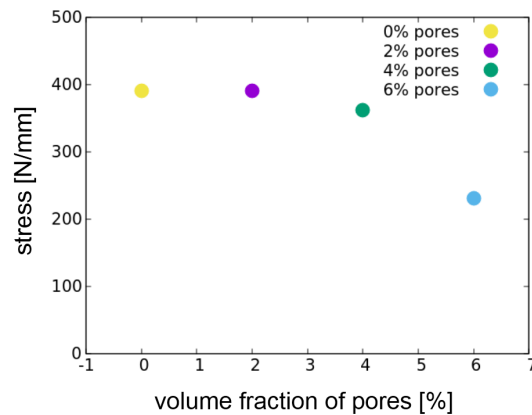
Fig. 6: Maximum average stress over pore volume fraction.

In this case, the conventional scale transition criteria aren't satisfied, i.e., the depicted behavior is related to the unit cell (not the composite) and thus only qualitative. While the Young's modulus for the matrix material is decreasing (second column in Tab. 1) and the fracture toughness which is corresponding to the energy release rate G_c is increasing, it is reasonable that the maximum average stress of the unit cell increases, too.

3.3 Unit cell simulations with variations of pore volume

In the next numerical example the volume fraction of pores is modified with 0%, 2%, 4% and 6%. The initial material parameter set is taken from subsection 3.2 for the matrix material without incorporation of CSR particles (0% CSR volume fraction). Geometry, fiber volume fraction as well as fiber material parameters stay the same.

Representing only first qualitative observations these UC simulations show that with increasing volume fraction of pores the average maximum stress is decreasing, which is visualized in Fig. 6. Crack initiation starts in the matrix material near a pore and propagates along the interface, but does not pass through the rubber particles.

Furthermore Fig. 6 emphasizes that 2% volume fraction of pores does not have a remarkable influence on the maximum average stress. This is different between 4% and 6% volume fraction where a bigger difference of the average stress is noticeable. This observation has to be investigated with using more representative unit cells.

4 Conclusion

In the present work, an anisotropic gradient-extended brittle damage framework of Fassin et al. (2019a) was presented. In addition, the model enables tension compression asymmetry (crack-closure) extension recently published in Fassin et al. (2019b). The numerical examples make use of the simplification of the model to isotropic damage.

The two numerical examples of unit cell simulations, where first the fracture toughness and second the pore volume fraction was varied, were shown. Both results demonstrate reasonable overall response. Though for statistical representation more unit cell simulations have to be done considering bigger unit cells. For the purpose of investigation of the performance of carbon reinforced epoxy resin the next (macro) scale has to consider anisotropic damage with crack-closure consideration for a more realistic material response.

Acknowledgment and Funding Information

References

B. Bourdin, G. A. Francfort, and J.-J. Marigo. The variational approach to fracture. *Journal of elasticity*, 91(1-3):5–148, 2008.

M. Fassin, R. Eggersmann, S. Wulfinghoff, and S. Reese. Efficient algorithmic incorporation of tension compression asymmetry into an anisotropic damage model. *Computer Methods in Applied Mechanics and Engineering*, 2019b.

M. Fassin, R. Eggersmann, S. Wulfinghoff, and S. Reese. Gradient-extended anisotropic brittle damage modeling using a second order damage tensor–theory, implementation and numerical examples. *International Journal of Solids and Structures*, 167: 93–126, 2019a.

S. Forest. Micromorphic approach for gradient elasticity, viscoplasticity, and damage. *Journal of Engineering Mechanics*, 135 (3):117–131, 2009.

G. A. Francfort and J.-J. Marigo. Revisiting brittle fracture as an energy minimization problem. *Journal of the Mechanics and Physics of Solids*, 46(8):1319–1342, 1998.

P. Ladeveze and J. Lemaitre. Damage effective stress in quasi unilateral conditions. In *16th International congress of theoretical and applied mechanics, Lyngby, Denmark*, 1984.

K. Pham, H. Amor, J.-J. Marigo, and C. Maurini. Gradient damage models and their use to approximate brittle fracture. *International Journal of Damage Mechanics*, 20(4):618–652, 2011.

Development of a thermomechanically coupled damage approach for modeling woven ceramic matrix composites

Marie-Christine Reuvers[1]⋆, Shahed Rezaei[1], Tim Brepols[1] and Stefanie Reese[1]

[1] RWTH Aachen University, Institute of Applied Mechanics, Mies-van-der-Rohe-Str. 1, 52074 Aachen, Germany

Abstract: Ceramic matrix composites (CMCs) as an enhancement of classical technical ceramics overcome limitations such as low fracture toughness and brittle failure under mechanical or thermomechanical loading. Their low weight and high temperature stability makes them attractive for use in various fields, especially aerospace industry, where they improve engine efficiency as substitutions for metal components. Despite their positive attributes current CMCs lack well established material property design databases for a reliable use in critical aerospace structures. Demonstrating the durability and lifespan of this relatively new class of materials is the present task. Therefore their failure mechanisms need to be investigated further, taking into account the extensive range of temperatures the components are subjected to. This contribution deals with the successive development of a woven representative volume element (RVE) for arbitrary CMCs. In contrast to previously developed approaches, the introduced model combines various damage formulations. The fiber bridging effect is governed using a cohesive zone (CZ) formulation to adress the debonding mechanism in the weak interface between matrix and reinforcement and a continuum mechanical approach to account for matrix damage. To cover the temperature dependency of the material parameters, thermal coupling is included in both element formulations.

Keywords: CMC, RVE, cohesive zone, continuum damage, composites, woven

1 Introduction

Materials in aerospace engines are exposed to high temperatures, oxidizing environments and have to withstand numerous load cycles during their lifetime. Until now most of the engines components are made out of metal alloys which have a rather short lifespan. Current research therefore focuses on the development of a new class of materials to replace these metal components with ceramics to increase temperature resistace and lifetime under high cyclic loading while reducing weight at the same time. Ceramics are inorganic materials with a high service temperature and elastic modulus. They are designed to be corrosion resistant and lightweight, however ceramics have a very low crack resistance and are therefore considered brittle materials see Krenkel (2008), Chawla (2013). To increase fracture thoughness classic ceramic matrices are improved with a reinforcement. Ceramic matrix composites (CMCs) make up a rather new class of engineered ceramic materials, consisting of matrix and fiber reinforcement. The fibers, produced as fiber bundles or so called toes, are often manufactured as a woven mesh to form 2D or 3D composites. Characteristically CMC components often consist of the same or similar materials for example silicon carbide(SiC/SiC) or aluminium oxide (Ox/Ox). Depending on the presence of oxygen, CMCs are categorized into non-oxide (NO-CMC) or oxide (O-CMC) materials. NO-CMCs have a higher temperature resistance, whereas O-CMCs are more corrosion resistant. To compensate for the low corrosion resistance, fibers of non-oxide ceramics are coated with boron nitride (BN), forming an interphase between fiber and matrix Bansal (2006). In order to increase the fracture toughness of the ceramic with the reinforced fibers, the interface between the two compounds is the deciding factor. A weak interface is desirable to achieve a separation between matrix and fiber in the case of damage. During failure, cracks will first form in the ceramic matrix of the composites and propagate through the material. Once a fiber-matrix interface is reached, the crack will deflect there, starting a separation process between the two components. Undamaged fibers remain, briding the open crack. In the case of ultimate failure, the fibers start to slide along the matrix adding an additional fracture mechanism to the otherwise brittle material which results in a pseudo-plastic material response Evans and Zok (1994). If the fibers are coated, the interphase works as a protective layer. With a material fracture energy lower than the interface resistance between fiber and coating, the crack is supposed to deflect in the interphase, leaving a thin film of coating to the fibers to ensure corrosion resistance Bansal and Lamon (2014). Due to production processes to the authors best knowledge to this day it is not possible to produce a strong fiber-coating interface with BN, therefore a crack will lead to debonding between fiber and coating Rebillat et al. (2000a). Under temperature the maximum strength of CMCs decreases due to material degradation, resulting in a lower Young's modulus and a softened material response Bansal (2006). In addition the location of the deflecting crack in coated CMCs is shown to shift to the matrix-coating interface, due to changes in the BN maximum strength Trice and Halloran (1999), Guo and Kagawa (2001).

On the numerical side brittle fracture has been modeled by many authors using cohesive elements. For example Samimi et al. (2009, 2011) has developed a CZ formulation to acount for delamination in brittle interfaces, using an effective separation law. Rezaei et al. (2017) extended the formulation to predict fracture in micro/nano coating systems between grain boundaries and also simulated plastic behavior between multiple grains by using molecular dynamics (MD) simulations to calculate the

traction-separation-law (t-s-law) Rezaei et al. (2019). The inclusion of fiber briding has been investigated for example by Höwer et al. (2018) in the case of delaminating sandwich panels. To compare experimimental results for SiC/SiC material to numerical simulations Kumar and Welsh (2012); Kumar (2013) investigated the failure mechanisms between but also within plies and extended the CZ formulation to include fiber bridging for more accurate results Kumar (2017); Kumar et al. (2018). Mital et al. (2009) studied different methods to efficiently determine the elastic properties of melt-infiltrated (MI) SiC/SiC composites using multiscale laminate analysis, finite element analysis etc..Chaboche and Maire (2002) developed a micromechanics bases continuum damage model including second order tensor while Marcin et al. (2011) adressed the woven characteristics of CMCs with a macroscopic damage model using inetrnal variables. A general overview of modeling schemes for the damage mechanisms of CMCs at multiple scales, can be found in Baranger (2017). Experimental data for different SiC/SiC composites and scales under room and elevated temperatures can be found for example in Rebillat et al. (2000b), Guo and Kagawa (2001), Hinoki et al. (2003) and Morscher (2010). The influence of thermal loading on interface fracture has also been studied by various authors. E.g.Dandekar and Shin (2011) included a temperature dependence in the traction-separation-law, acounting for a softer interface response under temperature using MD simulations to parametrize the t-s-law. To investigate the evolving heat transfer through interfaces Hattiangadi and Siegmund (2004) introduced a temperature jump in the cohesive formulation modeling fiber bridging under bending and buckling deformation. Özdemir et al. (2010) also included fiber briding as well as a damage dependend heat flux to simulate crack closure and Wu and Wriggers (2015) took up the idea to model the influence of the transition zone between cement paste and aggregates on the thermal properties of concrete. Quasi brittle crack propagation in a thermo-hyperelastic material including heat generation within the cohesive zone due to the fracture process is simulated by Fagerström and Larsson (2008) including a discontinous heat flux across the interface. Focussing on the time evolution of displacement and temperature fields before debonding Paggi and Sapora (2013), Sapora and Paggi (2014) established a coupled model formulation in analogy to contact mechanics between rough surfaces for photovoltaics.

In this work a material model combining various damage formulations based on Rezaei et al. (2017) and Brepols et al. (2017) is established, to model the characteristic failure mechanisms in CMC. Unlike existing modeling approaches for CMC failure behavior in this formulation a cohesive zone model is combinded with a gradient extended continuum damage model to take various damage mechanisms of CMC (e.g. matrix cracking, interface debonding) into account. The model is then extended to include thermal phenomena, as for example the decrease of interface resistance under thermal loading as well as the heat flux across the interface and then tested in different numerical examples.

2 Modeling Approach

2.1 Cohesive Zone

Mechanical Problem Separation at the fiber-matrix interface is modeled using a cohesive zone formulation based on the work of Geubelle and Baylor (1998), Ortiz and Pandolfi (1999) and Rezaei et al. (2017) with a bilinear traction-separation-law. Two bodies B_t^+ and B_t^- are considered in 2D which are connected by a cohesive region see Fig.1. The Helmholtz free mechanical energy is defined as

$$\psi_{cz}(g_s, g_n) = \frac{1}{2}(1-d)k_0\lambda^2 + \frac{1}{2}k_p\langle -g_n\rangle^2, \tag{1}$$

where $\lambda = \sqrt{\langle g_n\rangle^2 + \beta^2 g_s^2}$ describes the effective separation of the cohesive zone, which depends on the gap in normal g_n and shear g_s direction. The amount of shear contribution is controlled via the parameter β to consider materials with anisotropic damage behavior. the influence on the traction can be seen in Fig.1. Further material parameters are k_0 which can be interpreted as the undamaged stiffness of the cohesive zone. To prevent penetration of the two bodies, if the normal gap becomes negativ ($g_n < 0$), a penalty term is introduced, depending on the penalty parameter k_p. Analogously to the gap the traction vector $\boldsymbol{t}$ is decomposed into a normal t_n and a shear traction t_s and follows to

$$\boldsymbol{t} = \begin{cases} t_n &= \partial_{g_n}\psi_{cz} &= (1-d)k_0\langle g_n\rangle - k_p\langle -g_n\rangle \\ t_s &= \partial_{g_s}\psi_{cz} &= (1-d)k_0 g_s\beta^2. \end{cases} \tag{2}$$

Similarly an effective traction t can be defined as

$$t = \partial_\lambda\psi_{cz} = \sqrt{t_n^2 + \beta^{-2}t_s^2} = (1-d)k_0\lambda. \tag{3}$$

The damage parameter d is chosen to follow the softening-behavior of the bilinear traction-separation law see Fig.2 and follows to

$$d = \begin{cases} 0 & \text{if } \lambda < \lambda_0 \\ \dfrac{\lambda_f}{\lambda_f - \lambda_0}\dfrac{\lambda - \lambda_0}{\lambda} & \text{if } \lambda_0 < \lambda < \lambda_f \\ 1 & \text{if } \lambda_f < \lambda. \end{cases} \tag{4}$$

If the maximum strength t_0 is reached at the corresponding amount of separation (λ_0), the cohesive zone starts to fail. The damage now develops nonlinearly until the maximum elongation λ_f is reached. Via Integration of the traction-separation-law the fracture energy

$$G_c = 0.5 t_0\lambda_f \tag{5}$$
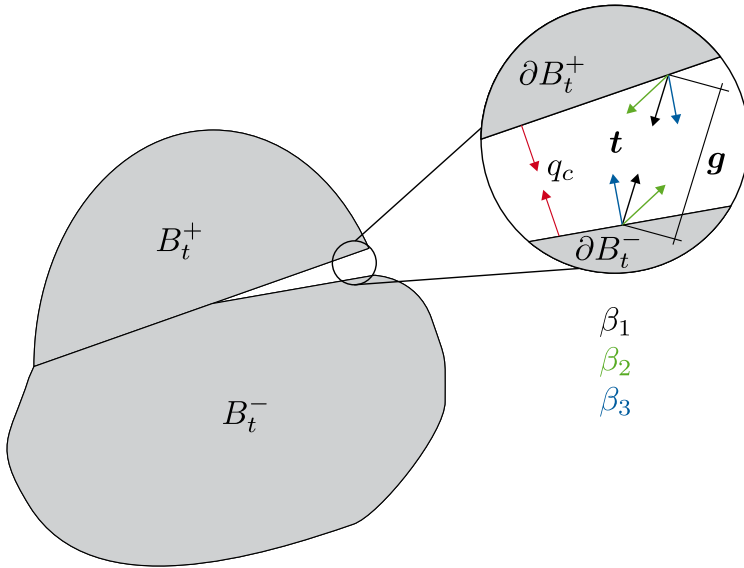
Fig. 1: Separation of two bodies. Gap and traction vectors for different parameters β.
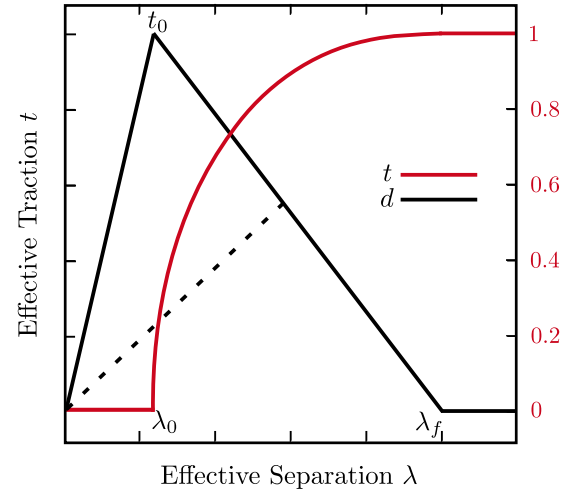
Fig. 2: Effective traction t over effective separation λ and damage evolution.

can be determinded, which serves as an important material parameter for the characterization of the overall interface resistance.

Thermal Problem Ideally there is no temperature jump and no thermal flux jump when two bodies of different materials are assumed to be bonded perfectly. However in reality a perfectly bonded interface doesn't exist, due to either pre-existing microcracks or imperfections as for example pores at the interface or the debonding induced by external loads. Therefore in this application a lowly-conducting interface is assumed, allowing for a jump of the temperature based on the Kapitza assumption (Sapora and Paggi (2014)).
In anaolgy to the work of Özdemir et al. (2010) and Wu and Wriggers (2015) a temperature jump g_θ in normal direction is introduced to the gap (see Fig. 1). Taking into account only stationary problems a heat flux

$$q_c = -((1 - d_c^\theta)k_s + k_a)g_\theta \tag{6}$$

is introduced through Fourier's law, depending on the heat conductivity of the solid phase k_s and the heat conductivity of air k_a. d_c^θ is a thermal damage variable for illustrating the progressive thermal resistance due to interface cracking

$$d_c^\theta = \begin{cases} \dfrac{\lambda}{\lambda_f} & \text{if } \lambda < \lambda_f \\ 1 & \text{if } \lambda_f < \lambda. \end{cases} \tag{7}$$

It starts to develop linearly even before the formation of the main interface crack to take into account the effect of microcracks forming in the elastic regime of the cohesive zone. Due to limited available data on the thermal behavior of the closing surfaces, the thermal model in this research stage does not consider crack closure. In addition to conduction, temperature has also been shown to have an influence on the material parameters of CMCs interfaces (see Trice and Halloran (1999) and Guo and Kagawa (2001)). To capture the softening behavior of the interface restistance in CMCs under temperature loading the Helmholtz free mechanical energy of the cohesive zone is extended with a temperature softening term

$$\psi_{cz}(g_s, g_n, \theta_m) = \frac{1}{2}(1 - d)k_0(1 - c_c\theta_m)\lambda^2 + \frac{1}{2}k_p\langle-g_n\rangle^2, \tag{8}$$

depending on a temperature softening parameter c_c which has to be determined experimentally, as well as the mid-temperature of the cohesive zone θ_m. The effective traction then follows to

$$t = \partial_\lambda\psi_{cz} = (1 - d)k_0(1 - c_c\theta_m)\lambda. \tag{9}$$

Thermal effects like heat radiation and convection are neglected at this stage of the model development and the model formulation is only valid for service temperatures.

2.2 Bulk Material

To model damage in the matrix material, an elastic gradient-extended damage formulation based on a more general model by Brepols et al. (2017, 2018) is used. The formulation of Brepols et al. (2017, 2018) also takes plasticity into account which is neglected in this work due to the brittle material behavior. The free energy

$$\psi = (1 - D)^2\psi_e(\boldsymbol{\varepsilon}_e) + \psi_d(\xi_d) + \psi_{\bar{d}}(D - \bar{D}, \nabla\bar{D}) \tag{10}$$

61

M. Reuvers, S. Rezaei, T. Brepols and S. Reese

Tech. Mech., Vol. 40, Is. 1, (2020), 59–65
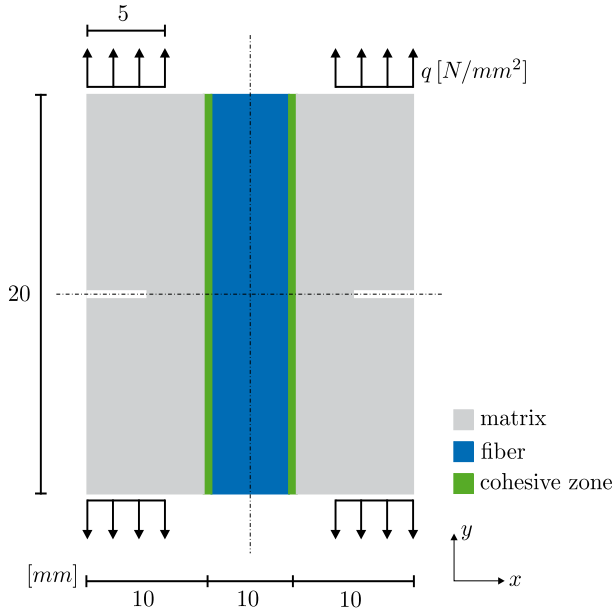
Fig. 3: Mechanical model
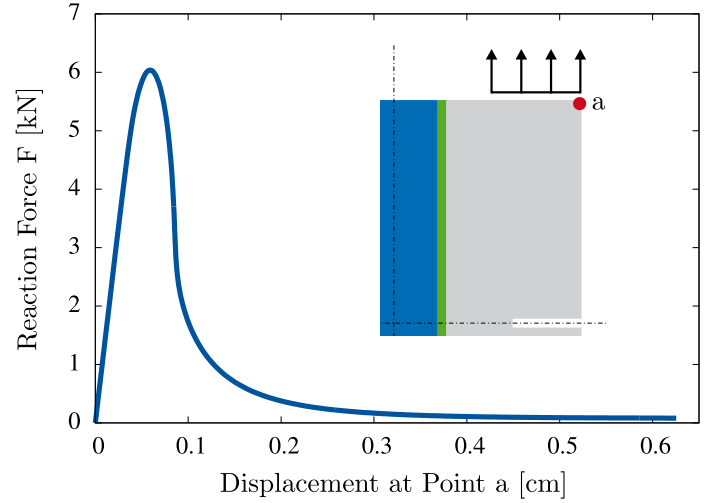
Fig. 4: Force-displacement curve in load-direction

is decomposed into three parts, the first being the elastic energy $\psi_e = \frac{1}{2}\varepsilon_e \cdot \mathbb{C}[\varepsilon_e]$. A damage hardening term $\psi_d = r\left(\xi_d + \frac{\exp(-s\xi_d)-1}{s}\right)$, depending on the damage material parameters r and s is introduced as well as a micromorphic extension $\psi_{\bar{d}} = \frac{A}{2}\nabla\bar{D} \cdot \nabla\bar{D} + \frac{H}{2}(D-\bar{D})^2$, depending on the micromorphic damage $\bar{D}$, its first gradient and the penalty parameter H as well as the parameter A, that implicitly introduces an 'internal material length', to achieve mesh independent results (see Forest (2009)). For a detailed model description the reader is referred to Brepols et al. (2017, 2018).

3 Numerical Examples

3.1 Crack deflection at the interface

A pre-cracked matrix (length of the notch = 2.5mm), reinforced with a single fiber on microlevel is modeled in the finite element program FEAP, using hexahedral cohesive zone elements with linear shape functions at the interface (see Fig. 3). Due to its minimal thickness, the coating is neglected during simulation, its effect is however modeled in the cohesive zone. In order to proof that the fiber is being spared during the interface separation process, both fiber and matrix are simulated as bulk material. In Table 1 and 2 the arbitrarily chosen material parameters for the presented example are displayed seperately for the two element formulations, with Λ and μ being the Lamé constants and Y_0 the onset of damage. Throughout the plane strain simulation the load is controlled by means of the arclength method, only one half of the structure (4880 elements) is plotted (due to symmetry).

Tab. 1: Cohesive zone material parameters

$\lambda_0\,[\mu m]$	$t_0\,[MPa]$	$\beta[-]$	$\lambda_f\,[\mu m]$	$k_p[-]$
0.5	1.0	0.5	10	100

Tab. 2: Matrix and fiber material parameters

Λ [MPa]	μ [MPa]	Y_0 [MPa]	A [MPamm^2]	H [MPa]	r [$-$]	s [MPa]
5000	7500	0.1	10	10^5	0.5	0.1

During the simulation it can be seen in reaction force-displacement-curve (see Fig. 4) and the damage plots (see Fig. 5), that the crack evolves at the notch of the pre-crack where the stress concentrates. The crack then propagates along the matrix until it reaches the interface. As soon as the maximum traction of the cohesive elements at the interface is exeeded, the crack deflects now gradually separating the two components, fiber and matrix from each other. It can be demonstrated, that the fiber remains undamaged during the whole simulation. Since the material parameters are arbitrarily chosen, the resulting reaction force-displacement curve in Fig. 4 does not reflect the actual brittle material behavior. However the intention of the example in modeling crack deflection at the interface by the combination of different damage models is fullfilled.

3.2 Interface resistance under temperature

As a second example the interface resistance under temperature influence is simulated in the finite element program FEAP via a double cantilever beam (DCB). On the mesoscale the two bulk materials, modeled using standard thermomechanically coupled,

$F = 5.9218$　　　$F = 5.601$　　　$F = 4.0459$

$F = 1.9877$　　　$F = 0.3991$　　　$F = 0.0807$
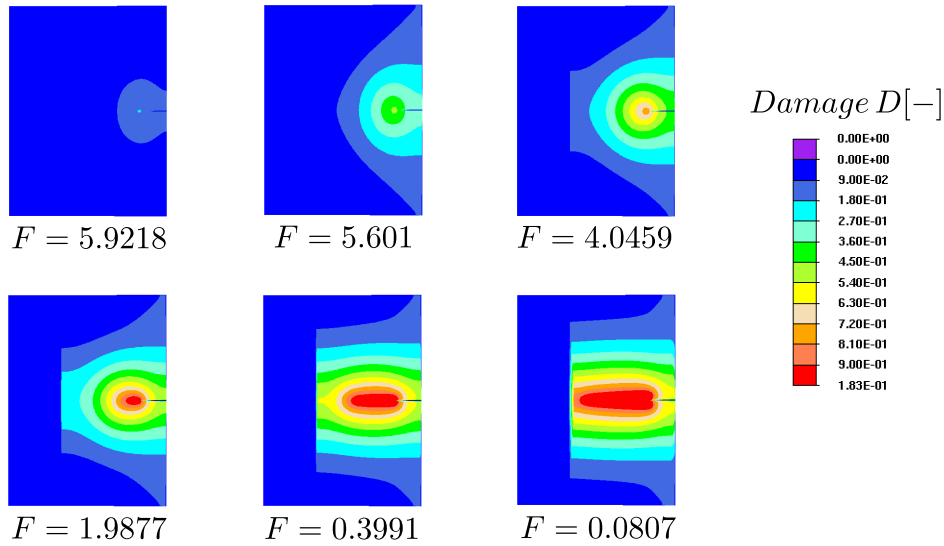
Fig. 5: Damage evolution at the notch

linear elastic FEAP elements, represent CMC plies, each consisting of matrix, coating and reinforcement. The interface between those plies is modeled using a layer of cohesive elements. The dimensions as well as the boundary conditions for the problem can be found in Fig. 6 and Table 3 and 4. At the beginning of the plane strain simulation the body is heated up to a constant temperature between $0°C$ and $500°C$. Then holding the temperature constant, the displacement is applied linearly over time, separating the two plies.

The reaction force at the loading point over the corresponding displacement is displayed in Fig. 7. One can observe a decrease in the maximum force with increasing temperature, which can be explained in accordance to Dandekar and Shin (2011) by an overall reduced interface resistance between the plies. In addition at higher temperatures the failure starts earlier due to the degradation of the interface characteristics.
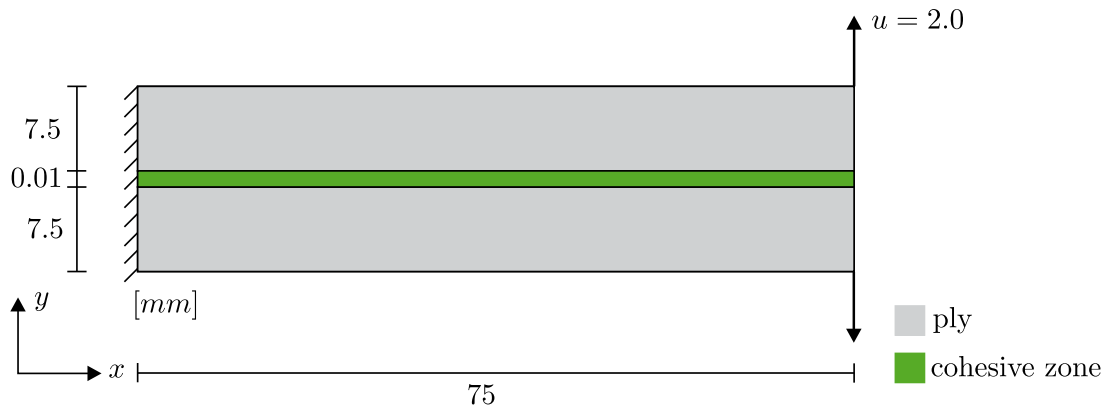
Fig. 6: Double Cantilever beam under thermal and mechanical loading.

Tab. 3: Thermal cohesive zone parameters

λ_0 [μm]	t_0 [MPa]	β[−]	λ_f [μm]	k_p[−]	k_c [W/mK]	k_a [W/mK]	c_c [1/K]
0.5	1.0	0.5	10	100	9.8	0.0262	0.001

Tab. 4: Thermal bulk material parameters

E [MPa]	ν [−]	α_T [1/K]	k [W/mK]	c [J/kgK]
380	0.2	0	9.8	0

4　Conclusion and outlook

A new strategy for modeling the different damage mechanisms in ceramic matrix composites is presented and tested at different material levels. With the combination of cohesive elements for brittle interface fracture and a continuum damage formulation for elastic materials it can be shown that the model is able to capture both, matrix cracking as well as the characteristic crack deflection at the fiber/matrix interface. The model formulation is then extended to include thermal effects, showing a decrease in interface resistance under elevated temperatures. In addition the effect of an earlier damage initiation due to material degradation is captured nicely in the simulation.
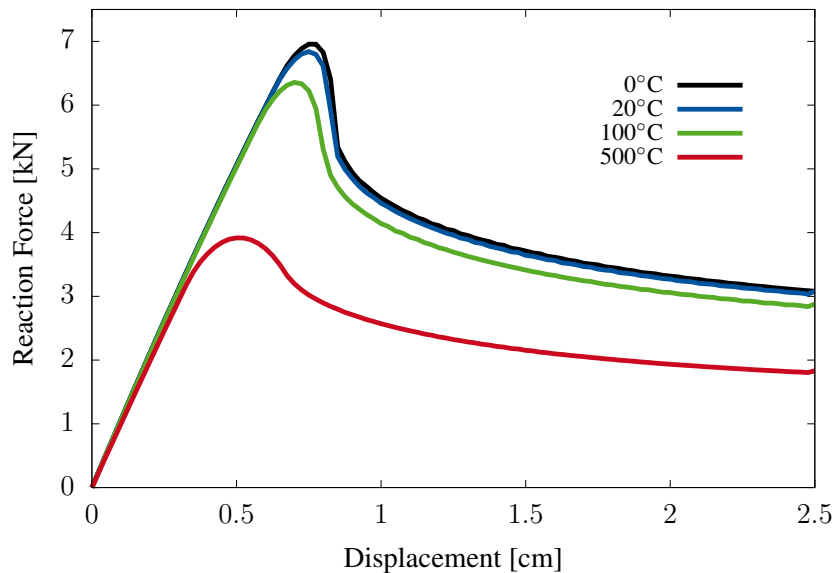
Fig. 7: Force-displacement curve of DCB under constant temperatures.

As the cohesive zone formulation in this work only includes a temperature dependence of the material stiffness, for future applications other material parameters who are shown to change significantly under temperature (e.g. thermal conductivity of solid or gaseous phase) will be thermocoupled. Furthermore the interface model at this point does not contain fiber briding in mechanical or thermal form. The formulation will be extendend thereby, introducing an additional heat flux in tangential direction to account for fibers with arbitrary directions and also the continuum damage model will be extended to include thermal effects. In addition there is a need to determine accurate material parameters for the interface to compare the simulation results to realistic experimental data. To simulate the real material behavior the formulation will then be extended to 3D to model woven material structures, characteristically for CMCs.

References

N. P. Bansal. *Handbook of ceramic composites*, volume 200. Springer Science & Business Media, 2006.

N. P. Bansal and J. Lamon. *Ceramic matrix composites: materials, modeling and technology*. John Wiley & Sons, 2014.

E. Baranger. *Modeling Mechanical Behavior of Ceramic Matrix Composites*. 12 2017. ISBN 9780128035818. doi: 10.1016/B978-0-12-803581-8.09993-8.

T. Brepols, S. Wulfinghoff, and S. Reese. Gradient-extended two-surface damage-plasticity: micromorphic formulation and numerical aspects. *International Journal of Plasticity*, 97:64–106, 2017.

T. Brepols, S. Wulfinghoff, and S. Reese. A micromorphic damage-plasticity model to counteract mesh dependence in finite element simulations involving material softening. In *Multiscale Modeling of Heterogeneous Structures*, pages 235–255. Springer, 2018.

J.-L. Chaboche and J.-F. Maire. A new micromechanics based cdm model and its application to cmc's. *Aerospace Science and Technology*, 6(2):131–145, 2002.

K. K. Chawla. *Ceramic matrix composites*. Springer Science & Business Media, 2013.

C. R. Dandekar and Y. C. Shin. Molecular dynamics based cohesive zone law for describing al–sic interface mechanics. *Composites Part A: Applied Science and Manufacturing*, 42(4):355–363, 2011.

A.G. Evans and F.W. Zok. The physics and mechanics of fibre-reinforced brittle matrix composites. *Journal of Materials science*, 29(15):3857–3896, 1994.

M. Fagerström and R. Larsson. A thermo-mechanical cohesive zone formulation for ductile fracture. *Journal of the Mechanics and Physics of Solids*, 56(10):3037–3058, 2008.

S. Forest. Micromorphic approach for gradient elasticity, viscoplasticity, and damage. *Journal of Engineering Mechanics*, 135 (3):117–131, 2009.

Philippe H Geubelle and Jeffrey S Baylor. Impact-induced delamination of composites: a 2d simulation. *Composites Part B: Engineering*, 29(5):589–602, 1998.

S. Guo and Y. Kagawa. Temperature dependence of tensile strength for a woven boron-nitride-coated hi-nicalon sic fiber-reinforced silicon-carbide-matrix composite. *Journal of the American Ceramic Society*, 84(9):2079–2085, 2001.

A. Hattiangadi and T. Siegmund. A thermomechanical cohesive zone model for bridged delamination cracks. *Journal of the Mechanics and Physics of Solids*, 52(3):533–566, 2004.

M. Reuvers, S. Rezaei, T. Brepols and S. Reese

Tech. Mech., Vol. 40, Is. 1, (2020), 59–65

T. Hinoki, E. Lara-Curzio, and L. L. Snead. Mechanical properties of high purity sic fiber-reinforced cvi-sic matrix composites. *Fusion science and technology*, 44(1):211–218, 2003.

D. Höwer, B. A. Lerch, B. A. Bednarcyk, E. J. Pineda, S. Reese, and J.-W. Simon. Cohesive zone modeling for mode i facesheet to core delamination of sandwich panels accounting for fiber bridging. *Composite Structures*, 183:568–581, 2018.

W. Krenkel. *Ceramic matrix composites: fiber reinforced ceramics and their applications*. John Wiley & Sons, 2008.

R. S. Kumar. Analysis of coupled ply damage and delamination failure processes in ceramic matrix composites. *Acta materialia*, 61(10):3535–3548, 2013.

R. S. Kumar. Crack-growth resistance behavior of mode-i delamination in ceramic matrix composites. *Acta Materialia*, 131: 511–522, 2017.

R. S. Kumar and G. S. Welsh. Delamination failure in ceramic matrix composites: Numerical predictions and experiments. *Acta Materialia*, 60(6-7):2886–2900, 2012.

R. S. Kumar, M. Mordasky, and G. Ojard. Delamination fracture in ceramic matrix composites: From coupons to components. In *ASME Turbo Expo 2018: Turbomachinery Technical Conference and Exposition*, pages V006T02A003–V006T02A003. American Society of Mechanical Engineers, 2018.

L. Marcin, J.-F. Maire, N. Carrère, and E. Martin. Development of a macroscopic damage model for woven ceramic matrix composites. *International Journal of Damage Mechanics*, 20(6):939–957, 2011.

S. K. Mital, B. A. Bednarcyk, S. M. Arnold, and J. Lang. Modeling of melt-infiltrated sic/sic composite properties. 2009.

G. N. Morscher. Tensile creep and rupture of 2d-woven sic/sic composites for high temperature applications. *Journal of the European Ceramic Society*, 30(11):2209–2221, 2010.

Michael Ortiz and Anna Pandolfi. Finite-deformation irreversible cohesive elements for three-dimensional crack-propagation analysis. *International journal for numerical methods in engineering*, 44(9):1267–1282, 1999.

I. Özdemir, W.A.M. Brekelmans, and M.G.D. Geers. A thermo-mechanical cohesive zone model. *Computational Mechanics*, 46 (5):735–745, 2010.

M. Paggi and A. Sapora. Numerical modelling of microcracking in pv modules induced by thermo-mechanical loads. *Energy Procedia*, 38:506–515, 2013.

F. Rebillat, J. Lamon, and A. Guette. The concept of a strong interface applied to sic/sic composites with a bn interphase. *Acta materialia*, 48(18-19):4609–4618, 2000a.

F. Rebillat, J. Lamon, and A. Guette. Importance of fiber/matrix bonding in sic/bn/sic on mechanical and interfacial properties. In *Proceedings of the 12th International Conference on Composite Materials (ICCM12), Paris*, pages 4–9, 2000b.

S. Rezaei, S. Wulfinghoff, and S. Reese. Prediction of fracture and damage in micro/nano coating systems using cohesive zone elements. *International Journal of Solids and Structures*, 121:62–74, 2017.

S. Rezaei, D. Jaworek, J. R. Mianroodi, S. Wulfinghoff, and S. Reese. Atomistically motivated interface model to account for coupled plasticity and damage at grain boundaries. *Journal of the Mechanics and Physics of Solids*, 124:325–349, 2019.

M. Samimi, J.A.W. Van Dommelen, and M.G.D. Geers. An enriched cohesive zone model for delamination in brittle interfaces. *International Journal for Numerical Methods in Engineering*, 80(5):609–630, 2009.

M. Samimi, J.A.W. Van Dommelen, and M.G.D. Geers. A three-dimensional self-adaptive cohesive zone model for interfacial delamination. *Computer Methods in Applied Mechanics and Engineering*, 200(49-52):3540–3553, 2011.

A. Sapora and M. Paggi. A coupled cohesive zone model for transient analysis of thermoelastic interface debonding. *Computational Mechanics*, 53(4):845–857, 2014.

R. W. Trice and J. W. Halloran. Influence of microstructure and temperature on the interfacial fracture energy of silicon nitride/boron nitride fibrous monolithic ceramics. *Journal of the American Ceramic Society*, 82(9):2502–2508, 1999.

T. Wu and P. Wriggers. Multiscale diffusion–thermal–mechanical cohesive zone model for concrete. *Computational Mechanics*, 55(5):999–1016, 2015.

Thermo-Viscoplastic Material Modelling for Self-heating Loads and its Experimental Verification

Holger Sparr*, Robert Roszak, Ilja Sagradov, Daniela Schob and Matthias Ziegenhorn

BTU Cottbus–Senftenberg, Universitätsplatz 1, 01968 Senftenberg, Germany

Abstract: The paper examines a modelling approach for thermomechanically coupled problems and an experimental concept for a material law validation and verification for self-heating with small to moderate temperature ranges. The study compares two different model formulations and is generally applicable to a variety of material classes. One model is based on a rheological network with an extension for dissipative deformation below the elastic limit. The other model operates without a yield condition. Both models are applied to published experimental data in terms of rate-independent behaviour and the evaluation is carried out on stress-strain-level, temperature evolution and the energy transformation ratio. Furthermore the two models are applied to a strain rate-dependent load case conducted at our institute discussing the same entities. It is pointed out, that the approach of a thermomechanical analysis is valuable and informative to assess the observed deformation processes and to describe the material behaviour with a thermodynamically valid parameter set.

Keywords: Thermomechanics, self–heating, viscoplasticity, energy transformation ratio, thermography

1 Introduction

The foundation of the thermomechanical analysis was given by Thomson's work and the publication of the thermoelastic effect Thomson (1853). By the end of the 1960ies, the fully coupled thermomechanical problem was formulated in the framework of continuum mechanics enhanced with the concept of internal state variables (see Truesdell and Noll (2004); Coleman and Gurtin (1967)).

In the same period, scientists exploited the often experimentally observed temperature build-up during cyclic mechanical testing. Oldyrev and others tried to quantify fatigue properties related to damage in glass fibre reinforced plastics by measuring the temperature evolution by thermocouples (see Oldyrev (1967); Oldyrev and Tamuzh (1969)).

Since then, the experimental equipment has improved towards contact-free measurement principles, which has led to high-resolution infrared (IR) camera systems. This development initialised a new series of publications dealing with thermomechanics from the theoretical and/or experimental point of view. The general principle of IR cameras is limited to certain temperature ranges but not restricted to any specific material class, since thin black coatings improve reflection and radiation properties and do not effect the thermomechanical properties of the specimen [Ummenhofer and Medgenberg (2006); Chrysochoos (2012); Fedorova et al. (2014); Cholewa et al. (2016)].

In general, a deformation process can be considered as a full thermomechanical process, while viscoelastic and (visco)plastic deformations are dissipative and lead to self-heating. Most often, the thermal and mechanical boundary conditions are chosen in a way that the temperature evolution is negligible. If not, a suitable combination of loading regime and thermal boundary condition is exploitable for material characterization by solving a coupled thermomechanical problem [Muracciole et al. (2008); Guzmán et al. (2010); Knysh and Korkolis (2015)].

Deformation processes going beyond thermoelasticity and covering a transfer of internal energy to dissipation and finally from an internal heat supply to a temperature evolution is connected to load-induced modifications of the microstructure, which plays an important role in describing the material behaviour of an actual component in its lifetime with a complex loading history and is a major topic in engineering and material science.

In recent years, the successfully employed analytical methods, numerical simulations and measurement principles for metals and alloys have been applied to other material classes and the capability of specific material models to sub-sets of new design materials has been improved. The complex methodology w.r.t. cyclic loading of metals incorporating viscoplasticity has been widely studied (*e.g.* in Chaboche (1989) and many other contributions).

When a specimen on the load path is subjected to an intermediate holding period and furthermore a relaxation is observed, Haupt assigned the term *equilibrium hysteresis* to a repeated holding period on a complete load cycle Haupt (2002). According to the associated material scheme, rate-dependency with an equilibrium hysteresis is classified as general viscoplastic behaviour. Hence, one observes a significant temperature rise due to inelastic deformation at a sufficiently high strain rate and in a subsequent holding period, the temperature drops due to a dominating heat conduction from the specimen to the environment. Therefore, the load regimes, that Haupt (2002) discussed, serve as a proof of viscoplastic behaviour.

Two different viscoplastic material models are considered in this contribution. The first model was proposed in Bodner and Lindenfeld (1995) and abstained from introducing a yield condition. The extended model of Bröcker and Matzenmiller (2013)

doi: 10.24352/UB.OVGU-2020-015

as the second approach is based on a rheological network with an explicit yield condition. In a first setting the experimental findings in Chrysochoos et al. (1989) are confirmed by the to models and furthermore compared to the elastic-plastic approach of Kamlah and Haupt (1998). Secondly, an optimised parameter set from a pure mechanical modelling approach is post-evaluated thermomechanically. And finally, own experimental data based on a loading regime originally suggested in Bodner and Partom (1975) are evaluated and discussed.

Therefore the section 2 summarises the general thermomechanical framework and highlights the most important aspects of the material models mentioned above. The following section continues with the description of the experimental setups in the two settings referred to before. Afterwards the numerical results are presented and assessed.

2 Thermomechanical Framework and Material Models

2.1 Governing principles and equations

To account for an evolving temperature field in a thermomechanical analysis, we start with the second fundamental law of thermodynamics. Incorporating the balances of energy[1] and the balance of entropy into the second law of thermodynamics leads to the inequality for the internal dissipation δ (CLAUDIUS-DUHEM inequality) (1) with $\boldsymbol{q}$ as the heat flux vector, $\boldsymbol{\sigma}$ as the CAUCHY stress tensor, $\dot{\boldsymbol{\varepsilon}}$ as strain rate tensor, $\boldsymbol{g}$ as the temperature gradient and ϱ as the density. The introduced symbols, which are not denominated here explicitly, are explained in following paragraphs.

$$\delta = \frac{1}{\varrho}\boldsymbol{\sigma}\cdot\dot{\boldsymbol{\varepsilon}} - \dot{\psi} + \theta\dot{\eta} - \frac{1}{\varrho\theta}\boldsymbol{q}\cdot\boldsymbol{g} \geq 0 \tag{1}$$

Considering small deformations the usual additive split of the strain tensor $\boldsymbol{\varepsilon}$ into an elastic $\left(\boldsymbol{\varepsilon}^e\right)$, a plastic $\left(\boldsymbol{\varepsilon}^p\right)$ and, also quite common, a thermal part is applied (2), where the thermal part is an isotropic volume expansion indicated by the product of the thermal expansion coefficient α, the temperature change (difference of current θ to the reference temperature θ_0) and the unity tensor $\boldsymbol{I}$. In terms of the principle of equipresence the specific free energy Ψ in (3), the specific internal energy e, the specific entropy η and the stress tensor $\boldsymbol{\sigma}$ depend on the same set of variables, while the variables denoted by $\boldsymbol{a}_i$ represent internal variables and are either scalar or tensor valued. With the assumptions that the named entities depend on the difference $\left(\boldsymbol{\varepsilon} - \boldsymbol{\varepsilon}^p\right)$ the list of dependencies can be altered and switched to the elastic strain tensor (Kratochvil and Dillon (1969)).

$$\boldsymbol{\varepsilon} = \boldsymbol{\varepsilon}^e + \boldsymbol{\varepsilon}^p + \alpha\left(\theta - \theta_0\right)\boldsymbol{I} \tag{2}$$

$$\Psi = \hat{\Psi}\left(\boldsymbol{\varepsilon}, \boldsymbol{\varepsilon}^p, \theta, \boldsymbol{a}_1, \ldots, \boldsymbol{a}_n\right) \overset{!}{=} \hat{\Psi}\left(\boldsymbol{\varepsilon}^e, \theta, \boldsymbol{a}_1, \ldots, \boldsymbol{a}_n\right) \quad \text{and} \quad \Psi = e - \theta\eta \tag{3}$$

$$\boldsymbol{g} = \boldsymbol{\nabla}\theta \quad \text{and} \quad \boldsymbol{q} = -k\boldsymbol{g} \tag{4}$$

The coupling of the independent variables is completed by assuming Fourier's law (4), where the positive thermal conductivity k is the proportionality factor between the heat flux and the negative temperature gradient.

The constitutive consequences for thermodynamically admissible processes are given in eqn. (5) and (6):

$$\eta = -\frac{\partial\hat{\Psi}}{\partial\theta} \overset{!}{=} \alpha\frac{\partial\hat{\Psi}}{\partial\boldsymbol{\varepsilon}^e} - \frac{\partial\hat{\Psi}}{\partial\theta} \tag{5}$$

$$\boldsymbol{\sigma} = \varrho\frac{\partial\hat{\Psi}}{\partial\boldsymbol{\varepsilon}^e} \quad \text{with} \quad \boldsymbol{\sigma} = p\boldsymbol{I} + \boldsymbol{S} \quad , \tag{6}$$

which leads furthermore to the CLAUDIUS-DUHEM inequality in the form:

$$\delta = \frac{1}{\varrho}\boldsymbol{\sigma}\cdot\dot{\boldsymbol{\varepsilon}}^p - \sum_{j=1}^{n}\frac{\partial\hat{\Psi}}{\partial\boldsymbol{a}_j}\dot{\boldsymbol{a}}_j - \frac{1}{\varrho\theta}\boldsymbol{q}\cdot\boldsymbol{g} \geq 0 \quad . \tag{7}$$

Assuming that the internal dissipation is completely transferred into heat, the energy balance delivers an additional equation for calculating the evolving temperature field. It should be noted, that according to for instance Helm (2006) and Shutov and Ihlemann (2011) the contitutive ansatz for the free energy might be extended to include certain parts not related to any hardening mechanisms. These phenomenological and micromechanically justified approaches introduce new material parameters to control the amount of dissipation consistently. In the next two subsections, expressions for the internal dissipation are layed down for the two distinct viscoplastic material models under consideration following the outlined ansatz for the free energy.

To discuss the thermomechanical analysis in more detail, additional energy related quantities are defined by having a closer look at the first two summands of eq. (7). The first summand is denoted as the specific *plastic stress power* e_p, while the second is often called specific *rate of stored energy of cold work* e_s:

$$e_p := \frac{1}{\varrho}\boldsymbol{\sigma}\cdot\dot{\boldsymbol{\varepsilon}}^p \quad \text{and} \quad e_s := \sum_{j=1}^{n}\frac{\partial\hat{\Psi}}{\partial\boldsymbol{a}_j}\dot{\boldsymbol{a}}_j \quad . \tag{8}$$

---

[1]neglecting the heat supply per unit mass
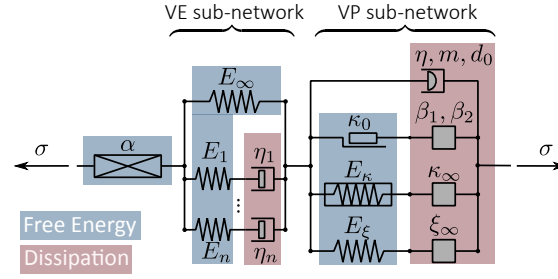
Fig. 1: Modified rheological network (originally proposed by Bröcker and Matzenmiller (2013))

The expression for the plastic work and the stored energy of cold work can then be obtained by time integration:

$$w_p = \int_{t_0}^{t} e_p(\tau)\,\mathrm{d}\tau \quad \text{and} \quad w_s = \int_{t_0}^{t} e_s(\tau)\,\mathrm{d}\tau \tag{9}$$

To quote Kamlah and Haupt (1998): "It is common use to plot the ratio w_s/w_p over the plastic work or the plastic strain. Besides the instantaneous rate of energy storage, [the ratio] $\varphi := e_s/e_p$ as a function of w_p is considered, since it **reflects the dynamics of dislocational processes**." The rate of the energy storage to the plastic stress power ratio φ is also referred to as (rate of) energy transformation ratio (ETR) and gives insight into the reasonability and the physics of the considered deformation process. Identical or similar formulations can be found in Oliferuk and Raniecki (2018), Håkansson et al. (2008), Helm (2006), Johnsen et al. (2019) and others. To illustrate the calculated results the ETR (φ) is depicted in the graphs of section 4.

Since the model analysis is conducted for pure one-dimensional loading the tensor notation is dropped in the subsequent equations, which also suits the rheological network approach in the next section. For further derivation of the complete set of the differential equations we assume only small temperature changes, which means that the material parameters are temperature-independent. Furthermore the deformation process does not influence the parameters for heat conduction and heat capacity.

2.2   Rheological network with yield condition

The intuitive fundamental network rules (equal stress in consecutive network members in separated branches; equal strain in parallel branches) simplifies the generation of complex material models by connecting a set rheological elements. A network member is understood as either a single rheological element (e.g. the thermal expansion element as the first chain member from the left in Fig. 1) or a so-called sub-network (here the viscoelastic resp. viscoplastic sub-network following the thermal expansion element in the same figure).

By introducing expressions for the free energy ψ_i of each element type i and the association of the general internal variables $\boldsymbol{a}_i$ to specific deformation mechanisms according to the assumed network the implementation point of experimentally motivated material models is achieved. The main idea followed by Bröcker and Matzenmiller (2013) is the classification of each element contributing purely either to free energy or to internal dissipation as indicated by the colours in Fig. 1. Therefore an original element (e.g. the traditional friction element) might be represented now by two elements to separate the energetic contributions. For the actual mathematical expression and the detailed corresponding arguments based on experimental observations for each rheological element the authors of this article would like to refer the reader to the original publication.

In the modification of the original network depicted here, the singular linear elastic spring on position two of the main chain is replaced by a viscoelastic sub-network (generalised Maxwell element) to cover viscous deformation below the elastic limit, which becomes relevant when polymer based material come into focus. The elastic limit or yield point is realised by the friction element, there the modification needs to take place outside the viscoplastic sub-network. Taking into account this modification, the internal variable belong either to the viscoelastic $((\cdot)_{\mathrm{ve}})$ or the viscoplastic $((\cdot)_{\mathrm{vp}})$ sub-network (cf. (12)).

With the aforementioned assumption that the difference $(\varepsilon - \varepsilon_{vp})$ enters the list of dependencies, the free energy for the one-dimensional case reads:

$$\varepsilon = \varepsilon_{\mathrm{ve}} + \varepsilon_{\mathrm{vp}} + \alpha(\theta - \theta_0) \tag{10}$$

$$\Psi = \hat{\Psi}(\varepsilon_{\mathrm{ve}}, \theta, \boldsymbol{a}_1, \dots, \boldsymbol{a}_k, \boldsymbol{a}_{k+1}, \dots, \boldsymbol{a}_l) \tag{11}$$

Again this leads to the Claudius-Duhem inequality in the following form for the one-dimensional case:

$$\delta = \left(\frac{1}{\varrho}\sigma - \frac{\partial\psi}{\partial\varepsilon_{\mathrm{ve}}}\right)\dot{\varepsilon}_{\mathrm{ve}} + \left(\frac{1}{\varrho}\sigma\alpha_{\mathrm{th}} - \frac{\partial\psi}{\partial\theta} - \eta\right)\dot{\theta} + \frac{1}{\varrho}\sigma\dot{\varepsilon}_{\mathrm{vp}} - \frac{\partial\psi}{\partial\boldsymbol{a}_{\mathrm{ve}}}\cdot\dot{\boldsymbol{a}}_{\mathrm{ve}} - \frac{\partial\psi}{\partial\boldsymbol{a}_{\mathrm{vp}}}\cdot\dot{\boldsymbol{a}}_{\mathrm{vp}} - \frac{1}{\varrho\theta}q\frac{\partial\theta}{\partial x} \geq 0 \tag{12}$$

where the expression $\boldsymbol{a}_{\mathrm{ve}}$ (resp. $\boldsymbol{a}_{\mathrm{vp}}$) collects the internal variables with the index from 1 to k (resp. from $k+1$ to l) regarding the corresponding sub-network.

Therefore the n viscoelastic branches do have an impact on the true stress, the entropy and the internal dissipation as the detailed constitutive consequences (13) show.

$$\sigma = \varrho\frac{\partial\psi}{\partial\varepsilon_{\mathrm{ve}}}; \quad \eta = \frac{1}{\varrho}\sigma\alpha_{\mathrm{th}} - \frac{\partial\psi}{\partial\theta} = \alpha_{\mathrm{th}}\frac{\partial\psi}{\partial\varepsilon_{\mathrm{ve}}} - \frac{\partial\psi}{\partial\theta} \quad \text{and} \quad \frac{1}{\varrho}\sigma\dot{\varepsilon}_{\mathrm{vp}} - \frac{\partial\psi}{\partial\boldsymbol{a}_{\mathrm{ve}}}\cdot\dot{\boldsymbol{a}}_{\mathrm{ve}} - \frac{\partial\psi}{\partial\boldsymbol{a}_{\mathrm{vp}}}\cdot\dot{\boldsymbol{a}}_{\mathrm{vp}} - \frac{1}{\varrho\theta}q\frac{\partial\theta}{\partial x} \geq 0 \tag{13}$$

The equation of heat conduction then follows from the local balance of energy. It depends on the sign of the spatial temperature gradient $\boldsymbol{g}$ how the heat flux is contributing to the temperature evolution. The equation of heat conduction can be expressed as:

$$c_d \dot{\theta} = -\theta \frac{\partial \eta}{\partial \varepsilon_{ve}} \dot{\varepsilon}_{ve} - \frac{\partial (\psi + \theta \eta)}{\partial \boldsymbol{a}_{ve}} \cdot \dot{\boldsymbol{a}}_{ve} + \frac{1}{\varrho} \sigma \dot{\varepsilon}_{vp} - \frac{\partial (\psi + \theta \eta)}{\partial \boldsymbol{a}_{vp}} \cdot \dot{\boldsymbol{a}}_{vp} + \frac{1}{\varrho} \operatorname{div} q \tag{14}$$

The first summand reflects the thermoelastic coupling and the second term corresponds to the dissipation in all MAXWELL elements of the viscoelastic sub-network. The next two terms of the sum belong to the viscoplastic sub-network. It can be seen, that the plastic stress power as the third term is not completely transferred into heat. A fraction of the mechanically introduced energy is stored as internal energy.

Eqn. (15) to (19) summarise the core of the initial value problem to solve.

$$\sigma = E^* \varepsilon_{ve} = E^* (\varepsilon - \varepsilon_{vp} - \alpha_{th} \theta) \qquad \text{with } E^* = E^*(t) \quad \text{and} \quad \lim_{t \to -\infty} E^*(t) = E_\infty \tag{15}$$

$$\text{with eqns for} \quad \dot{\varepsilon}_{\eta_i} = \dot{\varepsilon}_{\eta_i}(\dot{\varepsilon}_{ve})$$

$$\mathscr{E}_\sigma := \left\{ (\sigma, \xi, \kappa) \in \mathscr{R} \times \mathscr{R} \times \mathscr{R} \mid f(\sigma, \xi, \kappa) \le 0 \right\} \qquad \text{with} \quad f(\sigma, \xi, \kappa) = |\sigma - \xi| - (\kappa_0 + \kappa) \tag{16}$$

$$\dot{\varepsilon}_{vp} = \frac{1}{\eta} \left\langle \frac{f}{d_0} \right\rangle^m \operatorname{sgn}(\sigma - \xi) \qquad \text{with eqns for } \dot{\varepsilon}_\beta = \dot{\varepsilon}_\beta(\dot{\varepsilon}_{vp}), \ \dot{\xi} = \dot{\xi}(\dot{\varepsilon}_{vp}) \ \text{and} \ \dot{\kappa} = \dot{\kappa}(\dot{\varepsilon}_{vp}) \tag{17}$$

$$\dot{\varepsilon}_{th} = \alpha_{th} \dot{\theta} \tag{18}$$

$$c_d \dot{\theta} = -\frac{1}{\varrho} E \alpha \theta \dot{\varepsilon}_{ve} + \frac{1}{\varrho} \lambda \nabla \cdot (\nabla \theta) + \delta_{mat} \qquad \text{with} \quad \delta_{mat} = \frac{1}{\varrho} \left[f + \delta_{\kappa_0} + \delta_\kappa + \delta_\xi \right] \dot{\varepsilon}_{vp} + \delta_{ve} \ge 0 \tag{19}$$

The first two equations cover the viscoelastic domain. The yield condition in eq. (16) incorporates kinematic and isotropic hardening, where ξ represents the backstress to shift the yield surface in stress space. Eg. (17) collects the evolutionary equations for the mechanical deformation fractions. The entity $\dot{\varepsilon}_\beta$ resembles the strain evolution in the dissipative element of the friction path in the rheological network (Fig. 1). The internal variables for hardening ξ and κ account for saturation effects (see Bröcker and Matzenmiller (2013)). The coupling is given through eq. (18) and the equation of heat conduction (19) completes the set. The full problem formulation has to be accompanied by the initial conditions, which are an undeformed stress-free state at room temperature. The initial values of the evolving inner variables are given by the (indentified) material parameters (cf. sections 5.1 and 5.2).

2.3 Model without yield condition and additional constitutive assumption for free energy

The second material model investigated is based back to the very first publication Bodner and Partom (1975) and has been refined or adjusted ever since. The thermomechanical consistent material model was published in Bodner and Lindenfeld (1995) 20 years later without following the approach by Chrysochoos *et al.* described above to quantify the amount of dissipation. Instead the authors suggested well designed shear tests (decoupling strategy) to overcome the difficulties of an accurate temperature measurement.

Considering again the fundamentals outlined above, evolutionary equations for the viscoplastic strain as well as for the internal variables forming an initial value problem are the objective.

The viscoplastic strain rate is proportional to the stress deviator (20), while the factor λ is bound to a well-designed exponential function with saturation.

$$\dot{\boldsymbol{\varepsilon}}^P = \lambda \boldsymbol{S} \tag{20}$$

$$\lambda^2 = D_2^P / J_2 \quad \text{with} \quad D_2^P = \frac{1}{2} \dot{\boldsymbol{\varepsilon}}^P \cdot \dot{\boldsymbol{\varepsilon}}^P \quad \text{and} \quad J_2 = \frac{1}{2} \boldsymbol{S} \cdot \boldsymbol{S} \tag{21}$$

The power function obtained the following structure:

$$D_2^P = D_2^P(J_2) = D_0^2 \exp \left[-\left(\frac{Z^2}{3 J_2} \right)^n \right] \tag{22}$$

where Z represents a material state and combines all internal variables into a single scalar. The hardening approach in this form is quite unique and splits the deformation processes into isotropic and directional hardening:

$$Z = Z^I + Z^D \qquad . \tag{23}$$

Both, isotropic and directional, hardening parameters are proportional to the plastic stress power. To cover well described phenomenological effects the original function for $\dot{Z}^I$ resp. $\dot{Z}^D$ has been improved and enriched.

$$\dot{Z}^I = m_1 (Z_1 - Z^I) \dot{W}_p \quad \text{with } Z^I(0) = Z_0, \ \dot{W}_p = \boldsymbol{S} \cdot \dot{\boldsymbol{\varepsilon}}^P \qquad \text{and } m_1 = m_{11} + m_{12} \exp\left(-m_{13} Z^I\right) \tag{24}$$

$$Z^D = \boldsymbol{\beta} \cdot \boldsymbol{U} \text{ and } \dot{\boldsymbol{\beta}} = m_2 (Z_3 \boldsymbol{U} - \boldsymbol{\beta}) \dot{W}_p \quad \text{with } \boldsymbol{\beta}(0) = \boldsymbol{0}, \ \boldsymbol{U} = \frac{\boldsymbol{\sigma}}{|\boldsymbol{\sigma}|} \quad \text{and } m_2 = m_{21} + m_{22} \exp\left(-m_{23} Z^D\right) \tag{25}$$

Due to the assumed small temperature changes the original terms for considering thermal recovery in (24) and (25) are neglected.

Eq. (26) serves as an additional constitutive assumption by introducing four new material parameters (a, b, p_1 and p_2).

$$\Psi_Z = \frac{a}{\varrho}\left(\frac{Z^I}{Z_1}\right)^{p_1} + \frac{b}{\varrho}\left(\frac{\boldsymbol{\beta}\cdot\boldsymbol{\beta}}{Z_3^2}\right)^{p_2} \tag{26}$$

By choosing the exponents $p_1 = 2$ and $p_2 = 1$ a quadratic form is achieved but might not reflect the desirable non-linearity. Kamlah *et al.* argued with the analogy to thermoelasticity and developed their model with a quadratic energy expression as well. In the original paper Bodner *et al.* operate with $p_1 = 4$ for copper specimen.

The expressions for the rate Ψ_Z (rate of stored energy of cold work):

$$\dot{\Psi}_Z = p_1 \frac{a}{\varrho}\frac{\dot{Z}^I}{Z_1}\left(\frac{Z^I}{Z_1}\right)^{p_1-1} + 2p_2\frac{b}{\varrho}\frac{\boldsymbol{\beta}\cdot\dot{\boldsymbol{\beta}}}{Z_3^2}\left(\frac{\boldsymbol{\beta}\cdot\boldsymbol{\beta}}{Z_3^2}\right)^{p_2-1} \tag{27}$$

and the mechanical fraction of the internal dissipation δ_M

$$\delta_M = \frac{1}{\varrho}\dot{W}_P - p_1\frac{a}{\varrho}\frac{\dot{Z}^I}{Z_1}\left(\frac{Z^I}{Z_1}\right)^{p_1-1} - 2p_2\frac{b}{\varrho}\frac{\boldsymbol{\beta}\cdot\dot{\boldsymbol{\beta}}}{Z_3^2}\left(\frac{\boldsymbol{\beta}\cdot\boldsymbol{\beta}}{Z_3^2}\right)^{p_2-1} \geq 0 \tag{28}$$

are then straightforward and lead to similar structured equation of heat conduction as presented above. Having the equations outlined above at hand, a similar rheological network in analogy to the Bröcker–Matzenmiller model with just a single viscoplastic sub-network can be drawn (cf. Fig. 2). The elements in the viscoplastic sub-network represent the analytical non-linearity of the function above. A separation of internal dissipation and free energy is possible by eq. (26), while the internal variables Z^I resp. $\boldsymbol{\beta}$ appear in the dissipative element on top and the corresponding non-linear spring.

For the solution of this system of differential equations the same initial conditions apply as stated at the end of the previous section.

3 Experiments

3.1 Caloric resp. temperature measurement in tensile test for the XCrNi18.9 stainless steel

In 1998, Kamlah & Haupt presented their thermomechanical elastoplastic model by proving it against experimental data provided by the group of Chrysochoos. The XCrNi18.9 stainless steel material behaviour was investigated by tensile testing at room temperature.

Reliable experimental data depend on a sophisticated measurement strategy, which was established in two distinct ways in the group of Chrysochoos. The first method is the application of a microcalorimeter with a suitable calibration scheme.

The second method is based on measuring the temperature evolution and a calibration of the heat losses due to radiation and conduction for the plain thermoelastic effect. Convection heat losses were eliminated by a primary vacuum chamber. In contrast to the thermography applied in our own experiments the observation zone is limited to a rectangle of $15\,\text{mm} \times 25\,\text{mm}$. Current IR cameras with an increased pixel field on the detector can cover the complete sample and its surroundings (essentially the grips of the testing machine). The experiments are quantitatively evaluated by solving the heat conduction equation for the observation zone.

Both methods lead to results in close agreement, which validates the experimental findings at low strain rates of $10^{-4}\,\text{1/s}$.

3.2 Change of strain rate in tensile test for the copper

The setup for our own experiments is similar as outlined above but chosen to be as simple as possible, which excludes any special measures to control the thermal boundary conditions. The tests were conducted at room temperature. Flat copper samples with a thickness of 1.5 mm (standard: DIN 50125 - Shape Type H) were tested under different loading conditions. The reflection of sample surface were eliminated by blackening.

As the observing camera the ImageIR 8300 of InfraTec was applied, which is characterised by a detector format of 640×512 pixel, a temperature resolution of at least 0.02 K at room temperature and a usable frame rate of 100 Hz. The data evaluation is conducted interactively on the IR images by averaging the temperature values measured on well-defined geometric objects on the sample surface. The averaging reduces the thermal noise due to reflexions of the surroundings and inhomogenous emission
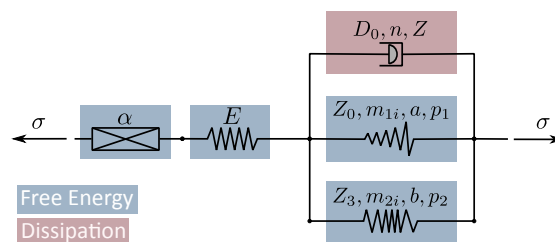
Fig. 2: Rheological analogy of the Bodner–Lindenfeld model

Fig. 3: Stress-strain curves (*left*) and temperature evolution (*right*) for a uni-axial tension (XCrNil8.9 stainless steel)

Fig. 4: Energy transformation ratio over plastic strain (*left*) resp. plastic work (*right*) for a uni-axial tension (XCrNil8.9 stainless steel)

properties on the sample surface. The thermal noise can be minimised by an additional radiation sources pointed on the sample. This heat source needs to be reflected in the heat conduction equation appropriately, which is still under investigation. Temperature profiles along and perpendicular to the loading direction are assessed as well.

The load was applied on a servohydraulic testing machine of a maximal possible load of 25 kN where the grips are not thermally decoupled to the pressure aggregates. The temperature of the upper grip is directly connected to the piston and is observably elevated compared to the lower grip. The lower grip behaves nearly as an ideal heat sink at constant temperature, while the temperature of the upper grip is slowly increasing in time of operation. Nonetheless the upper grip temperature can be assumed constant for loadings times lower than 500 s .

The applied loading scheme was adopted from the paper Bodner and Partom (1975). The authors suggested a displacement controlled rate change during a simple tensile test. The rate change covers approximately two orders of magnitudes. The test starts with a lower rate of $1.34 \cdot 10^{-4} 1/s$ up to a total strain value of 0.026 and increases then to $1.29 \cdot 10^{-2} 1/s$ up to a total strain value of 0.079. It follows a second lower rate load increase up to total strain value of 0.106 and a subsequent unloading at a rate $-6.80 \cdot 10^{-4} 1/s$.

The evaluation of the machine data confirmed the constant strain rates in each section of the load path. The evaluation of the experimental data for the true stress accounts for a cross-section reduction, while the numerical calculation remains in stress-strain space and therefore reflects a point-wise evaluation without considering the actual dimensions of the specimen and justifies total strain values up-to 0.1 .

4 Numerical evaluation and comparison to experimental data

4.1 Caloric evaluation of tensile test

The diagrams in Fig. 3 and 4 gather the responses of three different material models. The parameter set for the Bröcker-Matzenmiller (BM) model is chosen to reflect approximately rate-independent behaviour ($\eta = 1.0$ s). In the Bodner-Lindenfeld (BL) model the viscous deformation fraction is not clearly controllable by a single parameter, therefore its response is by model definition rate-dependent. The data of the rate-independent Kamlah-Haupt (KH) model is added as a source of a stress-strain curve to compare to and as a further reference in the remaining diagrams. The nomimal (engineering) strain is used in all diagrams with the strain on the abscissa.

With an optimised parameter set both material models to be investigated are able to reflect the stress-strain curve given by the parameter set in Kamlah and Haupt (1998) (cf. Fig. 3 *left*). Minor deviations are visible for the BM model in the transition range of purely elastic to elastoplastic deformation.

To compare the temperature evolution artificial adiabatic boundary conditions have been formulated, since the experimental data of the temperature-time are not available. The diagram in Fig. 3 *right* shows a larger deviation of the BM model to the other two formulations of ≈ 1.7 K at the end of the load path. The thermoelastic effect in the elastic deformation range is covered by all three models.

Even more significant deviations can be found in the energy transformation ratio (ETR) plotted in Fig. 4 over the plastic (*left*) resp. over the plastic work (*right*). The KH model meets the maximum of the ETR at a plastic strain of about 0.03, but the overall qualitative behaviour is approximated better by the BL model. The quasi-rate-independent ETR-curve of the BM model has its

H. Sparr, R. Roszak, I. Sagradov, D. Schob, and M. Ziegenhorn

Tech. Mech., Vol. 40, Is. 1, (2020), 66–76
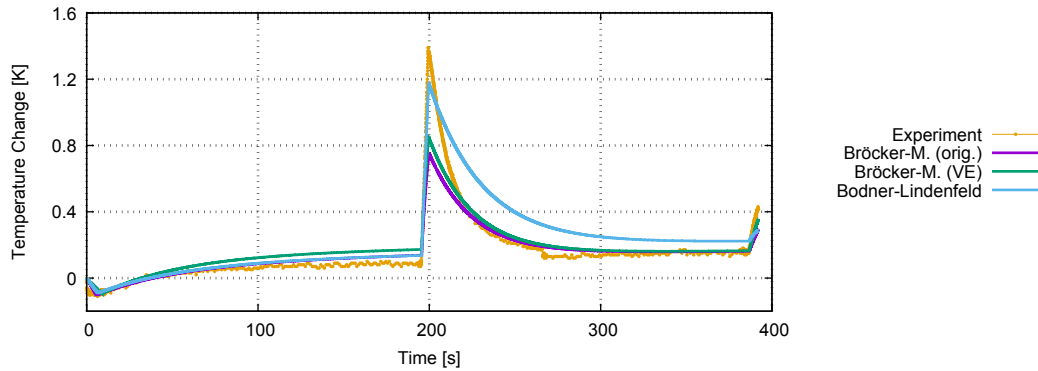
Fig. 5: Temperature evolution curves for a tensile test with two different strain rates and final unloading (flat copper specimen)
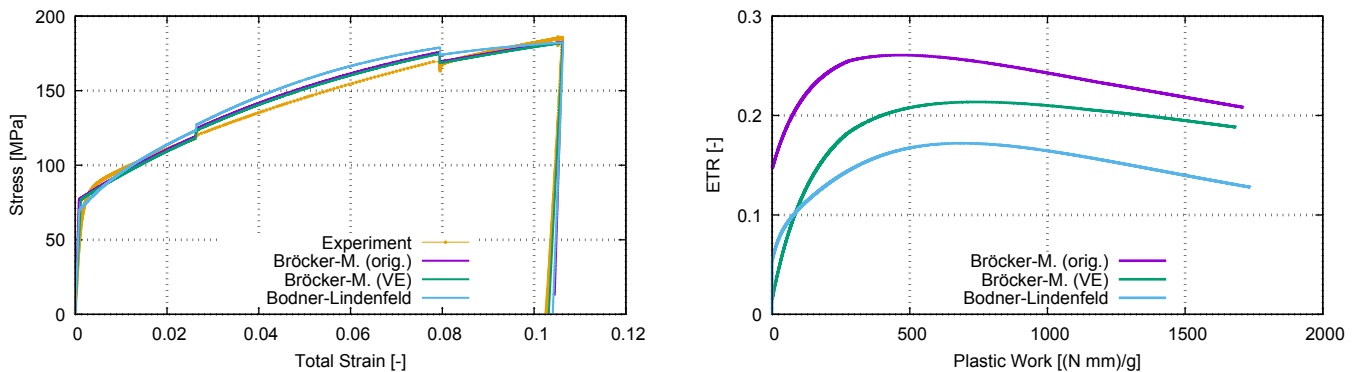
Fig. 6: Stress-strain (*left*) and ETR-plastic work (*right*) curves for a tensile test with two strain rates and final unloading (flat copper specimen)

maximum at the very beginning of the plastic deformation. Looking at the curves plotted over the plastic work, it is remarkable that the maximum value of plastic work of the KH model is almost 20% lower than the other two maxima. Therefore the absolute fraction of stored energy of cold work is lower likewise in the KH model.

4.2 Change of strain rate in tensile test

The data in the following three diagrams (Fig. 5 and 6) assemble the measured values and the calculated values of the original BM model, the extended BM model and the BL model for copper samples. The extension of the Bröcker-Matzenmiller model includes just one single Maxwell element in the viscoelastic sub-network.

In the analysis of the tensile test with alternating strain rate the adiabatic thermal boundary conditions are not valid. In Kamlah *et al.* an analytical solution was suggested, which assumes a constant temperature value for both grips. As outlined in section 3.2, the temperature evolution observed in the grips does not match the presumption of this analytical approach. Therefore the identical assumption as proposed in Chrysochoos et al. (1989) was chosen. It suggests an additional linear term for the rate of temperature to account for the heat losses in the equation of heat conduction (cf. eq. (19)). The corresponding additional parameter captures the ambient conditions, the specimen shape as well as the heat transfer at the grip-sample interface integratively. This parameter can be calibrated for the expected temperature range.

In Fig. 5 the different temperature-time curves for the full testing period are plotted. All curves start with a thermoelastic cooling phase at the lower strain rate. The turning pointing after ca. 10 s indicates the beginning of plastic deformation associated with internal dissipation. Until the end of the first lower strain rate section the balance of heat supply and heat loss is nearly approached. In the second section of the higher strain rate, the temperature change is strongly increasing and a maximum in the experimental data of 1.4 K is found at the end of the section at 200 s. It follows a period of temperature equalisation in the third section of the lower strain rate. The unloading is matched by a thermoelastic heating.

The optimised parameter sets for all models reflect the general behaviour, while the BL model approximates the maximum significantly better than the original and the extended BM model. It is noted here that the BM model for copper operates with an elevated module of elasticity taking the additional viscous model capability of the viscoelastic sub-network into account. This is visible in the unloading section in the left diagram of Fig. 6 where the slope is best matched by the extended BM model.

The accompanying results of the stress-strain resp. ETR-plastic work curves are shown in Fig. 6. A good agreement of experimental and model data is observed in the stress-strain curves on the *left*. It is pointed out, that the effect of the viscoelastic extension is slightly visible by a reduced slope in the (visco-)elastic unloading section. An explanation can be found in the ETR-plastic work curves on the *right*. The maximum value of plastic work of the extended BM model is significantly smaller compared to the other two models because a fraction of plastic work is shifted to the viscoelastic sub-network. In general all curves in the right diagram exhibit a similar characteristic with the maxima at a similar position on the load path. Comparing the materials themselves the ETR maxima of the copper sample are clearly smaller than the maxima of the steel sample (see Fig. 4 *right*). This holds especially

true for the BL model.

5　Conclusion

The phenomenological approach in a thermomechanical context gives an informative insight into dissipative and conservative deformation mechanisms concerned for all discussed models. The concept of internal variables relates these mechanisms to the evolution of state variables. A more detailed evaluation produces further information in terms of mechanisms attributing to stored energy of cold work (which is not shown in this paper). In general this means, that for engineering tasks where an assessment of plastic deformation is essential, the phenomenological approach is a powerful tool and the model capabilities have been shown in both testing scenarios.

Usually the coupling due to the full thermomechanical description is neglected. The problems, that arise here, are a necessary validity check of the material parameter set and the extensibility to different loading regimes. As outlined in this paper, three curves and not just a stress-strain characteristic is used for a plausibility check.

To examine a material likewise, the experimental effort is increased, since the temperature evolution needs to be observed. But as the observations of section 4.1 show, even with unrealistic thermal boundary conditions - identical with dropping the temperature measurement altogether, the thermomechanical analysis leads to sensible parameter sets with a more solid foundation, when a thermomechanically derived state variable like the energy transformation ratio (ETR) is additionally introduced into the parameter identification process. The ETR characteristic is linked to specific materials resp. material classes and can therefore be integrated in the identification process qualitatively. Thermodynamically consistent parameter bounds were notified by Kamlah and Haupt (1998) and derived in Kamlah (1994), which is an open topic for future research.

In the second experiment with alternating strain rates differing by two orders of magnitude in a tension test with unloading, an accurate agreement is harder to achieve and the model capabilities need to be questioned.The effect of the viscoelastic extension in the Bröcker-Matzenmiller model in this setup is not particularly large, but the influence on the temperature-time as well as on the ETR-plastic work characteristic is clearly visible.

As a consequence the thermomechanical analysis is to be extended in terms of the loading regime and other design materials. More complex loading regimes like cyclic loading, tension-compression loading and an alternation of different strain rates are going to be investigated. The applicability of the extended Bröcker-Matzenmiller model and the Bodner-Lindenfeld model without a yield condition to polymer material is of major interest in future research work.

Acknowledgement

Appendix

5.1   Parameter sets related to section 4.1

Tab. 1: Parameter set for Bodner–Lindenfeld model for the XCrNil8.9 stainless steel

Thermoelasticity				Isotropic Hardening		
Modulus of Elasticity E_∞	N mm^{-2}	200 000		Z_0	MPa	220
Density ϱ	kg/m^3	7 800.0		Z_1	MPa	500
Expansion Coefficient α	K^{-1}	$1.6 \cdot 10^{-5}$		m_{11}	MPa^{-1}	0.01
Heat Capacity c_{def}	J/(kg K)	480.0		m_{12}	MPa^{-1}	16.7
Thermal conductivity k	W/(m K)	20.0		m_{13}	MPa^{-1}	0.007
Scaling factor D_0	s^{-1}	10 000		Directional Hardening		
Exponent n	$[-]$	3		Z_3	MPa	340
Plastic work *resp.* Free energy parameter				m_{21}	MPa^{-1}	0.055
Factor for isotropic h. Ψ-fraction a	MJ m^{-3}	0.02		m_{22}	MPa^{-1}	0.23
Corr. exponent p_1	$[-]$	4.0		m_{23}	MPa^{-1}	0.05
Factor for directional h. Ψ-fraction b	MJ m^{-3}	1.0				
Corr. exponent p_2	$[-]$	14.0				

The BM model is capable to describe isotropic as well as kinematic hardening behavoir. The presented experimental data are not sufficient to calibrate the backstress ξ. Therefore the hardening mechanisms are treated equally in terms of modulus and saturation for the pure tensile loading regime (cf. Tab. 2 and Tab. 4 in the next section).

Tab. 2: Parameter set for Bröcker–Matzenmiller model for the XCrNil8.9 stainless steel

Thermoelasticity			Kinematic Hardening		
Modulus of Elasticity E_∞	N mm^{-2}	200 000	Kin. Hardening Modulus E_κ	N mm^{-2}	4 000
Density ϱ	kg/m^3	7 800.0	Kin. Saturation κ_∞	N mm^{-2}	155.0
Expansion Coefficient α	KI	$1.6 \cdot 10^{-5}$	Isotropic Hardening		
Heat Capacity c_{def}	J/(kg K)	480.0	Iso. Hardening Modulus E_ξ	N mm^{-2}	4 000
Thermal conductivity k	W/(m K)	20.0	Iso. Saturation ξ_∞	N mm^{-2}	155.0
Friction Element			Viscoplasticity		
Yield Stress κ_0	N mm^{-2}	273	Strain rate scaling factor η	s	1.0
Lin. Dissipation Coeff. β_1	$[-]$	0.4	Strain rate exponent m	$[-]$	1
Non-lin. Dissipation Coeff. β_2	$[-]$	50			

5.2   Parameter sets related to section 4.2

Tab. 3: Parameter set for Bodner–Lindenfeld model for pure copper

Thermoelasticity				Isotropic Hardening		
Modulus of Elasticity E_∞	N mm^{-2}	80 000		Z_0	MPa	100
Density ϱ	kg/m^3	8 920		Z_1	MPa	120
Expansion Coefficient α	K^{-1}	$16.5 \cdot 10^{-6}$		m_{11}	MPa^{-1}	1.0
Heat Capacity c_{def}	J/(kg K)	385.0		m_{12}	MPa^{-1}	2.0
Thermal conductivity k	W/(m K)	400.0		m_{13}	MPa^{-1}	0.01
Scaling factor D_0	s^{-1}	10 000		Directional Hardening		
Exponent n	$[-]$	5		Z_3	MPa	150
Plastic work *resp.* Free energy parameter				m_{21}	MPa^{-1}	0.18
Factor for isotropic h. Ψ-fraction a	MJ m^{-3}	0.08		m_{22}	MPa^{-1}	0.1
Corr. exponent p_1	$[-]$	4.0		m_{23}	MPa^{-1}	0.1
Factor for directional h. Ψ-fraction b	MJ m^{-3}	2.2				
Corr. exponent p_2	$[-]$	1.0				

Tab. 4: Parameter set for Bröcker–Matzenmiller model for pure copper

Thermoelasticity			Kinematic Hardening		
Modulus of Elasticity E_∞	N mm^{-2}	100 000	Kin. Hardening Modulus E_κ	N mm^{-2}	2 000
Density ϱ	kg/m^3	8 920	Kin. Saturation κ_∞	N mm^{-2}	135.0
Expansion Coefficient α	K^{-1}	$16.5 \cdot 10^{-6}$	**Isotropic Hardening**		
Heat Capacity c_{def}	J/(kg K)	385.0	Iso. Hardening Modulus E_ξ	N mm^{-2}	2 000
Thermal conductivity k	W/(m K)	400.0	Iso. Saturation ξ_∞	N mm^{-2}	135.0
Friction Element			**Viscoplasticity**		
Yield Stress κ_0	N mm^{-2}	75	Strain rate scaling factor η	s	700
Lin. Dissipation Coeff. β_1	[−]	0.15	Strain rate exponent m	[−]	1.0
Non-lin. Dissipation Coeff. β_2	[−]	30			

References

S. R. Bodner and A. Lindenfeld. Constitutive modelling of the stored energy of cold work under cyclic loading. *European Journal of Mechanics - A/Solids*, 14(3):333–348, 1995.

S. R. Bodner and Y. Partom. Constitutive Equations for Elastic-Viscoplastic Strain-Hardening Materials. *Journal of Applied Mechanics*, 42(2):385–389, 06 1975. ISSN 0021-8936. doi: 10.1115/1.3423586.

C. Bröcker and A. Matzenmiller. An enhanced concept of rheological models to represent nonlinear thermoviscoplasticity and its energy storage behavior. *Continuum Mechanics and Thermodynamics*, 25(6):749–778, 2013. doi: 10.1007/s00161-012-0268-3.

J.L. Chaboche. Constitutive equations for cyclic plasticity and cyclic viscoplasticity. *International Journal of Plasticity*, 5(3):247 – 302, 1989. ISSN 0749-6419. doi: 10.1016/0749-6419(89)90015-6.

N. Cholewa, P. T. Summers, S. Feih, A. P. Mouritz, B. Y. Lattimer, and S. W. Case. A technique for coupled thermomechanical response measurement using infrared thermography and digital image correlation (tdic). *Experimental Mechanics*, 56(2): 145–164, 2016. doi: 10.1007/s11340-015-0086-1.

A. Chrysochoos. Infrared thermography applied to the analysis of material behavior: a brief overview. *Quantitative InfraRed Thermography Journal*, 9(2):193–208, 2012. doi: 10.1080/17686733.2012.746069.

A. Chrysochoos, O. Maisonneuve, G. Martin, H. Caumon, and J.C. Chezeaux. Plastic and dissipated work and stored energy. *Nuclear Engineering and Design*, 114(3):323–333, 1989. doi: 10.1016/0029-5493(89)90110-6.

B. D. Coleman and M. E. Gurtin. Thermodynamics with internal state variables. *The Journal of Chemical Physics*, 47(2):597–613, 1967. doi: 10.1063/1.1711937.

A. Yu. Fedorova, M. V. Bannikov, A. I. Terekhina, and O. A. Plekhov. Heat dissipation energy under fatigue based on infrared data processing. *Quantitative InfraRed Thermography Journal*, 11(1):2–9, 2014. doi: 10.1080/17686733.2013.852416.

R. Guzmán, J. Meléndez, J. Zahr, and J. L. Pérez-Castellanos. Determination of the constitutive relation parameters of a metallic material by measurement of temperature increment in compressive dynamic tests. *Experimental Mechanics*, 50(3):389–397, 2010. doi: 10.1007/s11340-009-9223-z.

P. Haupt. *Continuum Mechanics and Theory of Materials*. Springer-Verlag, 2nd edition, 2002. doi: 10.1007/978-3-662-04775-0.

D. Helm. Stress computation in finite thermoviscoplasticity. *International Journal of Plasticity*, 22(9):1699–1727, 2006. doi: 10.1016/j.ijplas.2006.02.007.

P. Håkansson, M. Wallin, and M. Ristinmaa. Prediction of stored energy in polycrystalline materials during cyclic loading. *International Journal of Solids and Structures*, 45(6):1570 – 1586, 2008. doi: 10.1016/j.ijsolstr.2007.10.009.

J. Johnsen, A. H. Clausen, F. Grytten, A. Benallal, and O. S. Hopperstad. A thermo-elasto-viscoplastic constitutive model for polymers. *Journal of the Mechanics and Physics of Solids*, 124:681–701, 2019. doi: 10.1016/j.jmps.2018.11.018.

M. Kamlah. *Zur Modellierung des Verfestigungsverhaltens von Materialien mit statischer Hysterese im Rahmen der phänomenologischen Thermomechanik*. PhD thesis, Universität Gesamthochschule Kassel, 1994.

M. Kamlah and P. Haupt. On the macroscopic description of stored energy and self heating during plastic deformation. *International Journal of Plasticity*, 13(10):893–911, 1998. doi: 10.1016/S0749-6419(97)00063-6.

P. Knysh and Y. P. Korkolis. Determination of the fraction of plastic work converted into heat in metals. *Mechanics of Materials*, 86:71 – 80, 2015. doi: 10.1016/j.mechmat.2015.03.006.

J. Kratochvil and O. W. Dillon. Thermodynamics of elastic-plastic materials as a theory with internal state variables. *Journal of Applied Physics*, 40(8):3207–3218, 1969. doi: 10.1063/1.1658167.

J.-M. Muracciole, B. Wattrisse, and A. Chrysochoos. Energy balance of a semicrystalline polymer during local plastic deformation. *Strain*, 44(6):468–474, 2008. doi: 10.1111/j.1475-1305.2007.00412.x.

P. P. Oldyrev. Self-heating and failure of plastics under cyclic loading. *Polymer Mechanics*, 3(3):322–328, 1967. doi: 10.1007/BF00858775.

P. P. Oldyrev and V. P. Tamuzh. Energy dissipation in a glass-reinforced plastic during prolonged cyclic deformation. *Strength of Materials*, 1(3):244–248, 1969. doi: 10.1007/BF01543209.

H. Sparr, R. Roszak, I. Sagradov, D. Schob, and M. Ziegenhorn

Tech. Mech., Vol. 40, Is. 1, (2020), 66–76

W. Oliferuk and B. Raniecki. Thermodynamic description of the plastic work partition into stored energy and heat during deformation of polycrystalline materials. *European Journal of Mechanics - A/Solids*, 71:326 – 334, 2018. doi: 10.1016/j.euromechsol.2018.04.002.

A. V. Shutov and J. Ihlemann. On the simulation of plastic forming under consideration of thermal effects. *Materialwissenschaft und Werkstofftechnik*, 42(7):632–638, 2011. doi: 10.1002/mawe.201100821.

W. Thomson. XV.— On the dynamical theory of heat, with numerical results deduced from mr joule's equivalent of a thermal unit, and m. regnault's observations on steam. *Transactions of the Royal Society of Edinburgh*, 20(2):261–288, 1853. doi: 10.1017/S0080456800033172.

C. Truesdell and W. Noll. *The Non-Linear Field Theories of Mechanics*. Springer-Verlag, Berlin, 3rd edition, 2004. doi: 10.1007/978-3-662-10388-3.

T. Ummenhofer and J. Medgenberg. Numerical modelling of thermoelasticity and plasticity in fatigue-loaded low carbon steels. *Quantitative InfraRed Thermography Journal*, 3(1):71–91, 2006. doi: 10.3166/qirt.3.71-91.

Modeling of hyperelastic material accounting for the Mullins effect by defining a new stiffness reduction variable

Elisabeth Toups[1]⋆, Robert Seewald[2], Benjamin Schaaf[3], Hagen Holthusen[1], Uwe Reisgen[2], Markus Feldmann[3], Stefanie Reese[1],and Jaan-Willem Simon[1]

[1] RWTH Aachen University, Institute of Applied Mechanics, Mies-van-der-Rohe-Str. 1, 52074 Aachen, Germany

[2] RWTH Aachen University, Welding and Joining Institute, Pontstraße 49, 52062 Aachen, Germany

[3] RWTH Aachen University, Institute of Steel Construction, Mies-van-der-Rohe-Str. 1, 52074 Aachen, Germany

Abstract: Supporting structures in the field of glass façade construction are increasingly relying on making use of silicone adhesives. Hence, predicting the hyperelastic behavior and the stiffness reduction (Mullins effect) of such adhesives is essential for the economical dimensioning of load-bearing bonds. For this, a phenomenological hyperelastic model at finite strains is defined, which enables an accurate prediction of the real material behavior. The presented model is based on the Ogden model. Two internal variables are defined, which describe stiffness reduction during loading and unloading procedures and hardening or softening behavior, to model the experimentally observed behavior. For the calibration of the corresponding material parameters, a staggered parameter identification scheme is proposed in order to obtain a unique parameter set for the representation of multiaxial stress states. The excellent model prediction is shown by selected examples.

Keywords: rubberlike material, hyperelasticity, Mullins effect, silicone adhesives, continuum damage mechanics, finite strains

1 Introduction

Load bearing bonds become increasingly common in glass-façade structures. This is due to their beneficial characteristics, such as the more continuous load transfer between glass and the supporting elements compared to alternative connections, and the possibility to achieve a more transparent design. Utilized adhesives show rubber-like, hyperelastic material response under large deformations. During experimental investigations, stiffness reduction is observed referred to as Mullins effect (see e.g. Mullins (1948), Bueche (1961)). Until now, German regulations for the dimensioning of load bearing bonds include very high safety factors (ETAG (2012)) which could be reduced by using a more sophisticated prediction of the real material behavior (Richter et al. (2014)). Thereby, a higher material utilization would be possible. To provide better predictions, a material model representing the complex behavior mentioned above is needed to enable a less time consuming and less cost intensive realistic calculation and design. To the phenomenological material models belong above all the classical approaches of Mooney (1940) and Rivlin (1948) as well as of Ogden (1984). These models are still frequently used today because they are relatively simple and contain only a small number of material constants to be characterized. Comparisons between these and other phenomenological models for the mechanical behavior of hyperelastic materials and the characterization of the associated parameters can be found in Steinmann et al. (2012), Martins et al. (2006), Meunier et al. (2008). There, it is shown that these models are suitable to describe the nonlinear elastic stress-strain behavior of rubber-like materials. However, these material models are not able to represent stress softening which occurs in the considered adhesives. This softening occurs particularly under repeated loading as is referred to as Mullins effect, which was first observed by Bouasse and Carrière (1903). In the last decades, a lot different approaches were figured out to model the Mullins effect. Ogden and Roxburgh proposed the idea that the model response of the material behavior can be described in terms of a pseudo-energy function. To describe the elastic behavior, an internal variable is set to a constant value and activated, so that damage occurs during relief (Ogden and Roxburgh (1999)). Dorfmann and Ogden developed a new approach based on the Ogden-Roxburgh model. They defined two variables within the free energy. The first variable describes the damage and softening behavior, the second variable describes the accumulation of residual strain during loading and unloading cycles and is called the residual strain variable (Dorfmann and Ogden (2004)). A more detailed overview of selected models describing the Mullins effect can be found in Diani et al. (2009). textcolorblackIt is known from the literature that the stress strain behavior depends strongly on the angle between the current and the previous direction of loading. This anisotropy induced by the Mullins effect in the deformation history was already observed by e.g. Mullins (1948), Arruda and Przybylo (1995), Pawelski et al., Besdo et al. (2003). Studies on this topic can be found in e.g. Ihlemann (2005), Itskov et al. (2006), Kahraman et al. (2010).

This paper presents a phenomenological model to describe the softening (Mullins effect) of silicone adhesives based on the Ogden model with a thermodynamically consistent extension to account for the stiffness reduction, neglecting the above mentioned anisotropy and further effects like viscosity, hysteresis and plasticity. The model parameters are identified in a staggered procedure in such a way that a unique set of parameters is created which also enables the modeling of multi-axial stress states. Selected validation examples under consideration of multi-axial stress states are presented at the end.

2 Experimental studies and material behavior

To model the behavior of the silicone adhesive, at first, the experimental material behavior was observed. A uniaxial tension test was performed under cyclic loading up to a maximum technical strain of 100%. The experimental results were observed from that part of the specimen in between the white lines (see Fig. 1), where a homogeneous material behavior can be expected. The distance between these white lines is 20 mm and the dimensions of the test's relevant area, marked with the red box in Fig. 1 are 60 mm x 10 mm x 4 mm. The corresponding relation of logarithmic strain and first Piola Kirchhoff stress is shown in Fig. 1.
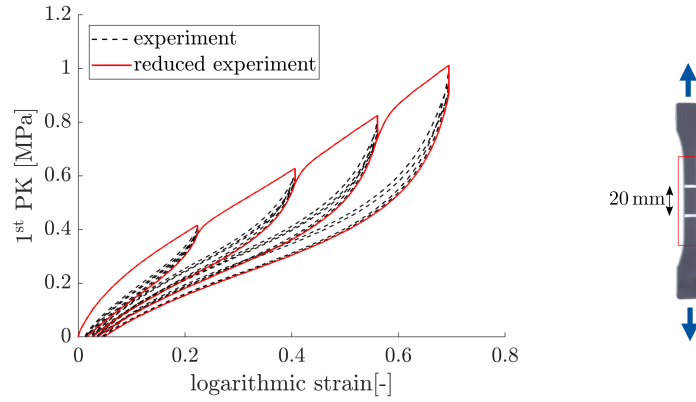
Fig. 1: Experimental observation: Uniaxial tension test

The stress strain behavior represents an S-shaped curve typical for hyperelastic materials. Furthermore, stiffness reduction can be observed, which is also described by the Mullins effect. The Mullins effect occurs during cyclic loading and in particular, the stress softening during the first and second loading and unloading cycles is noticeable. After about five to ten cycles, depending on the material, a stabilized hysteresis loop can be reached, see e.g. Harwood et al. (1965), Johnson and Beatty (1993), Beatty and Krishnaswamy (2000), Cantournet et al. (2009). There are different physical explanations and interpretations of the Mullins effect in literature. Rubbers in general consists of polymers. These polymer chains can be strengthened by adding particles, so that the filled rubber consists of a network of polymer chains filled with some particles Böl (2005). The anisotropy induced by the Mullins effect, as observed e.g. by Mullins (1948), is neglected and in addition, no hysteresis effects, viscosity or plasticity are taken into account in the material model presented here. Therefore, the experimental data were reduced accordingly so that the idealized Mullins effect is preserved. For this the experimental data are read out in such a way that the load curves and the last relief curves per cycle are taken into account, the cycles in between are neglected. This is shown in Fig. 1 by the red curve. For the investigation of shear behavior, a pure shear test was studied. In a pure shear test, a special geometry of the specimen is required: One edge of the thin specimen must be much longer than the other. Investigations show that the dimension of the adhesive with 200 mm x 50 mm x 3 mm is suitable to generate a pure shear behavior within the considered adhesive. The pure shear behavior is observed in the center of the specimen. For illustration, the specimen in the loaded state due to elongation in y-direction, perpendicular to the longer edge length, is shown schematically in Fig. 2.
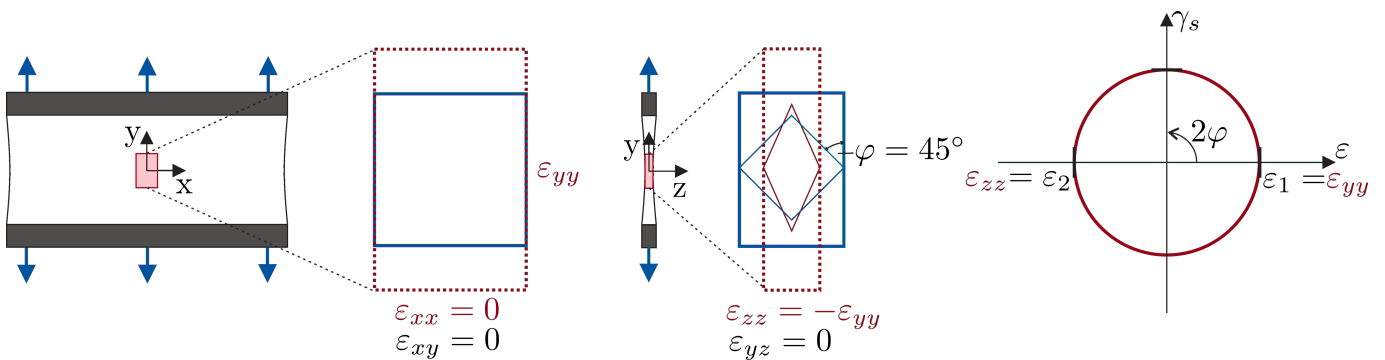
Fig. 2: Details about pure shear behavior in an incompressible material

Due to the chosen geometry there is no influence from the transversal contraction in the center of the specimen, so that $\varepsilon_{xx} = 0$, and ε_{yy} increases because of the elongation. In contrast, ε_{zz} decreases due to the contraction in z-direction. Considering an incompressible material, the contraction in z-direction is equal to the elongation in y-direction, $\varepsilon_{zz} = -\varepsilon_{yy}$. This is indicated by the following deformation gradient:

$$F_{ij} = \begin{bmatrix} 1 & 0 & 0 \\ 0 & \lambda & 0 \\ 0 & 0 & \lambda^{-1} \end{bmatrix}, \tag{1}$$

where λ is the respective stretch. The plotted strains into y- and z-direction, which are exactly the same size, imply that a pure shear deformation is obtained at an angle of 90° in Mohr's circle. The maximum shear strain is reached when $\varepsilon_{yy} = \varepsilon_{zz} = 0$.
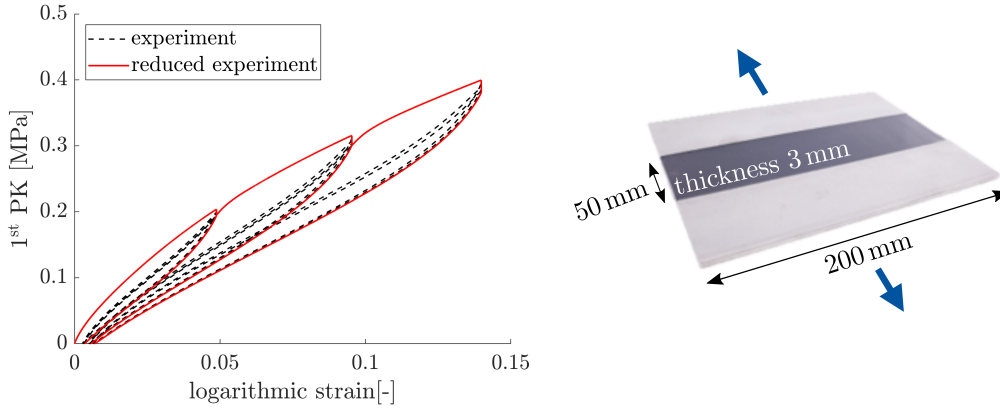
Fig. 3: Experimental observation: Pure shear test

In Fig. 3 the specimen used for the test procedure is shown. If the specimen constricts strongly due to its almost incompressible behavior at high strains, a pure sample may slip slightly out of the clamp each time a new strain level is approached. Joined specimens were used to avoid the remaining strain resulting from these friction losses in the clamping area. Stainless steel sheets were used as joining partners and clamped into the test bench. Since the stainless steel practically does not deform at the comparatively very low loads and thus does not change thickness, the problem of friction loss and the associated successive slippage of the specimen could be avoided. The load was thus transferred to the adhesive via adhesion to the parts to be joined and no longer via a frictional clamping effect. For evaluation, the logarithmic longitudinal strain perpendicular to the longer edge length and the first Piola Kirchhoff stress in the stretched direction are considered, see Fig. 3. Here, too, the curve obtained from the experiment is reduced to the envelope red curve.

At least a compression test was performed to investigate the volumetric deformation. Here, a cylindrical pure substance sample with a diameter of 20 mm and a height of 30 mm, is uniaxially loaded, while deformation in the other two spatial directions is prevented, see Fig. 4. A change in shape is only possible by reducing the volume. The experimental implementation takes place in a precisely fitting steel tube into which the test specimen is inserted and then loaded with a punching force. The nearly linear relation of pressure p and the specific volume ratio $\Delta V / V$ is shown in Fig. 4.
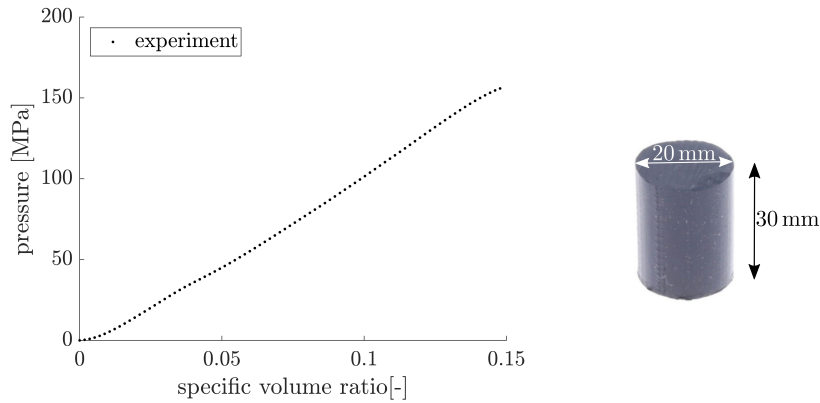
Fig. 4: Experimental observation: Compression test

3   Material modeling

The total Helmholtz free energy of this model is defined as

$$\psi = \psi_{el}(\lambda_1, \lambda_2, \lambda_3, \rho) + \psi_c(\delta), \tag{2}$$

where the first part is based on the Ogden model for hyperelasticity

$$\psi_{el}(\lambda_1, \lambda_2, \lambda_3, \rho) = \sum_{k=1}^{3} \mu_k(\rho) \left[\frac{1}{\alpha_k} (\lambda_1^{\alpha_k} + \lambda_2^{\alpha_k} + \lambda_3^{\alpha_k} - 3) - \ln J \right] + \frac{\Lambda}{4} (J^2 - 1 - 2\ln J), \tag{3}$$

the free energy function of which is defined as a function of the principal stretches λ_i, $i = 1, 2, 3$, and contains the material parameters μ_k and α_k. J is the product of the principal stretches and Λ is the Lamé constant. As a new variable ρ is defined for taking into account stiffness reduction. This variable is assumed to be a scalar and works as an internal variable taking values

between 0 and 1. The following formulation $\mu_k(\rho)$ is defined, which is used instead of the original parameters μ_k:

$$\mu_k(\rho) = \begin{cases} \mu_k^0 & \text{if} \quad \rho = 0 \\ (1-\rho)^{p_k}(\mu_k^0 - \mu_k^\infty) + \mu_k^\infty & \text{if} \quad 0 < \rho < 1 \\ \mu_k^\infty & \text{if} \quad \rho = 1 \end{cases} \tag{4}$$

In the standard continuum damage mechanics approach, the model response results in failure for the case $D = 1$ (D is the damage variable). On the contrary, in the current formulation, $\rho = 1$ does not refer to failure but to a final stress-strain relationship which can be represented by the model. The parameters μ_k^∞ are needed to describe this last stress-strain curve. In contrast, μ_k^0 (the value of $\mu_k(\rho = 0)$) are artifical parameters, which are needed to describe the stress-strain behavior during the stiffness reduction, and do not reflect any physical properties. The advantage of this embedded variable ρ is, that stiffness reduction is considered specifically in each Ogden term. The consideration of the newly introduced variable leads to an additional term ψ_c, which is added in the free energy function in order to control the development of stiffness reduction and to model the softening/hardening behavior (cf. e.g. Brepols et al. (2017), Simon et al. (2017)). For this control part, the following exponential formulation

$$\psi_c(\delta) = c_1\left(\delta + c_2 e^{-\frac{\delta}{c_2}} - 1\right) \tag{5}$$

was chosen, which depends on the softening/hardening variable δ and also contains the two model parameters $c_1 > 0$ and $c_2 > 0$. Both parts, $\mu_k(\rho)$ and $\psi_c(\delta)$, can be chosen freely and independently, making the model very flexible. Following general thermodynamical considerations, the second law of thermodynamics must be fulfilled and is therefore exploited to derive the state relations of the model.

$$-\dot{\psi} + \mathbf{P} \cdot \dot{\mathbf{F}} \geq 0 \tag{6}$$

$$\underbrace{\left(\mathbf{P} - \frac{\partial \psi}{\partial \mathbf{F}}\right)}_{\mathbf{P} = \frac{\partial \psi}{\partial \mathbf{F}}} \cdot \dot{\mathbf{F}} - \underbrace{\frac{\partial \psi}{\partial \rho}}_{:= Y} \dot{\rho} - \underbrace{\frac{\partial \psi}{\partial \delta}}_{:= \gamma} \dot{\delta} \geq 0 \tag{7}$$

In the considered case, the first Piola-Kirchhoff stress tensor is denoted by $\mathbf{P}$, and $\mathbf{F}$ is the deformation gradient. The remaining dissipation inequality provides the thermodynamic conjugated forces of the model, which can be computed by $\frac{\partial \psi}{\partial \rho}$ and $\frac{\partial \psi}{\partial \delta}$, which are abbreviated to Y and γ, respectively. In order to define the onset of stiffness reduction as well as the hardening or softening behavior, the stiffness reduction criterion is defined as

$$\Phi = Y - Y_0 - \gamma(\delta) \leq 0 \tag{8}$$

Here, Y_0 is an additional material parameter and defines the threshold of stiffness reduction. According to the generalized normality rule, the evolution of stiffness reduction and hardening/softening variables are given by

$$\dot{\rho} = \dot{\kappa}\frac{\partial \Phi}{\partial Y} = \dot{\kappa}, \quad \dot{\delta} = -\dot{\kappa}\frac{\partial \Phi}{\partial \gamma} = \dot{\kappa} \tag{9}$$

where $\dot{\kappa}$ represents the required multiplier. Further, the Karush-Kuhn-Tucker-conditions must hold:

$$\dot{\kappa} \geq 0, \quad \Phi \leq 0, \quad \dot{\kappa}\Phi = 0 \tag{10}$$

The condition $\Phi = 0$ induce that thermodynamic driving force is generated whenever the stress is high enough and stiffness reduction is accumulating. On the contrary stiffness reduction does not evolve, for example in case of unloading, if $\Phi < 0$. Therefore, in this framework, stiffness reduction can only grow ($\dot{\kappa} \geq 0$).

4　Fitting procedure and selected experiments

The model contains fifteen parameters in total. The influence of the Lamé constant Λ in the second part of ψ_{el} can be neglected if the material is nearly incompressible and if $\Lambda >> \mu_k(\rho)$ is adhered to for all k and ρ. In order to determine Λ in the correct order of magnitude, a computation based on the bulk modulus K from a compression test can be done separately at the beginning of the fitting procedure. For the computational determination of Λ, the compression modulus K was determined from the compression test in Fig. 4 with

$$K = \frac{p}{\frac{dV}{V}} = 1176\,\text{MPa} \tag{11}$$

With the Poisson's ratio ν, the following relationship between the Lamé constant Λ and the bulk modulus K applies from linear theory

$$\Lambda = \frac{3K}{1 + \frac{1}{\nu}} \tag{12}$$

With $\nu = 0.495$ one obtains $\Lambda = 1168$ MPa. This means that strictly speaking, the value only applies exactly to the linear initial range. To get one parameter set for a representation of all loading conditions, it is necessary to fit the remaining parameters simultaneously to results of a tension test and a shear test. Experiments to consider tension could be uniaxial or biaxial tension tests, and simple shear or pure shear experiments are both suitable for the consideration of shear tests. For the fitting procedure, the remaining parameters are initially divided into two groups. The first parameter group comprises the parameters μ_k^∞ and α_k, which describe the general S-shape of the stress-strain curve. The second group contains the parameters from the stiffness reduction (p_k), the control term (c_1, c_2) and the artificial parameters (μ_k^0). This group influences the occurrence and progression of stiffness reduction. These two groups can be fitted independently. The first group containing μ_k^∞, which relates to the last unloading path, can be fitted together with α_k to the last stress-strain curve measured in the experiment and the remaining parameters (group 2) are fitted to the experimental results of the cyclically loaded tests, Fig. 5.
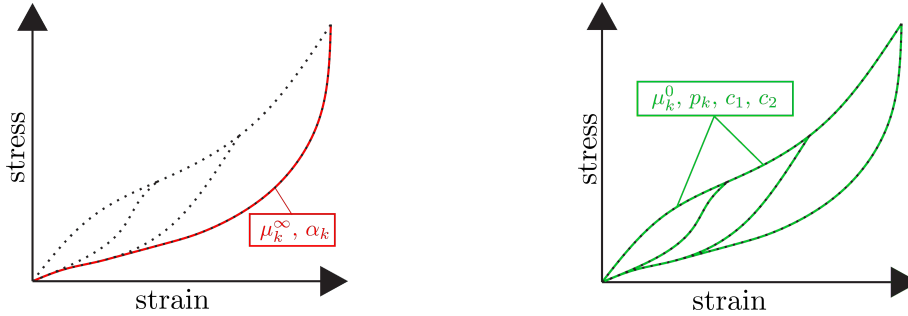
Fig. 5: Separate parameter fitting to last unloading path and to cyclic experimental data

The parameters were adjusted using the Optimization Toolbox$^{\text{TM}}$ in MATLAB, which enables a nonlinear algorithm for least squares, *lsqcurvefit*. For a simultaneous fit it is necessary to feed the test data into the algorithm in matrix form. The number of data points of all test data must correspond to each other. With manual weighting of the test data to achieve better fitting results, the matrix entries of different lengths can be filled by adding zero vectors. The fitted parameter set (Tab. 1) results in a very good representation of the uniaxial tension test and of a pure shear test, shown in Fig. 6.
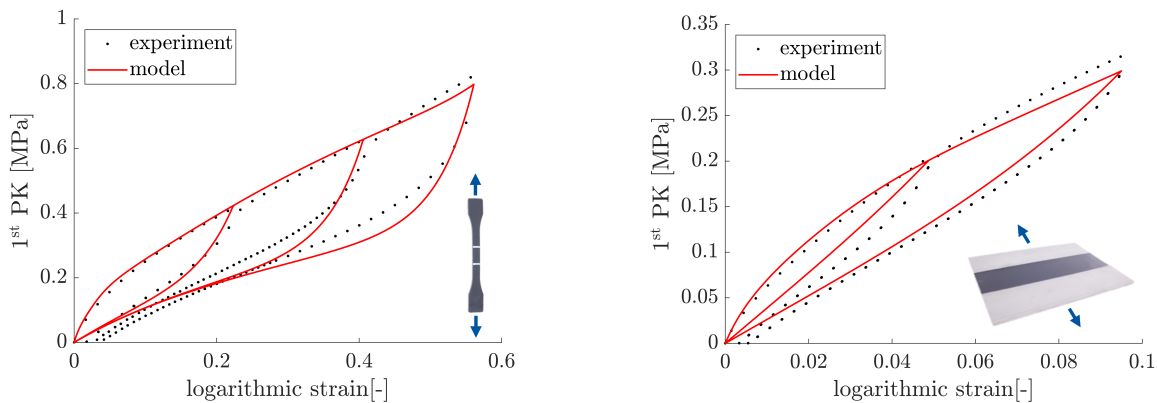
Fig. 6: Simultaneous fit to uniaxial tension test and pure shear test

Tab. 1: Model parameters of the proposed model

elastic parameters						
μ_1^∞ [MPa]	μ_2^∞ [MPa]	μ_3^∞ [MPa]	α_1 [-]	α_2 [-]	α_3 [-]	Λ [MPa]
0.250	$3.91E-07$	-0.195	0.011	21.422	-4.398	1168
stiffness reduction parameters						
μ_1^0 [MPa]	μ_2^0 [MPa]	μ_3^0 [MPa]	p_1 [-]	p_2 [-]	p_3 [-]	c_1 [MPa]	c_2 [-]
33.496	0.118	-0.523	4312.2	149.27	1017.6	3327.8	43.73

In general, the material parameters are determined to positive values. However, in order to map the S-shaped curve observed in the experiment, one exponent α_k must be negative as also shown by Ogden (1984). In Ogden (1972) the stability condition $\mu_k \alpha_k > 0$ is defined. From this, it follows that with a negative exponent α_k the corresponding μ_k must also be negative.

5 Model validation

To validate the model, its prediction regarding multiaxial stress states is compared with experimental data. For this, the model formulation was implemented as user material subroutine into the FEM software FEAP Taylor (2014). In addition to the possibility

of using the standard element $Q1$, the use and suitability of an advanced finite element technology was investigated, because modeling hyperelastic materials can evoke mesh distortion. The used element formulation, which is very efficient and robust against mesh distortion was formulated in Reese (2005). This formulation makes use of a reduced integration plus adaptive hourglass stabilization concept. The stabilization factors are computed based on the enhanced strain method. Moreover, this element formulation is very efficient from computational point of view, due to the integration in only one Gaussian point.

For validation, two examples will be shown and discussed in the following. As a first example, a so called butt joint tensile test was chosen. This bonded specimen shows a large number of shows a large number of practice-relevant multi-axial stress states and is therefore particularly suitable for checking material laws. Two steel cylinders are connected to each other by an adhesive layer. The test was carried out under strain-control with cyclic loading. During loading the adhesive layer was elongated in axial direction. By using symmetry, the test specimen can be calculated two-dimensionally or three-dimensionally on a circular cylinder sector. The following results were generated with the displacement-controlled calculation of a circular cylinder sector whose cross-section is shown in Fig. 7. Based on the study of mesh convergence, shown in Fig. 8, 390 elements were chosen, because this mesh has already reached a converged solution.

The model prediction compared to experimental results is shown in Fig. 9 and shows a very good match. For this computation the fitted parameters from Section 4 were used.
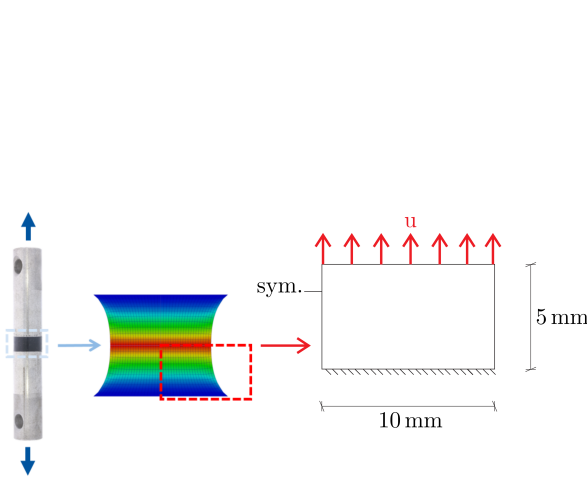
Fig. 7: Butt joint tensile test
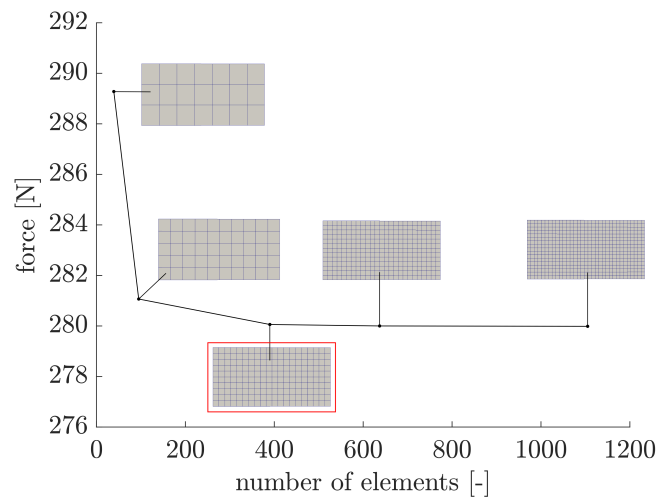
Fig. 8: Mesh convergence butt joint tensile test

A comparison of the advanced finite element formulation $Q1SP$ used here and the standard element $Q1$ of FEAP, in Fig. 10, shows that 390 elements with the standard element $Q1$ are obviously not sufficient to predict the experimental results well enough, whereas 390 elements with $Q1SP$ provide a reliable prediction. Also, increasing the number of elements to 1000 elements does not sufficiently improve the prediction using the $Q1$ elements. As already shown in the study of mesh convergence, about 1000 elements with $Q1SP$ lead to a similar prediction as 390 elements, these curves lie exactly on top of each other.
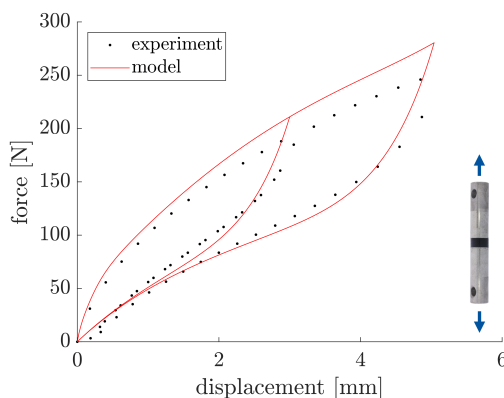
Fig. 9: Model prediction in comparison to experimental results for the butt joint tensile test
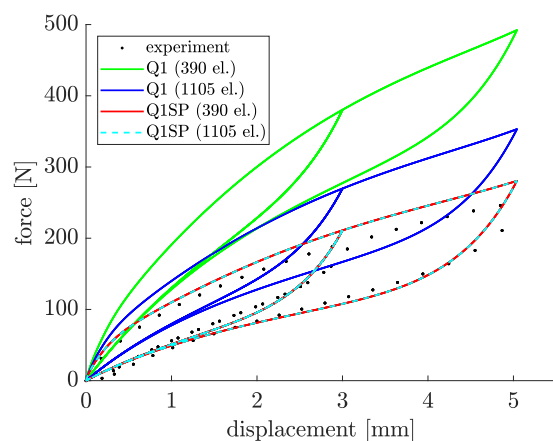
Fig. 10: Model prediction with different discretization and element types for the butt joint tensile test

The second example of validation is the specimen shown in Fig. 11, which is intended to resemble a component-like sample. With the aid of the component-like sample, a mixed stress state is to be generated within the connection. This results, for example, from a wind suction load on a façade element that is glued on all sides. Due to the plate loading of the glass pane, it undergoes a deflection which leads to a rotation in the joint.
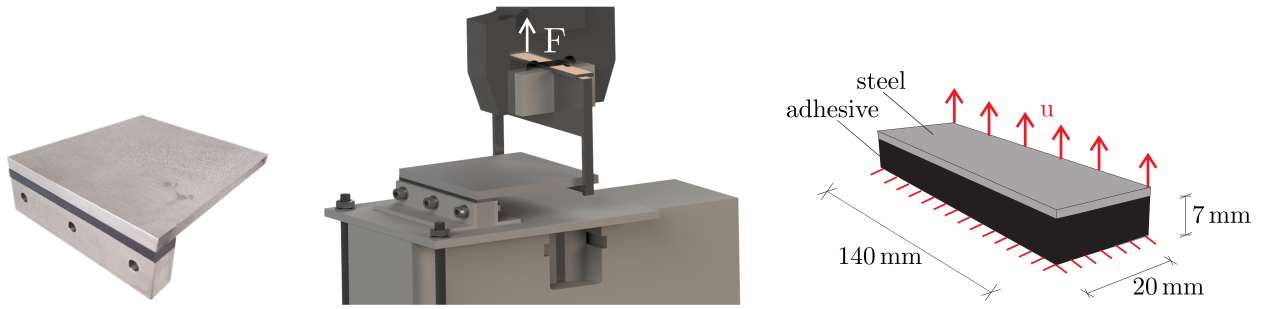
Fig. 11: Validation specimen in testing machine and simple sample for simulation

The specimen consists of a steel beam and a steel plate connected to each other by the adhesive layer. The lower steel beam is clamped in the test stand and at the end of the lever the sheet metal of the bonded specimen is pulled upwards in the load axis. For the simulation, the entire specimen was reduced to the sample section in Fig. 11, considering only the adhesive layer and a section of the upper steel plate. The bottom is completely fixed and the steel plate edge is moved upwards. The displacement applied to the lever end during the test was converted to the required displacement at the selected steel edge using the deflection angle for the displacement specification in the FE calculation. Since the evaluation of a force-displacement curve in this experiment is dependent on the length of the lever arm, the load-bearing behavior of the adhesive was represented in the form of a torsional momentum curve. As can be seen in Fig. 12, the length l_φ can be used to determine a momentum with $M = F \cdot l_\varphi$ that is independent of the length of the lever arm. The model prediction is in good match with the experimental results, see in Fig. 12. In particular, the maximum point from the prediction matches very well to the experimental data.
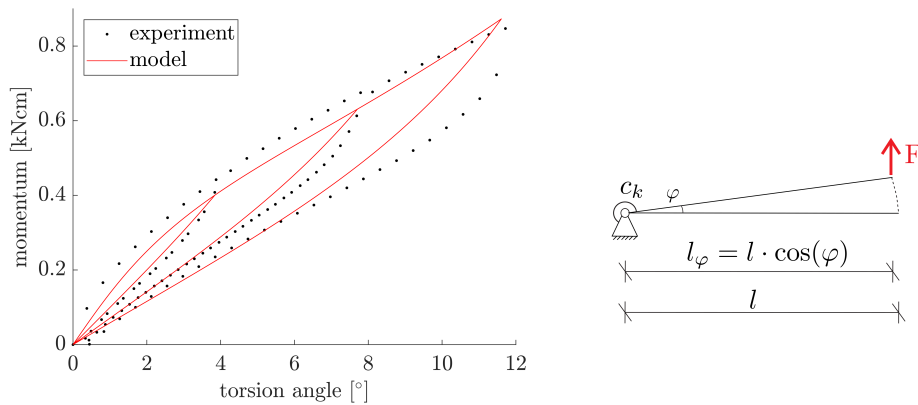
Fig. 12: Torsion angle and momentum relation

6 Comparison of the proposed model with the Ogden-Roxburgh model

To investigate the behavior of the proposed model in comparison to existing models from literature, the proposed model is also compared to the Ogden-Roxburgh model (Ogden and Roxburgh (1999)). First, the results of the simultaneous parameter fit to the uniaxial tension test and the pure shear test are compared, followed by the calculation of the butt joint tensile test, already shown in Section 5. The Ogden-Roxburgh model already implemented in the FE software Abaqus Systèmes (2016) was used for this comparison. The in Abaqus modified strain energy density function has the form

$$\psi(\bar{\lambda}_i, \eta) = \eta \psi_{dev}(\bar{\lambda}_i) + \Phi(\eta) + \psi_{vol}(J). \tag{13}$$

This function is splitted into a deviatoric part $\psi_{dev}(\bar{\lambda}_i)$ and a volumetric part $\psi_{vol}(J)$, depending on the deviatoric principal stretches $\bar{\lambda}_i = J^{-\frac{1}{3}} \lambda_i$ and the volume ratio J respectively. The continuous damage function $\Phi(\eta)$ depends on the damage variable η, which varies according to

$$\eta = 1 - \frac{1}{r} erf\left(\frac{\psi_{dev}^m - \psi_{dev}}{m + \beta \psi_{dev}^m}\right), \tag{14}$$

where the Gauss error function $erf(x)$ contains the ratio of ψ_{dev}^m, which is the maximum value of ψ_{dev} at a material point during

its deformation history. Corresponding to the Ogden model in Abaqus, $\psi_{dev}(\bar{\lambda}_i)$ is defined by

$$\psi_{dev}(\bar{\lambda}_i) = \sum_{i=1}^{N=3} \frac{2\mu_i}{\alpha_i^2} (\bar{\lambda}_1^{\alpha_i} + \bar{\lambda}_2^{\alpha_i} + \bar{\lambda}_3^{\alpha_i} - 3). \tag{15}$$

The volumetric part of the strain energy is defined by

$$\psi_{vol}(J) = \sum_{i=1}^{N=3} \frac{1}{D_i} (J - 1)^{2i}. \tag{16}$$

The corresponding elastic parameters μ_i, α_i, compression parameter D_i and the damage parameters r, β and m were determined in Abaqus itself on the basis of imported test data from the uniaxial tension test and the pure shear test (see Section 2) and are shown in Tab. 2.

Tab. 2: Model parameters of the Ogden-Roxburgh model

elastic parameters								
μ_1 [MPa]	μ_2 [MPa]	μ_3 [MPa]	α_1 [-]	α_2 [-]	α_3 [-]	D_1 [MPa^{-1}]	D_2 [MPa^{-1}]	D_3 [MPa^{-1}]
-44.051	19.112	25.859	1.524	2.039	0.969	$2.18E-02$	0.0	0.0
damage parameters								
r [MPa]	m [MPa]	β [MPa]						
1.248	$3.01E-02$	1.038						

In contrast to the parameter limitation of the proposed model presented in Section 4, the parameters in Abaqus are controlled during the fit to the experimental data by checking the Drucker stability Systèmes (2016). A limitation of the parameters μ_i and α_i, as in the proposed model by $\mu_i\alpha_i > 0$, does not exist in Abaqus.
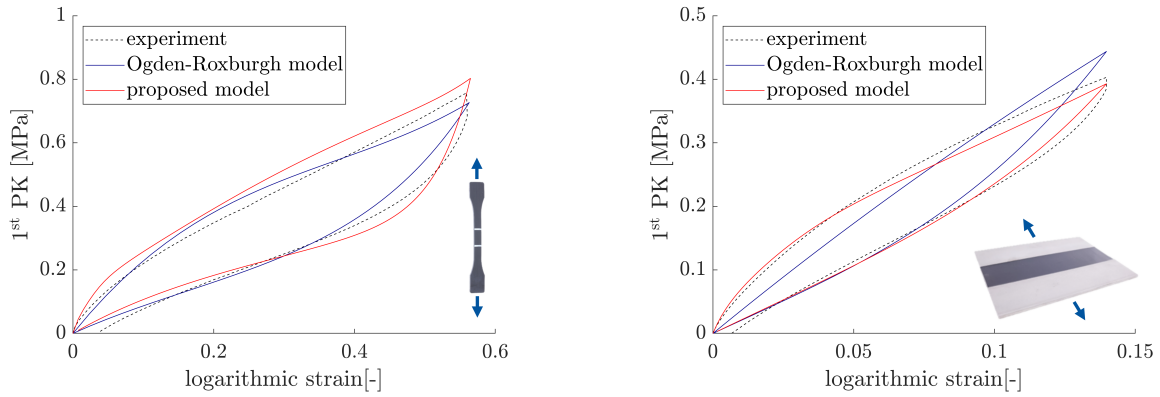
Fig. 13: Comparison of Ogden-Roxburgh model and proposed model in simultaneous fit to uniaxial tension test and pure shear test
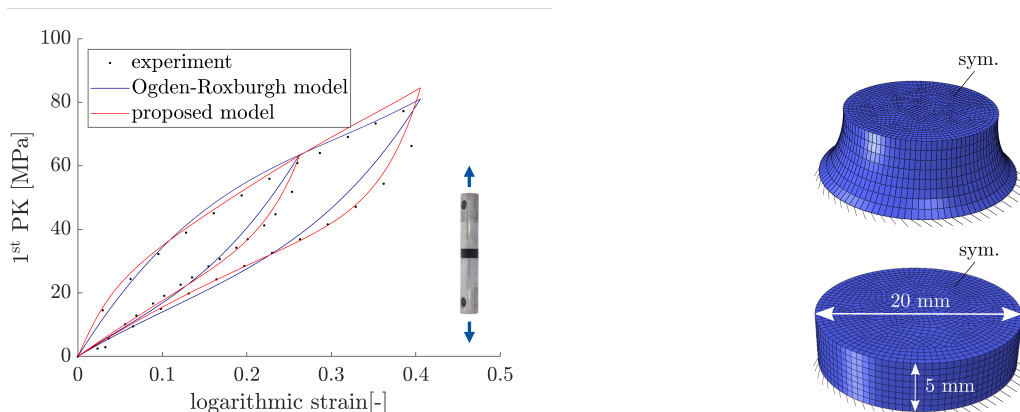
Fig. 14: Comparison of Ogden-Roxburgh model and proposed model in simulation of butt joint tensile test

The results fitted by the Ogden-Roxburgh model compared to the results fitted by the proposed model in Section 4 are shown in Fig. 13. A significantly better fitting result is provided by the proposed model for the unloading path in the uniaxial tension test compared to the Ogden-Roxburgh model. The pure shear test is described much better in the initial range by the proposed model and up to an elongation of 10% also in the relief range. The Ogden-Roxburgh model, on the other hand, strongly underestimates the initial range of the pure shear test and overestimates the actual material behavior at higher strains. The further investigation shows the comparison of the model responses for the calculation of the butt joint tensile test from Section 5. For this, the element C3D8RH was used in Abaqus. The stress-strain behavior of the sample with corresponding geometry from Fig. 7 is shown in Fig. 14. Similar to the comparison with the fits on the uniaxial tension test, the proposed model also matches the unloading paths better than the Ogden-Roxburgh model. On the other hand, the maximum stress is better predicted by the Ogden-Roxburgh model.

7   Conclusion and outlook

A flexible model for a hyperelastic material with exchangeable parts such as the stiffness reduction function, the elastic formulation, and the control term was presented. The parameters of the model were obtained from a staggered fitting procedure and were successfully fitted to compression test, uniaxial tensile, and pure shear test data simultaneously. First computational results demonstrated the accurate prediction of the proposed model, enabling the representation of multi-axial stress states of a hyperelastic material behavior considering stiffness reduction (Mullins effect) at large deformations. For the implementation in the FE program FEAP the element formulation Q1SP was used. It could be observed that compared to the standard element formulation Q1 for Q1SP a significantly smaller number of elements is required to achieve acceptable results. In a further step, the efficiency, parameter determination and the accuracy of the new model were compared with the Ogden-Roxburgh model from the literature and will also be compared with other models from the literature in future research work. In order to extend the proposed material model by a failure prediction, it would first be necessary to investigate the failure behavior within experimental studies. Based on these results, the model formulation can be extended to improve the prediction possibilities. Furthermore, the consideration of plastic deformation could be another step to make the model formulation more flexible and to achieve a higher agreement between the real material behavior and the model response.

Acknowledgments

References

E. M. Arruda and P. A. Przybylo. An investigation into the three-dimensional stress-birefringence-strain relationship in elastomers. *Polymer Engineering and Science*, 35(5):395–402, 1995.

M. F. Beatty and S. Krishnaswamy. The Mullins effect in equibiaxial deformation. *Zetischrift für angewandte Mathematik und Physik ZAMP*, 51(6):984–1015, 2000.

D. Besdo, J. Ihlemann, J. G. R. Kingston, and A. H. Muhr. Constitutive Models for rubber III. *Balkema*, page 309, 2003.

M. Böl. *Numerische Simulation von Polymernetzwerken mit Hilfe der Finite-Elemente-Methode; Dissertation*. Number 135. Ruhr- Universität Bochum; Institut für Mechanik; Mitteilungen aus dem Institut für Mechanik Nr. 135, 2005.

H. Bouasse and Z. Carrière. Courbes de traction du caoutchouc vulcanisé. *Annales de la Faculté des Sciences*, 5:257–283, 1903.

T. Brepols, S. Wulfinghoff, and S. Reese. Gradient-extended two-surface damage-plasticity: micromorphic formulation and numerical aspects. *International Journal of Plasticity*, 97:64–106, 2017. doi: 10.1002/pamm.201610048.

F. Bueche. Mullins effect and rubber-filler interaction. *Journal of Applied Polymer Science*, 5(15):271–281, 1961.

S. Cantournet, R. Desmorat, and J. Besson. Mullins effect and cyclic stress softening of filled elastomers by internal sliding and friction thermodynamics model. *International Journal of Solids and Structures*, 46(11-12):2255–2264, 2009.

J. Diani, B. Fayolle, and P. Gilormini. A review on the Mullins effect. *European Polymer Journal*, 45:601——612, 2009. doi: 10.1016/j.eurpolymj.2008.11.017.

A. Dorfmann and R. W. Ogden. A constitutve model for the Mullins effect with permanent set in particle-reinforced rubber. *International Journal of Solids and Structures*, 41:1855–1878, 2004.

ETAG. *ETAG no. 2. Guideline for European technical approval for structural sealant glazing kits.*, 2012.

J. A. C. Harwood, L. Mullins, and A. R. Payne. Stress softening in natural rubber vulcanizates. Part II. Stress softening effects in pure gum and filler loaded rubbers. *Journal of Applied Polymer Science*, 9(9):3011–3021, 1965.

J. Ihlemann. Richtungsabhängigkeiten beim Mullins-Effekt . *KGK Kautschuk Gummi Kunststoffe*, 58:438, 2005.

M. Itskov, E. Haberstroh, A. E. Ehret, and M. C. Vöhringer. Experimental observation of the deformation induced anisotropy of the Mullins effect in rubber. *KGK Kautschuk Gummi Kunststoffe*, 59:93, 2006.

M. A. Johnson and M. F. Beatty. The Mullins effect in uniaxial extension and its influence on the transverse vibration of a rubber string. *Continuum Mechanics and Thermodynamics*, 5(2):83–115, 1993.

H. Kahraman, G. W. Weinhold, E. Haberstroh, and M. Itskov. Anisotroper Mullins-Effekt bei rußgefüllten Elastomeren. *KGK Kautschuk Gummi Kunststoffe*, 63(3):64–69, 2010.

P. A. L. S. Martins, R. M. Natal Jorge, and A. J. M. Ferreira. A comparative study of several material models for prediction of hyperelastic properties: Application to silicone-rubber and soft tissues. *Strain*, 42:135–147, 2006.

L. Meunier, G. Chagnon, D. Favier, L. Orgéas, and P. Vacher. Mechanical experimental characterisation and numerical modelling of an un-filled silicone rubber. *Polymer Testing*, 27:765–777, 2008.

M. Mooney. A theory of large elastic deformation. *Journal of Applied Physics*, 11:582–592, 1940.

L. Mullins. Effect of stretching on the properties of rubber. *Rubber Chemistry and Technology*, 21(2):281–300, 1948.

R. W. Ogden. Large deformation isotropic elasticity–on the correlation of theory and experiment for incompressible rubberlike solids. *Proceedings of the Royal Society of London. Series A: Mathematical and Physical Sciences*, 326(1567):565–584, 1972.

R. W. Ogden and D. G. Roxburgh. A pseudo-elastic model for the Mullins effect in filled rubber. *The Royal Society*, 455: 2861–2877, 1999.

R.W. Ogden. *Non-linear elastic deformations*. Dover Publications, 1984.

H. Pawelski, D. Besdo, R. H. Schuster, and J. Ihlemann. *Constitutive Models for Rubber II*, volume 27.

Stefanie Reese. On a physically stabilized one point nite element formulation for three-dimensional nite elasto-plasticity. *Computer Methods in applied Mechanics and Engineering*, 194:4685–4715, 2005. doi: 10.1016/j.cma.2004.12.012.

C. Richter, B. Abeln, A. Geßler, and M. Feldmann. Structural steel-glass facade panels with multi-side bonding - Nonlinear stress-strain behaviour under complex loading situations. *International Journal of Adhesion and Adhesives*, 55:28–28, 2014. URL https://doi.org/10.1016/j.ijadhadh.2014.07.004.

R.S. Rivlin. Large elastic deformations of isotropic materials. IV. Further developments of the general theory. *Philosophical Transactions of the Royal Society London A: Mathematical, Phys-ical and Engineering Sciences*, 241:379–397, 1948.

J.-W. Simon, D. Höwer, B. Stier, S. Reese, and J. Fish. A regularized orthotropic continuum damage model for layered composites: intralaminar damage progression and delamination. *Computational Mechanics*, 60(3):445–463, 2017. doi: 10.1007/s00466-017-1416-1.

P. Steinmann, M. Hossain, and G. Possart. Hyperelastic models for rubber-like materials: consistent tangent operators and suitability for Treloar's data. *Archive of Applied Mechanics*, 82(9):1183–1217, 2012. doi: 10.1007/s00419-012-0610-z. URL http://link.springer.com/article/10.1007/s00419-012-0610-z.

Dassault Systèmes. Abaqus, Release 6.16. 2016.

R. L. Taylor. *FEAP - A finite element analysis program*, 2014.

Variational material modeling of the transformation induced plasticity in polycrystalline steel

Johanna Waimann[1]⋆, Stefanie Reese[1], and Philipp Junker[2]

[1] RWTH Aachen University, Institute of Applied Mechanics, Mies-van-der-Rohe-Straße 1, 52074 Aachen, Germany
[2] Ruhr-University Bochum, Institute of Continuum Mechanics, Universitätsstraße 150, 42801 Bochum, Germany

Abstract: The effect of transformation induced plasticity (TRIP) describes the coupling of plastic deformations and solid/solid phase transformations in steel. A result of this complex microstructural evolution is an improved ductility and strength of the so-called TRIP-steels, which is the reason for their attractiveness for industrial applications, e.g., in the automobile industry.

Modeling of the mentioned effects is an important aspect for enhancing the knowledge about the challenging processes that evolve in TRIP-steels. To this end, we present a variational material model that is based on the principle of the minimum of the dissipation potential. Considering kinematic hardening, the model describes the simultaneous evolution of an overall plastic strain and of the volume fractions of austenite and of several martensitic variants. Compared to our previous work Waimann et al. (2015), the polycrystalline structure is considered by an evolving orientation distribution function, which results in a much faster computation compared to our former investigations. Our analysis also covers the implementation into a finite element algorithm as well as the presentation of numerical results, which show the model's ability to give a first estimation for the complex material behavior.

Keywords: TRIP-steel, variational modeling, polycrystal, phase transformation, plasticity, kinematic hardening

1 Introduction

The eponymous effect of transformation induced plasticity (TRIP) in steel describes a simultaneous phase transformation and plastic deformation. The literature related to the particular modeling of the individual microstructural effects - the plastic deformation and the phase transformation - is huge. A good overview of plasticity is given in Lubliner (2008). Plasticity models based on variational concepts are exemplary given in Han et al. (1995); Lubliner (1984); Mühlhaus and Alfantis (1991) and for the case of crystal plasticity in, e.g., Svendsen and Bargmann (2010); Hackl et al. (2014); Conti et al. (2009). To mention but a few modeling concepts for martensitic phase transformations, we would like to refer to Govindjee and Hall (2000); Auricchio and Petrini (2004); Govindjee and Miehe (2001); Turteltaub and Suiker (2006b); Babaei et al. (2019). In the past, also, a lot of works have been related to the modeling of the special material behavior of TRIP-steels. Besides earlier works which couple the martensitic phase transformation with plastic deformation by ,e.g., Greenwood and Johnson (1965), Leblond et al. (1986), Leblond et al. (1989), Fischer (1990). The model of Levitas (1998) also examined the martensitic transformation at interfaces and thus at discontinuities of the displacement field in an inelastic material. The model by Olson and Cohen (1975) is the basis for the later studies Iwamoto and Tsuta (2000, 2002): the martensitic transformation is driven by a shear band intersection and a stochastic ansatz is used for the formation of a nucleus. The extension Iwamoto and Tsuta (2000) accounts for a dependence on the austenitic grain size and furthermore, a high fracture toughness is examined in Iwamoto and Tsuta (2002). A study on the change of material properties related to hardening due to the TRIP effect based on Iwamoto and Tsuta (2000) is given in Dan et al. (2008). Another promising approach based on stochastic considerations is presented in Ostwald et al. (2011) for one-dimensional problems; its 3D-extension and finite-element-implementation is given in Ostwald et al. (2012). The models are based on the probabilistic approach for phase transformations by Govindjee and Hall (2000) which may not only be applied for modeling the TRIP effect, but also for shape memory alloys. Also the work Bartel et al. (2011) of the same group presents an energy relaxation based approach, which uses a classical J_2-vonMises-type plasticity. In this work a special focus lies on the inheritance of the plastic strain. Another energetic approach to predict the transformation induced plasticity is presented in Bhattacharyya and Weng (1994), wherein the phase fractions evolve depending on the reduction of the Gibb's energy. Fischer et al. (2000) the TRIP-effect is experimentally and theoretically examined and a constitutive material model is presented. The works of Suiker and Turteltaub (2005), Turteltaub and Suiker (2006a) and Tjahjanto et al. (2007) are based on the idea of a critical driving force. Representing the basic model, in Suiker and Turteltaub (2005) the material is divided into a transforming and a stable ferritic part. In its extensions in Turteltaub and Suiker (2006a) and Tjahjanto et al. (2007), the influence of both the material parameters, which characterize the microstructure, and the crystal sizes are studied. A rather phenomenological approach but thus computationally very fast ansatz was presented in Thibaud et al. (2006), in which an evolution equation for the martensitic volume fraction is assumed which depends on the plastic strain rate.

In this work, we present a variational material model which is based on our previous approach presented in Waimann et al.

(2015). Using the principle of the minimum of the dissipation potential (PMDP), we derived coupled evolution equations for the plastic deformation and phase transformation. Now, we present a computationally improved model: instead of accounting for the polycrystalline character by discretizing the orientation distribution function using a large number of distinct orientations for which calculating the grain-wise phase transformation was necessary, we make use of an ansatz for an evolving orientation distribution function, given by Junker (2014). This approach takes into account the polycrystalline structure and thus different oriented grains of the examined material by Euler angles that parameterize the "effective" orientation of transforming grains. The material model is then equipped with evolution equations for the Euler angles. Although evolution equations for the volume fractions, the plastic strains, and the Euler angles have to be solved, the numerical effort is smaller by orders of magnitude as compared to the original ansatz with volume fractions and plastic strains for a large number of individually discretized grains as in Waimann et al. (2015).

In the first chapter, we introduce the variational concept and present the micromechanical model describing the TRIP effect. In the following section we show the results of a material point calculation with prescribed strain and a finite-element-simulation for a plate with a hole. Our article is completed by a conclusion and an outlook on further investigations.

2   Variational modeling of TRIP-steel

Our material model is based on the so-called principle of the minimum of the dissipation potential (PMDP) [cf. Carstensen et al. (2002); Hackl and Fischer (2008)] and it represents an extension of the model for phase transformation in shape memory alloys Hackl and Heinen (2008). As presented in Junker (2016), the PMDP represents a special case of the well-known Hamilton's principle presented in Hamilton (1834, 1835) which allows to derive evolution equations that have a field function character. The variational concept is based on the idea of formulating a Lagrange function $\mathcal{L}$ which includes the rate of the Helmholtz free energy ψ as well as a dissipation function $\mathcal{D}$. The energy ψ depends on primary variables, e.g., the symmetrized gradient of the displacement field $\nabla^{\mathrm{sym}} \boldsymbol{u} = \frac{1}{2}(\nabla \boldsymbol{u} + \boldsymbol{u}\nabla) =: \boldsymbol{\varepsilon}$, indicating the strains, and/or the temperature θ, and a set of internal variables $\boldsymbol{\Lambda}$ which describe the microstructure. The dissipation function denotes the energy which dissipates due to the microstructural change and thus, depends at least on the rate of $\boldsymbol{\Lambda}$. Assuming that every material prefers a state of minimum energy, the minimization of the Lagrangean with respect to $\dot{\boldsymbol{\Lambda}}$ directly results in evolution equation for the internal variables. The minimization problem reads

$$\mathcal{L} = \dot{\psi}\left(\boldsymbol{\varepsilon}, \theta, \boldsymbol{\Lambda}\right) + \mathcal{D}(\dot{\boldsymbol{\Lambda}}) \to \min_{\dot{\boldsymbol{\Lambda}}} . \tag{1}$$

During the later minimization a further summand is added to the Lagrange function, which enables the consideration of the constraints to be observed. We will show this in the following sections.

2.1   Internal variables

To describe the microstructure of the polycrystalline TRIP-steel, we make use of four internal variables:

- the volume fractions of the austenite and the martensites $\boldsymbol{\lambda}$
- the plastic strain $\boldsymbol{\varepsilon}^{\mathrm{p}}$
- the kinematic hardening variable $\boldsymbol{a}^{\mathrm{v}}$
- a set of Euler angles $\boldsymbol{\alpha} = \{\varphi, \vartheta, \omega\}$,

consequently: $\boldsymbol{\Lambda} = \{\boldsymbol{\lambda}, \boldsymbol{\varepsilon}^{\mathrm{p}}, \boldsymbol{a}^{\mathrm{v}}, \boldsymbol{\alpha}\}$. The vector $\boldsymbol{\lambda}$ contains the individual phase fractions which are related to the transformation process: the austenitic ($i = 0$) and the n different martensitic ($1 \leq i \leq n$) phases. It has to fulfill the constraints of non-negativity and mass conservation. In contrast to our material models for shape memory alloys [cf. Waimann et al. (2019)], where the complete material is able to transform, we consider here that only a small amount of the material at the observed material point is able to show the phase transition between austenite and martensite. The rest of the material is ferritic or bainitic and has a fixed, time- and load-invariant volume fraction of λ_{BF}. Due to mass conservation, the sum of all evolving fractions must be equal to the volume fraction of the transforming area:

$$\sum_{i=0}^{n} \lambda_i = 1 - \lambda_{\mathrm{BF}} , \tag{2}$$

see also the sketched material point in Figure 1. When the condition (2) is fulfilled for the initialization, it is sufficient to guarantee that the sum of changes of $\boldsymbol{\lambda}$ is zero. The two constraints, which are considered later in the model, thus read:

$$\lambda_i \geq 0 \quad \forall i , \qquad \sum_{i=0}^{n} \dot{\lambda}_i = 0 . \tag{3}$$

The second and third internal variables, $\boldsymbol{\varepsilon}^{\mathrm{p}}$ and $\boldsymbol{\alpha}^{\mathrm{v}}$, account for the plastic deformation with kinematic hardening. We make the assumption that the formed dislocations which are related to the plastic strain are spatially fixed and do not move with the phase fronts. Therefore, the plastic strain state of the entire polycrystal is described by only one plastic strain tensor. We also want to point out that there are works in the literature which take into account a phase-wise plastic strain and thus, also consider the problem of inheritance of plastic strains [e.g., Bartel et al. (2011), Ammar et al. (2014)]. Following our - in a sense - more homogenized description and thus an averaged plastic strain and kinematic hardening variable comes along with a reduced
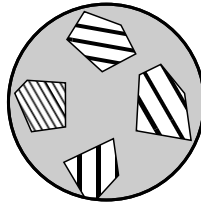
Fig. 1: Schematic transforming austenitic/martensitic (*white and black*) and non-transforming feritic/bainitic (*grey*) regions at the material point.

computational effort. Furthermore, we have to consider the volume preservation during plastic deformation. Hence,

$$\dot{\boldsymbol{\varepsilon}}^{\mathrm{p}} : \boldsymbol{I} = 0 \qquad \text{and} \qquad \dot{\boldsymbol{\alpha}}^{\mathrm{v}} : \boldsymbol{I} = 0 \tag{4}$$

hold. Based on classical linear kinematic hardening rules [e.g., Lubliner (2008); Wriggers (2008)], we additionally fulfill:

$$\dot{\boldsymbol{\varepsilon}}^{\mathrm{p}} = -\dot{\boldsymbol{a}}^{\mathrm{v}} . \tag{5}$$

Up to here, the current model substantially corresponds to our former model Waimann et al. (2015). However, one remarkable difference is the consideration of the polycrystalline structure. In our previous work Waimann et al. (2015), we assumed a coupled Voigt-Reuß-energy and modelled the austenitic/martensitic phase-transformation and plastic deformation for each particular grain. Thus, we used the volume fraction of transforming phase i in the grain j λ_i^j and the plastic strain in the grain j $\boldsymbol{\varepsilon}^{\mathrm{p}j}$ as internal variables. To get rid of such a numerically expensive grain-wise computation of the internal variables, we are now calculating an averaged volume fraction of the austenitic and martensitic phases as well as an overall plastic strain for the whole material point. To this end, let us introduce the set of Euler angles $\boldsymbol{\alpha}$ which describes the averaged orientation of the transforming grains [see Junker (2014)]. The set of Euler angles allows us to take into account the orientation by use of a rotation tensor $\boldsymbol{Q} = \boldsymbol{Q}(\boldsymbol{\alpha})$. Thereby, we significantly decrease the numerical effort of the new model.

2.2 Helmholtz free energy

Using the internal variables defined in the last section, we can formulate our Helmholtz free energy, which describes the energy of the examined TRIP-steel. We use a Reuss energy bound and thus, assume a constant stress at the material point:

$$\psi = \frac{1}{2} \left(\boldsymbol{\varepsilon} - \bar{\boldsymbol{\eta}}_{\mathrm{R}} - \boldsymbol{\varepsilon}^{\mathrm{p}} \right) : \bar{\mathbb{E}} : \left(\boldsymbol{\varepsilon} - \bar{\boldsymbol{\eta}}_{\mathrm{R}} - \boldsymbol{\varepsilon}^{\mathrm{p}} \right) + \bar{c} + \frac{1}{3} \boldsymbol{a}^{\mathrm{v}} : \bar{\mathbb{H}} : \boldsymbol{a}^{\mathrm{v}} . \tag{6}$$

In Equation (6), the variable $\boldsymbol{\varepsilon}$ is the total strain. As a result of the applied Reuss bound, the effective quantities of the phase-wise transformation strain $\boldsymbol{\eta}_i$, stiffness tensor $\mathbb{E}_i$, hardening tensor $\mathbb{H}_i$, and the caloric energy c_i can be calculated by

$$\bar{\boldsymbol{\eta}}_{\mathrm{R}} = \boldsymbol{Q}^{\mathrm{T}}(\boldsymbol{\alpha}) \cdot \sum_{i=0}^{n} \lambda_i \boldsymbol{\eta}_i \cdot \boldsymbol{Q}(\boldsymbol{\alpha}) \qquad\qquad \bar{c} = \sum_{i=0}^{n} \lambda_i c_i$$

$$\bar{\mathbb{E}} = \left(\sum_{i=0}^{n} \lambda_i \mathbb{E}_i^{-1} + \lambda_{\mathrm{BF}} \mathbb{E}_{\mathrm{BF}}^{-1} \right)^{-1} \qquad\qquad \bar{\mathbb{H}} = \left(\sum_{i=0}^{n} \lambda_i \mathbb{H}_i^{-1} + \lambda_{\mathrm{BF}} \mathbb{H}_{\mathrm{BF}}^{-1} \right)^{-1} . \tag{7}$$

Assuming isotropy for stiffness and hardening tensor, only the transformation strain is rotated in the orientation given by the set of Euler angles. Of course, other (and less) assumptions on the stress in the material point are possible. However, such much more sophisticated mixture energies stand in contrast to our goal of presenting a material law which can be implemented using a computationally more efficient algorithm compared to our previous model Waimann et al. (2015). We therefore stick to the rather simplified assumption of a constant stress in all crystallographic phases.

For the use of the Lagrange function (1), we need to calculate the rate of the Helmholtz free energy. Therefore, we are introducing the thermodynamical driving forces

$$P_{\mathrm{T}i} = -\frac{\partial \Psi}{\partial \lambda_i} = \boldsymbol{Q}^{\mathrm{T}} \cdot \boldsymbol{\eta}_i \cdot \boldsymbol{Q} : \boldsymbol{\sigma} + \frac{1}{2} \boldsymbol{\sigma} : (\mathbb{E}_i)^{-1} : \boldsymbol{\sigma} - c_i + \frac{1}{3} \boldsymbol{a}^{\mathrm{v}} : \bar{\mathbb{H}} : \mathbb{H}_i^{-1} : \bar{\mathbb{H}} : \boldsymbol{a}^{\mathrm{v}}$$

$$\boldsymbol{P}_{\mathrm{P}} = -\frac{\partial \Psi}{\partial \boldsymbol{\varepsilon}^{\mathrm{p}}} = \boldsymbol{\sigma}$$

$$\boldsymbol{P}_{\mathrm{V}} = -\frac{\partial \Psi}{\partial \boldsymbol{a}^{\mathrm{v}}} = \frac{2}{3} \bar{\mathbb{H}} : \boldsymbol{a}^{\mathrm{v}}$$

$$\boldsymbol{P}_{\mathrm{R}} = \left\{ P_{\varphi}, P_{\vartheta}, P_{\omega} \right\}^{T} = -\frac{\partial \Psi}{\partial \boldsymbol{\alpha}} = 2\bar{\boldsymbol{\eta}} \cdot \boldsymbol{Q} \cdot \boldsymbol{\sigma} : \frac{\partial \boldsymbol{Q}}{\partial \boldsymbol{\alpha}} , \tag{8}$$

whereby $\boldsymbol{\sigma}$ describes the stress tensor, which is calculated by

$$\boldsymbol{\sigma} = \bar{\mathbb{E}} : \left(\boldsymbol{\varepsilon} - \bar{\boldsymbol{\eta}}_R - \boldsymbol{\varepsilon}^p \right) \; . \tag{9}$$

By use of the chain rule, we can calculate the rate of the Helmholtz free energy by

$$\dot{\psi} = -\boldsymbol{P}_T \cdot \dot{\boldsymbol{\lambda}} - \boldsymbol{P}_P : \dot{\boldsymbol{\varepsilon}}^p - \boldsymbol{P}_V : \dot{\boldsymbol{a}}^v - \boldsymbol{P}_R \cdot \dot{\boldsymbol{\alpha}} \; . \tag{10}$$

2.3 Dissipation function

As mentioned before, the dissipation function describes the energy which is dissipated during microstructural evolution. For the simultaneous phase transformation and plastic deformation, we use a coupled dissipation function based on Waimann et al. (2016) which will result in rate-independent evolution equations. For the change of the Euler angles, we use the approach given by Junker (2014) which is homogeneous of second order and will result in evolution equations of viscous type. The dissipation function reads

$$\mathcal{D} = r_T \sqrt{\sum_{i=0}^{n} \dot{\lambda}_i^2 + a^2 \dot{\boldsymbol{\varepsilon}}^p : \dot{\boldsymbol{\varepsilon}}^p} + \frac{\sqrt{2}\, r_R}{2} \left(\dot{\varphi}^2 + \dot{\vartheta}^2 + 2\dot{\varphi}\dot{\omega} \cos \vartheta + \dot{\omega}^2 \right) \; , \tag{11}$$

wereby r_T is the dissipation parameter which describes the amount of energy necessary for the microstructural change and r_R is the viscosity parameter for the dynamic orientation distribution function. The parameter a is a coupling factor which accounts for the different amount of energy for the plastic deformation compared to the transformation. It is calculated in dependence of the plastic yield limit Y_0 by $a = Y_0/r_T$. Considering now a pure plastic deformation and thus $\dot{\boldsymbol{\lambda}} = \boldsymbol{0}$, the dissipation function reduces to its classical form used for plasticity. Note that the part for the rates of the Euler angles ensures objectivity.

2.4 Lagrange function, evolution equations and related yield function

Inserting now the rate of the Helmholtz free energy (10) and the dissipation function (11) into the Lagrangean (1) results in the minimization problem

$$\mathcal{L} = -\boldsymbol{P}_T \cdot \dot{\boldsymbol{\lambda}} - (\boldsymbol{P}_P - \boldsymbol{P}_V) : \dot{\boldsymbol{\varepsilon}}^p - \boldsymbol{P}_R \cdot \dot{\boldsymbol{\alpha}} + r_T \sqrt{\sum_{i=0}^{n} \dot{\lambda}_i^2 + a^2 \dot{\boldsymbol{\varepsilon}}^p : \dot{\boldsymbol{\varepsilon}}^p} + \frac{\sqrt{2}\, r_R}{2} \left(\dot{\varphi}^2 + \dot{\vartheta}^2 + 2\dot{\varphi}\dot{\omega} \cos \vartheta + \dot{\omega}^2 \right)$$

$$+ \kappa_T \sum_{i=0}^{n} \dot{\lambda}_i - \sum_{i=0}^{n} \gamma_{Ti} \dot{\lambda}_i + \kappa_P \dot{\boldsymbol{\varepsilon}}^p : \boldsymbol{I} \quad \rightarrow \quad \min_{\dot{\boldsymbol{\alpha}}, \dot{\boldsymbol{\lambda}}, \dot{\boldsymbol{\varepsilon}}^p} \; , \tag{12}$$

whereby the constraints (3) and (4) are considered by the Lagrange parameters κ_T and κ_P and the Kuhn-Tucker parameter γ_T. The fourth constraint (5) is directly inserted.

By solving the minimization problem, we can now directly calculate the evolution equations for the internal variables. The viscous evolution equations for the three Euler angles read

$$\dot{\varphi} = \frac{1}{\sqrt{2}r_R} \frac{1}{1 - \cos^2 \vartheta} \left(P_\varphi - P_\omega \cos \vartheta \right)$$

$$\dot{\vartheta} = \frac{1}{\sqrt{2}r_R} P_\vartheta$$

$$\dot{\omega} = \frac{1}{\sqrt{2}r_R} \frac{1}{1 - \cos^2 \vartheta} \left(P_\omega - P_\varphi \cos \vartheta \right) \; . \tag{13}$$

The rate-independent evolution equations for the volume fractions and the plastic strain have the form

$$\dot{\lambda}_i = \beta \, \mathrm{dev}_{\mathcal{A}} P_{Ti} \quad \forall i \in \mathcal{A}$$

$$\dot{\boldsymbol{\varepsilon}}^p = -\dot{\boldsymbol{a}}^v = \frac{\beta}{a^2} \mathrm{dev} \left(\boldsymbol{P}_P - \boldsymbol{P}_V \right) \tag{14}$$

with the active and the plastic deviator

$$\mathrm{dev}_{\mathcal{A}} P_{Ti} = P_{Ti} - \frac{1}{n_{\mathcal{A}}} \sum_{k \in \mathcal{A}} P_{Tk} \tag{15}$$

$$\mathrm{dev} \left(\boldsymbol{P}_P - \boldsymbol{P}_V \right) = (\boldsymbol{P}_P - \boldsymbol{P}_V) - \frac{1}{3} \left((\boldsymbol{P}_P - \boldsymbol{P}_V) : \boldsymbol{I} \right) \boldsymbol{I} \; . \tag{16}$$

Introducing the set of $n_{\mathcal{A}}$ active phases $\mathcal{A} = \{i | \lambda_i > 0\} \cup \{i | \lambda_i = 0 \wedge \dot{\lambda}_i > 0\}$, the active deviator compares the driving force of a single phase with the averaged driving force of the active phases. The parameter β in (14) is called consistency parameter. It is a scalar function $\beta = \sqrt{\sum_{i=0}^{n} \dot{\lambda}_i^2 + a^2 \dot{\boldsymbol{\varepsilon}}^p : \dot{\boldsymbol{\varepsilon}}^p}/r_T$, which couples the evolution equations of the simultaneous phase transformation

and plastic deformation. For closing the system of equations, we apply a Legendre transformation of the dissipation function for the simultaneous processes

$$
\mathcal{D}_{\mathrm{T}}^* = \sup_{\lambda, \dot{\boldsymbol{\varepsilon}}^{\mathrm{p}}} \left\{ \mathrm{dev}_{\mathcal{A}} \boldsymbol{P}_{\mathrm{T}} \cdot \dot{\boldsymbol{\lambda}} + \mathrm{dev}\,(\boldsymbol{P}_{\mathrm{P}} - \boldsymbol{P}_{\mathrm{V}}) : \dot{\boldsymbol{\varepsilon}}^{\mathrm{p}} - \mathcal{D}_{\mathrm{T}} \,\Big|\, \mathcal{A} \right\} ,
\tag{17}
$$

which directly results in the yield function

$$
\Phi_{\mathrm{T}} = \mathrm{dev}_{\mathcal{A}} \boldsymbol{P}_{\mathrm{T}} \cdot \mathrm{dev}_{\mathcal{A}} \boldsymbol{P}_{\mathrm{T}} + \frac{1}{a^2} \mathrm{dev}\,(\boldsymbol{P}_{\mathrm{P}} - \boldsymbol{P}_{\mathrm{V}}) : \mathrm{dev}\,(\boldsymbol{P}_{\mathrm{P}} - \boldsymbol{P}_{\mathrm{V}}) - r_{\mathrm{T}}^2
\tag{18}
$$

and the Karush-Kuhn-Tucker conditions

$$
\beta \geq 0, \qquad \Phi_{\mathrm{T}} \leq 0 \qquad \beta \Phi_{\mathrm{T}} = 0 ,
\tag{19}
$$

which enable us to quantify β. With the evolution equations (14) and (13), the yield function (18) and the Karush-Kuhn-Tucker conditions (19) our model is set. Note that the coupled approach for the dissipation function in (11) gives one single yield function that indicates the onset and offset of the coupled evolution of volume fractions, plastic strains, and back stress. The evolution of the "effective" orientation, indicated by the Euler angles, is not constrained and is determined solely by the driving forces $\boldsymbol{P}_{\mathrm{R}} \neq \boldsymbol{0}$. This case is present as soon as martensitic variants are present, i.e., $\lambda_{i>0} \neq 0$ for any variant i.

3   Numerical results

In the following subsections, we used the material parameters presented in Ostwald et al. (2011) and thus six different martensitic phases with the transformation strains (in Voigt notation):

$$
\begin{aligned}
\boldsymbol{\eta}_1 &= -\boldsymbol{\eta}_4 = \hat{\eta}\{1, -\hat{v}, -\hat{v}, 0, 0, 0\}^T \\
\boldsymbol{\eta}_2 &= -\boldsymbol{\eta}_5 = \hat{\eta}\{-\hat{v}, 1, -\hat{v}, 0, 0, 0\}^T \\
\boldsymbol{\eta}_3 &= -\boldsymbol{\eta}_6 = \hat{\eta}\{-\hat{v}, -\hat{v}, 1, 0, 0, 0\}^T
\end{aligned}
\tag{20}
$$

with $\hat{v} = 0.3$ [-] and $\hat{\eta} = 0.04$ [-]. We choose the austenite as the reference phase for the transforming part of the material. Therefore, the transformation strain of the austenite is zero. In addition, we also set the transformation strain of the bainitic/ferritic phases to zero and interpret the two phases as the reference phases for the non-transforming part of the material. However, the constant phase composition leads to a constant energy contribution which has no influence on the performed minimization. For the stiffness tensors of all the individual phases, we choose an elasticity modulus of $160\,\mathrm{GPa}$ and a Poisson's ratio of 0.3 [-]. The hardening tensor is for the austenitic phase $\mathbb{H}_0 = \mathbb{E}/4$ and for the other phases $\mathbb{H}_{i>0} = \mathbb{H}_{\mathrm{BF}} = \mathbb{E}/12$. We neglect any temperature dependence, i.e. we set the caloric energy $c_i = 0$. The plastic yield limit is chosen to be $Y_0 = 1.00\,\mathrm{GPa}$ and the non-transforming volume fraction $\lambda_{\mathrm{BF}} = 0.8$ [-]. Additionally, the initial set of Euler angles is randomly generated: $\boldsymbol{\alpha}_0 = \{2.6260, 1.8406, 5.9814\}$ [-].

For the implementation of our problem, we choose a broken Taylor series for the descretization of the stress and the internal variables, see also Junker and Hempel (2017):

$$
\boldsymbol{\Lambda}^{n+1} \approx \boldsymbol{\Lambda}^n + \frac{\partial \boldsymbol{\Lambda}}{\partial t}\Big|^n \Delta t .
\tag{21}
$$

Therein, $\boldsymbol{\Lambda}$ is a general discretized variable, n is the former and $n+1$ the current load step. The partial derivative $\dfrac{\partial \boldsymbol{\Lambda}}{\partial t}\Big|^n$ is the rate of the individual quantity at the previous load step. For the update of the internal variables this exemplary means

$$
\lambda^{n+1} = \lambda^n + \frac{\partial \lambda}{\partial t}\Big|^n .
\tag{22}
$$

The update of the volume fraction is thus performed using the already calculated, and thus fixed, quantities of the previous step. Applying the explicit scheme also on the stress evolution

$$
\boldsymbol{\sigma}^{n+1} = \boldsymbol{\sigma}^n + \frac{\partial \boldsymbol{\sigma}}{\partial \boldsymbol{\varepsilon}}\Big|^n : \left(\boldsymbol{\varepsilon}^{n+1} - \boldsymbol{\varepsilon}^n\right) + \frac{\partial \boldsymbol{\sigma}}{\partial \lambda}\Big|^n : \left(\lambda^{n+1} - \lambda^n\right) + \frac{\partial \boldsymbol{\sigma}}{\partial \boldsymbol{\varepsilon}^{\mathrm{p}}}\Big|^n : \left(\boldsymbol{\varepsilon}^{\mathrm{p},n+1} - \boldsymbol{\varepsilon}^{\mathrm{p},n}\right) + \frac{\partial \boldsymbol{\sigma}}{\partial \boldsymbol{\alpha}}\Big|^n : \left(\boldsymbol{\alpha}^{n+1} - \boldsymbol{\alpha}^n\right)
\tag{23}
$$

results in the material tangent

$$
\frac{\partial \boldsymbol{\sigma}}{\partial \boldsymbol{\varepsilon}}\Big|^n = \bar{\mathbb{E}}\big|^n
\tag{24}
$$

for the performed implementation in a finite element setting. The explicit scheme results in a very stable and robust algorithm which can be easily implemented.

3.1 Material point level

In our first simulation, we use a step-wise loading in form of a prescribed strain tensor (in Voigt notation):

$$\boldsymbol{\varepsilon} = \tilde{\varepsilon}\{1, -0.45, -0.45, 0, 0, 0\}^T \tag{25}$$

with $\tilde{\varepsilon} \in [-0.03, 0.03]$. The results of the tension/compression cycle are presented in Figure 2. We choose the dissipation parameter and the time-dependent discretized viscous parameter to be $r_T = 0.05\,\text{GPa}$ and $\Delta t_R = \Delta t / (\sqrt{2} r_R) = 0.01\,1/\text{GPa}$, respectively.
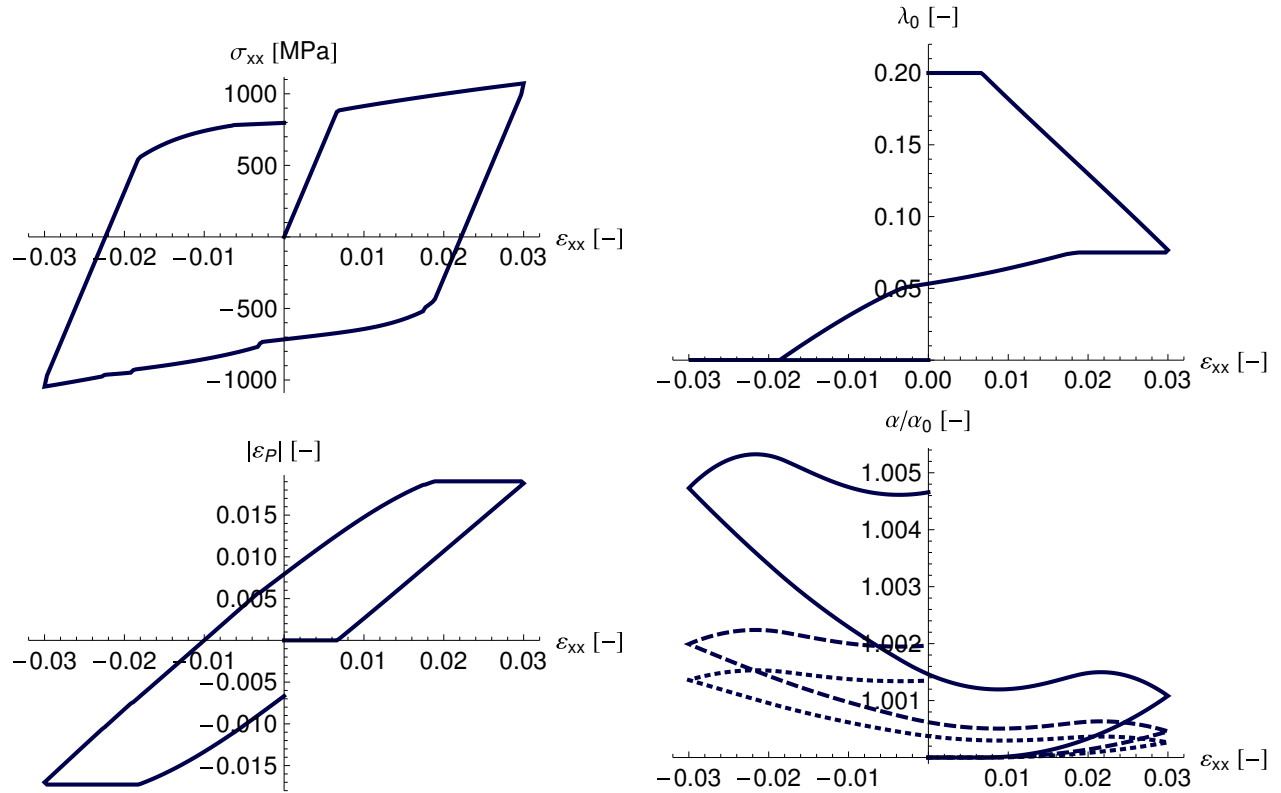
Fig. 2: Material point calculation: stress/strain diagram (*upper left*), austenitic volume fraction (*upper right*), norm of the plastic strain (*lower left*), relative change of the Euler angles (*lower right*).

As can be seen in the stress/strain diagram in Figure 2 (*upper left*), the material behaves linear elastic until reaching a critical stress, where the transformation and, simultaneously, the plastic deformation is initiated: the originally austenitic material transforms into martensite, see Figure 2 (*upper right*). Unloading leads again to a linear relation between stress and strain, until the transform starts again and the material transforms into the martensitic variants which are energetically favored for the unloading and afterwards compression. Unloading from the compressed state, leads again to a linear relation and a following transformation. After the load cycle, the material is not austenitic again. As can be seen in Junker and Hempel (2017), this is an effect of the plastic deformation within the model and reflects the experimentally observed behavior. Due to the coupled evolution equations, the transformation is accompanied by the evolution of the plastic strain, see Figure 2 (*lower left*). The relative change of the Euler angles in Figure 2 (*lower right*) show a permanent update of the orientation. Summarily, the variational model is able to qualitatively show the experimentally observed material behavior.

In Figure 3, the calculation is compared with results of the former model which is presented in Waimann et al. (2015). We used 100 randomly oriented grains for the grain-wise calculations of the polycrystalline material. The calculation time of the previous model Waimann et al. (2015) is 2.87042 s. The approach presented in this work and based on Junker (2014) needs only $1.56001\,10^{-2}$ s. The outstanding speed-up factor of 184, show the high improvement of the approach's efficiency by the dynamically evolving orientation distribution function. Nevertheless, although the plateau stress are in good accordance, the stress/strain curve shows a smoother initiation of the transformations, which results in a smooth transition between the elastic part and the stress plateaus. The reason for that is that some of the 100 grains start to transform earlier than others. Both models show a good first estimation for the expected material behavior and a good qualitative accordance to simulations performed, e.g., by Ostwald et al. (2012). However, an experimental comparison is necessary to further quantitatively examine the two modeling approaches.

J. Waimann, S. Reese, P. Junker

Tech. Mech., Vol. 40, Is. 1, (2020), 87–96

3.2 Finite element simulation of a a plate with a hole

For our finite element simulation, we implemented an explicit solution scheme for the used internal variables, see Junker and Hempel (2017); Waimann et al. (2019). The boundary value problem of the loaded plate with a hole is presented in Figure 4 (*left*). The resulting force/displacement diagram of the applied tension/compression cycle is presented in Figure 4 (*right*). This global structure reaction shows similarities to the local behavior at the material point observed in the last section. The austenitic volume fraction as well as the absolute plastic deformation and the *xx*-component of the plastic strain are presented in Figures 5, 6 and 7, which show the simultaneous evolution of the coupled internal variables. Whereby the first and third plateaus in the force/displacement diagram are a result of the transformation from austenite to martensite, the major cause of the second plateau is a transformation between the martensitic variants. Finally, we showed that the implemented finite element algorithm using the explicit scheme is able to show the simultaneous microstructural evolutions, whereby a comparison with experiments is still pending.

4 Conclusion and outlook

We presented a variational material model, which is able to show a first estimation for the simultaneous plastic deformation and phase transformation in TRIP-steels. Compared to our previous model Waimann et al. (2015), we improved the computational effort by introducing an evolving orientation distribution function. The presented simulations for the material point level and a finite element calculation show the expected macroscopic behavior and are in good accordance with simulations by Ostwald et al. (2012). However, no experimental comparison and validation is done so far. Our next step is a more detailed examination of our model: by use of more simulations and an experimental validation, we will investigate the applicability of our model and calibrate the material parameters. In addition, the two different approaches for the polycrystalline structure - a grain-wise computation of the microstructural change presented in Waimann et al. (2015) and the here presented use of a dynamically evolving orientation distribution function - need a detailed examination and comparison based on experiments.

References

K. Ammar, B. Appolaire, S. Forest, M. Cottura, Y. Le Bouar, and A. Finel. Modelling inheritance of plastic deformation during migration of phase boundaries using a phase field method. *Meccanica*, 49(11):2699–2717, 2014.

F. Auricchio and L. Petrini. A three-dimensional model describing stress-temperature induced solid phase transformations: solution algorithm and boundary value problems. *International journal for numerical methods in engineering*, 61(6):807–836, 2004.

H. Babaei, A. Basak, and V. I. Levitas. Algorithmic aspects and finite element solutions for advanced phase field approach to martensitic phase transformation under large strains. *Computational Mechanics*, pages 1–21, 2019.

T. Bartel, A. Menzel, and B. Svendsen. Thermodynamic and relaxation-based modeling of the interaction between martensitic phase transformations and plasticity. *Journal of the Mechanics and Physics of Solids*, 59(5):1004–1019, 2011.

A. Bhattacharyya and G. J. Weng. An energy criterion for the stress-induced martensitic transformation in a ductile system. *Journal of the Mechanics and Physics of Solids*, 42(11):1699–1724, 1994.

C. Carstensen, K. Hackl, and A. Mielke. Non–convex potentials and microstructures in finite–strain plasticity. *Proceedings of the Royal Society of London. Series A: Mathematical, Physical and Engineering Sciences*, 458(2018):299–317, 2002.

S. Conti, G. Dolzmann, and C. Klust. Relaxation of a class of variational models in crystal plasticity. *Proceedings of the Royal Society A: Mathematical, Physical and Engineering Sciences*, 465(2106):1735–1742, 2009.

W. J. Dan, S. H. Li, W. G. Zhang, and Z. Q. Lin. The effect of strain-induced martensitic transformation on mechanical properties of TRIP steel. *Materials & Design*, 29(3):604–612, 2008.
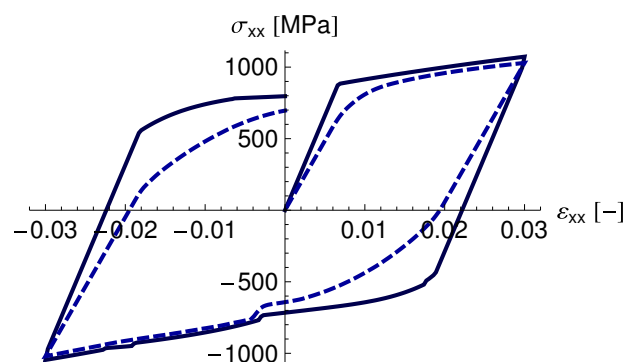
Fig. 3: Comparison of resulting stress/strain diagram of previous model (*dashed*) and current model.
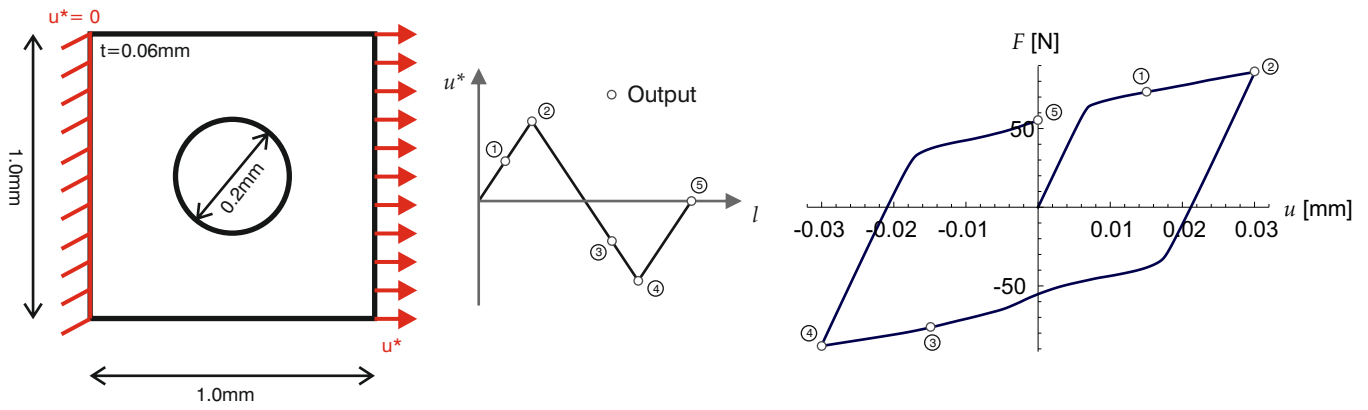
Fig. 4: Plate with a hole: boundary value problem (*left*), force/displacement diagram (*right*).
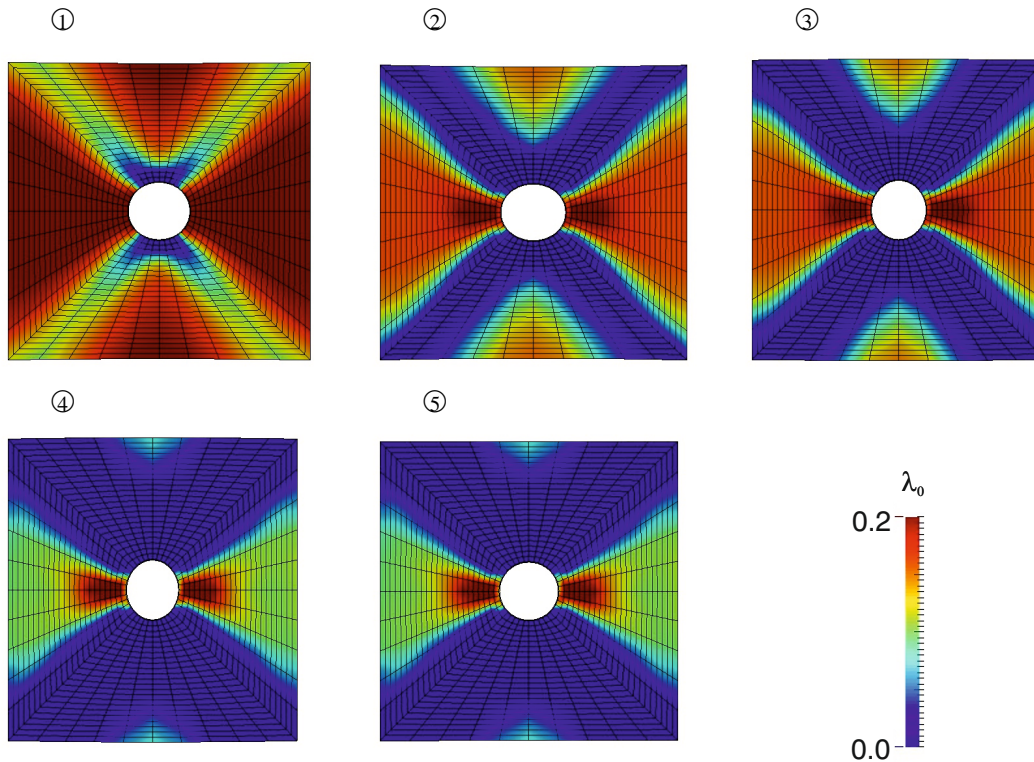
Fig. 5: Plate with a hole: austenitic volume fraction.

F. D. Fischer. A micromechanical model for transformation plasticity in steels. *Acta Metallurgica et Materialia*, 38(8):1535–1546, 1990.

F. D. Fischer, G. Reisner, E. Werner, K. Tanaka, G. Cailletaud, and T. Antretter. A new view on transformation induced plasticity (TRIP). *International Journal of Plasticity*, 16(7):723–748, 2000.

S. Govindjee and G. J. Hall. A computational model for shape memory alloys. *International Journal of Solids and Structures*, 37 (5):735–760, 2000.

S. Govindjee and C. Miehe. A multi-variant martensitic phase transformation model: formulation and numerical implementation. *Computer Methods in Applied Mechanics and Engineering*, 191(3-5):215–238, 2001.

G. W. Greenwood and R. H. Johnson. The deformation of metals under small stresses during phase transformations. *Proceedings of the Royal Society of London. Series A. Mathematical and Physical Sciences*, 283(1394):403–422, 1965.

K. Hackl and F. D. Fischer. On the relation between the principle of maximum dissipation and inelastic evolution given by dissipation potentials. *Proceedings of the Royal Society A: Mathematical, Physical and Engineering Science*, 464(2089): 117–132, 2008.

K. Hackl and R. Heinen. A micromechanical model for pretextured polycrystalline shape-memory alloys including elastic anisotropy. *Continuum Mechanics and Thermodynamics*, 19(8):499–510, 2008.

K. Hackl, U. Hoppe, and D. M. Kochmann. Variational modeling of microstructures in plasticity. In *Plasticity and Beyond*, pages 65–129. Springer, 2014.

94

J. Waimann, S. Reese, P. Junker

Tech. Mech., Vol. 40, Is. 1, (2020), 87–96
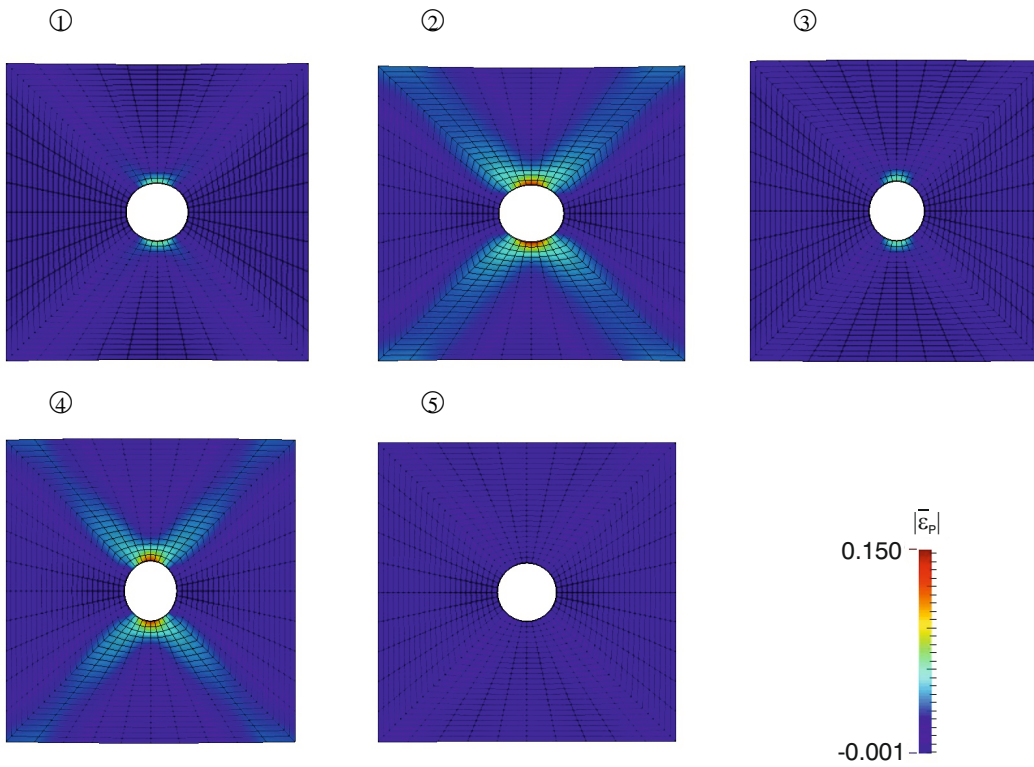
Fig. 6: Plate with a hole: norm of the plastic strain.
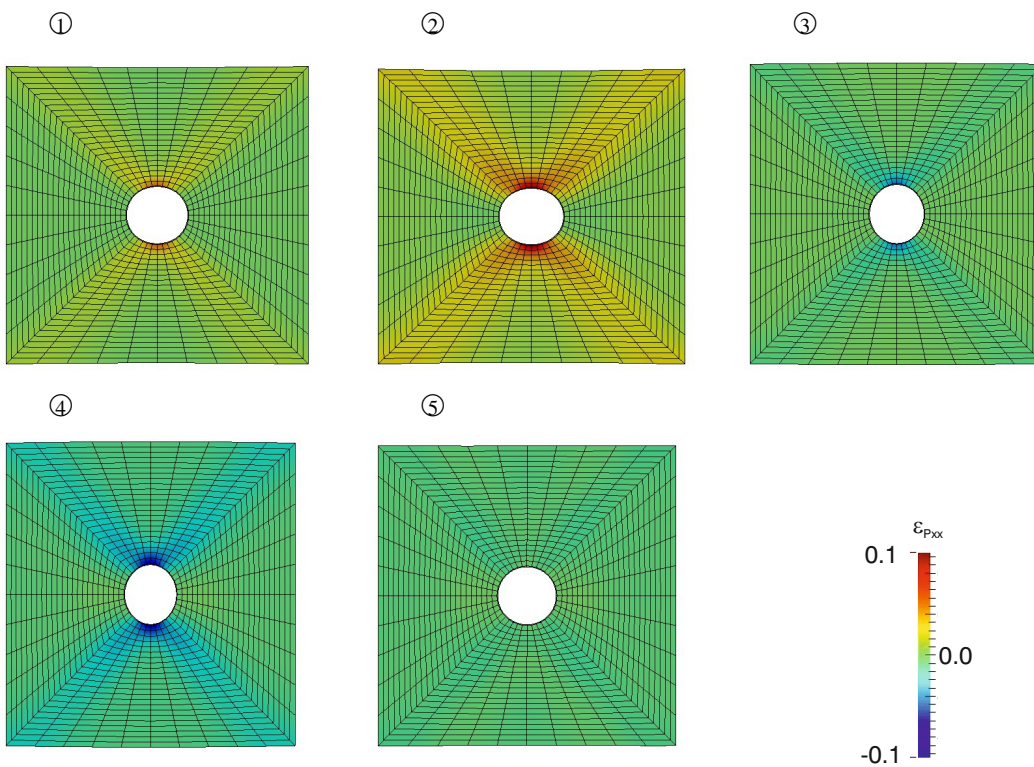
Fig. 7: Plate with a hole: xx-component of the plastic strain.

W. R. Hamilton. Xv. on a general method in dynamics; by which the study of the motions of all free systems of attracting or repelling points is reduced to the search and differentiation of one central relation, or characteristic function. *Philosophical transactions of the Royal Society of London*, (124):247–308, 1834.

W. R. Hamilton. Vii. second essay on a general method in dynamics. *Philosophical Transactions of the Royal Society of London*, (125):95–144, 1835.

W. Han, B. D. Reddy, and J. T. Oden. Computational plasticity: the variational basis and numerical analysis. 1995.

T. Iwamoto and T. Tsuta. Computational simulation of the dependence of the austenitic grain size on the deformation behavior of TRIP steels. *International Journal of Plasticity*, 16(7):791–804, 2000.

T. Iwamoto and T. Tsuta. Computational simulation on deformation behavior of CT specimens of TRIP steel under mode I loading for evaluation of fracture toughness. *International Journal of Plasticity*, 18(11):1583–1606, 2002.

P. Junker. An accurate, fast and stable material model for shape memory alloys. *Smart Materials and Structures*, 23(11):115010, 2014.

P. Junker. Variational modeling of martensitic phase transformations. 2016.

P. Junker and P. Hempel. Numerical study of the plasticity-induced stabilization effect on martensitic transformations in shape memory alloys. *Shape Memory and Superelasticity*, 3(4):422–430, 2017.

J.-B. Leblond, G. Mottet, and J. C. Devaux. A theoretical and numerical approach to the plastic behaviour of steels during phase transformations—I. Derivation of general relations. *Journal of the Mechanics and Physics of Solids*, 34(4):395–409, 1986.

J.-B. Leblond, J. Devaux, and J. C. Devaux. Mathematical modelling of transformation plasticity in steels I: case of ideal-plastic phases. *International journal of plasticity*, 5(6):551–572, 1989.

V. I. Levitas. Thermomechanical theory of martensitic phase transformations in inelastic materials. *International Journal of Solids and Structures*, 35(9-10):889–940, 1998.

J. Lubliner. A maximum-dissipation principle in generalized plasticity. *Acta Mechanica*, 52(3-4):225–237, 1984.

J. Lubliner. *Plasticity theory*. Courier Corporation, 2008.

H.-B. Mühlhaus and E. C. Alfantis. A variational principle for gradient plasticity. *International Journal of Solids and Structures*, 28(7):845–857, 1991.

G. B. Olson and M. Cohen. Kinetics of strain-induced martensitic nucleation. *Metallurgical transactions A*, 6(4):791, 1975.

R. Ostwald, T. Bartel, and A. Menzel. A one-dimensional computational model for the interaction of phase-transformations and plasticity. *The International Journal of Structural Changes in Solids*, 3(1):63–82, 2011.

R. Ostwald, T. Bartel, and A. Menzel. Phase-transformations interacting with plasticity–A micro-sphere model applied to TRIP steel. *Computational Materials Science*, 64:12–16, 2012.

A. S. J. Suiker and S: Turteltaub. Computational modelling of plasticity induced by martensitic phase transformations. *International journal for numerical methods in engineering*, 63(12):1655–1693, 2005.

B. Svendsen and S. Bargmann. On the continuum thermodynamic rate variational formulation of models for extended crystal plasticity at large deformation. *Journal of the Mechanics and Physics of Solids*, 58(9):1253–1271, 2010.

S. Thibaud, N. Boudeau, and J.-C. Gelin. TRIP steel: Plastic behaviour modelling and influence on functional behaviour. *Journal of materials processing technology*, 177(1):433–438, 2006.

D. D. Tjahjanto, A. S. J. Suiker, S. Turteltaub, P. E. J. Rivera Diaz Del Castillo, and S. Van der Zwaag. Micromechanical predictions of TRIP steel behavior as a function of microstructural parameters. *Computational Materials Science*, 41(1):107–116, 2007.

S. Turteltaub and A. S. J. Suiker. Grain size effects in multiphase steels assisted by transformation-induced plasticity. *International journal of solids and structures*, 43(24):7322–7336, 2006a.

S. Turteltaub and A. S. J. Suiker. A multiscale thermomechanical model for cubic to tetragonal martensitic phase transformations. *International Journal of Solids and Structures*, 43(14-15):4509–4545, 2006b.

J. Waimann, P. Junker, and K. Hackl. A variational material model for transformation-induced plasticity in polycrystalline steels. *Journal of the Mechanical Behavior of Materials*, 24(5-6):153–159, 2015.

J. Waimann, P. Junker, and K. Hackl. A coupled dissipation functional for modeling the functional fatigue in polycrystalline shape memory alloys. *European Journal of Mechanics-A/Solids*, 55:110–121, 2016.

J. Waimann, K. Hackl, and P. Junker. Variational modeling and finite-element simulation of functional fatigue in polycrystalline shape memory alloys. *Journal of Optimization Theory and Applications*, pages 1–27, 2019.

P. Wriggers. *Nonlinear finite element methods*. Springer Science & Business Media, 2008.

Computation of Cauchy heterogeneous stress field in a cruciform specimen subjected to equibiaxial tensile within parameter identification of isotropic hyperelastic materials

Kamel Yaya[1]*, Hocine Bechir[1], and Safia Bouzidi[1]

[1]Laboratoire de Mécanique, Matériaux & Énergétique (L2ME), Faculté de Technologie, Université de Bejaia, 06000, Bejaia, Algeria

Abstract: Heterogeneous stress and strain fields have been investigated by Finite Element Method (FEM) in a cruciform specimen holed at the center and subjected to equibiaxial tensile. The stress field is zero at the boundary of the hole; it is a useful boundary condition to compute local stress field. Also, the heterogeneity proves out to be an advantage in order to increase the variety of deformation states. So, a digital image correlation (DIC) system could provide the local deformations, and the corresponding stress field was optimized and adapted to the specimen geometry. Indeed, on the basis of FE results, the heterogeneous Cauchy stress field has been computed analytically in a sub-core region of the sample. As a result, the local strain and stress fields may be related; so that, the material parameters of isotropic and incompressible rubber-like materials could be identified from experimental data arising from a single heterogeneous test. Besides, the key ideas have been highlighted in order to solve the inverse problem related to the identification procedure.

Keywords: Hyperelasticity, Multiaxial testing, Heterogeneous fields, Finite element method, Analytic, Parameter identification

1 Introduction

Modeling the behavior of elastomeric materials is commonly carried out within the framework of hyperelasticity, cf. Ogden (1997); Holzapfel (2000). Nevertheless, the parameter identification is still difficult task, cf. Hartmann and Gilbert (2018). It should be noticed that, the numerical values of these parameters are input-data of the FE-codes. Due to the multi-axial behavior of elastomeric materials, accurate mechanical test data is crucial for both obtaining the model form and model parameter calibration. Standard tests related with this purpose require sample geometries that can lead to homogeneous deformations (uni-axial tensile, pure shear and equi-bi-axial tensile), cf. Galliot and Luchsinger (2011); Sasso et al. (2008). In practice, the constitutive parameters that are identified with those three types test performed separately are generally different, cf. Guo and Sluys (2006).

To bypass the problem, the material parameters could be identified from experimental data of the biaxial tensile test in order to ensure predictive ability of a hyperelastic model, cf. Seibert et al. (2014). We emphasize that, the biaxial testing was performed on cruciform specimens. So, the heterogeneous deformation states of equibiaxial tensile test and an inverse method (so-called, the virtual fields method) have been used, cf. Promma et al. (2009), in order to compute the Mooney-Rivlin model constants, cf. Mooney (1940). Nevertheless, the Mooney-Rivlin model does not suitable to reproduce the multi-axial behavior of elastomeric materials; so that, more than two parameters are required in the range of large strains. We notice that an optimal shape of a cruciform specimen depends on its geometry and specific constraints that are imposed by the cutting or molding. The computation of deformation and stress states in core region of cruciform specimen is a subject of debate, cf. Seibert et al. (2014); Hu et al. (2014); Hartmann et al. (2018) (and the literature cited therein). The strains distribution seems to be uniform; nevertheless, the corresponding stress distribution does not. Thereby, the biaxial tensile test seems to give rise to heterogeneous stress and strain fields even near core region of a cruciform sample. Therefore, we cannot establish a relationship between the local stresses in central region and applied forces on the arms of a cruciform sample, even by assuming that the strains are homogeneous in a small core area of the test specimen, and the corresponding stress distribution is homogeneous too (for homogeneous, elastic materials). Nowadays, digital image correlation (DIC) is a powerful experimental technique to determine displacement and deformation fields in solids, cf. Hild and Roux (2006); it provides full field displacement and deformation values. Consequently, it is straightforward to determine the in-plane components of the deformation gradient; however, its corresponding stress state is undetermined. A simplified method has been proposed by Chevalier et al. (2001) to evaluate a quasi-uniform Cauchy stress, so-called σ_B, in core region of a cruciform specimen. Recently, both experimental study and finite element analysis have shown that a homogeneous stress distribution cannot be obtained in near center of a cruciform sample. So the computation of stresses represents a critical issue for biaxial tensile tests. Indeed, no method to date addresses the relationship between the applied forces and the stress state in core region of a cruciform specimen, cf. Hartmann et al. (2018). As a result, errors made in the computation of stress tensor components will propagate into the parameter identification, ultimately limiting our ability to accurately simulate the hyperelastic behavior of elastomeric materials.

This work concerns with an original computation method of Cauchy stresses around a small circular hole in a cruciform sample subjected to equibiaxial tensile. The hole (of radius a) is located in the center; that is leading to increase the heterogeneity of strain field, which is assumed to be provided by a DIC-system. As a result, heterogeneity turns out to be an advantage to analyze both the

stresses state and deformations distribution around the hole. We show that the proposed stress field can be used for the parameter identification of isotropic hyperelastic solids. To be clear, we consider a core area of radius ρ around the hole that is located between the extremity of such hole to the intersection of the arc whose center is the intersection of the arms and that is tangent to these arms. In the core region, we will compute the Cauchy stresses numerically by FE: $\sigma_{rr}(\xi, \theta)$, $\sigma_{r\theta}(\xi, \theta)$ and $\sigma_{\theta\theta}(\xi, \theta)$ by using the generalized Gent model, cf. Gent (1996). Based on these numerical results, we show that, it is possible to formulate analytically a Cauchy stress field in a core region around the hole. The stress field is depending on the spatial variables $\xi = r/\rho$ and θ, distribution of nominal traction along border of arms, i.e. σ_U and geometrical parameter, i.e. a/ρ. As a consequence, the parameter identification is reduced to solving an inverse problem by combining both the data provided by DIC-system and of proposed stresses field. Also, we could use the data arising from this heterogeneous test in order to validate known hyperelastic constitutive equations.

2 Material modeling

In continuum mechanics, the mechanical properties of elastomeric materials are described in terms of strain-energy density function Ψ, cf. Ogden (1997); Holzapfel (2000). For isotropic elastic material, depends on the strain principal invariants

$$I_1 = \mathrm{tr}(\boldsymbol{B}), I_2 = 1/2 \left[(\mathrm{tr}(\boldsymbol{B}))^2 - \mathrm{tr}\left(\boldsymbol{B}^2\right) \right], I_3 = \det(\boldsymbol{B}) \tag{1}$$

where $\boldsymbol{B} = \boldsymbol{F}\boldsymbol{F}^T$ is the left Cauchy-Green tensor and $\boldsymbol{F}$ is the gradient of the deformation.

Rubber-like materials are often assumed to be incompressible provided that the hydrostatic stress does not become too large and so the admissible deformations must be isochoric, i.e. $\det(\boldsymbol{F}) = 1$ so that $I_3 = 1$. Cauchy stress of an incompressible isotropic elastic material can be determined as follows:

$$\sigma = -p\boldsymbol{I} + 2\Psi_{,1}\boldsymbol{B} - 2\Psi_{,2}\boldsymbol{B}^{-1} \tag{2}$$

where p is the Lagrange multiplier, $\boldsymbol{I}$ is the identity tensor and $\Psi_{,i} = (\partial\Psi/\partial I_i)_{i=1,2}$ are the partial derivatives of the strain-energy density function.

We consider the phenomenological model of Gent, cf. Gent (1996) which is able to represent limiting chain extensibility of the molecular chains; its strain-energy density is

$$\Psi = \frac{\mu_0}{2} \left[-\alpha J_m \ln\left(1 - \frac{I_1 - 3}{J_m}\right) + (1 - \alpha)(I_2 - 3) \right] \tag{3}$$

where μ_0 is the shear modulus for infinitesimal deformations, $\alpha \in]0, 1]$ is a dimensionless constant and J_m is the limiting value of $I_1 - 3$, taking into account limiting polymeric chain extensibility. On taking the limit $J_m \to \infty$ in Eq. (3), we recover the well-known Mooney-Rivlin model, cf. Mooney (1940). For further discussion of Eq. (3) and related constitutive models, (see Horgan and Saccomandi (1999, 2001)) where the solutions to the torsion, axial shear and circular shear problems have been obtained.

2.1 Finite element simulations

A finite element calculation is performed by assuming both plane stress state and a nearly incompressibility approach. Thus, a mixed formulation pressure-displacement was used in order to avoid element locking. For that purpose, the strain-energy density function is decomposed into an isochoric and volumetric parts. To this end, we declare the model of Eq. (3) as slight compressible by replacing the principal invariants I_1 and I_2 by equivalent invariant ones, cf. Simo and Hughes (2006). Consequently, the strain-energy density function has been decomposed as the sum of the two energies related to distortional and dilatational deformations, so that Eq. (3) becomes

$$\Psi = \tilde{\Psi}(\bar{I}_1, \bar{I}_2) + \hat{\Psi}(J) \tag{4}$$

where $\bar{I}_1 = I_1 \left/ I_3^{1/3} \right.$ and $\bar{I}_2 = I_2 \left/ I_3^{2/3} \right.$.

We point out that, $\tilde{\Psi}(\bar{I}_1, \bar{I}_2) = (\mu_0/2) \left\{ \left[-\alpha J_m \ln\left(1 - \left((\bar{I}_1 - 3)/J_m\right)\right) \right] + (1 - \alpha)(\bar{I}_2 - 3) \right\}$ and $\hat{\Psi}(J) = (\kappa_0/2)(J - 1)^2$, where κ_0 is the bulk modulus. The strain-energy density function (Eq. (4)) was implemented in a FE code. First, we used the material constants of Mooney-Rivlin model, cf. Mooney (1940), i.e. $c_{10} = \alpha\mu_0/2$ and $c_{01} = (1 - \alpha)\mu_0/2$ of a Silicone rubber that are given in Seibert et al. (2014), and by varying the material constant, i.e. J_m (see, Tab. A.1). Also, these authors have designed and optimized cruciform shape specimen in order to obtain quasi-homogeneous strain state in the core region. Consequently, the numerical simulations were performed on a cruciform specimen defined by the circle of radius $R = 18.75\,mm$, length $L_0 = 25\,mm$ and hole of radius $a = 0.01\rho$ ($\rho = 16.66\,mm$); the thickness of the sample is assumed uniform ($e_0 = 2\,mm$). For symmetry reasons, only one quarter of the specimen is taken into account. The geometry and the boundary value problem including boundary and symmetry conditions are shown in Fig. 1. The displacements $U_1 = U_2 = U$ are prescribed in the extremities of the arms in order to ensure equibiaxial loading conditions. Boundary conditions were applied on the nodes that were in perfect contact (no slip) with the clamps. The deformed specimen is depicted in Figs. 2 along with initial shape to illustrate that large strains exist in the core region. The components of the Green-Lagrange strain tensor, i.e. $\boldsymbol{E}_{11}$, $\boldsymbol{E}_{12}$ and $\boldsymbol{E}_{22}$ are obtained from finite element results, are shown in Figs. 3 versus dimensionless radius ξ for different values of θ. We notice that, the large strains are located

K. Yaya, H. Bechir, and S. Bouzidi

Tech. Mech., Vol. 40, Is. 1, (2020), 97–107

near the hole; and the strain state is highly heterogeneous in the core region of radius ρ. The component E_{11} has a minimum and increases gradually in the ξ-direction from the side of the hole. While the component E_{22} decreases and showing an opposite behavior with respect to the corresponding E_{11}. Due to the large deformability of elastomeric materials, the specimen may rotate causing some shearing, i.e. E_{12}, that reach a maximum near the hole. The shear strain E_{12} depends on the radius ρ (or R), near
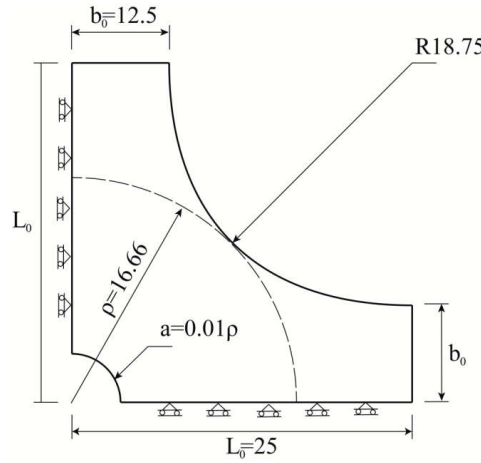
Fig. 1: One quarter of the cruciform specimen, a small hole is located in the center of the sample with applied boundary conditions

core region of the sample, if $R \ll L_0$ then E_{12} tends to zero, so that, planar-biaxial stretching of the cruciform sample may be considered as a "perfect" equibiaxial tension. Consequently, the effects of free and clampedF edges influence the strain and stress fields in the sample. We notice that, the shear deformations are zero on the symmetry axes of the sample, i.e. $\theta = 0$ and $\theta = \pi/2$. Ideally, the specimen subjected to equibiaxial stretching (without hole and $R \ll L_0$) should not develop local rigid-body-rotation. Let us analyze the stress state in the core area of radius ρ around the hole. The Cauchy stresses i.e. $\sigma_{11}(x,y)$, $\sigma_{12}(x,y)$, $\sigma_{22}(x,y)$ and the mean value of the nominal stress σ_U at the extremity of one arm are inferred from the FE-simulations. Thereafter, the Cauchy stresses are computed in polar coordinates as follows:

$$\begin{pmatrix} \sigma_{rr}(r,\theta) & \sigma_{r\theta}(r,\theta) \\ \sigma_{r\theta}(r,\theta) & \sigma_{\theta\theta}(r,\theta) \end{pmatrix} = \begin{pmatrix} \cos\theta & \sin\theta \\ -\sin\theta & \cos\theta \end{pmatrix} \begin{pmatrix} \sigma_{11}(x,y) & \sigma_{12}(x,y) \\ \sigma_{12}(x,y) & \sigma_{22}(x,y) \end{pmatrix} \begin{pmatrix} \cos\theta & -\sin\theta \\ \sin\theta & \cos\theta \end{pmatrix} \tag{5}$$

where σ_{rr}, $\sigma_{r\theta}$ and $\sigma_{\theta\theta}$ are respectively, radial, shear and hoop Cauchy stresses, $x = r\cos\theta$, $y = r\sin\theta$ and $\tan\theta = y/x$. The results are shown in Figs. 4 for the radial stress, shear stress and hoop stress versus dimensionless radius ξ for different values of θ. Accordingly, no shear is observed on the symmetry axes of the sample corresponding to the directions of $\theta = 0$, $\pi/4$ and $\pi/2$. Radial stress reaches its maximum on the symmetry axes of the sample ($\theta = 0$ and $\theta = \pi/2$); also the free edge condition leads to $\sigma_{rr}(\xi = 1, \theta = \pi/4) = 0$. Hoop stress reaches maximum on the edge of the hole and tending to zero far from the hole. We point out that, the presence of the hole requires satisfying the following boundary conditions:

$$\sigma_{rr}(\xi_a = a/\rho, \theta) = \sigma_{r\theta}(\xi_a = a/\rho, \theta) = 0 \tag{6}$$

We notice that, the presence of the hole requires satisfying the following boundary conditions:

$$\sigma_{rr}(\xi_a = a/\rho, \theta) = \sigma_{r\theta}(\xi_a = a/\rho, \theta) = 0 \tag{7}$$

In Fig. 5, we plot the nominal stress i.e. $\sigma_U = \langle force \rangle / e_0 b_0$ versus a prescribed displacement U and by varying the material constant J_m; $\langle Force \rangle$ is the mean applied force on the nodes of an arm. On taking the limit of $J_m = 500$ in Eq. (3), the well-known Mooney-Rivlin model, cf. Mooney (1940) is recovered.

2.2 Construction of an approximation of Cauchy stress field

The computation of Cauchy stress field around a hole has been well established in the framework of linear elasticity theory, cf. Timoshenko (1951). However, finding stress field in the framework of isotropic hyperelasticity remains scarce in the literature. In this paper, we propose an analytical approximation of Cauchy stress field in the core sub-region of the dimensionless radius ξ $(0.01 \le \xi = r/\rho \le 0.5)$ around the hole. First, consider the equilibrium equations in the deformed configuration

$$\frac{\partial \sigma_{rr}}{\partial r} + \frac{1}{r}\frac{\partial \sigma_{r\theta}}{\partial \theta} + \frac{1}{r}(\sigma_{rr} - \sigma_{\theta\theta}) = 0 \tag{8}$$

$$\frac{\partial \sigma_{r\theta}}{\partial r} + \frac{1}{r}\frac{\partial \sigma_{\theta\theta}}{\partial \theta} + \frac{2}{r}\sigma_{r\theta} = 0 \tag{9}$$

99

We may re-arrange the Eqs. (8) and (9) to get:

$$\sigma_{\theta\theta} = \frac{\partial \sigma_{r\theta}}{\partial \theta} + r \frac{\partial \sigma_{rr}}{\partial r} + \sigma_{rr} \tag{10}$$

$$\frac{\partial}{\partial \theta} \left(r \frac{\partial \sigma_{rr}}{\partial r} + \sigma_{rr} \right) = - \left(2\sigma_{r\theta} + r \frac{\partial \sigma_{r\theta}}{\partial r} + \frac{\partial^2 \sigma_{r\theta}}{\partial \theta^2} \right) \tag{11}$$

Accordingly, the radial stress and hoop stress are inferred from the shear stress. By using the previous FE-results, we may express the shear stress as follows:

$$\sigma_{r\theta}(\xi, \theta) = -\sigma_U h(\xi) \sin 4\theta \quad \text{for } 0.01 \leq \xi \leq 0.5 \tag{12}$$

where σ_U and $h(\xi)$ are respectively, the nominal stress tensile along border of arms and an unknown function to be determined. We emphasize that the function $h(\xi)$ is arising from the results of finite element simulations. It was shown that this function does not depend on both Jm, and θ for $(0.01 \leq \xi = r/\rho \leq 0.5)$. Therefore, we may assume that the function $h(\xi)$ does not depend on the strain energy function.
The function $h(\xi)$ can be evaluated as follows:

$$h(\xi) = -\frac{\sigma_{r\theta}}{\sigma_U \sin 4\theta} \quad \text{for } \theta \neq 0, \pi/4 \text{ and } \pi/2 \tag{13}$$

where $\sigma_{r\theta}$ is arisen from the FE-simulations.
$h(\xi)$ can be approximated with respecting the boundary conditions as follows:

$$h(\xi) = \beta \lambda (\xi - \xi_a)^2 \tag{14}$$

where $\lambda = 1 + \frac{U}{L_0}$ is the macroscopic stretch ratio and β is adjustable numerical constant.
The graphs of the function $h(\xi)$ versus ξ for $\theta \neq 0$, $\pi/4$ and $\pi/2$ and $\beta \approx 0.447$ are shown in Fig. 6. Noticing that, the graphs of $\frac{h(\xi)}{\lambda}$ are not depending on magnitude of displacement U, θ, and material constant, J_m. As a consequence, the variable separation of Eq. (13) seems to be reliable.
By substituting the Eqs. (12) and (14) into Eq. (11), we obtain the following differential equation:

$$\xi \frac{\partial \sigma_{rr}}{\partial \xi} + \sigma_{rr} = \frac{\sigma_U}{4} (14 h(\xi) - \xi h'(\xi)) \cos 4\theta + f(\xi) \tag{15}$$

Where $f(\xi)$ is a function to be determined and $\sigma_{rr}(\xi = \xi_a, \theta) = 0$.
The solution of Eq. (15) is

$$\sigma_{rr}(\xi, \theta) = \left(\frac{\sigma_U}{4} \beta \lambda \right) \left(4\xi^2 + 14\xi_a^2 - 13\xi_a\xi - 5\xi_a^3 \xi^{-1} \right) \cos 4\theta + F(\xi) \tag{16}$$

where $F(\xi)$ is inferred from the results of FE-simulations of radial Cauchy stress, i.e. $\sigma_{rr}(\xi, \theta)$ (see, **Appendix A**).

(a)   (b)
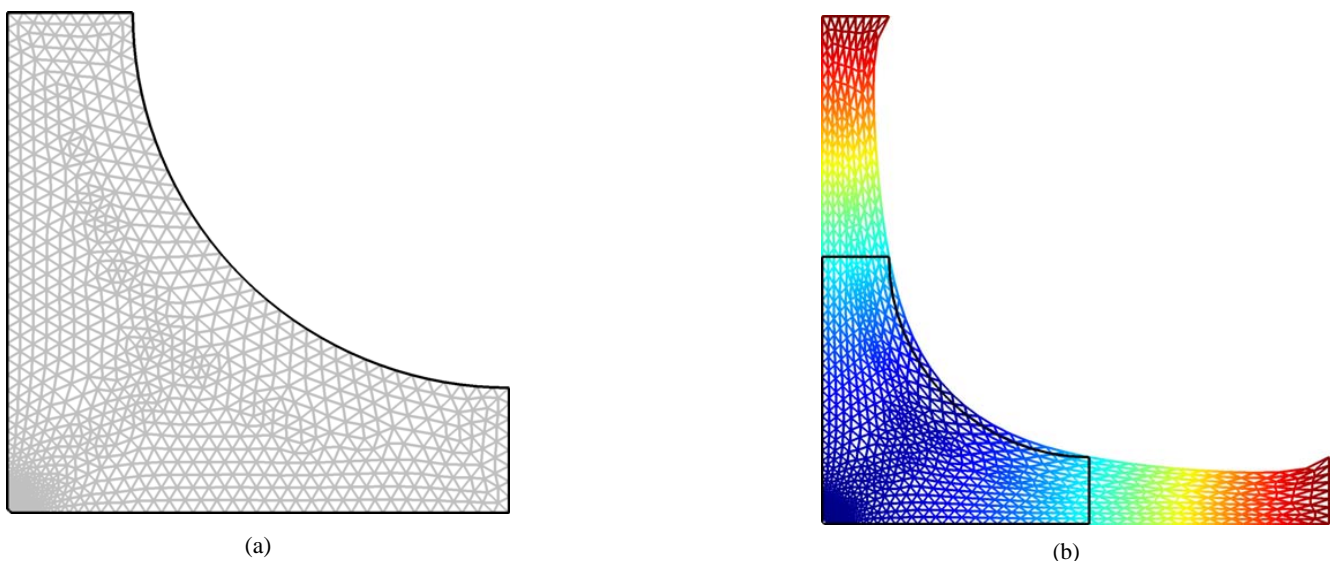
Fig. 2: (a) The undeformed specimen in the reference configuration and meshes of plane stress problem; (b) The deformed specimen in the current configuration for $U_1 = U_2 = U = 25\ mm$

(a)

(b)

(c)
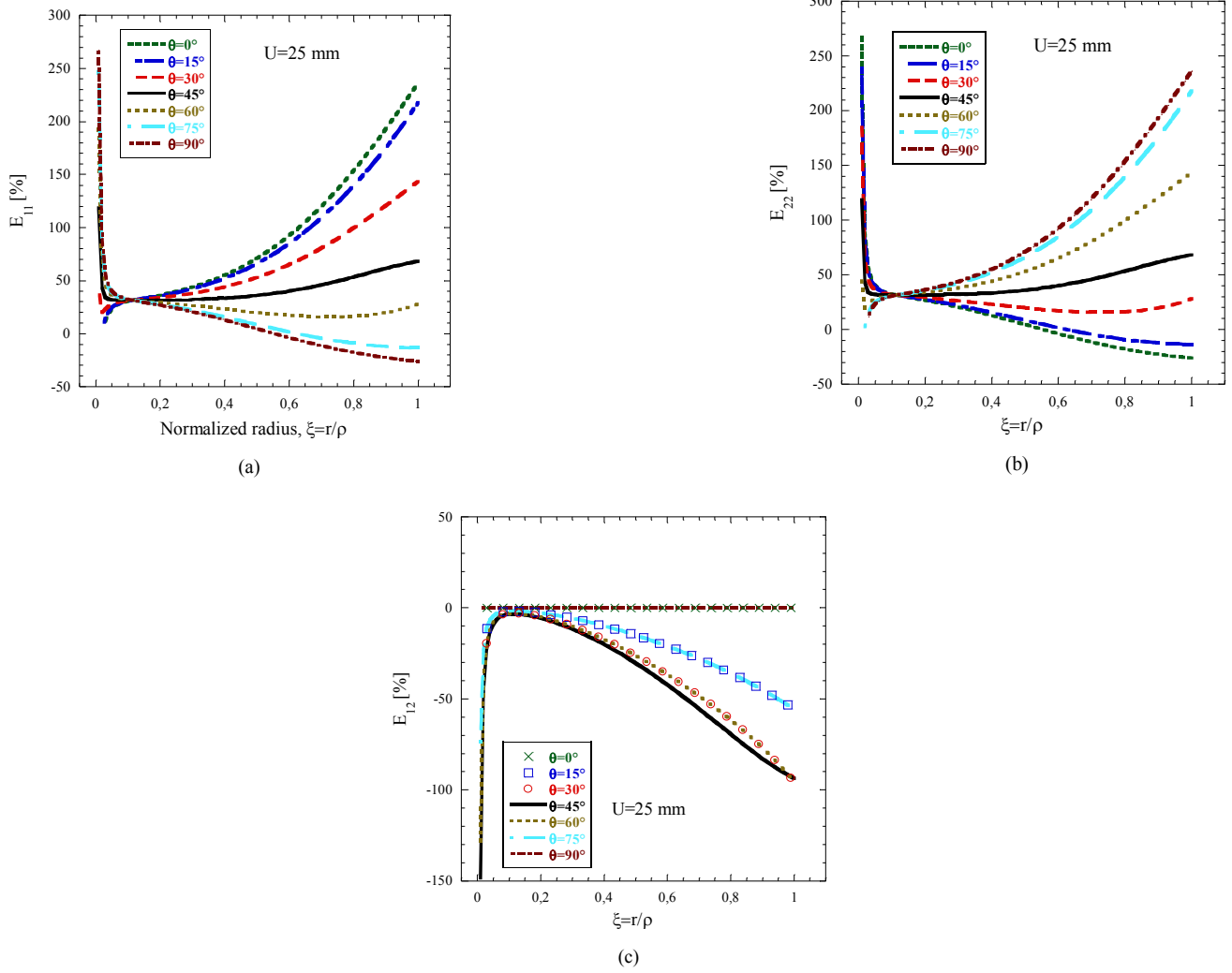
Fig. 3: Plots of the Green-Lagrange strain tensor component E_{ij} versus normalized radius ξ for $U_1 = U_2 = U = 25$ mm; (a) Component E_{11} versus normalized radius ξ; (b) Component E_{22} versus normalized radius ξ; (c) Component E_{12} versus normalized radius ξ

We get the hoop stress by substituting Eqs. (16) and (12) into Eq. (10)

$$\sigma_{\theta\theta}(\xi, \theta) = \left(\frac{\sigma_U}{4}\beta\lambda\right)\left(-4\xi^2 - 2\xi_a^2 + 6\xi_a\xi\right)\cos 4\theta + F(\xi) + \xi F'(\xi) \tag{17}$$

(a)

(b)

(c)

(d)

(e)

(f)
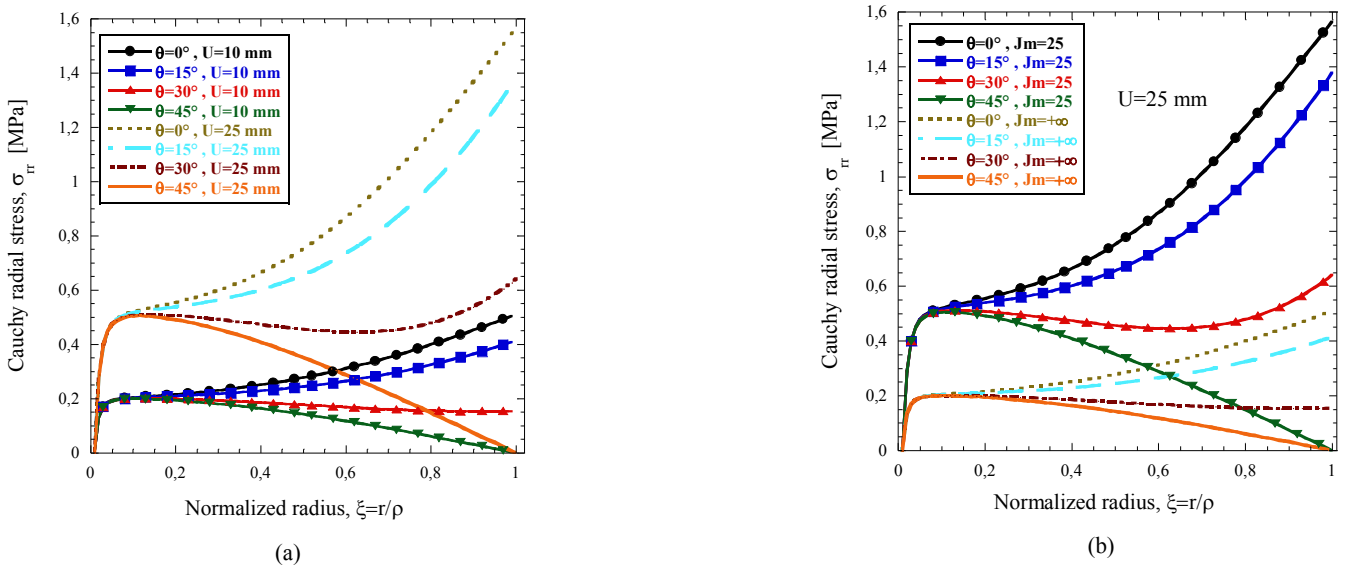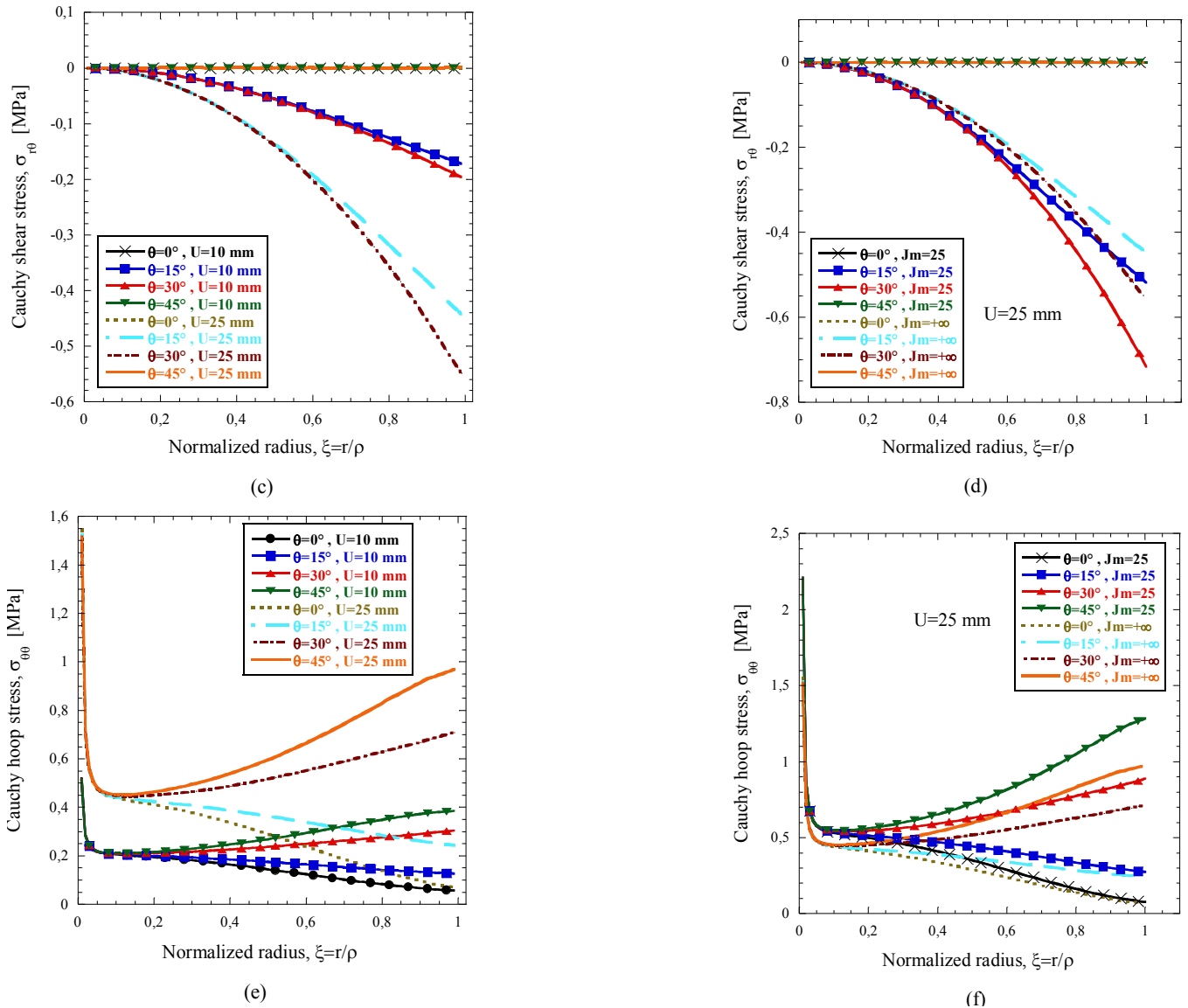
Fig. 4: (a) Cauchy radial stress, $\sigma_{rr}(\xi, \theta)$ versus normalized radius ξ for different values of θ and U; (b) Cauchy radial stress, $\sigma_{rr}(\xi, \theta)$ versus normalized radius ξ for different values of θ and J_m; (c) Cauchy shear stress, $\sigma_{r\theta}(\xi, \theta)$ versus normalized radius ξ for different values of θ and U; (d) Cauchy shear stress, $\sigma_{r\theta}(\xi, \theta)$ versus normalized radius ξ for different values of θ and J_m; (e) Cauchy hoop stress, $\sigma_{\theta\theta}(\xi, \theta)$ versus normalized radius ξ for different values of θ and U; (f) Cauchy hoop stress, $\sigma_{\theta\theta}(\xi, \theta)$ versus normalized radius ξ for different values of θ and J_m

The Cauchy stresses are explicitly given in **the Appendix A**. We notice that, the proposed stress field seems to be reliable to reproduce the FE-results in the core sub-region as shown in Figs. 7. This approximate stress field adapted to the test specimen geometry depends on prescribed displacement, i.e. U, resulting nominal stress, i.e. σ_U and geometrical ratio a/ρ. So, we may assume that, the Cauchy stress field does not depending on analytical form of strain-energy density function, since the stress state can be inferred from the geometrical variables alone and the applied force on the arms. Therefore, the data arising from this heterogeneous test can be exploited advantageously for the parameter identification. Real elastomeric materials typically exhibit time-dependent behavior due to viscous effects, implying that the strain and stress fields would not necessarily vary similarly. For instance, biaxial tensile test has been performed by Johlitz and Diebels, cf. Johlitz and Diebels (2011) in order to characterize effect of time on the behavior of a silicone rubber for which the viscoelasticity is nearly negligible. However, the analysis requires the mechanical properties of the material a priori. Thus not applicable approach if the "real" properties of the material have not yet to be determined. Besides, the proposed identification procedure could be extended to viscoelastic elastomers on the basis of a constitutive equation; so, we will solve a boundary value problem that can be challenging to achieve computationally.

3 New procedure of parameter identification

The material parameters of Mooney-Rivlin model can be estimated on basis of experimental data of the biaxial tensile, cf. Seibert et al. (2014); Promma et al. (2009). This heterogeneous single test has an advantage because three types of strain states coexist: uniaxial tensile, pure shear and equi-bi-axial tensile in different regions of the deformed sample. Consequently, we obtain weighted average values of model parameters; with comparison to the parameters that could be determined from the tests performing separately. We show that the partial derivatives of strain-energy densities can be determined without knowing their analytical
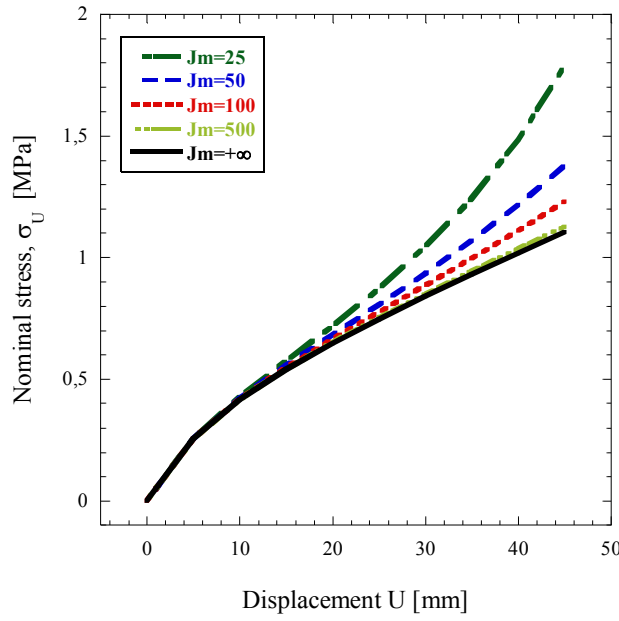
Fig. 5: Plots of nominal stress σ_U versus displacement U for different values of J_m

forms a priori. Moreover, the present approach can also be used for validation of hyperelastic models. We provide additional insights in order to explain the method of parameter identification. We assume that the deformation is relatively homogeneous around a material point in the framework of DIC measurements. As result, we may write the deformation gradient tensor of the planar biaxial test, cf. Zhang et al. (2015) as follows:

$$
(F) = \begin{pmatrix} \dfrac{\partial x_1}{\partial X_1} & \dfrac{\partial x_1}{\partial X_2} & \dfrac{\partial x_1}{\partial X_3} \\[2mm] \dfrac{\partial x_2}{\partial X_1} & \dfrac{\partial x_2}{\partial X_2} & \dfrac{\partial x_2}{\partial X_3} \\[2mm] \dfrac{\partial x_3}{\partial X_1} & \dfrac{\partial x_3}{\partial X_2} & \dfrac{\partial x_3}{\partial X_3} \end{pmatrix} = \begin{pmatrix} \lambda_1 & \gamma_1 & 0 \\ \gamma_2 & \lambda_2 & 0 \\ 0 & 0 & \lambda_3 \end{pmatrix}
\tag{18}
$$

where X_k and x_k are coordinates for material particles in the reference and current configuration, respectively, λ_k and γ_k are the stretch ratios and amount of shears, respectively.
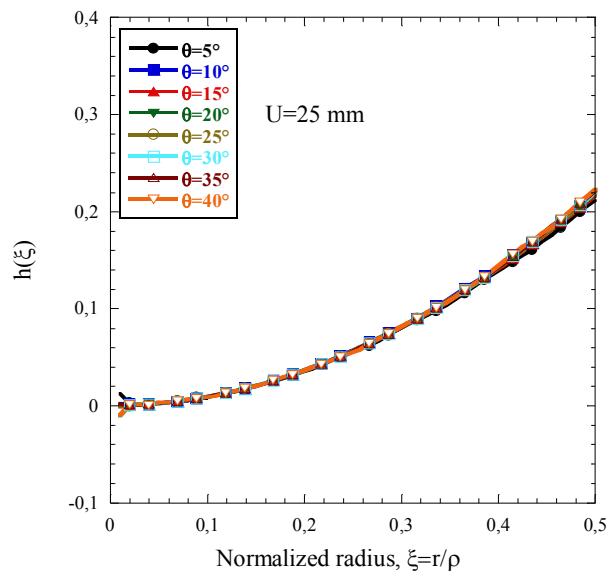
Fig. 6: Graphs of the function $h(\xi)$ versus normalized radius ξ

103

If we assume that the material is incompressible, i.e. $J = \det(\mathbf{F}) = 1$, we may write

$$J = \begin{vmatrix} \lambda_1 & \gamma_1 & 0 \\ \gamma_2 & \lambda_2 & 0 \\ 0 & 0 & \lambda_3 \end{vmatrix} = 1 \Rightarrow \lambda_3 = (\lambda_1\lambda_2 - \gamma_1\gamma_2)^{-1} \tag{19}$$

With DIC measurements techniques, it is straightforward to determine the components of the deformation gradient, λ_k and γ_k. Substituting Eq. (19) into Eq. (2), gives

$$\sigma_{11} = 2\left(\lambda_1^2 + \gamma_1^2 - \lambda_3^2\right)\Psi_{,1} - \left[\left(\lambda_2^2 + \gamma_2^2\right)\lambda_3^2 - \lambda_3^{-2}\right]\Psi_{,2}$$

$$\sigma_{12} = 2\left(\lambda_1\gamma_2 + \lambda_2\gamma_1\right)\left(\Psi_{,1} + \lambda_3^2\Psi_{,2}\right) \tag{20}$$

$$\sigma_{22} = 2\left(\lambda_2^2 + \gamma_2^2 - \lambda_3^2\right)\Psi_{,1} - \left[\left(\gamma_1^2 + \lambda_1^2\right)\lambda_3^2 - \lambda_3^{-2}\right]\Psi_{,2}$$

Cauchy stresses σ_{11}, σ_{12} and σ_{22} are inferred from the Eq. (5) as follows:

$$\begin{pmatrix} \sigma_{11} & \sigma_{12} \\ \sigma_{12} & \sigma_{22} \end{pmatrix} = \begin{pmatrix} \cos\theta & -\sin\theta \\ \sin\theta & \cos\theta \end{pmatrix} \begin{pmatrix} \sigma_{rr} & \sigma_{r\theta} \\ \sigma_{r\theta} & \sigma_{\theta\theta} \end{pmatrix} \begin{pmatrix} \cos\theta & \sin\theta \\ -\sin\theta & \cos\theta \end{pmatrix} \tag{21}$$

Where σ_{rr}, $\sigma_{r\theta}$ and $\sigma_{\theta\theta}$ are computed previously for given values of ξ, θ, U and J_m.

To estimate the partial derivatives, i.e. $\Psi_{,1}$ and $\Psi_{,2}$, we solve the system of Eqs. (21). If $\mathbf{X}$ is the unknown column vector that representing the partial derivatives, i.e. $\Psi_{,k}$ and σ the corresponding computed components of the Cauchy stress tensor, then Eqs.
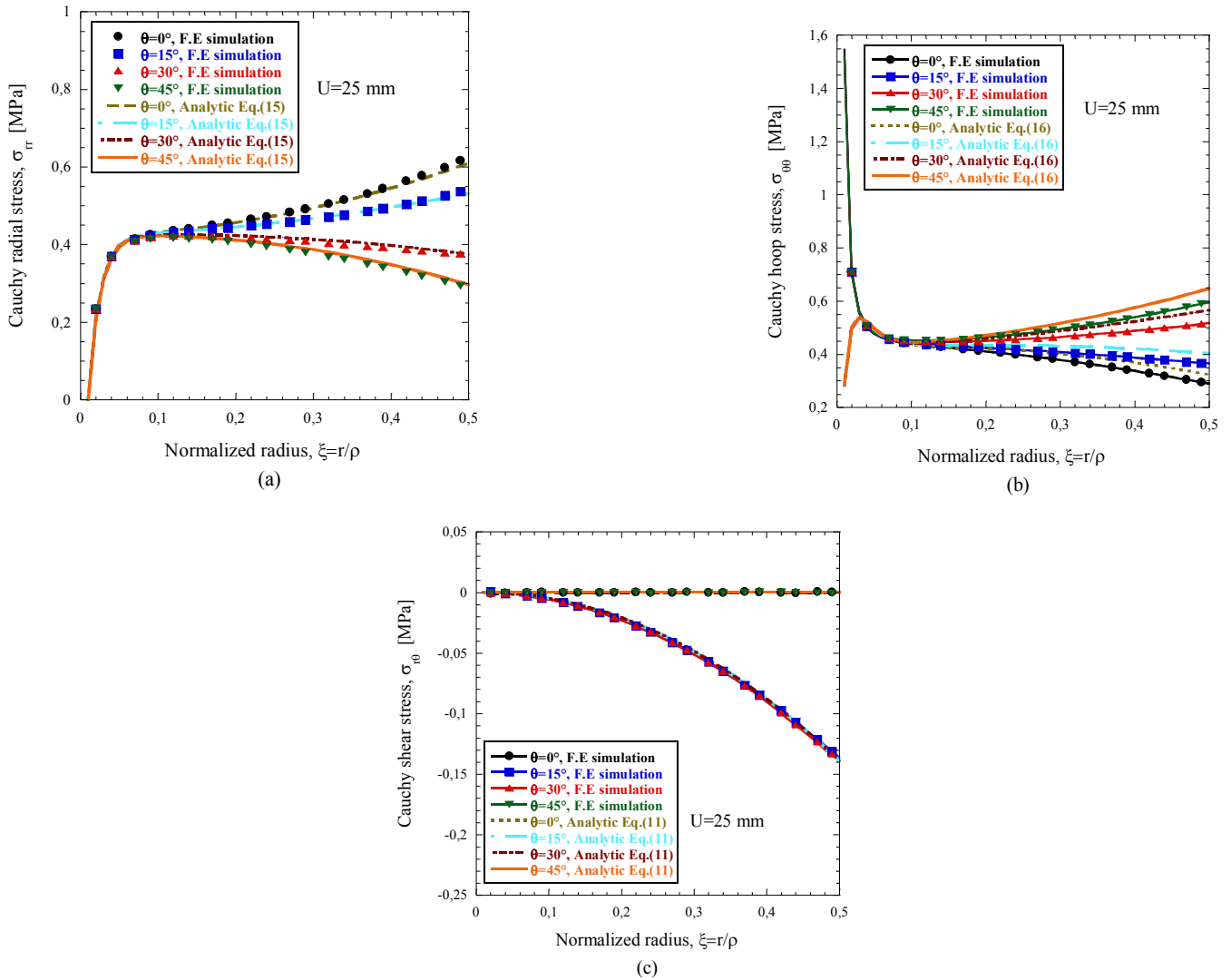
Fig. 7: (a) Comparison of the computed Cauchy radial stress $\sigma_{r\theta}(\xi, \theta)$ and simulated numerically by FE, versus normalized radius ξ and for different values of θ; (b) Comparison of the computed Cauchy hoop stress $\sigma_{rr}(\xi, \theta)$ and simulated numerically by FE, versus normalized radius ξ and for different values of θ; (c) Comparison of the computed Cauchy shear stress $\sigma_{\theta\theta}(\xi, \theta)$ and simulated numerically by FE, versus normalized radius ξ and for different values of θ

K. Yaya, H. Bechir, and S. Bouzidi

Tech. Mech., Vol. 40, Is. 1, (2020), 97–107
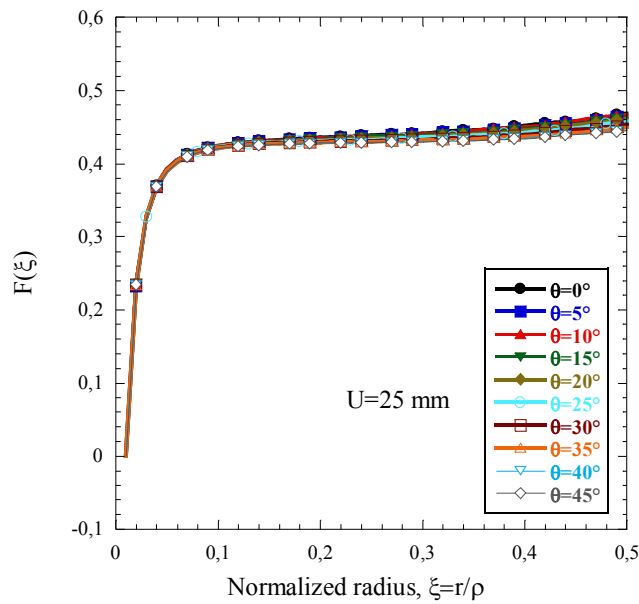
Fig. 8: Graphs of the function $F(\xi)$ versus ξ for different values of θ

(20) can be written as follows:

$$\mathbf{A}\,\mathbf{X} = \boldsymbol{\sigma} \tag{22}$$

where $\mathbf{A}$ is the 3×2 matrix of the linear system of Eqs. (20).

The right-hand side vector $\boldsymbol{\sigma}$ is contaminated by noise (error $\mathbf{e}$), which originates from computation of Cauchy stresses and measurement errors. The solution of Eq. (22) becomes ill-posed if the matrix $\mathbf{A}$ is not invertible; noting that $\mathbf{A}$, is not square. Mostly, the solution of an ill-posed problem without numerical stabilization is not acceptable **?**. A least squares fit of Eq. (22) is performed by first multiplying both sides with the transpose of $\mathbf{A}$:

$$\left(\mathbf{A}^T\mathbf{A}\right)^{-1}(\mathbf{A}^T\mathbf{A})\mathbf{X} = \left(\mathbf{A}^T\mathbf{A}\right)^{-1}\mathbf{A}^T\boldsymbol{\sigma} \tag{23}$$

Eq. (24) is the solution in the least squares sense, and the hyperelastic functions $\mathbf{X}$ are determined with minimizing the square of the sums of the squares of the differences between experimental and theoretical stresses at different strain values (error $\mathbf{e}^2 = e^T\mathbf{e}$) leading to the best fit:

$$\mathbf{X} = \left(\mathbf{A}^T\mathbf{A}\right)^{-1}\mathbf{A}^T\boldsymbol{\sigma} \tag{24}$$

4 Conclusion

An original method has been developed in order to compute the Cauchy stress field around a small hole located in the center of a cruciform specimen, which is subjected to equibiaxial tensile test (stretch ratio 1/1). It has been shown that, both the stress and strain fields are heterogeneous in the core region; the heterogeneity seems to be an advantage for parameter identification. To improve the accurate parameter identification, an analytical relationship has been established between the applied forces on the sample edges and Cauchy local stresses. We emphasize that, the strain-energy density of a rubber-like material could be obtained directly from experimental data arising from this heteregeneous test. Also, the experimental data of this test could be used for the validation of a given constitutive model. We recall that the first and second principal invariants, i.e. I_1 and I_2 are identical in the range of small deformations. As a result, the partial derivatives are very sensitive to experimental noise; thereby, the parameter-identification becomes then ill-posed problem. Besides, the present analysis could be validated experimentally, that will an interesting challenge.

Acknowledgment

K. Yaya, H. Bechir, and S. Bouzidi

Tech. Mech., Vol. 40, Is. 1, (2020), 97–107

Appendix A: Computation of the Cauchy stresses

The equilibrium equations are given by

$$\frac{\partial}{\partial\theta}\left(r\frac{\partial\sigma_{rr}}{\partial r} + \sigma_{rr}\right) = -\left(2\sigma_{r\theta} + r\frac{\partial\sigma_{r\theta}}{\partial r} + \frac{\partial^2\sigma_{r\theta}}{\partial\theta^2}\right) \tag{A.1}$$

$$\sigma_{\theta\theta} = \frac{\partial\sigma_{r\theta}}{\partial\theta} + r\frac{\partial\sigma_{rr}}{\partial r} + \sigma_{rr} \tag{A.2}$$

$$\sigma_{r\theta} = -\sigma_U\, h\,(\xi)\ \sin 4\theta,\ \text{for } \theta \neq 0,\ \pi/4 \text{ and } \pi/2 \tag{A.3}$$

By substituting Eq. (A.3) into Eq. (A.1), we obtain the following differential equation

$$\xi\frac{\partial\sigma_{rr}}{\partial\xi} + \sigma_{rr} = \frac{\sigma_U}{4}\,(14\,h\,(\xi) - \xi\,h'\,(\xi))\cos 4\theta + f\,(\xi) \tag{A.4}$$

The solution of Eq. (A.4) is

$$\sigma_{rr}\,(\xi, \theta) = A\,(\xi, \theta)\,\xi^{-1} = \Omega\,(\xi, \theta) + \xi^{-1}N\,(\theta) \tag{A.5}$$

where

$$\Omega\,(\xi, \theta) = \left(\beta\frac{\sigma_U}{4}\lambda\right)\left(4\xi^2 + 14\xi_a^2 - 13\xi_a\xi\right)\cos 4\theta + F\,(\xi) \tag{A.6}$$

where $F\,(\xi)$ is a function to be determined and related to the function $f\,(\xi)$.
The boundary condition leads to $\sigma_{rr}\,(\xi_a, \theta) = 0$

$$N\,(\theta) = \left(-\frac{5}{4}\beta\sigma_U\lambda\right)\xi_a^3\cos 4\theta \tag{A.7}$$

The radial Cauchy stress is given by

$$\sigma_{rr}\,(\xi, \theta) = \left(\beta\frac{\sigma_U}{4}\lambda\right)\left(4\xi^2 + 14\xi_a^2 - 13\xi_a\xi - 5\xi_a^3\xi^{-1}\right)\cos 4\theta + F\,(\xi) \tag{A.8}$$

where $F\,(\xi)$is inferred from the results of FE-simulations of radial Cauchy stress.
The graphs of the function $F\,(\xi) = \sigma_{rr}\,(\xi, \theta) - \left(\beta\frac{\sigma_U}{4}\lambda\right)\left(4\xi^2 + 14\xi_a^2 - 13\xi_a\xi - 5\xi_a^3\xi^{-1}\right)\cos 4\theta$ versus ξ for different values of θ are shown in Fig. 8.
This function can be approximated by

$$F\,(\xi) = \sigma_U\sqrt{\lambda}\,\Upsilon\,(\lambda),\ \Upsilon\,(\lambda) = a\left[1 - e^{-b\,(\xi-\xi_a)}\right] + c\,(\xi - \xi_a) \tag{A.9}$$

where the constants $a = 0.4,\ b = 67$ and $c = 0.06.$. .
The hoop stress is inferred from Eq. (A.2) as follows:

$$\sigma_{\theta\theta}\,(\xi, \theta) = \left(\beta\frac{\sigma_U}{4}\lambda\right)\left(-4\xi^2 - 2\xi_a^2 + 6\xi_a\xi\right)\cos 4\theta + F\,(\xi) + \xi\,F'\,(\xi) \tag{A.10}$$

Tab. A.1: Model parameters values

parameter	value
c_{10} [MPa]	0.111
c_{01} [MPa]	0.039
μ_0 [MPa]	0.9
κ_0[MPa]	10000

K. Yaya, H. Bechir, and S. Bouzidi

Tech. Mech., Vol. 40, Is. 1, (2020), 97–107

References

L. Chevalier, S. Calloch, F. Hild, and Y. Marco. Digital image correlation used to analyze the multiaxial behavior of rubber-like materials. *European Journal of Mechanics-A/Solids*, 20(2):169–187, 2001.

C. Galliot and R.H. Luchsinger. Uniaxial and biaxial mechanical properties of etfe foils. *Polymer testing*, 30(4):356–365, 2011.

A.N. Gent. A new constitutive relation for rubber. *Rubber chemistry and technology*, 69(1):59–61, 1996.

Z. Guo and L.J. Sluys. Application of a new constitutive model for the description of rubber-like materials under monotonic loading. *International Journal of Solids and Structures*, 43(9):2799–2819, 2006.

S. Hartmann and R.R. Gilbert. Identifiability of material parameters in solid mechanics. *Archive of Applied Mechanics*, 88(1-2): 3–26, 2018.

S. Hartmann, R. R. Gilbert, and C. Sguazzo. Basic studies in biaxial tensile tests. *GAMM-Mitteilungen*, 41(1):e201800004, 2018.

F. Hild and S. Roux. Digital image correlation: from displacement measurement to identification of elastic properties–a review. *Strain*, 42(2):69–80, 2006.

G.A. Holzapfel. *Nonlinear Solid Mechanics: A Continuum Approach for Engineering*, 2000.

C.O. Horgan and G. Saccomandi. Pure axial shear of isotropic, incompressible nonlinearly elastic materials with limiting chain extensibility. *Journal of elasticity*, 57(3):307–319, 1999.

C.O Horgan and G. Saccomandi. Pure azimuthal shear of isotropic, incompressible hyperelastic materials with limiting chain extensibility. *International journal of non-linear mechanics*, 36(3):465–475, 2001.

J.-J. Hu, G.-W. Chen, Y.-C. Liu, and S.-S. Hsu. Influence of specimen geometry on the estimation of the planar biaxial mechanical properties of cruciform specimens. *Experimental Mechanics*, 54(4):615–631, 2014.

M. Johlitz and S. Diebels. Characterisation of a polymer using biaxial tension tests. Part I: Hyperelasticity. *Archive of Applied Mechanics*, 81(10):1333–1349, 2011.

M. Mooney. A theory of large elastic deformation. *Journal of applied physics*, 11(9):582–592, 1940.

R.W. Ogden. *Non-Linear Elastic Deformations*. Courier Corporation, New York, 1997.

N. Promma, B. Raka, M. Grediac, E. Toussaint, J.-B. Le Cam, X. Balandraud, and F. Hild. Application of the virtual fields method to mechanical characterization of elastomeric materials. *International Journal of Solids and Structures*, 46(3-4):698–715, 2009.

M. Sasso, G. Palmieri, G. Chiappini, and D. Amodio. Characterization of hyperelastic rubber-like materials by biaxial and uniaxial stretching tests based on optical methods. *Polymer Testing*, 27(8):995–1004, 2008.

H Seibert, T Scheffer, and S Diebels. Biaxial testing of elastomers-experimental setup, measurement and experimental optimisation of specimen's shape. *Technische Mechanik*, 34(2):72–89, 2014.

J.C. Simo and T.JR. Hughes. *Computational inelasticity*, volume 7. Springer Science & Business Media, 2006.

S. Timoshenko. *Theory of Elasticity*. McGraw Hill Book Co., New York Toronto London, 1951.

W. Zhang, Y. Feng, C.-H. Lee, K. L. Billiar, and M. S. Sacks. A generalized method for the analysis of planar biaxial mechanical data using tethered testing configurations. *Journal of biomechanical engineering*, 137(6):064501, 2015.

Instructions for Authors

TECHNISCHE MECHANIK publishes articles in all fields of mechanics, theoretical as well as applied, including related disciplines, and in particular also articles demonstrating practical applications. The journal publishes full length papers, as well as discussions on papers which have appeared in the journal.
TECHNISCHE MECHANIK is a non-profit (open-access) journal, founded by the Otto-von-Guericke-University. It can be freely downloaded from the website.

Manuscripts have to be written with LaTeX. The most important features of the style guidelines are implemented in the files contained in **tm-article.zip** (download from http://www.ovgu.de/techmech/).

Each submitted paper runs through a standard peer review process. Please suggest three international well known reviewers for your paper when you submit it.

Please submit your paper in electronic form by email.

Hinweise für Autoren

Die Zeitschrift TECHNISCHE MECHANIK veröffentlicht Forschungsarbeiten aus dem Gesamtgebiet der Mechanik, d. h. allen Zweigen der theoretischen und angewandten Mechanik einschließlich angrenzender Fachgebiete sowie Diskussionsbeiträge zu in dieser Zeitschrift erschienenen Arbeiten. Die Zeitschrift ist ein open-access Journal das 1980 von der Otto-von-Guericke-Universität gegründet wurde. Alle Artikel können kostenfrei von unserer Webseite herunter geladen werden.

Artikel werden ausschließlich in englischer Sprache veröffentlicht.

Die Manuskripte müssen in LaTeX geschrieben werden. Die wichtigsten Stil-Richtlinien sind in den Dateien umgesetzt, die in **tm-article.zip** (bereit gestellt unter http://www.ovgu.de/techmech/) enthalten sind.

Jeder eingereichte Beitrag durchläuft einen standardmäßigen Begutachtungsprozess. Bitte schlagen Sie bei Einreichung des Artikels drei mögliche, international renommierte Gutachter vor.

Bitte reichen Sie Ihren Beitrag elektronisch per E-Mail ein.

Inhalt / Contents

Coverphoto by Stefanos Athanasopoulus, © 2019